eman ta zabal zazu

Universidad del País Vasco

Euskal Herriko Unibertsitatea

High voltage cathodes for Na-ion batteries: $Na_3V_2O_{2x}(PO_4)_2F_{3-2x}$ system

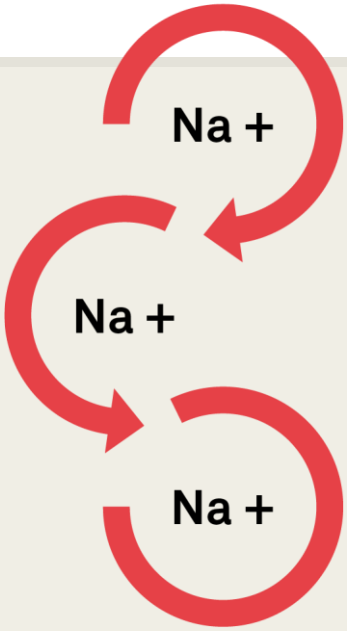

Paula Serras Malillos

July 2014

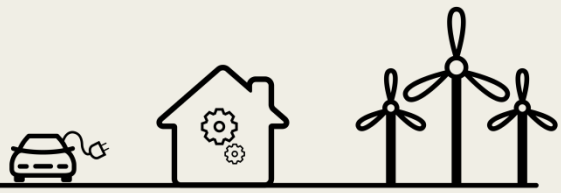

ZTF-FCT
Zientzia eta Teknologia Fakultatea
Facultad de Ciencia y Tecnología

Dpto. de
Química
Inorgánica

eman ta zabal zazu
Universidad del País Vasco
Euskal Herriko Unibertsitatea

High voltage cathodes for Na-ion batteries: $Na_3V_2O_{2x}(PO_4)_2F_{3-2x}$ system

Submitted for the Degree of PhD at the University of the Basque Country

presented by

Paula Serras Malillos

Leioa, July 2014

CIC energiGUNE
energy cooperative research centre

BCMaterials
BASQUE CENTER FOR MATERIALS, APPLICATIONS & NANOSTRUCTURES
ehu.group

icmcb

UNSW
AUSTRALIA

Acknowledgements

Haber estudiado Ingeniería Química y hacer la tesis en el ámbito de la Química Inorgánica hace que tengas que agradecer algo a casi todo el que te ha rodeado a lo largo de estos 4 años ya que para mí, éste ha sido un micromundo nuevo que explorar en el que sin duda me habría perdido sin la ayuda de todos aquellos que han hecho posible que hoy esté escribiendo estas palabras.

Me gustaría empezar agradeciendo por tanto al Director del Departamento de Química Inorgánica de la Facultad de Ciencia y Tecnología de la UPV/EHU Pascual Román por haberme acogido en el mismo. Asimismo, mi más sincero agradecimiento al Profesor Teófilo Rojo por haberme permitido trabajar bajo su dirección y por hacer posible que esta tesis se haya llevado a cabo.

Querría extender mi agradecimiento a las doctoras Izaskun Gil de Muro y Maite Insausti por sus micrografías de transmisión y análisis termogravimétricos respectivamente, y a la Dra. Aintzane Goñi porque su trabajo y ayuda han contribuido a importantes descubrimientos en esta tesis. Mención especial para el Profesor Luis Lezama, no sólo por las medidas de EPR realizadas sino porque su profesionalidad, seriedad y sabiduría han hecho que siempre haya podido contar con su ayuda y consejo, cuantas veces ha sido necesario.

En lo que a mis compañeros respecta no cabe duda de que en 4 años se conoce a muchas personas y se comparten anécdotas con gente tan dispar como Dorleta, Beñat, Jagoba, Aroa, Oihane, Imanol, Joseba, Irune, Javi, Aritza o Maider. Además, he disfrutado mucho con el humor y la inteligencia abrumadora de Idoia Castellanos y los momentos especiales con Amaia y Amaia. También con la cercanía y buen carácter de Xabi y Paula Sánchez. Ricardo, tú también eres uno de mis favoritos y aunque

pronto dejaré de ser *Wolowitz* para tí, siempre podrás contar con mis sabios consejos, ya sea en la ciencia o en la moda. Finalmente, me reservo a la Dra. Verónica Palomares en última posición para que un muy buen sabor de boca cierre este párrafo. Las palabras "equipo", "trabajo" y "constancia" han cobrado un nuevo significado para mí desde que te conozco. Me ha parecido que nos hemos complementado a la perfección y me has demostrado ser una Directora magnífica. He sentido tu apoyo siempre y eso me ha animado a seguir y a esforzarme con más fuerza. Gracias, de verdad.

Querría dar las gracias también a los miembros de los Servicios Generales de Investigación de la UPV/EHU, SGIker, en especial a los doctores Javier Sangüesa y Aitor Larrañaga por sus medidas de difracción de rayos X y su gran disponibilidad. A la Dra. Ana Martínez y al Dr. Sergio Fernández por sus micrografías SEM y a los doctores Iñaki Orue y Luis Bartolomé "Txesko" por su *magnetismo* y *analítica* respectivamente. Gracias a todos por vuestro buen humor y siempre buena disposición. Da gusto trabajar con gente así.

Me gustaría resaltar también la buena acogida de las personas del CICEnergigune en cuyo centro he podido llevar a cabo muchas de las medidas que se presentan en este trabajo. No sólo ha sido una cuestión de medidas y resultados sino también de buenos momentos con la gente de allí, siempre dispuestos a ayudar. Entre ellos me gustaría destacar especialmente a los doctores Javier Carretero, Elizabeth Castillo, Sofía Pérez, Naiara Fernández, Pierre Kubiak o Juan Miguel López del Amo.

Debido a que éste ha sido un trabajo de grandes colaboraciones no me puedo olvidar de la ayuda prestada por el Profesor Neeraj Sharma, quien desde la *University of New South Wales* en Australia me ha proporcionado resultados, explicaciones, consejos y un sinfín de pequeños detalles que sin duda hacen de él un gran profesional y una gran persona. *Thank you very much Neeraj for your hard work, your advices, your patience and the*

way you always see everything in such a positive way, it is a pleasure to work with people like you. En este sentido y aunque no haya tenido un trato tan cercano me gustaría agradecer también la ayuda prestada y el trabajo realizado por la Dra. Helen Brand perteneciente al *Australian Synchroton*. *Thank you very much for your work and help, Helen.*

Por otro lado, si hay algo que nunca pensé que llegaría a hacer es pisar no uno sino dos aceleradores de partículas como el de Elettra en Italia y Diamond en Inglaterra. Fueron experiencias intensas en las que el apoyo y ayuda de los doctores Luca Olivi y Giuliana Aquilanti en Elettra y la del Dr. Giannantonio Cibin en Diamond fueron indispensables. La disponibilidad del Dr. Robert Dominko fue de agradecer también. Por supuesto, mención especial para el Dr. Javi Alonso cuya implicación, tesón y amabilidad hacen que sea un placer trabajar con él. Gracias también a la Profesora María Luisa Fdez.-Gubieda por sus consejos y experiencia.

Merci beaucoup Dr. Laurence Croguennec pour votre accueil chaleureux au sein de l'ICMCB. It has been a real pleasure to work in Groupe 2. You made me feel at home. Special mention to the members of the "Dream Team" Mercedes, Cédric, my little teenagers Florian and Vincent, not only party boy Laurent (JP when he is serious) and my BFF Stéphane. You are very good person, "duck", and when "sometimes you need something" you are always there. I will miss you all. See you soon in Kelerville 2.0!

Por otro lado, mi incursión en el mundo laboral, no habría sido la misma sin mis compañeros de I+C en el centro tecnológico CEIT en San Sebastián, Elena, Jon, y Alaitz en origen y Oier e Izaro como nuevas incorporaciones. Fueron grandes años con grandes personas con las que a día de hoy sigo compartiendo grandes momentos, tan grandes como la cima de 3EM que alcanzamos con cacahuetes en una mano y una *Cuore Stylo* en la otra. Espero que sigamos recorriendo grandes valles y montañas juntos.

Otro gran bloque del que no me puedo olvidar es el de mis amigas, uno de los pilares que sostienen mi vida. Me proporcionáis serenidad, paz interior, amor y grandes momentos de “chicas” (incluso de “chicos” a veces). La verdad es que para no tener nada que ver con este ámbito sois una gran fuente de energía positiva para mí. Espero que sea inagotable.

Por supuesto, lo que soy hoy día no habría sido posible sin Mila e Iñaki, mis padres, que me han dado siempre la libertad de elegir, me han educado en el respeto y el trabajo duro y sobre todo me han enseñado que somos capaces de hacer lo que nos propongamos. Mi tío Antxon es también una de esas personas que dejan huella. Carismático donde los haya me ha enseñado los “valores” de la vida y aunque parezca que no, ha influido y mucho en mí. Mi hermana Adriana sin la que no imagino mi vida me enseña cada día lo que significa exprimir cada instante de la misma. Tus “Serrasadas” son mías también y aunque estemos un poco “chaladas” al menos nos tenemos la una a la otra. Por otro lado, la incorporación de Mikel Garate a nuestras vidas ha sido un acierto, a ti te ha hecho más feliz y a mí me ha proporcionado un magnífico diseño de portada. Milesker Mikel zure laguntzagatik.

Finalmente he de decir que una de las estructuras más sólidas y estables que he construido jamás es la que tengo con Alex. Lo que empezó como estudios y fiesta a partes iguales ha acabado siendo complicidad, apoyo, discusiones, sonrisas y muchas risas. Sobre todo eso, carcajadas que hacen que sienta que somos parte de algo que sólo tú y yo conocemos. No cabe duda de que entre nosotros hay…Química.

Richard Morris, profesor de Neurociencia de la Universidad de Edimburgo, interesado en la memoria de los roedores, llevó a cabo en su laboratorio un experimento que constaba de dos pruebas consecutivas.

Previamente había escogido al azar dos docenas de conejillos de Indias o "cobayas". En la primera prueba introdujo a la mitad en un estanque de agua enturbiada con un poco de leche, para que no vieran unos cuantos montículos que había colocado en el fondo. Éstas eran las cobayas "con suerte", porque mientras braceaban para flotar se podían apoyar y descansar temporalmente en los promontorios ocultos en el fondo del estanque, antes de proseguir su marcha en busca de una salida.

A la otra docena de cobayas las metió en un estanque similar pero sin los montículos. Estos conejillos "desafortunados" no tenían más remedio que nadar sin descanso para no ahogarse. Después de un buen rato, Morris sacó a todos los exhaustos animalitos del agua para que se recuperaran. Y después les hizo la segunda prueba: El investigador echó a las 24 cobayas en el estanque que no tenía montículos en el fondo. Mientras las cobayas del grupo "con suerte", a las que en el primer experimento les había tocado el estanque con montículos para apoyarse, nadaban a un ritmo tranquilo, el grupo de cobayas "desafortunadas" chapoteaba desesperadamente sin rumbo. Justo antes de ahogarse, Morris las rescató una a una y las devolvió a sus jaulas.

Cuando el investigador calculó los minutos que las cobayas se habían mantenido a flote, descubrió que las cobayas "con suerte" habían nadado más del doble del tiempo que las "desafortunadas".

Su conclusión fue que las cobayas "con suerte" nadaron más tranquilas y durante más tiempo porque recordaban los invisibles montículos salvadores de la primera prueba, lo que los motivaba a buscarlas con la "esperanza" de encontrarlas. Por el contrario, las cobayas que durante la primera prueba no habían encontrado apoyo alguno, tenían menos motivación para nadar y hasta para sobrevivir.

“La Fuerza del optimismo” – Luis Rojas Marcos

Summary

Batteries are one of the most determining energy storage devices due to their the wide range of sizes in which they can be manufactured, their ability to supply electrical power instantly, their portability and the option of single-use or multiple-use units. Among them, sodium-ion batteries are presented as the best alternative to lithium-ion batteries especially in the field of stationary energy storage due to the more abundance and lower cost of sodium. Thus, it is necessary to search and optimize new electrode and electrolyte materials in order to better understand the behaviour of these sodium based devices.

One of the most promising cathodic materials for sodium-ion batteries are the sodium vanadium fluorophosphates: $NaVPO_4F$, $Na_3V_2(PO_4)_2F_3$ and $Na_3V_2O_2(PO_4)_2F$. They show high voltage performance and long-term stability so that they could lead to high energy density materials. In this work, the family of compounds $Na_3V_2O_{2x}(PO_4)_2F_{3-2x}$ has been identified and a relation between V^{3+} $Na_3V_2(PO_4)_2F_3$ and V^{4+} $Na_3V_2O_2(PO_4)_2F$ extreme phases has been established. Different compounds belonging to the $Na_3V_2O_{2x}(PO_4)_2F_{3-2x}$ family have been hydrothermally synthesised by variating the type and amount of *in-situ* carbon in the final product. The obtained results have been analysed and among them, $Na_3V_2O_{2x}(PO_4)_2F_{3-2x}$ ($x = 0.8$) and $Na_3V_2O_2(PO_4)_2F$ samples have been deeply studied.

In the first chapter, an overview of the current energy situation and the future scenario is given. In this context, batteries emerge as an interesting alternative, and therefore, various types of these batteries are briefly introduced with special focus given to cathodic materials for room-temperature sodium-ion batteries.

Chapter 2 covers the synthesis and characterisation of the $Na_3V_2O_{2x}(PO_4)_2F_{3-2x}$ family with especial focus on $Na_3V_2O_{2x}(PO_4)_2F_{3-2x}$ (x = 0.8) and $Na_3V_2O_2(PO_4)_2F$ compounds. Several characterisation methods, such as X-ray diffraction, infrared spectroscopy, electronic microscopy, magnetic measurements and electron paramagnetic and nuclear magnetic resonance (EPR and NMR, respectively) are used to determine the most important features of each material. Besides, the real existence of $NaVPO_4F$ phase is also discussed.

Chapter 3 is based on the electrochemical characterisation of $Na_3V_2O_{2x}(PO_4)_2F_{3-2x}$ family where the influence of the *in-situ* carbon is discussed. The $Na_3V_2O_{2x}(PO_4)_2F_{3-2x}$ (x = 0.8) phase is further analysed and the influence of the carbon coating of raw $Na_3V_2O_2(PO_4)_2F$ sample is also investigated.

Finally, in Chapter 4 the electrochemical mechanism of $Na_3V_2O_{2x}(PO_4)_2F_{3-2x}$ (x = 0.8) and $Na_3V_2O_2(PO_4)_2F$ phases has been studied by both, *ex-situ* and *in-situ* analysis and the most remarkable differences and similarities between them have been discussed.

Contents

Chapter 1. Introduction

1.1 The need for Energy Storage

Energy production is becoming an important issue for the support of the society. According to British Petroleum, fuel consumption was growing significantly in the last 25 years from 7.300 Mtoe in 1987 (Mtoe: Million Tonnes of Oil Equivalent) to 10.900 Mtoe in 2012 [1]. On the other hand, the World Energy Outlook (WEO) estimates that, in the medium term, global CO_2 emissions from fuel combustion will continue growing, even if it is at a lower rate, reaching 37.2 $GtCO_2$ by 2035 [2]. Driven by the need to reduce the emissions of CO_2 and increase energy security, policy makers have implemented different measures in order to shift to low-carbon energy resources [3,4].

1.1.1 Energy Storage for Portable Electronic Devices and Electric Vehicle

The great demand for portable electronic devices supplied by light electric power sources as well as an increasing interest for electrically powered vehicles result in a

1 *BP-Statistical Review of World Energy*. June **2013**.

2 *International Energy Agency (IEA) Statistics.* "CO_2 emissions from fuel combustion. Highlights". **2013** Edition.

3 Pavley, F.;Nunez, F. *California Assembly Bil No. 32-GlobalWarming solutions Act of 2006*, **2006**.

4 CARPS, *California Codes: Public Utilities Code. Section 399.11-399.31. California Renewables Portfolio Standard Program,* **2009**.

continuous development of high-performance energy systems. Lithium-ion and nickel-metal hydride batteries, fuel cells, and supercapacitors belong to such promising energy supplies [5]. Among them, batteries are considered as the most suitable devices for energy storage due to their wide range of sizes in which they can be manufactured or assembled into packs, their portability (for smaller sizes) and the option of single-use or multiple-use units.

In the 1940s, the principal domestic uses for batteries were in pocket torches (flashlamps), in a few toys, in vehicles (for starting, lighting and ignition), and in radios. Over the past 70 years, the applications for small sealed batteries (customer batteries) have expanded considerably. Today, small primary or rechargeable batteries are employed in a huge number of devices as mobile phones, laptops or portable tools (hair trimmers, shavers, screwdrivers, etc.) and many of them are batteries of advanced design and performance as a result of developments in materials science and technology [6].

On the other hand, the transport sector is a key contributor to both greenhouse gas (GHG) emissions and local pollution. The International Energy Agency (IEA) estimates that 20% of global primary energy use and 25% of energy-related CO_2 emissions are due to this sector. If current trends persist, global energy demand for transport and energy-related CO_2 emissions are expected to double by 2050. The increasing concerns on rising GHG emissions and security of oil supply make the development of low-carbon and carbon-free technologies for transportation a high priority for policy makers around the world [7]. In fact, one of the strategies to limit long-term global temperature increase and dependence from fossil fuels is the development of electric vehicles (EVs). In December 2008, the European Parliament adopted the “Climate and Energy Package” legislation, which sets ambitious targets for the EU. Specifically, by 2020 GHG emissions should be at least 20% lower than 1990 levels, energy efficiency should increase by 20% and the share of renewable energy consumption and transport should reach 20% and 10%, respectively, so the development of cost-competitive EVs is therefore one of the priorities policy [7].

5 Chau, K.T.; Wong, Y.S.; Chan, C.C. *Ener. Conv. Manag.,* **1999,** 40, 1021-1039.

6 Dell, R.M.; Rand, D.A.J. “Understanding batteries” RSC paperbacks. **2001**.

7 Catenacci, M.; Verdolini, E.; Bosetti, V.; Fiorese, G. *Energy Policy*., **2013**, 61, 403-413.

Research, Development and Demonstration (RD&D) efforts are focused on reducing the high costs of EVs by developing better and more efficient battery technologies. Some of the different options are presented in Figure 1.1.

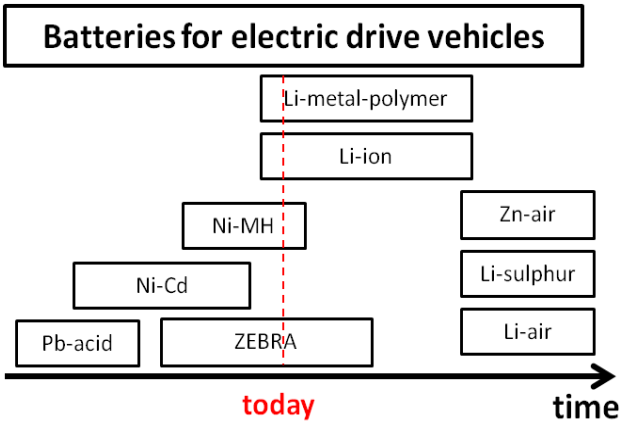

Figure 1.1 *Technology paths and their different state of development. "Reprinted from G. Energy Policy., 61, Catenacci, M.; Verdolini, E.; Bosetti, V.; Fiorese, Going electric: Expert survey on the future of battery technologies for electric vehicles 403-413, 2013, with permission from Elsevier."*

Lead acid (Pb-acid) are a well known technology but these batteries have very low specific energy so that they are limited to applications where short distances are travelled between recharges. Nickel–cadmium (Ni–Cd) batteries have been successfully used in the past decades, but they have been banned because of the toxicity of their components. Nickel Metal Hydride (Ni-MH) batteries are currently successfully used in hybrid, non plug-in, vehicles. However, for applications in plug-in hybrid electric vehicles (PHEVs) a higher specific energy is required and thus this technology will be probably replaced by Li-ion batteries [8-10]. Molten salt batteries

8 Cluzel, C.; Douglas, C. **2012**. "Cost and performance of EV batteries, Element Energy". *Final Report for the Committee on Climate Change*.

9 Armand, M.; Tarascon, J.M. *Nature*, **2008**, 451, 652–657.

10 Tollefson, J. *Nature*, **2008**, 456, 436–440.

(*e.g.*, Zebra) are also currently used in commercial EVs, but they have several drawbacks mainly related to the high temperature required [8]. Li-ion batteries are a promising technology for the high energy density requirements in EVs applications. However, there are still some remaining disadvantages related to safety standards, *e.g.*, thermal runaways that need to be solved. Finally, there are few technologies in lab/prototype stage which have the potential to offer superior battery performance. In particular, there is much interest in lithium-sulphur (Li-sulphur) and lithium-air (Li-air) batteries [11], which theoretically could achieve energy densities higher than 2500 $Wh \cdot kg^{-1}$ (the Li-ion current range for transport application is 100–180 $Wh \cdot kg^{-1}$).

1.1.2 Energy Storage for Renewable Energy Systems

A variety of renewable and clean energy sources, such as wind and solar power, are growing rapidly as low carbon electricity sources. However, the increasing use of these clean energy sources entails other problems, such as modulating time-variable energy production from renewable resources due to their dependence on the weather to integrate them into the grid. In order to solve the problem concerning the intermittency of renewable energy sources (RES) additional stationary energy storage devices are needed. For example, for every 10% wind penetration it is expected that, an extra balancing power of approximately 2-4% of the installed wind capacity is required in order to maintain the stability of the power system. This is an important issue for countries with a large implantation of solar and wind systems such as Denmark or Spain where about 20% and 10% of the electricity generation come from wind power, respectively [12]. Thus, a large-scale energy storage system (ESS) is extremely important to shift electrical energy from on-peak (high demand) to off-peak (low demand) periods to reach smart grid management [13]. Smart grid integrates advanced sensing technologies, control methods and integrated communications into current electricity network. These features optimise the operation of the whole power network

11 Christensen, J.; Albertus, P.; Sanchez-Carrera, R.S.; Lohmann,T.; Kozinsky, B.; Liedtke, R.; Ahmed, J.; Kojic, A. *J. Electrochem. Soc*., **2011**, 159, R1–R30.

12 Vazquez, S.; Lukic, S.M.; Galvan, E.; Franquelo, L.G.; Carrasco, J.M. *IEEE T. Ind. Electron.*, **2010**, 57, 3881-3895.

13 Pan, H.; Hu, Y.-S.; Chen, L. *Energy Environ. Sci*., **2013**, 6, 2338-2360.

balancing the generation, demand environment and market constrains [14,15]. It has been proven that the long-term storage system (up to 1 day) is more advantageous than the short-term one (less than 1 hour) since in the latter case a small increase in the amount of generated electricity can be absorbed by the power grid. However, the long-term storage systems are much more costly solutions than the short-term ones [16]. Thus, the operating policies applied for the storage devices (peak shaving) consist of storing cheap electricity during the off-peak demand period in order to return it back to the grid during the high demand and normally this process takes place within the time frame of 1-10 h [17]. Suitable candidates for peak shaving applications are compressed air energy storage (CAES), flywheel energy storage (FES) and pumped hydro energy storage (PHES) as mechanical energy storage technologies, thermal energy storage (TES) and batteries (BES) as electrochemical energy storage technologies. To gain a better view of the world´s energy storage scenario, a comparative estimation of current installed capacity of worldwide energy storage plant is shown in Figure 1.2 [18].

Both CAES and PHES are considered long-term time scale storage technologies with similar characteristics. However, installation of CAES or PHES should be permitted by the topographical conditions of local region. Besides, the response time of CAES or PHES is not fast enough to smooth or balance fluctuation of wind power [19-22]. Battery energy storage (BES) system is the most widely used storage technology available for power system application. High power and energy capacity of the battery can be obtained by electrically connecting the cells in series and parallel. Different types of batteries have been developed and many are mature technologies available on

14 Wade, N.S.; Taylor, P.C.; Lang, P.D.; Jones, P.R. *Energ. Policy*, **2010**, 38, 7180-7188.

15 Roberts, B.P.; Sandberg, C. *Proceedings of the IEEE* **2011**, 99, 1139-1144.

16 Koohi-Kamali, S.; Tyagi, V.V.; Rahim, N.A.; Panwar, N.L.; Mokhlis, H. *Renew. Sust. Energ. Rev.*, **2013**, 25, 135-165.

17 Díaz-González, F.; Sumper, A.; Gomis-Bellmunt, O.; Villafáfila-Robles, R. *Renew. Sust. Energ. Rev.*, **2012**, 16, 2154-2171.

18 EPRI. Electricity Energy Storage Technology Options. **2010**.

19 Hadjipaschalis, I.; Poullikkas, A.; Efthimiou, V. *Renew Sustain Energy Rev*. **2009**, 13, 1513-1522.

20 Ibrahim, H.; Ilinca, A.; Perron, J. *Renew Sustain Energy Rev*. **2008**, 12, 1221-1250.

21 Masaud, T.M.; Lee, K.; Sen, P.K. *NAPS 2010: proceedings of North American power symposium,* Arlington, TX, USA, September 26-28, **2010**.

22 Guerrero, M.A.; Romero, E.; Barrero, F.; Milanes, M.I.; Gonzalez, E. *CPE 2009: proceedings of compatibility and power electronics,* Badajoz, Spain, May 20-22, **2009**.

the market. Lithium-ion, sodium–sulfur (Na-S), and redox flow batteries (RFB) are the promising technologies for applications in power system. Lithium-ion batteries offer superior energy efficiency, high power density, fast charge and discharge capability, low weight, and long cycle life (3000 cycles at 80% depth of discharge (DOD)). However, they present high self-discharge rate (1–5% per day) and high cost due to special packaging and internal over charge protection circuits as the major obstacles for wider and larger applications. Vanadium Redox battery (VRB) and Zinc Bromine battery (ZBB) are widely considered RFB in the market. The principal characteristics of RFB are decoupled power and energy capacity, fast response, low self-discharge and long lifetime. RFBs are one of the appropriate options for long duration energy storages. The major weakness of RFB is the increased capital and running costs associated with pump and flow control systems.

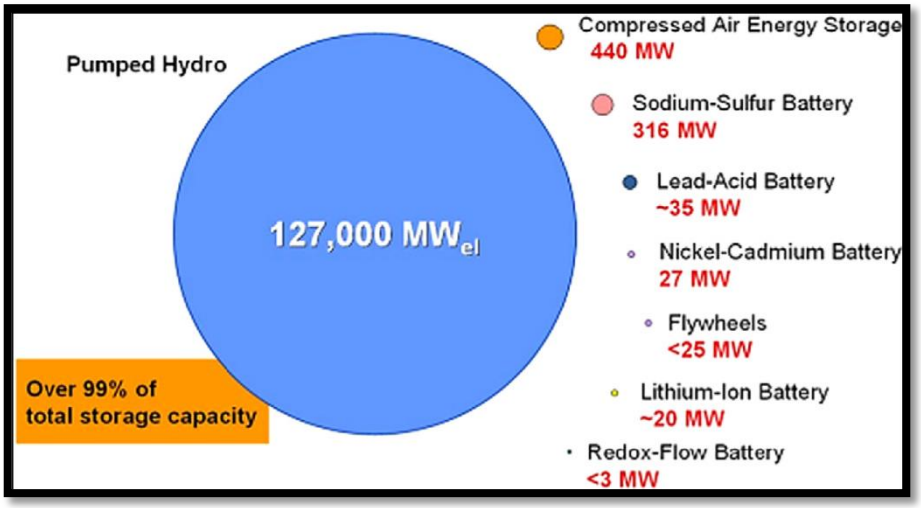

Figure 1.2 *Worldwide installed storage capacity for electrical energy [18].*

Na-S battery is also one of the leading technologies with high energy efficiency (75–89%), no self-discharge, long cycle life (2500 cycles at 100% DOD), pulse power capability and lower capital cost than other batteries except lead-acid battery. The main

defect of Na-S battery is high temperature operation (around 350ºC) [23-25]. From the above analysis, there exist a large variety of storage technologies with different attributes which are suitable for different applications. Thus, the ideal choice of storage technology for a specified application depends on a number of factors including the amount of energy or power to be stored, the time scale of stored or released energy to be required, spacing and environmental constraints, investment cost, the exact location in the network, and the functionality of storage to be required [19].

1.2 Batteries: Energy storage devices

A battery is a chemical device for the storage of electricity. Since electricity cannot be stored directly (except in electrolytic capacitors or superconducting coils, both of which have major technical and economic limitations) it is necessary to employ an indirect form of storage. The convenience of batteries lies in the wide range of sizes in which they may be manufactured or assembled into packs, their ability to supply electrical power instantly, their portability (for smaller sizes) and the option of single-use or multiple-use units. The last-mentioned feature provides useful means for classifying the many different battery systems into two broad categories: primary batteries, which use the chemicals once only in a single discharge, and secondary batteries or "rechargeable batteries", which may be recharged and used again. In the latter batteries, the charging process involves the uptake of electricity and the conversion of the chemicals back into their original forms, so that they are available for a further discharge.

Among the secondary batteries, the lead-acid battery is the oldest and most mature technology. The cycle life of this system is 1000–2000 cycles at 70% DOD, with an efficiency of 72–80%. The lifetime of a lead-acid battery is relatively short because of their poor performance at low and high ambient temperatures and short cycle life. The other major drawbacks of lead-acid battery are frequent water maintenance (flooded type) and heavy metals. On the other hand, nickel–cadmium (Ni-Cd) battery is a type of

23 Diaz-Gonzalez, F.; Sumper, A.; Gomis-Bellmunt, O.; Villafafila-Robles, R. *Renew Sustain Energy Rev*. **2012**, 16, 2154-2171.

24 Divya, K.C.; Ostergaard, J. *Electric Power Syst. Res*., **2009**, 79, 511-520.

25 Tan, X.G.; Li, Q.M., Wang, H. *Int. J. Electric Power Energy Syst.*, **2013**, 44, 179-191.

alkaline rechargeable battery, which is a well-established technology in the market. Compared to lead-acid battery, Ni-Cd battery has a longer cycle life (3000 cycles at 100% DOD) and less maintenance but it costs much more. Meanwhile, both of lead acid and Ni-Cd batteries contain toxic heavy metals and suffer from severe self-discharge.

The size and value of the market for different classes of battery is difficult to estimate but it is clear that it is focused on consumer primary and secondary cells, automotive batteries, and in industrial batteries for stationary energy storage.

1.2.1 Sodium-ion vs. Lithium-ion batteries

For several decades, lithium ions have been successfully employed as a charge carrier for secondary batteries. The outstanding electrochemical performance of lithium ions derives from their small ionic size, low atomic number, and the lowest redox potential in the periodic system. Among various metallic or semi-metallic cations located in s, p, d and f blocks lithium ions have the smallest ionic radius (0.76 Å) which permits fast kinetics by diminishing the diffusion barrier. Furthermore, the small atomic weight (6.941 $g \cdot mol^{-1}$) and low redox potential (-3.04 V *vs.* Standard Hydrogen Electrode (SHE)) enable high theoretical specific capacity and energy density for rechargeable energy storage systems. Due to their excellent electrochemical performance, lithium-ion batteries have been successfully integrated into mobile phones, medical and military devices and EVs [26]. However, the large-scale demand for this alkali would increase the price of its resources due to the low abundance of lithium in the Earth´s crust (see Figure 1.3) [27]. In 2008, the total global Li consumption was approximately 21.280 tons, so it has been estimated that the actual mineable resources could be sustained for approximately another 65 years, considering an average growth of 5% per year [28].

26 Hong, S.Y.; Kim, Y.; park, Y.; Choi, A.; Choi, N.-S.; Lee, K.T. *Energy and Environ. Sci*., **2013**, 6, 2067-2081.

27 Pan, H.; Hu, Y.-S.; Chen, L. *Energy and Environ. Sci.*, **2013**, 6, 2338-2360.

28 Lu, X.C.; Xia, G.G.; Lemmon, J.P.; yang, Z.G. *J. Power Sources*, **2010**, 195, 2431-2442.

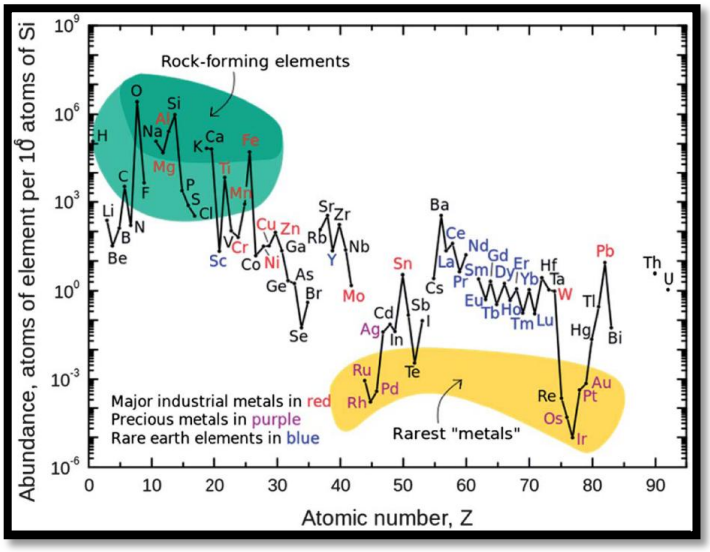

Figure 1.3 *The abundance of chemical elements in Earth´s crust "Reproduced from Ref 27 with permission of The Royal Society of Chemistry."*

Table 1.1 *The comparison between sodium (Na) and lithium (Li) elements [27,29].*

	Na	**Li**
Cation radius	1.02 Å	0.76 Å
Atomic weight	23 g·mol^{-1}	6.9 g·mol^{-1}
E^0 *vs.* SHE	-2.7 V	-3.04 V
Melting point	97.7 ºC	180.5 ºC
Abundance*	23.6·10^3 mg·kg^{-1}	20 mg·kg^{-1}
Distribution	Everywhere	70% in South America
Price, carbonates	0.07-0.37 euros per kg	4.11-4.49 euros per kg

*mg of Na or Li per kg of Earth crust.

The low lifespan together with an increasing production of batteries will lead to a growing waste of these devices. Indeed, in the United States (US), some states as California or New York have already attempted to avoid this waste stream by disposing

29 Palomares, V.; Serras, P.; Villaluenga, I.; Hueso, K.B.; Carretero-González, J.; Rojo, T. *Energy Environ. Sci.*, **2012**, 5, 5884-5901.

bans on rechargeable batteries [30,31]. However, infrastructure required to recycle batteries is still lagging. While some companies have developed recycling processes (*e.g.,* Toxco and Umicore), a fully recycling infrastructure for end-of-life (EOL) lithium-ion batteries is not well developed yet and the costs of such infrastructure have not been examined in depth. From an environmental point of view, the ability to recover materials (*e.g.*, cobalt and nickel) from waste lithium-ion batteries and return them to new battery production has the potential to reduce the battery's life cycle impact by about 51% [32]. However, these materials, especially cobalt, are costly metals, and manufacturers are moving toward low-cost cathode materials to reduce the cost of battery manufacturing [33].Therefore, there is an urgent need to explore low-cost, highly safe, and cycling stable rechargeable batteries based on abundant resources. In this sense, compared with lithium, sodium has similar physical and chemical properties and is very abundant and low cost (see Table 1.1) [27]. Indeed, sodium-based batteries are not new. From the 1970s to the 1980s, sodium-ion and lithium-ion batteries were investigated in parallel [34-36] but the research in sodium-ion batteries was significantly decreased after the success of the commercial application of lithium-ion batteries in the 1990s. Even if some Na-S batteries have already been commercialized [37,38] the safety issue of molten sodium and sulphur at 300-350ºC in Na-S batteries is still a problem for large-scale applications so that a renewed interest in the research of sodium-ion batteries operated at room-temperature has arisen because of both, the abundance and low cost of sodium. Thus, developing room-temperature "rocking chair" sodium-ion batteries with a similar working principle as lithium-ion batteries (Figure 1.4) for large scale ESS is considered a reasonable alternative.

30 Rechargeable Battery Recycling Act, **2006**.

31 New York Environmental Conservation Law, **2011.**

32 Dewulf, J.; Van der Vorst, G.; Denturck, K.; Van Langenhove, H.; Ghyoot, W.; Tytgat, J.; Vandeputte, K. *Resor. Conserv. Recy.*, **2010**, 54, 229-234.

33 Wang, X.; Gaustad, G.; Babbitt, C.W.; Richa, K. *Resor. Conserv. Recy.*, **2014**, 83, 53-62.

34 Mizushima, K.; Jones, P.C.; Wiseman, P.J.; Goodenough, J.B. *Mater. Res. Bull.*, **1980**, 15, 783-789.

35 Delmas, C.; Fouassier, C.; Hagenmuller, P. *Physica B+C*, **1980**, 99, 81-85.

36 Whittingham, M.S.; *Prog. Solid State Chem.*, **1978**, 12, 41-99.

37 Ellis, B.L.; Nazar, L.F. *Curr. Opin. Solid State Mater. Sci.*, **2012**, 16, 168-177.

38 Hueso, K.B.; Armand, M.; Rojo, T. *Energy Environ. Sci.*, **2013**, 6, 734-749.

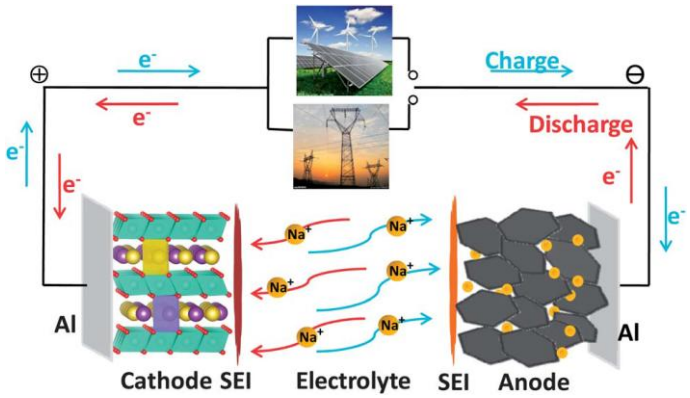

Figure 1.4 *The working principle of room-temperature "rocking chair" sodium-ion batteries. "Reproduced from Ref 13 with permission of The Royal Society of Chemistry."*

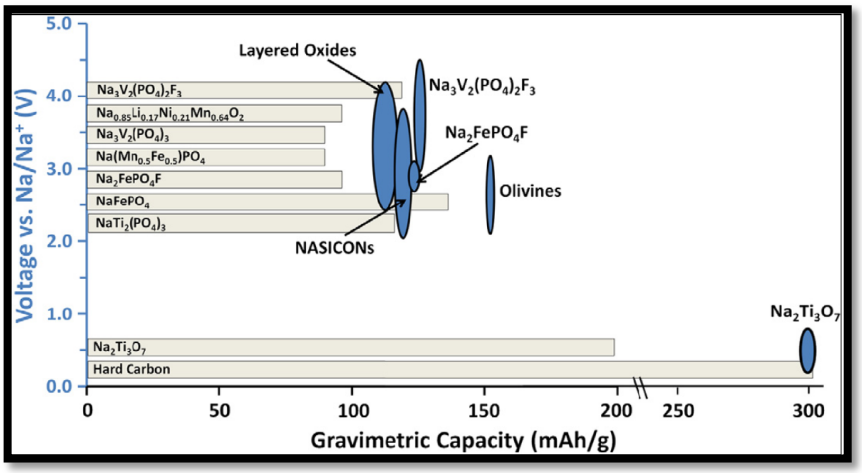

Figure 1.5 *Key cathodic and anodic electrode intercalation materials for sodium-ion batteries: theoretical capacities of the various materials at their various potentials are shown with blue ovals, while achieved capacities are shown with grey bars. "Reprinted from Curr. Opin. Solid State Mater. Sci., 16, Ellis, B.L.; Nazar, L.F, Sodium and sodium-ion energy storage batteries, 168-177, 2012, with permission from Elsevier."*

Figure 1.5 presents the most studied anodic and cathodic materials for non aqueous sodium-ion batteries up till now where many of these materials are similar to those which have been exhaustively researched over the past 20 years for lithium-ion batteries, including layered transition metal oxides, olivines and compounds with the NASICON framework [37,39].

1.2.2 Anodic materials for Sodium-ion batteries

Direct use of elemental alkali metals (lithium or sodium) as anodes in rechargeable alkaline ion batteries causes poor cycle performance and short-circuits because of their low melting point (180.5ºC for lithium and 97.7ºC for sodium), high chemical reactivity and dendritic growth during charge and discharge. Thus, in order to solve the cyclability and safety issues of rechargeable batteries, alkali metal-insertion host materials consisting on carbonaceous compounds, metal oxides and phosphates, alloy composites and organic compounds have been extensively studied [26,36,39].

Hard carbons remain the main candidates to be used as anodes for sodium-ion batteries, although their performance is still far from that achieved by graphite in lithium-ion batteries. Recent approaches to improve its cyclability have been the use of hierarchically porous carbons prepared by templating routes which have shown more than 100 $mAhg^{-1}$ at 5C with good coulombic efficiency after several cycles [40]. Other promising candidates for anodes in sodium-ion batteries are metal based oxides and phosphates, especially titanium based ones. For the moment, $Na_2Ti_3O_7$ has been the most studied compound where 2 sodium have been reversibly inserted at a voltage as low as 0.3 V *vs.* Na/Na^+ [41,42]. $Na_3Ti_2(PO_4)_3$ has also attracted attention in the recent years but as in the case of $Na_2Ti_3O_7$ capacity fading is a problem that prevents explotation of this low voltage insertion. A storage mechanism based on alloy reactions has also been investigated due to the high storage capacity of such materials. $Na_{15}Sn_4$

39 Palomares, V.; Casas-Cabanas, M.; Castillo-Martínez, E.; Han, M.H.; Rojo, T. *Energy Environ. Sci.*, **2013**, 6, 2312-2337.

40 Wenzel, S.; Hara, T.; Janek, J.; Adelhelm, P. *Energy Environ. Sci.*, **2011**, 4, 3342-3345.

41 Senguttuvan, P.; Rousse, G.; Seznec, V.; Tarascon, J.M.; Palacín, M.R. *Chem. Mater.*, **2011**, 23, 4109-4111.

42 Wang, W.; Yu, C.; Lin, Z.; Hou, J.; Zhua, H.; Jiao, S. *Nanoscale*, **2013**, 5, 594-599.

presented a specific capacity of 500 $mAhg^{-1}$ in a voltage range of 0-0.8 V [43] while Sb/C and SnSb/C composites exhibited a higher capacity of 610 $mAhg^{-1}$ and 544 $mAhg^{-1}$, respectively, with good rate capability and cycling stability [44,45]. However, these alloy materials can suffer from a 420% of the volume expansion after sodium insertion so the deterioration of these compounds is an issue that must be taken into account [46]. On the other hand, the use of organic electrodes, based on benzene-carboxylate chemically modified, has also been considered as anodic materials for sodium-ion batteries. Park *et al.* evaluated several terephthalate based derivatives and found that disodium therephthalate ($Na_2C_8H_4O_4$) showed an excellent cyclability with a specific capacity close to 300 $mAhg^{-1}$ over 90 cycles at C/10. The average voltage was 0.4 V *vs.* Na/Na^+, being therefore a promising candidate which could be produced from low cost renewable sources [47]. Abouimrane *et al.* also examined a series of organic carboxylate based materials, and assembled a 3.6 V full cell using $Na_2C_8H_4O_4$ as an anode and $Na_{0.75}Mn_{0.7}Ni_{0.23}O_2$ as a cathode. It exhibited a capacity above 268 $mAhg^{-1}$ (anode-limited capacity) after 50 cycles [48].

1.2.3 Cathodic materials for Sodium-ion batteries

A great variety of compounds are being studied as possible cathodic materials for sodium-ion batteries, but the most important ones can be divided into two general categories: oxides and phosphates [39,49].

Transition metal layered oxides $NaMO_2$ (M = Ni, Mn, Cr, Co, V, etc.) are considered promising cathode systems because of their material cost, high capacity and safety.

43 Komaba, S.; Matsuura, Y.; Ishikawa, T.; Yabuuchi, N.; Murata, W.; Kuze, S. *Electrochem. Commun.*, **2012**, 21, 65-68.

44 Qian, J.F.; Chen, Y.; Wu, L.; Cao, Y.L.; Ai, X.P.; Yang, H.X. *Chem. Commun.*, **2012**, 48, 7070-7072.

45 Xiao, L.F.; Cao, Y.L.; Xiao, J.; Wang, W.; Kovarik, L.; Nie, Z.M.; Liu, J. *Chem. Commun.*, **2012**, 48, 3321-3323.

46 Wang, W.; Liu, X.H.; Mao, S.X.; Huang, J.Y. *Nano Lett.*, **2012**, 12, 5897-5902.

47 Park, Y.; Shin, D.S.; Woo, S.H.; Choi, N.S.; Shin, K.H.; Oh, S.M.; Lee, K.T.; Hong, S.Y. *Adv. Mater.*, **2012**, 24, 3562-3567.

48 Abouimrane, A.; Weng, W.; Eltayeb, H.; Cui, Y.J.; Niklas, J.; Poluektov, O.; Amine, K. *Energy Environ. Sci.*, **2012**, 5, 9632-9638.

49 Masquelier, C.; Croguennec, L. *Chem. Rev.*, **2013**, 113, 6552-6591.

Due to their crystallographic nature, layered $NaMO_2$ compounds are very sensitive to ambient air and adsorb water molecules into the inter-slab space. The most typical crystal structures are the ones labelled as P2 and O3 where sodium occupies trigonal Prismatic sites with ABBA oxygen stacking and Octahedral sites with ABC oxygen stacking, respectively (see Figure 1.6). There is a wide range of transition metals and combinations of them that can lead to layered $NaMO_2$ compounds. Each of them possesses a different operating voltage and specific capacity, which defines its energy density (see Figure 1.7) [50].

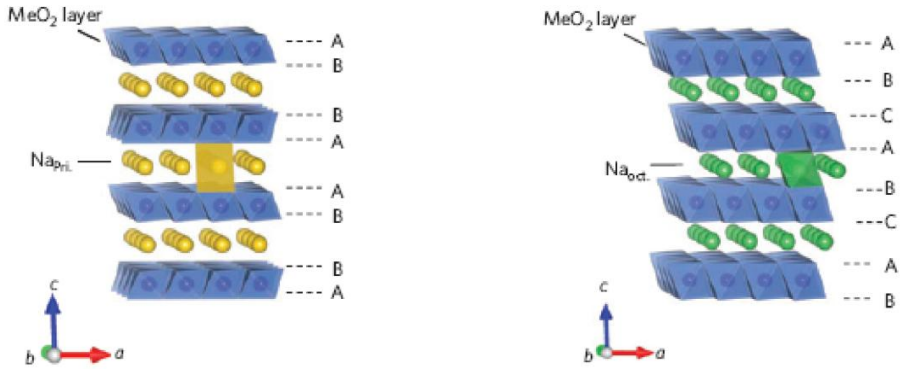

Figure 1.6 *Layered structure of P2-type (left) and O3-type (right) $NaMO_2$. "Reprinted by permission from Macmillan Publishers Ltd: Nat. Mater. (ref 50), copyright (2012)".*

In the first place, monoclinic O3-type $NaNiO_2$ shows multiple *plateaux* due to phase change during charge/discharge cycles. Overall, a 147 $mAhg^{-1}$ discharge capacity (0.62 Na) within the voltage range of 2.0 – 4.5 V at C/10 has been achieved. However, large capacity loss has been observed probably due to an irreversible phase change which is evidenced by the formation of an unidentifiable phase after cycling. Significant improvement in coulombic efficiency at lower cut-off voltage indicated that the phase

50 Yabuuchi, N.; Kajiyama, M.; Iwatate, J.; Nishikawa, H.; Hitomi, S.; Okuyama, R.; Usui, R.; Yamada, Y.; Komaba, S. *Nat. Mater.,* **2012**, 11, 512-517.

changes below 3.75 V are highly reversible although the fully sodiated phase is never achieved and $Na_{0.91}NiO_2$ is obtained instead [51-53].

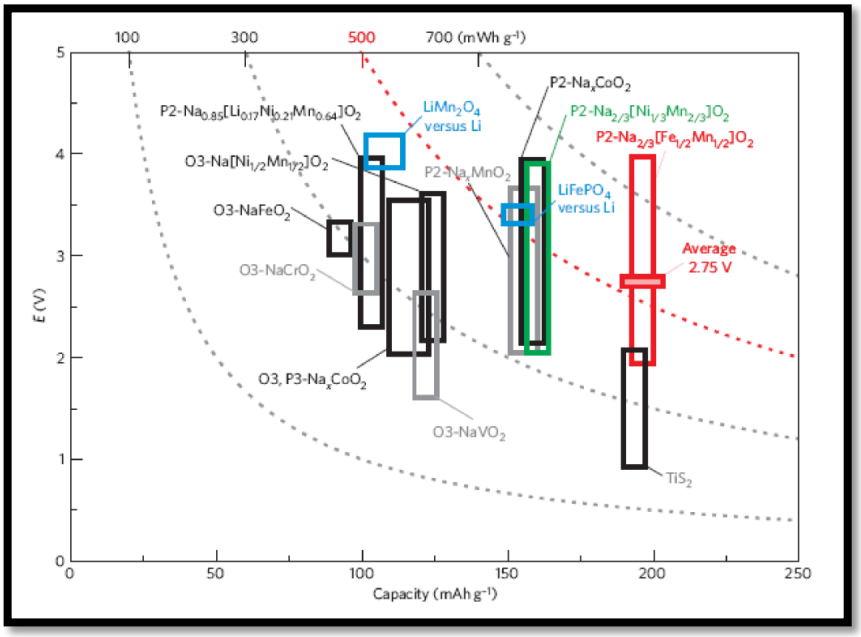

Figure 1.7 *A comparison of reversible capacity and operating voltage ranges of the layered sodium insertion materials. The energy density was calculated on the basis of the voltage vs. metallic sodium for simplicity. $LiFePO_4$ and $LiMn_2O_4$ are also shown for comparison based on the voltage vs. metallic lithium. "Reprinted by permission from Macmillan Publishers Ltd: [Nat. Mater.](ref 50), copyright (2012)"*

Similarly to $NaNiO_2$, the charge capacity of O3-type α-$NaFeO_2$ increases at high cut-off voltages but reversible capacity significantly decreases when charged above 3.5 V [54].

51 Fielden, R.; Obrovac, M.N.; *Structure and electrochemistry of $NaNiO_2$*. Poster at: Honolulu PRiME 2012, 2012 Fall Meeting of The Electrochemical Society, **2012** Oct. 7 – 12, Honolulu, Hi.

52 Vassilaras, P.; Ma, X.; Lin, X.; Ceder, G. *J. Electrochem Soc.,* **2013**, 160, A207-A211.

53 Han, M.H.; Gonzalo, E.; Casas-Cabanas, M.; Rojo, T. *J. Power Sources,* **2014**, 258, 266-271.

$NaCrO_2$ compound, with the same layered rock salt structure as α-$NaFeO_2$, presents multiple *plateaux* due to structural changes and a capacity fading of about 20% after 20 cycles [55]. However, the carbon coating of the material improves significantly its performance leading to a stable 100 $mAhg^{-1}$ specific capacity after 40 cycles [56]. On the other hand, P2-Na_xCoO_2 has been speculated as a very promising cathode material due to the excellent electrochemical performance of its lithium analogue although the high cost of cobalt makes its commercialization unviable. Electrochemical results from P2-Na_xCoO_2 samples with different microstructures showed an specific capacity of 105 $mAhg^{-1}$ within the voltage range of 2.0 – 3.9 V at a rate of C/25 when using smaller size particles [57]. Apart from that, different combinations of Ni, Mn, Fe and/or Co have been employed in order to improve the performance and stability of all these layered oxides. A full cell has even been reported for the $Na_yC/Na_{1-y}(Ni_{1/3}Fe_{1/3}Mn_{1/3})O_2$ system where a specific capacity of about 100 $mAhg^{-1}$ was maintained for 150 cycles at 1.5 – 4.0 V at C/2 [58].

On the other hand, framework materials based on the phosphate polyanion have also been identified as promising electro-active materials for sodium metal and sodium-ion battery applications. It is the strong inductive effect of the PO_4^{-3} polyanion that moderates the energetic of the transition metal redox couple to generate relatively high operating potentials for these compounds [59].

$NaFePO_4$ phase is being deeply studied due to its highest theoretical specific capacity among phosphate polyanion cathode materials. However, the direct preparation of this compound leads to the formation of the maricite polymorph which is electrochemically inactive. For this reason, it is necessary to use electrochemical or chemical sodiation of

54 Yoshida, H.; Yabuuchi, N.; Komaba, S. *Na insertion mechanism in α-$NaFeO_2$ as positive electrode materials for Na-ion batteries*. Paper presented at: Honolulu PRiME 2012, 2012 Fall Meeting of The Electrochemical Society, **2012** Oct. 7 – 12, Honolulu, Hi.

55 Komaba, S.; Takei, C.; Nakayama, T.; Ogata, A.; Yabuuchi, N. *Electrochem. Commun.,* **2010**, 12, 355.

56 Ding, J.J.; Zhou, Y.N.; Sun, Q.; Fu, Z.W. *Electrochem. Commun.,* **2012**, 22, 85-88.

57 D'Arienzo, M.; Ruffo, R.; Scotti, R.; Morazzoni, F.; Mari, C.M.; Polizzi, S. *Phys. Chem. Chem. Phys.* **2012**, 14, 5945-5952.

58 Kim, D.; Lee, E.; Slater, M.; Lu, W.; Rood, S.; Johnson, C.S. *Electrochem. Commun.,* **2012**, 18, 66-69.

59 Yamada, A.; Chung, S.C.; Hinokuma, K. *J. Electrochem. Soc.*, **2001**, 148, A224-A229.

delithiated $FePO_4$ in order to get the olivine-type $NaFePO_4$ [60]. For this latter phase, a specific capacity of 125 $mAhg^{-1}$ (80% of the theoretical capacity) has been obtained at C/20 with excellent capacity retention after 50 cycles [61].The authors observed a two-phase *plateaux* signature both upon charge and discharge although with changes in their reciprocal position and they attributed the increase in polarization with cycling to the poor ionic and electronic conductivity of $FePO_4$. Evidence of the existence of the intermediate phase $Na_{0.7}FePO_4$ both upon the charge and discharge was also reported by Casas-Cabanas *et al.* [60].

NASICON (Na^+ superionic conductor) structured compounds, $Na_3M_2(PO_4)_3$ (M = Fe, V. etc.), feature a three-dimensional framework that generates large interstitial spaces trough which sodium ions can diffuse. $Na_3V_2(PO_4)_3$ presents two *plateaux* at 3.4 and 1.6 V and is one of the most studied compounds up till now due to its highest gravimetric energy density among other NASICON compounds [62]. A recent publication showed an enhanced performance of a carbon coated porous $Na_3V_2(PO_4)_3$ where nearly 50% of the initial capacity was retained after 30.000 cycles at 40C [63]. $Na_3V_2(PO_4)_3$ is also an interesting compound due to the possibility of using it both as cathodic and anodic material. Indeed, a symmetrical full cell was reported by Plashnitsa *et al.* where a coulombic efficiency of 75% was obtained for the first cycle [64].

Pyrophosphates have also recently been pointed out as possible electroactive materials to be used as cathodes for sodium-ion batteries. Barpanda *et al.* have recently gathered the battery-related information about a large group of this type of compounds where Fe, Mn, Co, Cu and V are the most employed transition metals [65]. However, most of the attention is focused on $Na_2FeP_2O_7$ material which presents a theoretical capacity of

60 Casas-Cabanas, M.; Roddatis, V.; Saurel, D.; Kubiak, P.; Carretero-González, J.; Palomares, V.; Serras, P.; Rojo, T. *J. Mater. Chem.,* **2012**, 22, 34, 17421-17423.

61 Oh, S.M.; Myung, S.T.; Hassoun, J.; Scrosati, B.; Sun, Y.K. *Electrochem. Commun,.* **2012**, 22, 149–152.

62 Uebou, Y.; Kiyabu, T.; Okada, S.; Yamaki, J.-I. *The Reports of Institute of Advanced Material Study, Kyushu University*, **2002**, vol. 16, pp. 1–5.

63 Saravanan, K.; Mason, C.W.; Rudola, A.; Wong, K.H.; Balaya, P. *Adv. Energy Mater.*, **2013**, 3, 444-450.

64 Plashnitsa, L. S.; Kobayashi, E.; Noguchi, Y.; Okada, S.; Yamaki, J.-I. *J. Electrochem. Soc.*, **2010**, 157, A536–A543.

65 Barpanda, P.; Nishimura, S-I.; Yamada, A. *Adv. Energy Mater.,* **2012**, 2, 841-859.

97.17 $mAhg^{-1}$ and a *plateau* around 3 V. Non coated, micronsized $Na_2FeP_2O_7$ particles (3-5 μm) have shown a discharge capacity of 82 $mAhg^{-1}$ at C/20 [66].

Fluorophosphate materials possess higher operating voltages than phosphates, because the inductive effect of fluorine is added to the effect of phosphate group. This latter feature makes them key materials to solve the energy density issue of sodium-based batteries. Fe, Mn, and V have been the most investigated transition metals but the three compounds derived from them present different structures: Whereas the sodium-iron fluorophosphate possesses a two-dimensional layered structure [67], the sodium-manganese fluorophosphate presents a three-dimensional tunnel structure [68]. However, manganese compound has demonstrated to be poorly electrochemically active so more studies have been performed for the iron-based compound. At the moment, one of the best results achieved has been for carbon coated porous hollow spheres of Na_2FePO_4F phase [68]. This nanostructured material contained about 6-8 *wt.*% of carbon and presented a specific surface area of 8.7 $m^2 \cdot g^{-1}$ which led to a specific capacity of 90 $mAhg^{-1}$ at C/10 and a good cycling stability for 100 cycles [69].

Regarding sodium-vanadium fluorophosphates, three phases have been described in the literature: $NaVPO_4F$, $Na_3V_2O_2(PO_4)_2F$ and $Na_3V_2(PO_4)_2F_3$ (143 $mAhg^{-1}$, 130 $mAhg^{-1}$ and 128 $mAhg^{-1}$ theoretical specific capacity, respectively). Barker *et al.* first proposed $NaVPO_4F$ as a tetragonal structure with *I4/mmm* space group [70]. On the other hand, several groups reported also the existence of a $NaVPO_4F$ polymorph which they indexed with *C2/c* space group [71-73]. The $Na_3V_2O_2(PO_4)_2F$ phase has been described as a tetragonal symmetry compound with *I4/mmm* space group by Sauvage

66 Barpanda, P.; Ye, T.; Nishimura, S-I.; Chung, S-C.; Yamada, Y.; Okubo, M.; Zhou, H.; Yamada, A. *Electrochem. Commun.,* **2012**, 24, 116-119.

67 Ellis, B.L.; Makahnouk, W.R.M.; Rowan-Weetaluktuk, W.N.; Ryan, D.H.; Nazar, L.F. *Chem. Mater.,* **2010**, 22, 1059-1070.

68 Yakubovich, O.V.; Karimova, O.V.; Mel'nikov, O.K. *Acta Cryst. C,* **1997**, 53, 395-397.

69 Langrock, A.; Xu, Y.; Liu, Y.; Ehrman, S.; Manivannan, A.; Wang, C. *J. Power Sources*, **2013**, 223, 62-67.

70 Barker, J.; Saidi, M.Y.; Swoyer, J.L. *Electrochem Solid-State Lett.*, **2003**, 6, A1-A4.

71 Zhuo, H.; Wang, X.; Tang, A.; Liu, Z.; Gamboa, S.; Sebastian, P.J., *J. Power Sources*, **2006**, 160, 698-703.

72 Liu, Z.; Wang, X.; Wang, Y.; Tang, A.; Yang, S.; He, L., *T. Nonferr. Metal Soc.*, **2008**, 18, 346-350.

73 Lu, Y.; Zhang, S.; Li, Y.; Xue, L.; Xu, G.; Zhang, X. *J. Power Sources*, **2013**, 247, 770-777.

et al. [74] and Massa *et al.* [75] but, more recently, Tsirlin *et al.* [76] proposed the *P4₂/mnm* space group for the room temperature phase among the diverse polymorphs of this material at different temperatures.

The third of the sodium–vanadium fluorophosphates mentioned in the literature, $Na_3V_2(PO_4)_2F_3$, also possesses a tetragonal symmetry with *P4₂/mnm* space group [77-79]. A deep study of the bibliographic data related to these three sodium fluorophosphates leads to doubt about the real existence of these three different compounds. It is worth noting that the existence of the $NaVPO_4F$ phase has already been questioned by authors such as Sauvage *et al.* [74]. Furthermore, there are no structural data about the suggested monoclinic polymorph of $NaVPO_4F$ [71-73]. Moreover, the diffractogram shown in their works matches with the one of $Na_3V_2(PO_4)_3$ NASICON compound. In this case, the formation of a NASICON type phase instead of $NaVPO_4F$ could be possible because the samples were prepared by the ceramic method and sublimation of VF_3 could occur, as it has been described by Ateba Mba *et al.* for other lithium–vanadium fluorophosphates [80]. Thus, structural data of only two sodium vanadium fluorophosphates are found in the literature: $Na_3V_2O_2(PO_4)_2F$ [76] and $Na_3V_2(PO_4)_2F_3$ [77]. As both present the same space group and the diffractograms of both phases are so similar, it could be possible to establish a relationship between them. Electrochemical studies on the three mentioned compounds have been performed under different conditions *vs.* lithium or sodium [70-72,74,81-83] and in all

74 Sauvage, F.; Quarez, E.; Tarascon, J.; Baudrin, E. *Solid State Sci.*, **2006**, 8, 1215–1221.

75 Massa, W.; Yakubovich, O.; Dimitrova, O. *Solid State Sci.*, **2002**, 4, 495-501.

76 Tsirlin, A.; Nath, R.; Abakumov, A.; Furukawa, Y.; Johnston, D.; Hemmida, M.; Krug von Nidda, H.-A.; Loidl, A.; Geibel, C.; Rosner, H. *Phys. Rev. B,* **2011**, 84, 014429/1-014429/16.

77 Le Meins, J.-M.; Crosnier-Lopez, M.-P.; Hemon-Ribaud, A. and Courbion, G. *J. Solid State Chem.*, **1999**, *148*, 260-277.

78 Barker, J.; Gover, R.K.B.; Burns, P.; Bryan, A.J., *Electrochem Solid-State Lett.*, **2006**, 9, A190-A192.

79 Jiang, T.; Chen, G.; Li, A.; Wang, C.; Wei, Y., *J. Alloy Compd.*, **2009**, 478, 604-607.

80 Ateba Mba, J.-M.; Masquelier, C.; Suard, E.; Croguennec, L. *Chem. Mater.*, **2012**, 24, 1223-1234.

81 Xu, M.; Wang, L.; Zhao, X.; Song, J.; Xie, H.; Lu, Y.; Goodenough, J.B. *Phys. Chem. Chem. Phys.*, **2013**, 15, 13032-13037.

82 Shakoor, R. A.; Seo, D.-H.. Kim, H.; Park, Y.U.; Kim, J.; Kim, S.-W.; Gwon, H.; Lee, S.; Kang, K. *J. Mater. Chem*., **2012**, 22,20535-20541.

83 Ponrouch, A.; Dedryvère, R.; Monti, D.; Demet, A.E.; Ateba Mba, J.M.; Croguennec, L.; Masquelier, C.; Johansson, P.; Palacín, M.R. *Energy Environ. Sci.*, **2013**, 6, 2361-2369.

cases the charge–discharge curves display two voltage *plateaux* of similar length at the same voltages with little differences depending on the anode material used (*ca.* 3.6 and 4.1 V *vs.* Na/Na^+).

1.3 Aim of the present work

The need for the obtaining of cheap, stable and electrochemically good performing cathodic materials leads to sodium based vanadium fluorophosphates which posses every of these features. The study of sodium–vanadium fluorophosphates is especially relevant because of the high operating voltages offered by these compounds that could lead the way to high energy sodium-ion batteries. However, up till now, these materials have not been very deeply studied so some doubts have arisen concerning the real composition of these phases.

The similarity of the structures and X-ray diffraction patterns as well as the almost identical electrochemical data for $Na_3V_2O_2(PO_4)_2F$ and $Na_3V_2(PO_4)_2F_3$ suggests that both materials could belong to the same family of compounds. Besides, due to the unreliable data found in the literature concerning the $NaVPO_4F$ phase the real existence of this material will be also analysed. For this reason, this work aims to:

- Systematically study hydrothermal synthesis of sodium vanadium fluorophosphates variating carbon type and content, in order to analyze the possible existence of a family of intermediate compounds between these phases and their electrochemical behaviour.
- Synthesise the $Na_3V_2O_2(PO_4)_2F$ phase by a novel single-step hydrothermal process. To optimise carbon coating conditions for this material and study its influence in its electrochemical performance.
- Attempt to obtain the $NaVPO_4F$ phase by direct synthesis, and indirect chemical and electrochemical preparation in order to clear up the doubts about this compound found in literature.
- Analyze the electrochemical extraction/insertion mechanism of sodium in the $Na_3V_2O_{2x}(PO_4)_2F_{3-2x}/C$ composite and the $Na_3V_2O_2(PO_4)_2F$ phase by *ex-situ* and *in-situ* techniques.

Chapter 2. Synthesis and Characterisation

2.1 Introduction

In this chapter, a series of sodium-vanadium fluorophosphate samples were prepared by hydrothermal method, varying the type and amount of carbon used as reductive agent during the synthesis. The use of active carbon led to a set of samples labelled as MV_AC while the use of S-black electrochemical grade carbon resulted in MV_SC named composites. This way, the possible influence of the carbon on both the final properties of the samples and their composition is analysed.

Subsequently a sodium vanadium fluorophosphate composite was prepared by using a similar carbon content to the best performing sample from the carbon series. In this case, Ketjen black carbon was employed instead of S-black leading to a sample labelled as MV_KC, which is deeply characterised.

On the other hand, the synthesis and characterisation of $Na_3V_2O_2(PO_4)_2F$, named from here on as V4, is commented. The effects of an *ex-situ* carbon coating are also analysed.

A study on the reagents used for the synthesis of V4, due to the issues found when reproducing this material is also included and the need of a pretreatment before their use in order to obtain pure $Na_3V_2O_2(PO_4)_2F$ material is discussed.

The chapter ends with a brief study on the real existence of $NaVPO_4F$ phase where different attempts for its obtaining are presented.

2.2 Experimental

A series of sodium vanadium fluorophosphates was prepared by using different amounts and types of carbon. The synthesis process took place in two steps. First, VPO_4/C composite precursor was synthesised by the ceramic method. For this purpose, V_2O_5 (Sigma-Aldrich, 99.99% purity) and $NH_4H_2PO_4$ (Fluka, 99.5% purity) were mixed in an agate mortar in stoichiometric ratio. Two types of carbon, active carbon (AC) and TIMCAL Super S© S-black carbon (SC) were added as reducing agent in different molar proportions ranging from 25 to 75% molar excess. A sample with greater carbon excess was also prepared (1400% molar excess). This mixture was annealed twice under nitrogen atmosphere at 300 and 850ºC.

Second, sodium fluorophosphate samples were prepared under mild hydrothermal conditions (170ºC and autogenous pressure) by reacting NaF (Sigma-Aldrich, 99% purity) and VPO_4/C in 3.3:1 molar proportion. The reaction mixture was sealed in a polytetrafluoroethylene (PTFE)-lined steel pressure vessel, which was maintained at 170ºC for 65 hours. This procedure led to a series of powder samples named MV_AC (active carbon) and MV_SC (S-black carbon) that were further characterised (2.3.1 section).

A higher amount of material containing a ~6 *wt.*% carbon was prepared. This time a 25% molar excess of Ketjen black was used as carbon source leading to the as-named MV_KC sample. Its characterisation is presented in section 2.3.2 of this chapter.

V^{4+} $Na_3V_2O_2(PO_4)_2F$ phase (sample V4) was synthesised by a novel single-step hydrothermal treatment different to the two-step synthesis routes proposed up till now [130,131]. It was prepared under mild hydrothermal conditions (170ºC and autogenous pressure) by reacting V_2O_3 (Sigma-Aldrich, 98% purity, production year 2004), $NaH_2PO_4 \cdot H_2O$ (Fluka, 99% purity) and NaF (Sigma-Aldrich, 99% purity) in 1:2:1 molar

130 Sauvage, F.; Quarez, E.; Tarascon, J.; Baudrin, E. *Solid State Sci.*, **2006**, 8, 1215–1221.

131 Tsirlin, A.; Nath, R.; Abakumov, A.; Furukawa, Y.; Johnston, D.; Hemmida, M.; Krug von Nidda, H.-A.; Loidl, A.; Geibel, C.; Rosner, H. *Phys. Rev. B,* **2011**, 84, 014429/1-014429/16.

proportion. The reaction mixture was sealed in a polytetrafluoroethylene (PTFE)-lined steel pressure vessel, which was maintained at 170ºC for 65 hours. The reaction product was washed repeatedly with distilled water and acetone.

Two $Na_3V_2O_2(PO_4)_2F$/C composites were prepared from V4 sample by impregnation with sucrose as carbon precursor and annealed at different temperature and time conditions. For this purpose, 120 mg. of sucrose were dissolved in distilled water and then mixed with a previously stirred and sonicated suspension of 450 mg. of V4 in water. The mixture was then dried first at 80°C in air and subsequently in a vacuum oven at 120ºC for 3 days. After that, the dry powder was ground using a mortar and pestle and thermally treated in two different ways. In the first one the powder was heated at 600ºC for 8 hours in N_2 atmosphere, labelling the resulting sample as V4_LTT (LTT: Long Thermal Treatment). In the second one, the raw sample was heated in N_2 at 800ºC for only 10 minutes, and named V4_FTT (FTT: Fast Thermal Treatment). Both resulting materials presented greyish colour which indicated the presence of carbon in them. A third $Na_3V_2O_2(PO_4)_2F$/C composite was obtained by mixing raw V4 sample with TIMCAL C-nergy Super C65 electrochemical grade carbon by ball milling to get an approximately 20 *wt.*% of carbon in the final product before being thermally treated. The mixture was then heated at 600ºC for 8 hours in N_2 atmosphere resulting in the as-named V4_BMT sample (BMT: Ball Milling Treatment). Characterisation of these V^{4+} materials is shown in section 2.3.3.

2.3 Structural, Morphological and Magnetic Characterisation of $Na_3V_2O_{2x}(PO_4)_2F_{3-2x}$ family

2.3.1 Structural, Morphological and Magnetic Characterisation of $Na_3V_2O_{2x}(PO_4)_2F_{3-2x}$ ($0 < x < 1$)

The sodium vanadium fluorophosphate composites prepared with different amounts and types of carbon were subjected to elemental analysis. Table 2.2 gathers the synthesised samples, with the carbon excess that was used in the process and the remaining carbon weight percentage. All the materials were grey coloured.

Table 2.2 *Prepared materials, initial carbon excess and remaining carbon weight percentage.*

C type	Sample	Initial C excess in VPO_4 preparation	*wt.* % C in the final compound
Active carbon	MV_AC1	25 % molar	<1%
	MV_AC2	25 % molar	1.7
	MV_AC3	35 % molar	2.9
	MV_AC4	75 % molar	2.6
	MV_AC5	1400% molar= 25 % mass	34
S-black carbon	MV_SC1	25 % molar	6.8
	MV_SC2	35 % molar	6.1
	MV_SC3	75 % molar	8.7
	MV_SC4	1400% molar= 25 % mass	57

As it can be seen in Table 2.2, although the initial added carbon content increases gradually, remaining carbon weight percentage does not increase linearly and presents some irregularities due to slight changes in carbon elimination in the precursor ceramic synthesis. Besides, those materials prepared with electrochemical grade carbon present higher carbon content than those synthesised with active carbon. This fact can be due to the greater active surface of active carbons (500-1500 $m^2 \cdot g^{-1}$) compared to TIMCAL Super S (45 $m^2 \cdot g^{-1}$) [132].

A comparative study of the structures of $Na_3V_2(PO_4)_2F_3$ (V^{3+} compound [133]) and $Na_3V_2O_2(PO_4)_2F$ (V^{4+} compound [131]) phases showed a correlation between them. As it can be seen in Figure 2.8 they both present the same framework structure, where F or O can occupy the same crystallographic site, modulating vanadium oxidation state from V^{3+} to VO^{2+} (V^{4+}). This would lead to the following general formula

132 Liua,G.; Benyonb, P.; Benfella, K.E.; Bryanta, G.W.; Tatea, A.G.; Boydb, R.K.; Harrisc, D.J.; Walla, T.F. *Fuel*, **2000**, 79, 617-626.

133 Le Meins, J.-M.; Crosnier-Lopez, M.-P.; Hemon-Ribaud, A. and Courbion, G. *J. Solid State Chem.*, **1999**, *148*, 260-277.

$Na_3V_2O_{2x}(PO_4)_2F_{3-2x}$. The extreme members (x = 0 and x = 1) would correspond to the mentioned phases, $Na_3V_2(PO_4)_2F_3$ for x = 0 and $Na_3V_2O_2(PO_4)_2F$ for x = 1, whereas intermediate compounds (0 < x < 1) would be V^{3+}/V^{4+} mixed valence phases.

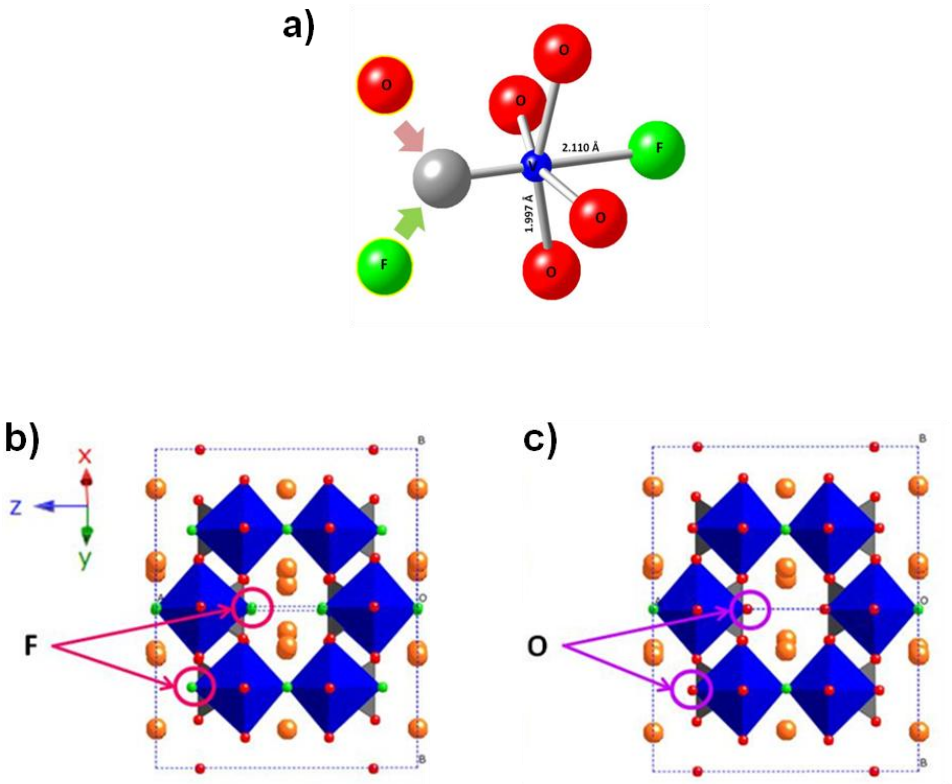

Figure 2.8 ***a)*** *Vanadium octahedron for mixed valent $Na_3V_2O_{2x}(PO_4)_2F_{3-2x}$ (0 < x < 1) compounds. Vanadium is represented in blue, oxygen in red and fluorine in green. Crystallographic structure of* ***b)*** *$Na_3V_2(PO_4)_2F_3$ and* ***c)*** *$Na_3V_2O_2(PO_4)_2F$. Oxygen in red and fluorine in green. Vanadium octahedron is represented in blue and phosphate tetrahedron in grey.*

Figure 2.9 shows the X-ray diffractograms for each sample classified by the type of carbon used in the synthesis. All of them present the same main diffraction maxima, characteristic of the isostructural $Na_3V_2O_2(PO_4)_2F$ and $Na_3V_2(PO_4)_2F_3$ phases.

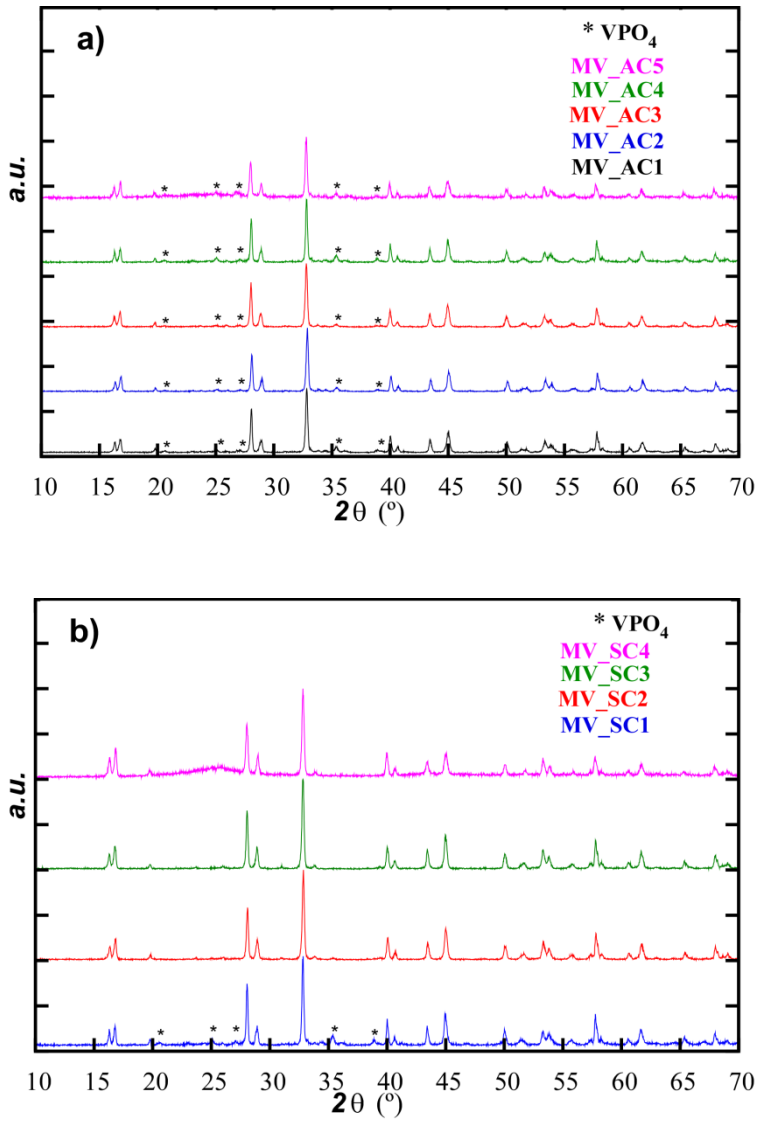

Figure 2.9 *X-ray diffractograms of* ***a)*** *MV_AC1-MV_AC4 and* ***b)*** *MV_SC1-MV_SC4 samples.*

The compounds from Figure 2.9 present the same general diffraction pattern and are indexed in the same space group, *$P4_2/mnm$*, with slightly different lattice parameters. It can be seen that the amount of impurities in these materials is related to the type and amount of carbon used in the synthesis.

As it can be observed in Figure 2.9a, the amount of active carbon employed does not have a strong influence on the amount of remaining unreacted VPO_4. On the other hand, when S-black carbon is employed (Figure 2.9b) the VPO_4 secondary phase disappears as the carbon content increases. The background elevation observed for both composite types at high carbon contents is due to the abundance of amorphous carbon.

Diffraction patterns of all samples were indexed with the Full Pattern Matching function of FULLPROF Suite software [134]. Table 2.3 shows the structural parameters of analysed materials, including those from the literature of $Na_3V_2O_2(PO_4)_2F$ and $Na_3V_2(PO_4)_2F_3$ as end-member phases.

Table 2.3 Structural parameters obtained from literature and from the synthesised samples.

$Na_3V_2O_2(PO_4)_2F$ [131]	*$P4_2/mnm$*	a = b = 9.03051 Å c = 10.62002 Å	Vol.= 866.1 Å^3
MV_AC1	*$P4_2/mnm$*	a = b = 9.02548 Å c = 10.63184 Å	Vol.= 866.1 Å^3
MV_AC2	*$P4_2/mnm$*	a = b = 9.03202 Å c = 10.63282 Å	Vol.= 867.4 Å^3
MV_AC5	*$P4_2/mnm$*	a = b = 9.04258 Å c =10.62738 Å	Vol.= 869.0 Å^3
MV_SC2	*$P4_2/mnm$*	a = b = 9.03158 Å c = 10.63747 Å	Vol.= 867.7 Å^3
MV_SC4	*$P4_2/mnm$*	a = b = 9.04499 Å c = 10.62133 Å	Vol.= 869.0 Å^3
$Na_3V_2(PO_4)_2F_3$ [133]	*$P4_2/mnm$*	a = b = 9.047 Å c = 10.705 Å	Vol.= 876.2 Å^3

The analysis of the cell volume and the carbon content of these samples indicates that all prepared composites except MV_AC1 material posses an intermediate cell volume

134 Rodríguez-Carvajal, J.; Roisnel, T. www.llb.cea.fr/fullweb/winplotr/winplotr.htm

between the two end-members of the proposed $Na_3V_2O_{2x}(PO_4)_2F_{3-2x}$ ($0 \leq x \leq 1$) family, which supports its existence. Moreover, as the remaining carbon content increases, the cell volume also rises, independently of the type of carbon used in the synthesis process. This suggests that the used carbon percentage would have an influence on the V^{3+}/V^{4+} proportion in the materials, that is, on the fluorine or oxygen content of the final compound. Moreover, as the ionic radii for V^{3+} and V^{4+} in octahedral coordination are 0.64 and 0.58 Å, respectively, this cell volume increase would imply a higher V^{3+} content in the samples [135]. In any case, the influence of carbon in the samples does not appear to be linear (see Figure 2.10).

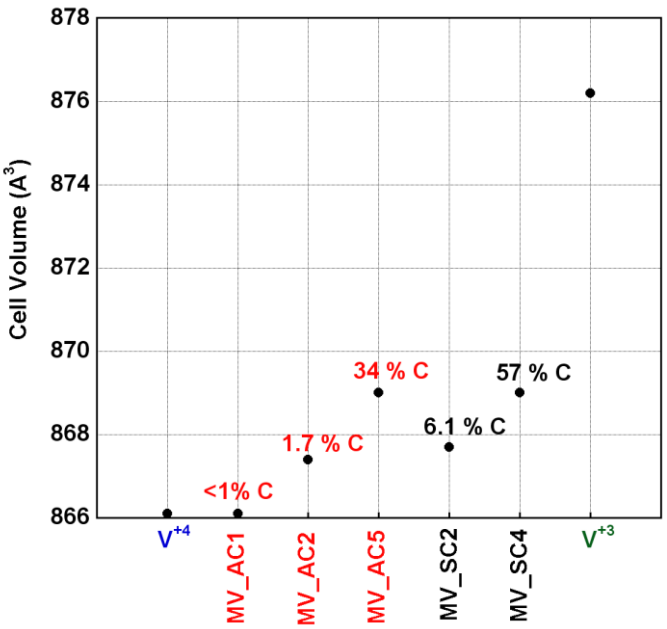

Figure 2.10 *Comparison of cell volume values for the synthesised samples with the V^{4+} and V^{3+} extremes also shown.*

The material containing less than 1 *wt.*% of carbon content, MV_AC1, shows similar cell volume than the one reported in the literature for the V^{4+} material ($Na_3V_2O_2(PO_4)_2F$).

135 *CRC Handbook of Chemistry and Physics*, ed. D.R. Lide, CRC Press, Boca Raton, 84th edn., **2003**

Nonetheless, it has not been possible to obtain the V^{3+} extreme even by using very high amounts of carbon, as for MV_AC5 and MV_SC4. This fact can be attributed to the oxidizing atmosphere present in the vessel used in hydrothermal method, where the carbon coating does not seem to be enough to affect the complete or partial oxidation of V^{3+} in VPO_4 precursor. In this sense, the proximity of the cell volume of all the samples to the V^{4+} extreme phase can be due to the greater stability of vanadium in the vanadyl (VO^{2+}) form when this latter is in an aqueous medium, such as the one used in hydrothermal process.

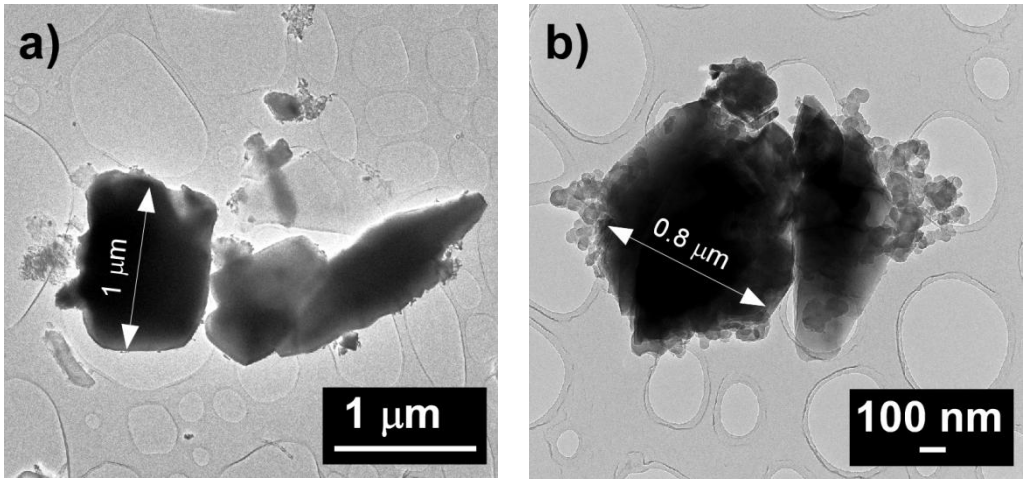

Figure 2.11 *TEM micrograph of material* ***a)*** *MV_AC1 and* ***b)*** *MV_SC4.*

The morphology of the samples was examined by Transmission Electron Microscopy (TEM). Figure 2.11 exhibits the micrographs of samples MV_AC1 and MV_SC4. In the case of MV_AC1, it was synthesised with active carbon and there was less than 1 *wt.*% of remaining carbon in the final compound. MV_SC4 was prepared with S-black and it contained 50 *wt.*% remaining carbon.

Both samples show particles of about 1 μm size with diverse shapes. Thus, neither the carbon type nor the carbon proportion could limit the growth of the particles. Besides, carbon present in MV_SC4 composite appears to form a coating around the particles, which could be beneficial for electrochemical performance.

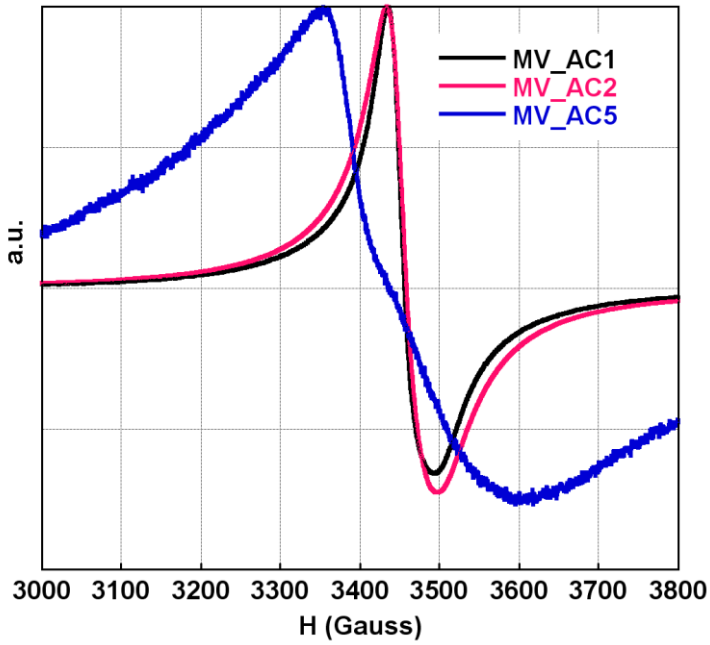

Figure 2.12 *EPR spectra of samples MV_AC1, MV_AC2 and MV_AC5.*

Figure 2.12 presents the Electronic Paramagnetic Resonance (EPR) spectra of samples MV_AC1, MV_AC2 and MV_AC5. The EPR spectrum of sample MV_AC1 shows an axial signal, typical of the vanadyl (VO^{2+}) ion, centred at 3450 Gauss, with $g_{\parallel}$ = 1.937 and $g_{\perp}$= 1.969 values and a <g>= 1.998. These parameters fullfil the condition 2 > ($g_{\parallel}$ < $g_{\perp}$), which is typical of a VO^{2+} ion with an unpaired electron in d_{xy} orbital. Thus, the analysis of the EPR spectrum of sample MV_AC1 confirms that its low carbon content (< 1 *wt.*%) leads to a material containing nearly only V^{4+}, that is, $Na_3V_2O_2(PO_4)_2F$ phase. It can be seen that, as the amount of active carbon increases in the composite, the EPR signal becomes broader, indicating the presence of a mixed V^{3+}/V^{4+} valence. This broadening only happens when the two vanadium types are coupled in the same phase. V^{3+} phases are hardly detected by this technique [136].

136 Carlin, R.L.; Va Duyneyeld, A.J. *Magnetic Properties of Transition Metal Compounds*, Springer-Verlag New York Heidelberg Berlin, **1935.**

For samples MV_SC2 and MV_SC4 (Figure 2.13), the presence of electrochemical grade carbon (S-black carbon) provokes the appearance of a narrow signal in the EPR spectra associated to free radicals in the carbon, that makes difficult the analysis of the complete signal from the material. In the inset from Figure 2.13 it can be appreciated that none of the samples containing S-black carbon (MV_SC set) presents a purely axial signal, indicating the presence of both V^{3+} and V^{4+} in the same phase.

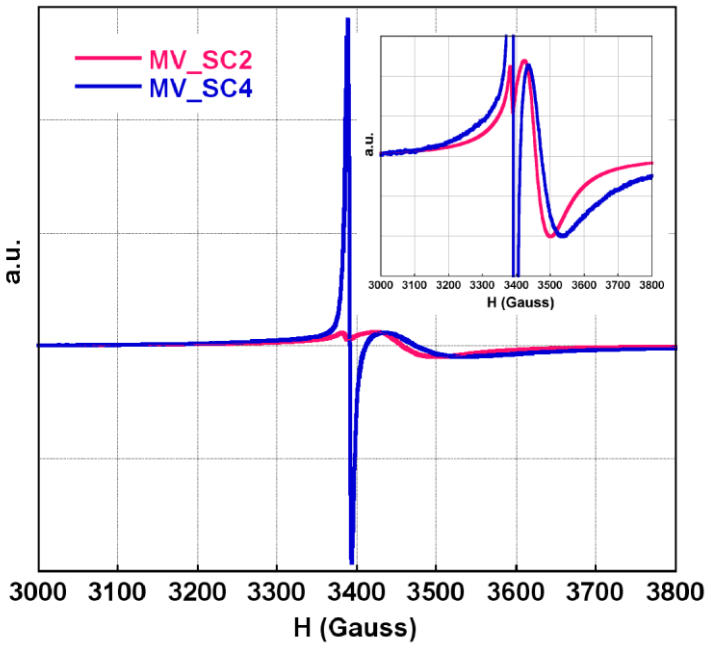

Figure 2.13 *EPR spectra of samples MV_SC2 and MV_SC4.*

In general, it can be said that the signal corresponding to V^{4+} in the EPR spectra becomes broader with an increasing V^{3+} amount in the sample until it cannot be detected. Nevertheless, the disappearance of the signal does not imply necessarily a 100% content in V^{3+}. For this reason, although it is not possible to use this technique to quantify the amount of V^{3+} and V^{4+} in each sample, EPR spectra have been necessary to confirm the presence of mixed valence compounds and to study the vanadium oxidation state evolution among them.

Magnetic susceptibility measurements were also carried out in order to obtain additional information about the vanadium oxidation state in the materials. Figure 2.14 shows the evolution of the inverse of molar magnetic susceptibility (χ_m^{-1}) together with the $\chi_m \cdot T$ product with temperature for samples MV_AC1 and MV_AC5. Thermal evolution of the magnetic effective moment shows a slight decrease at temperatures below 50 K, indicating that the materials present a weak antiferromagnetic behaviour, typical of most vanadium phosphates [137]. High temperature molar magnetic susceptibility follows Curie-Weiss law, where Weiss constant takes a negative value, $\theta \approx -9$ K for both cases. This confirms the antiferromagnetic character of the compounds.

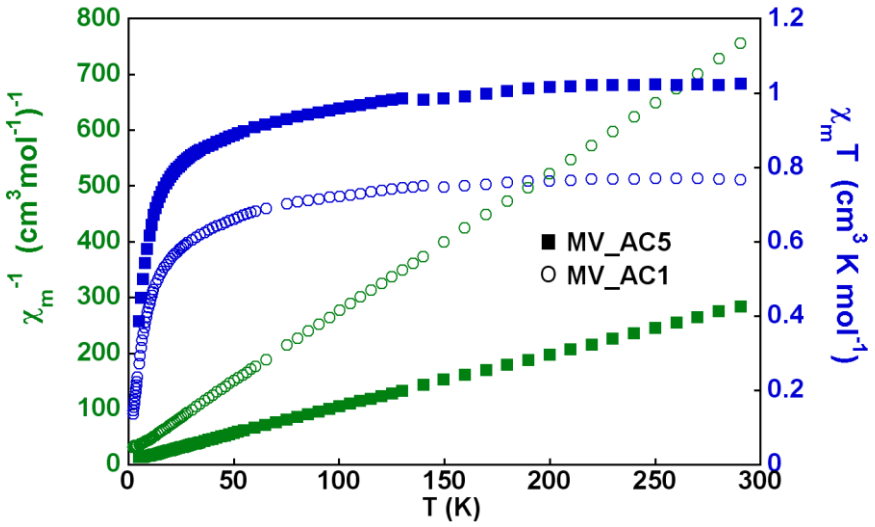

Figure 2.14 *Thermal variation of the inverse of molar susceptibility, χ_m^{-1}, (green) and χ_m T (blue) of MV_AC1 (circles) and MV_AC5 (squares) samples.*

Whereas for MV_AC1 the value of $\chi_m \cdot T$ at room temperature stabilises at *ca.* 0.71 $cm^3 \cdot K \cdot mol^{-1}$, $\chi_m \cdot T$ product for MV_AC5 at room temperature presents a value of about 1 $cm^3 \cdot K \cdot mol^{-1}$ per formula unit. This divergence in the $\chi_m \cdot T$ value indicates the different

137 Villeneuve, G.; Amorós, P.; Beltrán, D.; Drillon, M. "Dimers, regular and double chains in vanadyl phosphates" in "Organic and Inorganic Low Dimensional Crystalline Materials" (P. Delhaes *et al.* Eds.); NATO ASI Series **1987**, 168, 417-420, Springer Science, New York.

oxidation state of vanadium in the samples. On the one hand, the value obtained for sample MV_AC1 is very close to the theoretical $\chi_m \cdot T$ value for $V^{4+}(d^1)$, *i.e.,* 0.7 $cm^3 \cdot K \cdot mol^{-1}$ per formula unit. On the other hand, material MV_AC5 presents a $\chi_m \cdot T$ value that agrees with the presence of both V^{4+} and V^{3+} in the sample as predicted by EPR technique.

Thus, it has been demonstrated that all the synthesised samples present a varying composition that belongs to compounds with the general formula $Na_3V_2O_{2x}(PO_4)_2F_{3-2x}$ ($0 < x < 1$) depending on vanadium oxidation state. Park *et al.* published recently the existence of a mixed valence family of compounds between $Na_3V_2(PO_4)_2F_3$ and $Na_3V_2O_2(PO_4)_2F$, in good agreement with our conclusions [138,139]. The formation of these mixed-valence phases during the synthesis process described above could be explained according to the following chemical reactions:

$$0.5V_2O_5 + C + NH_4H_2PO_4 \rightarrow VPO_4 + NH_3 + CO + 1.5H_2O + \text{remaining C} \qquad \text{(Eq. 2.1)}$$

$$4VPO_4/C + 6NaF + xO_2 + 2xH_2O \rightarrow 2Na_3V_2O_{2x}(PO_4)_2F_{3-2x}/C + 4xHF \qquad \text{(Eq. 2.2)}$$

This way, the attainment of the different phases would be related to the carbon content in the sample. This carbon would play a protective role on the VPO_4 precursor during the hydrothermal process and hinder the complete oxidation of V^{3+} to V^{4+}, in spite of being developed in an aqueous medium. The protective function of carbon *versus* humid atmosphere or water has already been observed for other compounds such as $LiFePO_4$ [140-142].

138 Park, Y. U.; Seo, D. H.; Kim, B.; Hon, K. P.; Kim, H.; Lee, S.; Shakoor, R. A.; Miyasaka, K.; Tarascon, J. M.; Kang, K. *Sci. Rep.*, **2012**, 2:704.

139 Park, Y. U.; Seo, D. H.; Kim, B.; Kim, J.; Lee, S.; Kim, B.; Kang, K. *Adv. Funct. Mater.*, **2014**, DOI: 10.1002/adfm.201400561.

140 Martin, F.; Yamada, A.; Kobayashi, G.; Nishimura, S.I.; Kanno, R.; Guyomard, D. Dupré, N. *Electrochem. Solid-State Lett.*, **2008**, 11, A12-A16.

141 Cuisinier, M.; Martin, J-F.; Dupré, N.; Yamada, A.; Kanno, R.; Guyomard, D. *Electrochem. Comm.*, **2010**, 12, 238-241

2.3.2 Structural, Morphological and Magnetic Characterisation of $Na_3V_2O_{2x}(PO_4)_2F_{3-2x}$ ($x = 0.8$)

2.3.2.1 X-ray powder Diffraction (XRD)

The hydrothermal synthesis of MV_KC resulted in a material containing a 6.40 *wt.*% of Ketjen black carbon. The sample was examined by XRD, showing well-defined diffraction maxima, which indicate the crystallinity of the sample, with a small amount of unreacted VPO_4 initial precursor (see Figure 2.15). The diffraction pattern was indexed in the tetragonal $P4_2/mnm$ space group with the following lattice parameters: a = 9.0302(3) Å and c = 10.6444(7) Å (0).

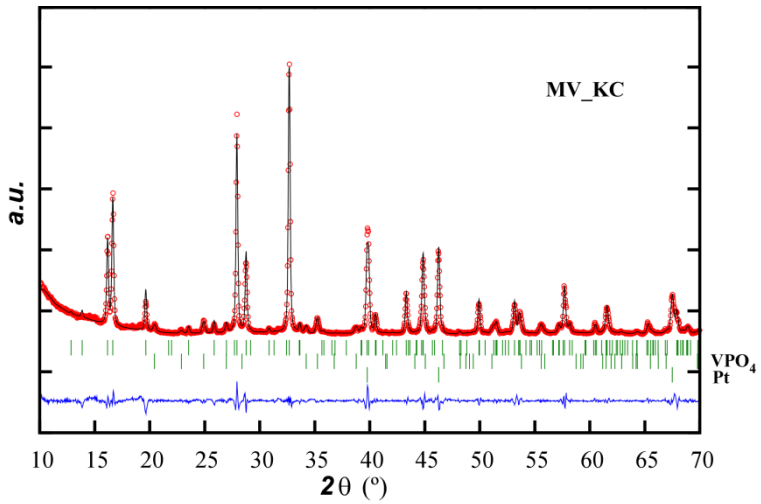

Figure 2.15 *Full Pattern matching of XRD diagram of MV_KC. Experimental (red circles), fitted (black line) and difference between them (blue lower line).*

142 Zaghib, K.; Dontigny, M.; Charest, P.; Labrecque, J.F.; Guerfi, A.; Kopec, M.; Mauger, A.; Gendron, F.;Julien, C.M. *J. Power Sources*, **2008**, 185, 698-710.

Table 2.4 Crystallographic and fitting parameters of MV_KC sample.

Cell parameters (Å)	a = b = 9.0302(3)	
	c = 10.6444(7)	
Space Group	*$P4_2/mnm$*	
R factors (%)	R_p = 14.4	R_B = 0.165
	R_{wp} = 15.1	R_F = 0.260
	R_{exp} = 7.52	χ^2 = 4.06

These cell parameters are intermediate between the extreme compositions of the $Na_3V_2O_{2x}(PO_4)_2F_{3-2x}$ family: $Na_3V_2O_2(PO_4)_2F$ (x = 1; *a* = 9.03051(2) Å, *c* = 10.62002(3) Å [131]) and $Na_3V_2(PO_4)_2F_3$ (x = 0; *a* = 9.047(2) Å, *c* = 10.705(2) Å [133]) The use of Vegard's law to calculate the average vanadium oxidation state resulted in a value of approximately $V^{3.82+}$.

2.3.2.2 Double Titration Method with $KMnPO_4$

A double titration method [138] was employed to quantify the average oxidation state of vanadium (AV) of sample MV_KC.

Table 2.5 Experimentally determined vanadium oxidation states for selected vanadium-containing compounds by the double titration method.

Sample	Theoretical oxidation state of vanadium	Experimental average oxidation state of vanadium (AV)
V_2O_3	+3	+3.04
VO_2	+4	+3.98
V_2O_5	+5	+5.00
MV_KC	_	+3.76

Different vanadium oxides (V_2O_3, VO_2 and V_2O_5) were also analysed in order to have reference standards. The results shown in Table 2.5 indicate that mixed valence MV_KC is composed of 76% V^{4+} and 24% V^{3+}. Although a low amount of VPO_4 impurity remains in the sample, it is in the detection limit for XRD data, so the vanadium oxidation state for MV_KC sample remains around $V^{3.8+}$.

2.3.2.3 Fourier Transform Infrared Spectroscopy (FTIR)

Figure 2.16 depicts FTIR spectrum of MV_KC sample.

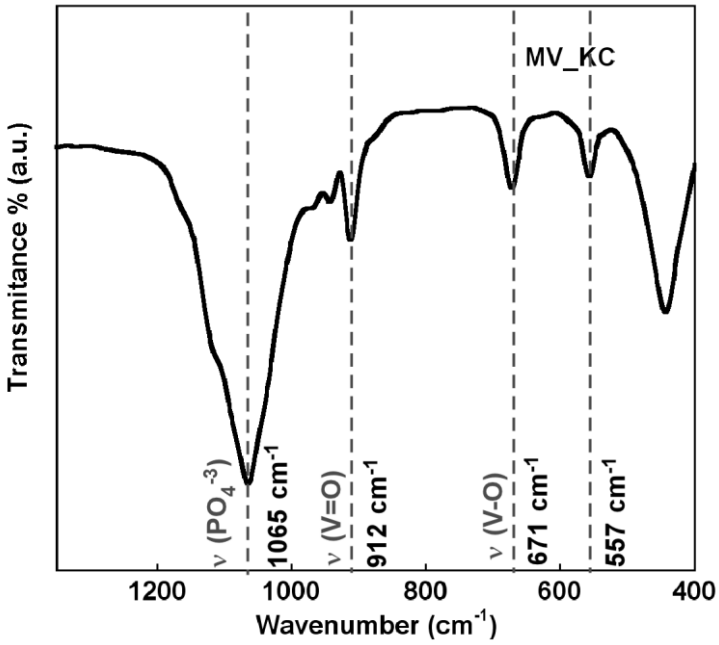

Figure 2.16 *FTIR spectrum of MV_KC sample.*

The narrow peaks between 400 and 1000 cm^{-1} correspond to vanadium – oxygen bonds. Thus, two V-O stretching vibrations can be distinguished within the low wavenumber region (557 and 671 cm^{-1}) while the peak, at 912 cm^{-1}, is typical of a stretching vibration of the short vanadyl V=O bond [130].

The FTIR spectrum of MV_KC sample presents another feature, consisting on an intense and large band at about 1056 cm^{-1} that corresponds to several stretching vibrations that can be ascribed to PO_4^{-3} tetahedra [143].

143 Nakamoto, K. "Infrared and Raman Spectra of Inorganic and Coordination Compounds" 5th ed. John Wiley &Sons, New York, **1997**.

2.3.2.4 Scanning Electron Microscopy (SEM)

Figure 2.17 shows SEM images of the MV_KC sample.

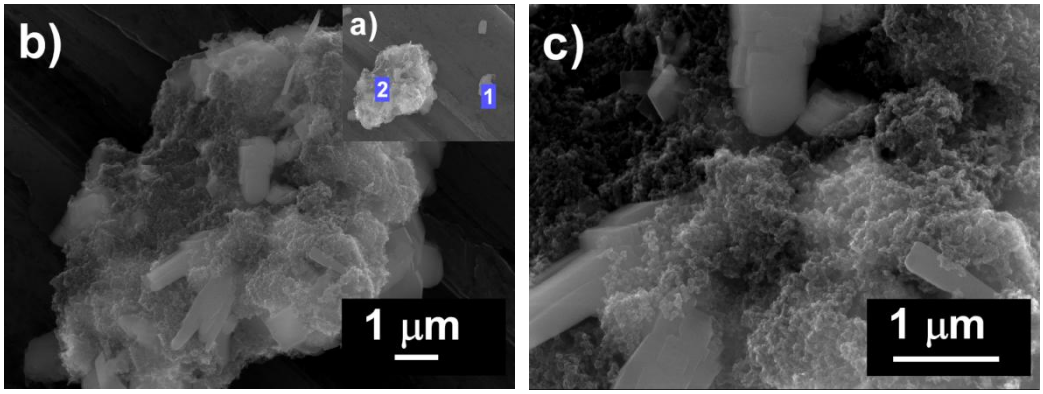

Figure 2.17 *SEM images of MV_KC sample* ***a)*** *X5000,* ***b)*** *X10000,* ***c)*** *X25000.*

Table 2.6 *Ratio of the different elements found by EDX in the SEM analysis of sample MV_KC.*

	Atomic ratio between elements				
	Na	**V**	**P**	**F**	**C**
Point 1	1.3	1	1	1.6	1.7
Point 2	1.5	1	1	2.6	43.3

The material is made of homogeneous agglomerates of several micrometres (Figure 2.17b). EDX analysis of two zones of the material (Table 2.6) indicated that the grains of about 1 μm size (point 1 from Figure 2.17a) posses the element ratio corresponding to the sodium-vanadium fluorophosphate with a minimum presence of carbon. However, the analysis on an agglomerate (point 2 from Figure 2.17a) presented a much larger proportion of carbon apart from the expected element ratio for the studied compound.

These data suggest that the agglomerates are composed of primary particles of about 1µm size embedded in a carbon matrix distributed all over the material. This way, the carbon introduced in the synthesis process is in intimate contact with the electroactive material, which can be beneficial for electrochemical performance (Figure 2.17c).

SEM micrographies also indicate that the composite material is porous, due to the mentioned active material-carbon distribution in the sample.

2.3.2.5 BET analysis

Composite surface properties were analysed by BET measurements.

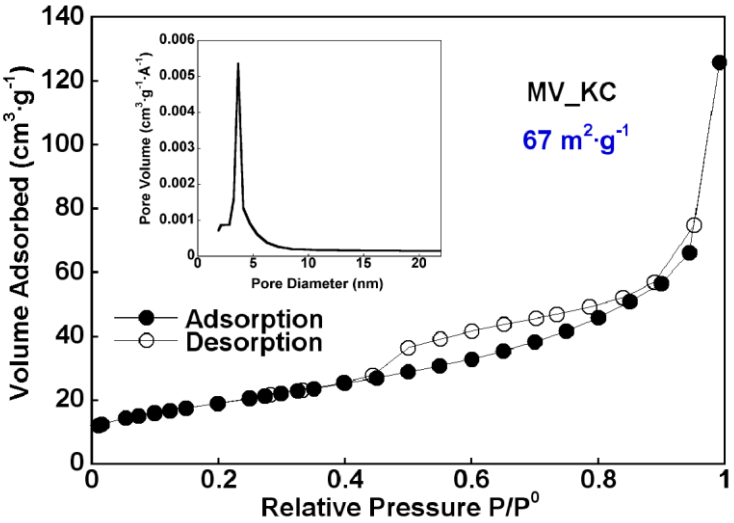

Figure 2.18 *N_2 adsorption-desorption isotherms of MV_KC sample.*

The isotherm shown in Figure 2.18 can be classified as type IV according to the classification given by Brunauer *et al.* [144]. The hysteresis H2 of this isotherm type is characteristic of mesoporous materials with drop shaped pores. The pore size distribution was obtained using the BJH (Barrett, Joyner & Halenda) method from the

144 Brunauer, S.; Emmett, P.; Teller, E. *J. Am Chem. Soc.*, **1938**, 60, 309-319.

adsorption isotherm. The MV_KC sample exhibits a narrow pore size distribution with a maximum at 3.6 nm (inset from Figure 2.18). Moreover, MV_KC presents a specific surface area of 67 m^2g^{-1}. Both, the high specific surface area and the presence of mesopores are related to the presence of carbon in the material.

2.3.2.6 Thermogravimetric Analysis (TGA)

Stability of MV_KC material when heating in inert atmosphere was examined by TGA.

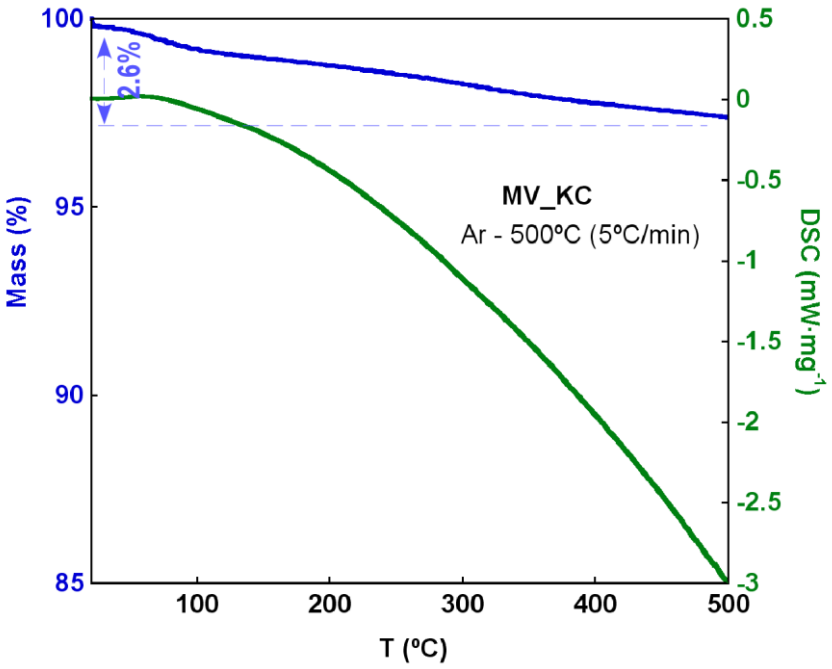

Figure 2.19 *TGA (blue) and DSC (green) curves of MV_KC sample.*

TGA and DSC curves of MV_KC sample heated up to 500ºC (5ºC·min^{-1}) under flowing argon atmosphere are shown in Figure 2.19. A loss of mass of 2.6% was observed during the process which could be attributed to the evaporation of some humidity. The obtained residue was analysed by X-ray diffraction showing the same pattern as initial MV_KC sample what means that this material is stable up to 500ºC under argon atmosphere.

2.3.2.7 Electron Paramagnetic Resonance (EPR)

Figure 2.20 displays the EPR spectrum of the MV_KC sample. It corresponds to an axial signal, centred at approximately 3450 Gauss. However, the signal is not purely axial indicating the presence of a mixed V^{3+}/V^{4+} valence.

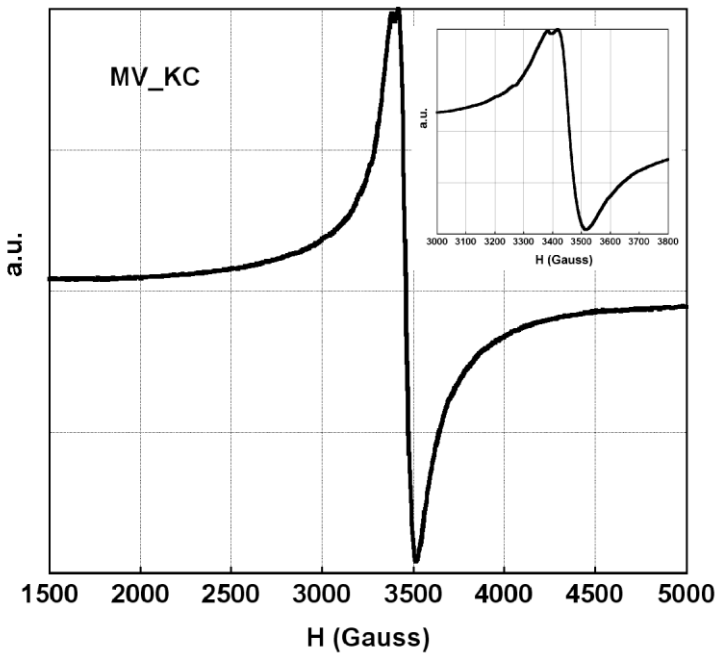

Figure 2.20 *EPR spectrum of MV_KC sample.*

As in the case of S-black carbon, the presence of electrochemical grade carbon Ketjen black provokes the appearance of a second peak in the upper part of the signal (see inset of Figure 2.20), associated to free radicals in the carbon.

2.3.2.8 Magnetic Suscpetibility measurements

Plots of the inverse of molar magnetic susceptibility (χ_m^{-1}), together with the $\chi_m \cdot T$ *vs*. T curves for sample MV_KC are shown in Figure 2.21. Thermal evolution of $\chi_m \cdot T$ product shows a slight decrease at temperatures below 50 K, indicating that the material

presents a weak antiferromagnetic behaviour, typical of most vanadium phosphates [137].

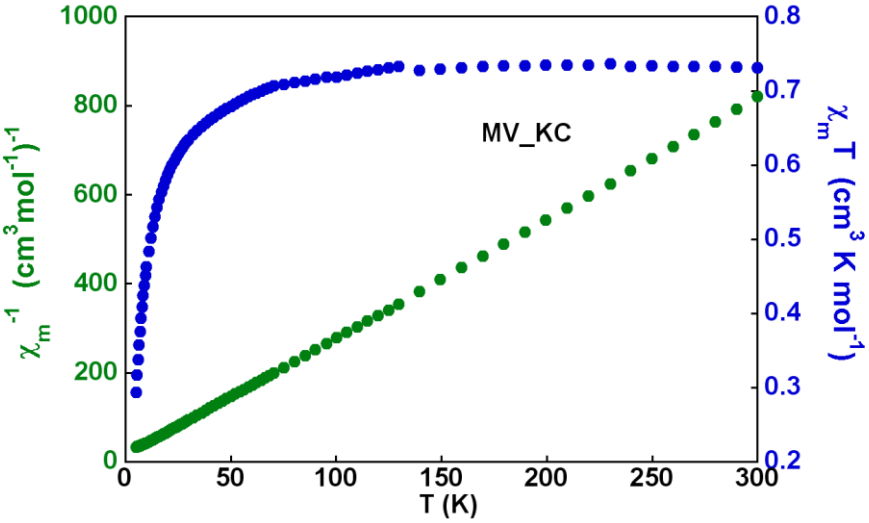

Figure 2.21 *Thermal variation of the inverse of molar susceptibility, χ_m^{-1}, (green circles) and χ_m T (blue circles) of MV_KC sample.*

High temperature molar magnetic susceptibility follows Curie-Weiss law, where Weiss constant takes a negative value, $\theta \approx -5.54$ K. This confirms the antiferromagnetic character of the compound. The C_m experimental value is 0.76 cm^3 K·mol^{-1} and the value of χ_m·T product at room temperature stabilises at *ca.* 0.73 cm^3·K·mol^{-1} (μ_{eff} = 3.42 BM) per formula unit which agrees with the presence of both V^{4+} and V^{3+} in the sample. This value is slightly higher than the one expected for only V^{4+} compounds, 0.7 cm^3·K·mol^{-1}per formula unit, so the presence of V^{3+} would be minimum.

2.3.2.9 Nuclear Magnetic Resonance (NMR)

Figure 2.22 shows the ^{23}Na solid state NMR (ssNMR) spectrum of MV_KC sample. Three main signals are present in the spectrum, which were fitted using the DMfit

program [145]. The relative intensities of the resonances observed at 74 ppm, 111 ppm and 158 ppm amount to 72%, 22% and 6%, respectively. These shifts indicate the presence of hyperfine interactions between the ^{23}Na and the paramagnetic vanadium ions [146]. Hyperfine shifts are very sensitive to interatomic distances, bond angles and to the oxidation states of the paramagnetic centres and are usually reflected by very large chemical shift values. In this case, close examination of the coordination sphere of the sodium sites indicates that each Na^+ is in the vicinity of two equidistant vanadium ions as highlighted by the dashed lines in Figure 2.22. V^{3+} ions generally cause a more positive chemical shift than V^{4+} by several tenths of ppms [138,139,147], and their effect is additive. Based on these observations, the three signals observed in the spectrum are assigned to the V^{4+}-V^{4+} (74 ppm), V^{3+}-V^{4+} (111 ppm) and V^{3+}-V^{3+} (158 ppm) pairs. Considering the relative populations of the three pairs as obtained by the fitting of the NMR spectrum (Figure 2.22), an average oxidation state of vanadium in the MV_KC phase of $V^{3.83+}$ is calculated. In the case of a completely random distribution of the vanadium oxidation states in a sample with an average oxidation state of +3.83, the expected relative intensities of the V^{4+}-V^{4+}, V^{3+}-V^{4+} and V^{3+}-V^{3+} pairs would be of 69%, 28% and 3% respectively. Although these values are very similar to the ones observed for MV_KC sample, the relative populations of the homogeneous pairs V^{4+}-V^{4+} and V^{3+}-V^{3+} in this material, are slightly favoured relative to the intermediate V^{3+}-V^{4+} pairs. This fact can be due to the local structural changes induced by the oxidation state of one vanadium atom, that can affect the stability of its neighbours.

The ^{19}F ssNMR spectrum of the MV_KC sample is shown in Figure 2.23. The inset on the left hand side illustrates the atomic positions of some F atoms resulting in these shifts. The best fit of the signal was obtained by considering two Lorentzian functions centred at 109 and 94 ppm. An average vanadium oxidation state has been calculated from the relative intensities of the two signals by taking into account that the population ratio of the two distinct ^{19}F sites (F(1) and F(2)) in the pure V^{3+} compound is 1:2. This way, 80 % V^{4+} and 20 % V^{3+} is obtained for MV_KC phase, giving rise to $V^{3.8+}$ valence.

145 Massiot, D.; Fayon, F.; Capron, M.; King, I.; Le Calvé, S.; Alonso, B.; Durand, J.O.; Bujoli, B.; Gan, Z.; Hoatson, G. *Magn. Reson. Chem*. **2002**, 40, 70-76.

146 Grey, C.P.; Dupre, N. *Chem. Rev*. **2004**, 104, 4493–4512

147 Ellis, B.L.; Ramesh, T.N.; Davis, L.J.M.; Goward, G.R.; Nazar, L.F. *Chem. Mater*. **2011**, 23, 5138–5148.

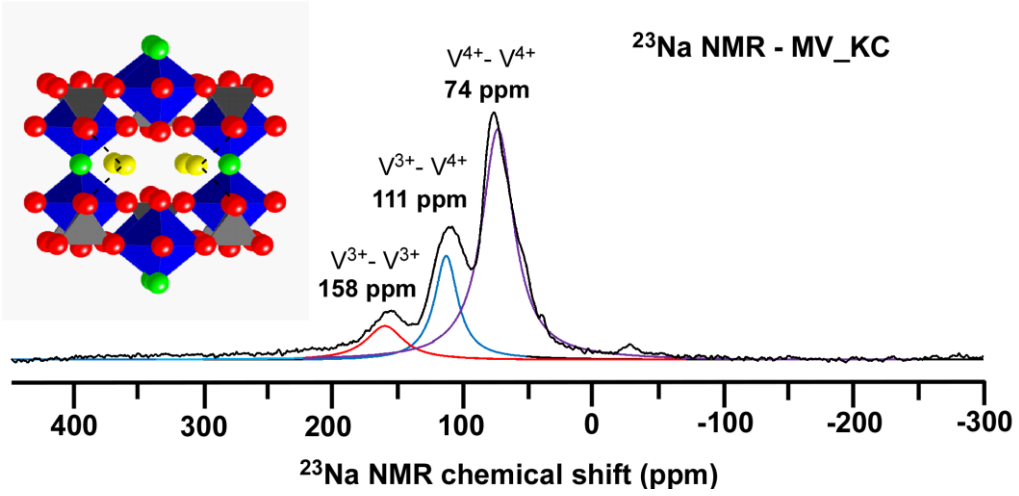

Figure 2.22 *^{23}Na ssNMR spectrum of MV_KC sample (black). Lines of fit for V^{4+}-V^{4+} (purple), V^{3+}-V^{4+} (blue) and V^{3+}-V^{3+} (red) pairs are also shown.*

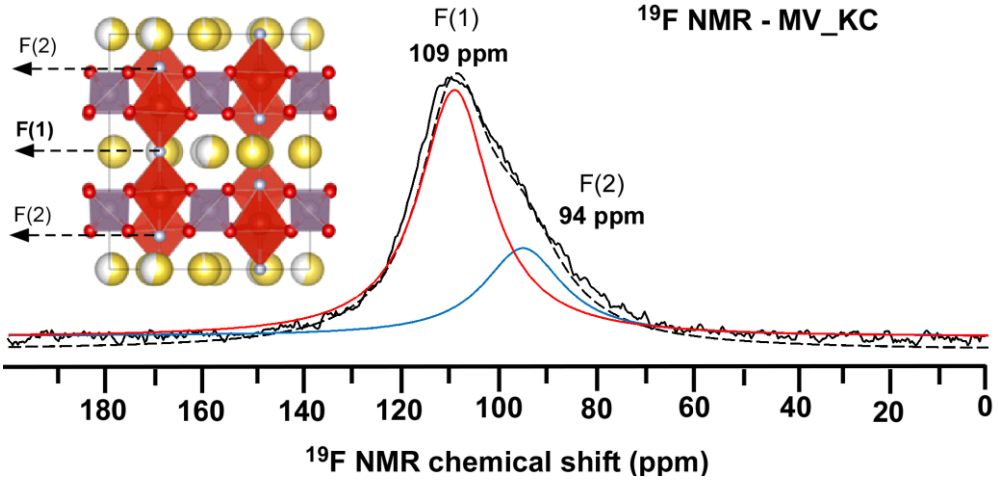

Figure 2.23 *^{19}F ssNMR spectrum of MV_KC sample. Lines of fit for F(1) (red) and F(2) (blue) are also shown.*

It must be noted that the discrepancy between the vanadium oxidation state obtained from the ^{19}F and ^{23}Na analyses in this material is very small ($V^{3.8+}$ and $V^{3.83+}$, respectively) and is considered to be within the error of the fitting procedures.

2.3.3 *Structural, Morphological and Magnetic Characterisation of $Na_3V_2O_2(PO_4)_2F$*

2.3.3.1 *X-ray powder Diffraction (XRD)*

Figure 2.24 presents the X-ray diffractogram of V4 sample. This material shows intense and well-defined diffraction maxima, that indicate good cristallinity, and that correspond to the characteristic diffraction pattern of the $Na_3V_2O_2(PO_4)_2F$ phase.

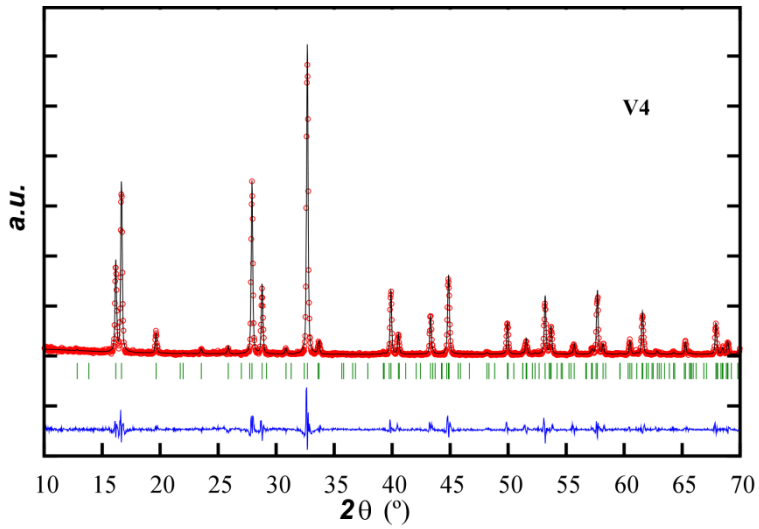

Figure 2.24 *Full Pattern matching of XRD diagram of V4. Experimental (red circles), fitted (black line) and difference between them (blue lower line).*

The pattern was indexed by using the Full Pattern Matching option of the FULLPROF program [134]. The obtained unit cell was in good agreement with that described in bibliography [131]. Table 2.7 lists the crystallographic and fitted parameters of sample V4.

Table 2.7 *Crystallographic parameters of $Na_3V_2O_2(PO_4)_2F$ and fitted parameters for V4 sample.*

	Bibliography [131]	**Fitting**
Cell parameters (Å)	a = b = 9.03051	a = b = 9.03126 (34)
	c = 10.62002	c = 10.62902 (69)
Space Group	*$P4_2/mnm$*	
R factors (%)	R_p = 22.9	R_B = 0.308
	R_{wp} = 30.1	R_F = 0.485
	R_{exp} = 18.91	χ^2 = 2.54

V4 material was subjected to different carbon coating strategies, giving rise to three composites with carbon: V4_LTT, V4_FTT and V4_BMT. Elemental analysis determined that these composites contained 2.65, 4.5 and 15 *wt.*% carbon, respectively.

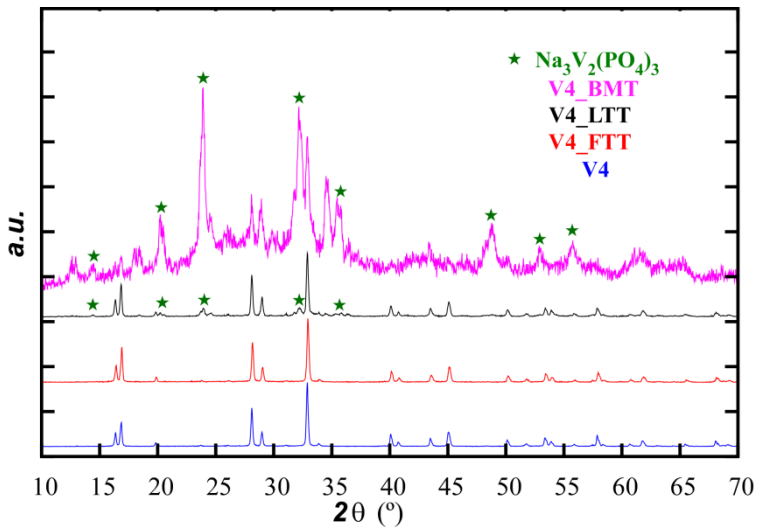

Figure 2.25 *X-ray diffractograms of the raw sample V4 (blue), V4_FTT (red) V4_LTT (black) and V4_BMT (pink).*

Figure 2.25 shows the diffraction pattern of the four obtained materials: the carbon free raw sample V4, long thermally treated V4_LTT, flash thermally treated V4_FTT and ball milled before long thermally treated V4_BMT. The four of them present the main diffraction peaks characteristic of the $Na_3V_2O_2(PO_4)_2F$ phase. A small amount of NASICON-type $Na_3V_2(PO_4)_3$ secondary phase appears when a long thermal treatment is used (V4_LTT) and this amount becomes considerably higher when V4_BMT sample is analysed. In this latter sample, diffraction maxima of $Na_3V_2O_2(PO_4)_2F$ phase can hardly be appreciated and there are some unidentified extra peaks. V4_FTT did not show any secondary phase or degradation product.

The partial decomposition of the main V^{4+} $Na_3V_2O_2(PO_4)_2F$ phase into a V^{3+} $Na_3V_2(PO_4)_3$ secondary phase after a long thermal treatment could be related to the presence of carbon in the sample, that could act as a reducing agent leading to the partial sublimation of the fluorine as VF_3 [148,149].

2.3.3.2 Double Titration Method with $KMnPO_4$

A double titration method [138] was employed to quantify the average oxidation state of vanadium (AV) in sample V4. Analysis of V_2O_3, VO_2 and V_2O_5 standards is also shown.

Table 2.8 Experimentally determined vanadium oxidation states for selected vanadium-containing compounds by the double titration method.

Sample	Theoretical oxidation state of vanadium	Experimental average oxidation state of vanadium (AV)
V_2O_3	+3	+3.04
VO_2	+4	+3.98
V_2O_5	+5	+5.00
V4	_	+4.01

The results shown in Table 2.8 indicate that vanadium oxidation state in V4 sample is +4.

148 Ateba Mba, J-M.; Masquelier, C.; Suard, E.; Croguennec, L.; *Chem. Mater*., **2012**, 24,1223 – 1234.
149 Recham, N.; Chotard, J.-N.; Dupont, L.; Djellab, K.; Armand, M.; Tarascon, J.-M. *J. Electrochem. Soc.*, **2009**,156, A993 – A999.

2.3.3.3 Fourier Transform Infrared Spectroscopy (FTIR)

Figure 2.26 depicts FTIR spectrum of V4 sample.

The narrow peaks between 400 and 1000 cm^{-1} correspond to vanadium – oxygen bonds. Two stretching V-O vibrations can be distinguished within the low wavenumber region (557 and 669 cm^{-1}) and the most intense peak, at 920 cm^{-1}, is typical of a stretching vibration of the short vanadyl V=O bond [150]. Similar values have been found for this compound in the literature [130].

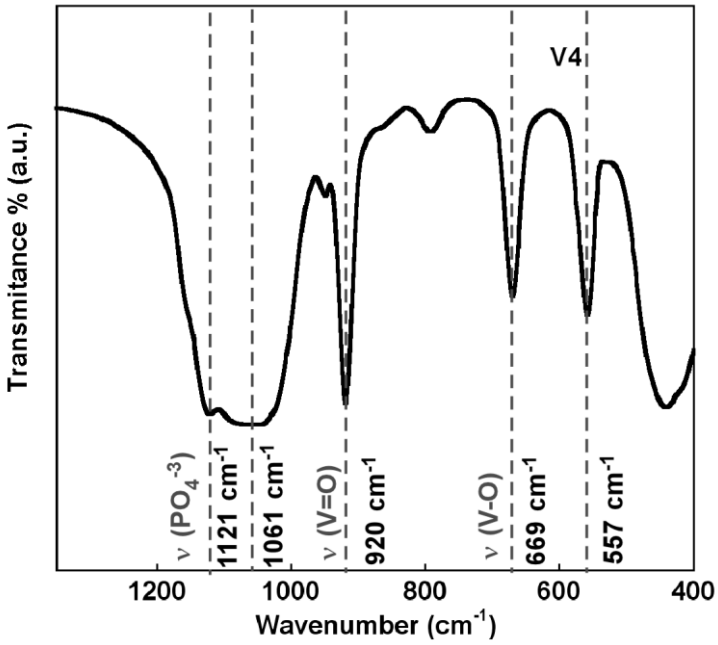

Figure 2.26 *FTIR spectrum of V4 sample.*

As previously commented in section 2.3.2.3, another feature of FTIR spectrum is the presence of an intense and large band (1000 – 1200 cm^{-1}) constituted of several stretching vibrations that can be ascribed to PO_4^{-3} tetahedra [143].

150 Prakash, A.S.; Rozier, P.; Dupont, L.; Vezin, H.; Sauvage, F.; Tarascon, J.-M. *Chem. Mater.*,**2006**, 18, 407-412.

2.3.3.1 Scanning Electron Microscopy (SEM)

Figure 2.27 depicts SEM micrographies corresponding to the V4 raw material and two of the three carbon coated samples, V4_LTT and V4_FTT.

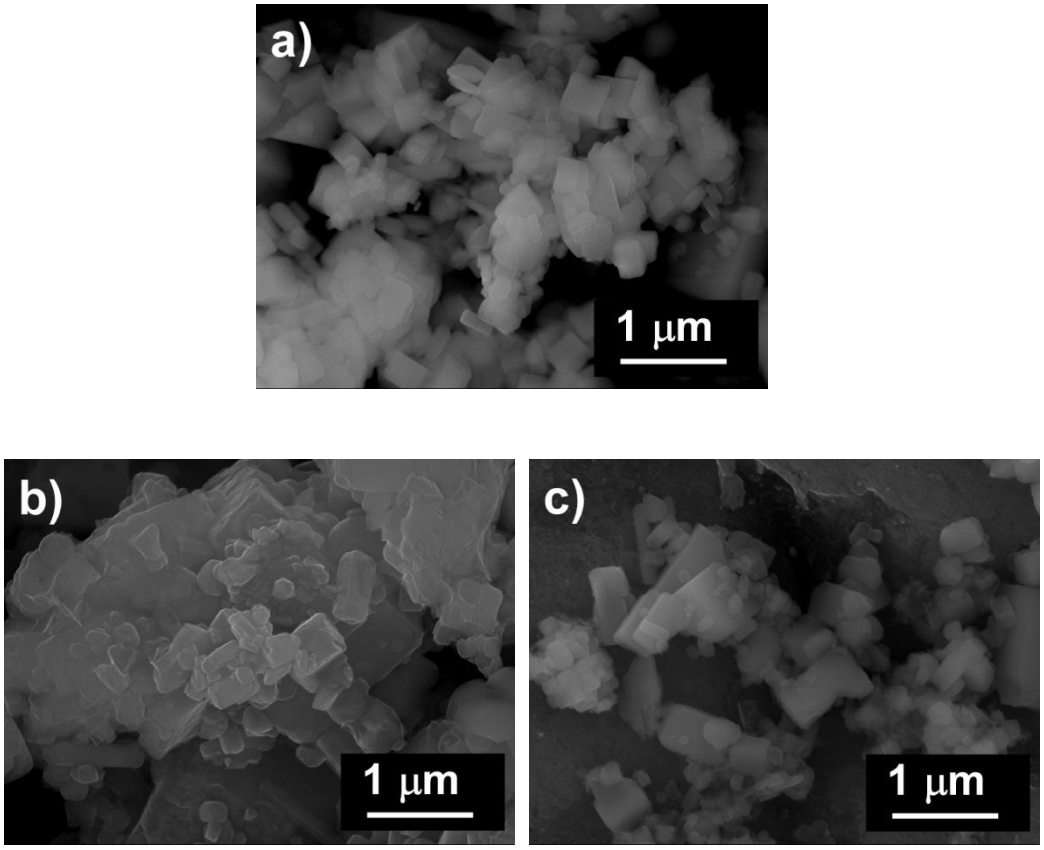

Figure 2.27 *SEM images of samples* ***a)*** *V4* ***b)*** *V4_LTT and* ***c)*** *V4_FTT.*

All of them are made up of well defined prism-shaped particles of about 0.5 μm size. Partial sintering of V4_LTT particles can be seen in Figure 2.27b, due to the long thermal treatment. No significant size changes are appreciated for V4_FTT (Figure 2.27c). The presence of carbon in V4_LTT and V4_FTT composites (2.65 and 4.5 *wt.* % respectively) was confirmed by EDX analysis.

2.3.3.2 BET analysis

Uncoated $Na_3V_2O_2(PO_4)_2F$ material´s (V4) surface area was studied by BET. It presents a specific surface of 5.4 m^2 g^{-1} which is related to the absence of *in-situ* carbon and the consequent decrease in the number of pores.

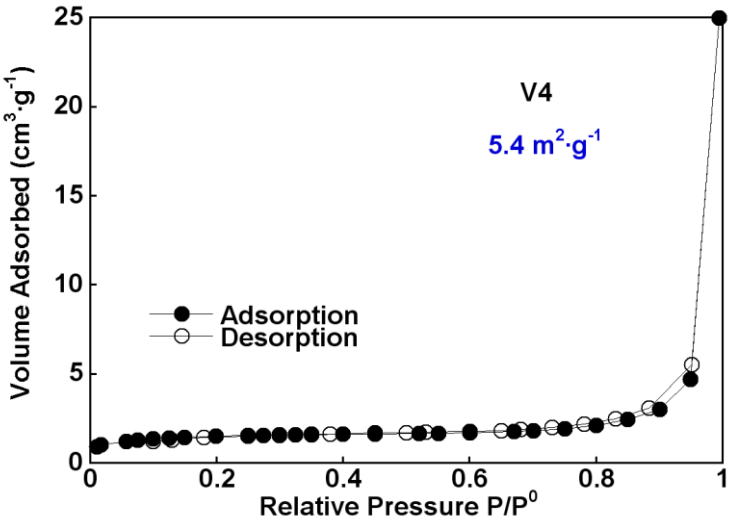

Figure 2.28 *N_2 adsorption-desorption isotherms of V4 sample.*

The isotherm shown in Figure 2.28 can be classified as type II according to the classification given by Brunauer *et al.* [144]. The slight hysteresis present in the P/P^0 = 0.8 – 1 range indicates the presence of some mesopores.

2.3.3.3 Thermogravimetric Analysis (TGA)

Thermal stability of the uncoated V4 sample under inert atmosphere was examined by thermogravimetric analysis. TGA and DSC curves of this material heated up to 500ºC (5ºC·min^{-1}) under flowing argon atmosphere are shown in Figure 2.29.

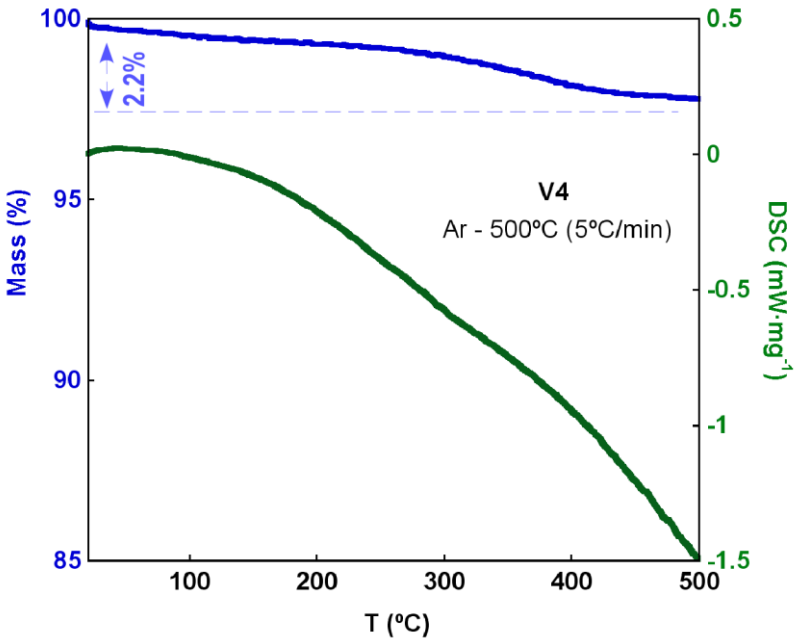

Figure 2.29 *TGA (blue) and DSC (green) curves of V4.*

A loss of mass of 2.2% was observed during the process which could be attributed to the evaporation of some humidity. The obtained residue was analysed by X-ray diffraction showing the same pattern as initial V4 sample. This means that V4, *i.e.,* $Na_3V_2O_2(PO_4)_2F$ compound, seems to be stable up to 500ºC under argon atmosphere.

2.3.3.4 Electron Paramagnetic Resonance (EPR)

Figure 2.30 displays the EPR spectrum of the V4 sample. It corresponds to an axial signal, centred at 3450 Gauss.

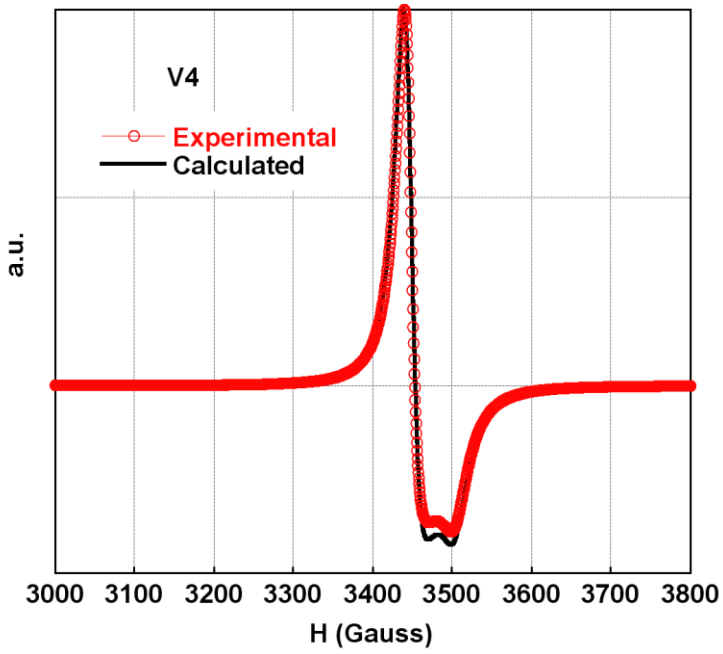

Figure 2.30 *Experimental (red circles) and calculated (black line) EPR spectrum of V4 sample.*

The spectrum fits exactly to a Lorentzian curve with $g_{\|}$ = 1.935 and $g_{\perp}$= 1.968 values, <g>= 1.957. These parameters fullfil the condition 2 > ($g_{\|}$ < $g_{\perp}$), which is typical of a VO^{2+} ion with an unpaired electron in d_{xy} orbital, confirming the obtaining of the V^{4+} $Na_3V_2O_2(PO_4)_2F$ phase. The narrow signal, ΔH_{pp} < 25 Gauss, indicates the high degree of order and crystallisation of the phase.

2.3.3.5 Magnetic Suscpetibility measurements

Plots of the molar magnetic susceptibility (χ_m), together with the $\chi_m \cdot T$ *vs.* T curves for sample V4 are given in Figure 2.31.

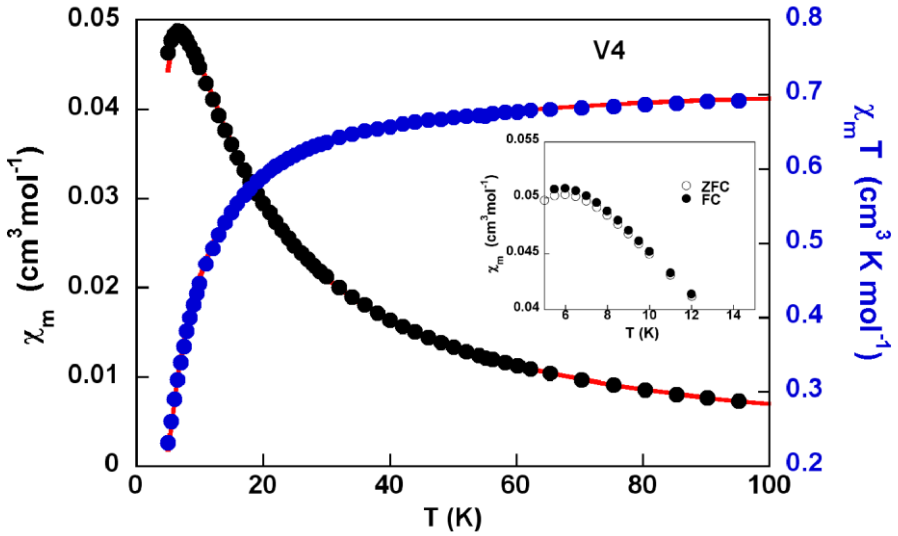

Figure 2.31 *Thermal variation of molar susceptibility, χ_m, (black circles) and χ_m T (blue circles) of V4 sample. Continuous red line represents the best fitting.*

The magnetic curves obey the Curie-Weiss law at temperatures higher than 50 K, with a Weiss temperature of - 5.7 K. The C_m experimental value is 0.74 $cm^3\ K \cdot mol^{-1}$ and the value of $\chi_m \cdot T$ at room temperature stabilises at 0.7 $cm^3 \cdot K \cdot mol^{-1}$ (3.35 BM) per formula unit which is the expected value for an only V^{4+} containing phase. The χ_m values increase with decreasing temperature up to reach maxima at 6.5 K (0.0488 $cm^3 \cdot mol^{-1}$). Below 50 K, the $\chi_m \cdot T$ value continuously decreases on lowering the temperature. These features indicate the presence of antiferromagnetic interactions in this sample which are typical of vanadium phosphate compounds [137]. The slight differences observed for Zero Field Cooling (ZFC) and Field Cooling (FC) molar susceptibility curves at low temperatures (see inset of Figure 2.31) could indicate the presence of a ferromagnetic impurity, *e.g.,* a little amount of VO_2.

Taking into account the dinuclear structure of $Na_3V_2O_2(PO_4)_2F$ compound, its susceptibility data have been fitted by the expression given by Bleaney–Bowers for dinuclear vanadium (IV) compounds [151] that is derived from the Heisenberg isotropic spin Hamiltonian ($H = -2JS_1S_2$) for two coupled S = 1/2 ions. In this formula we have considered the temperature-independent paramagnetism (TIP, $N\alpha$), see Eq. 2.3:

$$\chi_m = \frac{Ng^2\beta^2}{kT}\left(\frac{1}{\left(3+\exp\left(\frac{-2J}{kT}\right)\right)}\right) + N\alpha \qquad \text{(Eq. 2.3)}$$

where N is the Avogadro's number, β is the Bohr magneton and k is the Boltzmann constant. The best least-square fitting is obtained from the parameter J/k = -5.6 K (-3.9 cm^{-1}). The calculated g-value is 1.96 which is in good agreement with the one obtained from EPR, <g> 1.957. An approximate TIP value of $200 \cdot 10^{-6}$ $cm^3 \cdot mol^{-1}$ is introduced in the fitting. At first sight, the structural features make possible the existence of interdimeric magnetic interactions in this compound. Calculations carried out using the molecular field approach (Eq. 2.4) to evaluate the influence of intermolecular exchange pathways improve the fitting in sample V4, where they led to final J/k and z'J'/k values of -5.6 and -1.5 K (-3.9 and -1.0 cm^{-1}), respectively. These results lead to the smallest error in the fitting, but other possible combinations with similar magnitudes of J and J' cannot be discarded. The calculated g-value is 1.96, which agrees well with the empirical 1.957.

$$\chi'_m = \frac{\chi}{1-\frac{2z'J'\chi}{Ng^2\beta^2}} \qquad \text{(Eq. 2.4)}$$

151 Bleaney, B.; Bowers, K.D.; *Proc. R. Soc. London*, **1952**, Ser. A 214, 451-465.

2.3.3.6 Nuclear Magnetic Resonance (NMR)

Figure 2.32 shows the ^{23}Na solid state NMR (ssNMR) spectrum of the V4 sample. It presents one signal centred at 75 ppm which has been deconvoluted into two second order central transition signals corresponding to the two types of sodium present in the structure, Na(1) and Na(2) [131,152]. The fitting of the spectrum is in good agreement with the theoretical occupancies of the different sodiums, 1 and ½, respectively. The signal was fitted using the DMfit program [145]. The relative intensities of the resonances observed amount to a ratio of 1:0.5 respectively. This shift indicates the presence of hyperfine interactions between the ^{23}Na and the paramagnetic vanadium (IV) ion [146]. Hyperfine shifts are very sensitive to interatomic distances, bond angles and to the oxidation states of the paramagnetic centres and are usually reflected by very large chemical shift values.

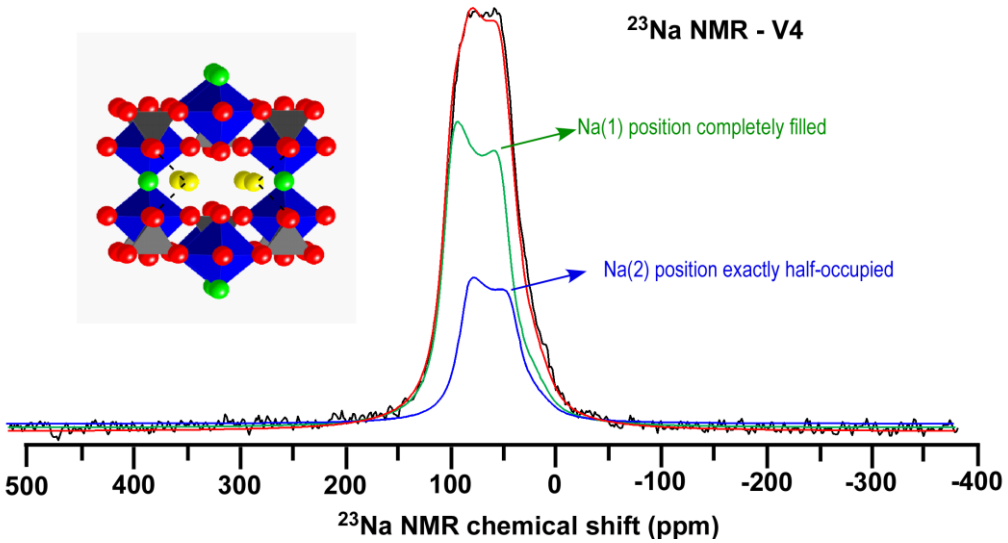

Figure 2.32 *^{23}Na ssNMR spectrum of V4 sample (black). Lines of fit for Na(1) (green) and Na(2) (blue) are also shown.*

152 Massa, W.; Yakubovich, O.; Dimitrova, O. *Solid State Sci.*, **2002**, 4, 495-501.

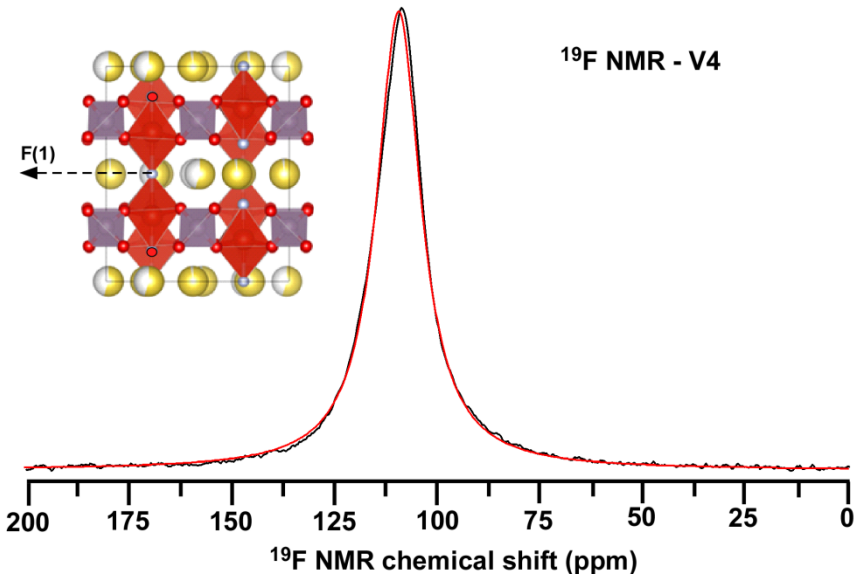

Figure 2.33 *^{19}F ssNMR spectrum of V4 sample (black). Line of fit for F(1) (red) is also shown.*

The ^{19}F ssNMR spectrum of the compound is shown in Figure 2.33. The best fit of the signal was obtained by considering a Lorentzian function centred at 109 ppm. The shift would correspond to the only type of fluorine present in the structure of $Na_3V_2O_2(PO_4)_2F$ compound [131,152].

2.3.4 Vanadium oxide reagents: the need of a pretreatment

There have been some issues in the replication of pure $Na_3V_2O_2(PO_4)_2F$ phase (V4 sample) related to the vanadium (III) oxide used as precursor that deserve to be analysed. As it has been said before, V_2O_3 reactant is used in the synthesis of $Na_3V_2O_2(PO_4)_2F$ compound according to the following reaction:

$$V_2O_3 + 2NaH_2PO_4{\cdot}H_2O + NaF + ½\ O_2 \rightarrow Na_3V_2O_2(PO_4)_2F + 4H_2O \qquad \text{(Eq. 2.5)}$$

Three different vanadium (III) oxide reagents have been employed for the preparation of $Na_3V_2O_2(PO_4)_2F$ phase. The production year for the as-named R-V_2O_3, Middle-Aged R-V_2O_3 and Aged R-V_2O_3 reactants was 2011, 2006 and 2004, respectively. All these reactants have been stored in normal ambient conditions (1 atm., room temperature).

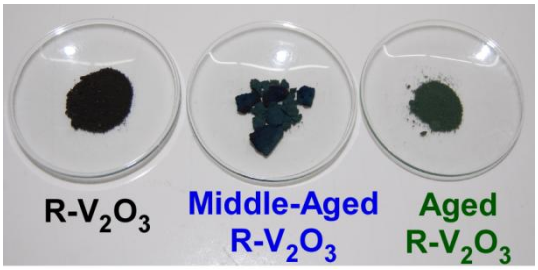

Figure 2.34 *External aspect of R-V_2O_3, Middle-Aged R-V_2O_3 and Aged R-V_2O_3 vanadium (III) oxides.*

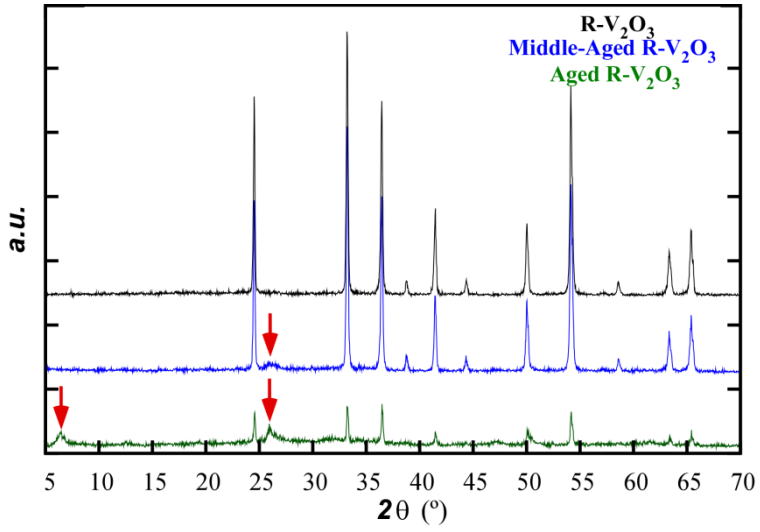

Figure 2.35 *XRD pattern of R-V_2O_3, Middle-Aged R-V_2O_3 and Aged R-V_2O_3 vanadium (III) oxides.*

Figure 2.34 presents the external aspect of the three different vanadium oxides. Reactant R-V_2O_3 is black coloured as specified by the manufacturer while Middle-Aged R-V_2O_3 and Aged R-V_2O_3 present turquoise and green colour, respectively.

The X-ray diffractograms obtained for the three reactants are shown in Figure 2.35. All vanadium compounds, R-V_2O_3, Middle-Aged R-V_2O_3 and Aged R-V_2O_3 exhibit the main diffraction peaks of V_2O_3 phase but only reactant R-V_2O_3 appears to be pure. Middle-Aged R-V_2O_3 and Aged R-V_2O_3 present some extra diffraction maxima, marked with red arrows, which have not been identified. These differences between the three reactants suggest that they have suffered some kind of modification or aging process during storage.

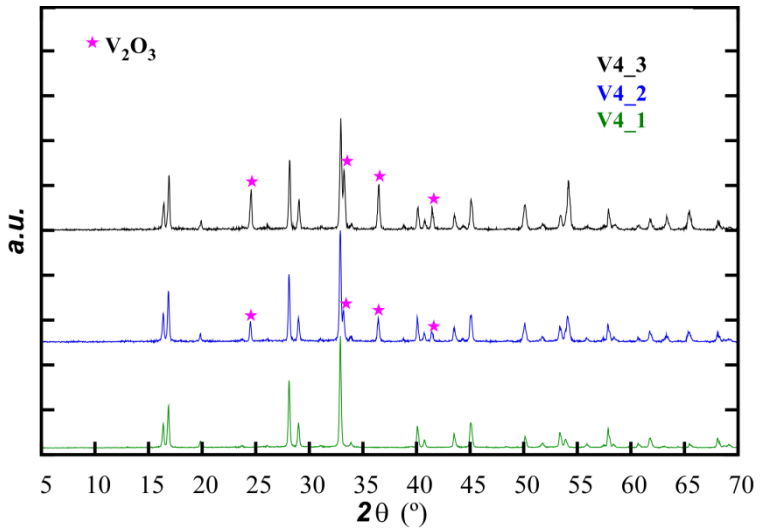

Figure 2.36 *XRD pattern of obtained compounds using Aged R-V_2O_3 Middle-Aged R-V_2O_3 and R-V_2O_3 as precursors.*

Figure 2.36 displays the XRD patterns of the sodium vanadium fluorophosphates obtained when R-V_2O_3, Middle-Aged R-V_2O_3 and Aged R-V_2O_3 are employed as precursors. V4 is produced when using Aged R-V_2O_3, while V4_2 and V4_3 products are obtained with Middle-Aged R-V_2O_3 and R-V_2O_3 precursors, respectively. As it can be observed, only when using Aged R-V_2O_3 reagent pure $Na_3V_2O_2(PO_4)_2F$ compound is

obtained (V4 sample). In the rest of the cases (samples V4_2 and V4_3), unreacted vanadium (III) oxide appears as impurity.

In order to analyze the aging process suffered by R-V_2O_3, Middle-Aged R-V_2O_3 and Aged R-V_2O_3 precursors and its influence on the obtaining of pure $Na_3V_2O_2(PO_4)_2F$ compounds, a deeper characterisation was carried out.

A double titration method with $KMnPO_4$ [138] was used to elucidate the real vanadium oxidation state of the three vanadium (III) reactants. Results are presented in Table 2.9. It can be seen that Middle-Aged R-V_2O_3 and Aged R-V_2O_3 have suffered from a partial oxidation resulting in +3.49 and +4.41 vanadium oxidation states, respectively. These data indicate the evolution of vanadium (III) to mixed valent oxides or hydroxides when exposing them to ambient air and humidity for years. The presence of V^{4+} in the degraded reagents was confirmed by EPR measurements.

Table 2.9 *Experimentally determined vanadium oxidation states for employed vanadium (III) oxides.*

Reagent	Theoretical oxidation state of vanadium	Experimental average oxidation state of vanadium (AV)
R-V_2O_3	+3	+3.04
Middle-Aged R-V_2O_3	+3	+3.49
Aged R-V_2O_3	+3	+4.41

In light of those data, and taking into account that the best performing reactant presented an oxidation state higher than +3, vanadium (IV) oxide was used as precursor for $Na_3V_2O_2(PO_4)_2F$ preparation. For this purpose, two different VO_2 reagents were employed. The production year for the as-called R-VO_2 and Aged R-VO_2 was 2011 and 2005, respectively. The external aspect of R-VO_2 and Aged R-VO_2 is shown in Figure 2.37. R-VO_2 reactant is dark grey as specified by the manufacturer while the colour for Aged R-VO_2 is green (Figure 2.37). X-ray diffractograms of both vanadium oxides are shown in Figure 2.38. As it can be seen, main diffraction peaks of VO_2 phase are present in both R-VO_2 and Aged R-VO_2, but there are also some unidentified extra maxima marked with blue arrows.

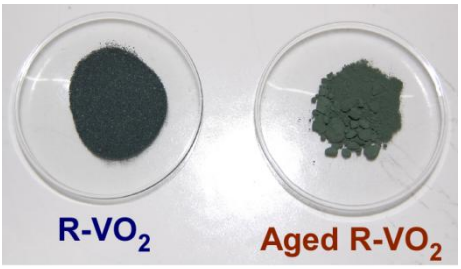

Figure 2.37 *External aspect of R-VO_2 and Aged R-VO_2 vanadium (IV) oxides.*

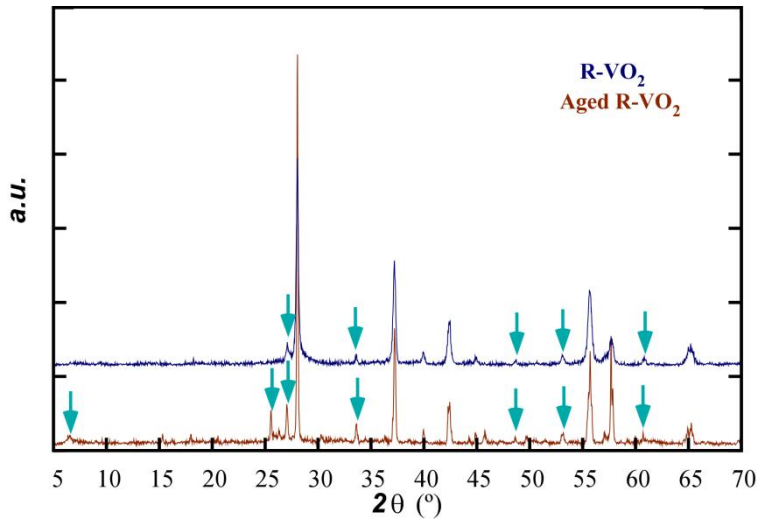

Figure 2.38 *XRD pattern of R-VO_2 and Aged R-VO_2 vanadium (IV) oxides.*

As in the case of vanadium (III) oxides, a double titration method with $KMnPO_4$ [138] was used to elucidate the real vanadium oxidation state of the two vanadium (IV) reactants. Results are presented in Table 2.10. A partial oxidation is observed again in the case of Aged R-VO_2 leading to a +4.27 vanadium oxidation state. These data indicate the evolution of vanadium (IV) to a mixed IV-V valence due to its exposure to air. The presence of V^{4+} in the aged reactant was confirmed by EPR measurements.

Table 2.10 *Experimentally determined vanadium oxidation states for employed vanadium (IV) oxides.*

Reagent	Theoretical oxidation state of vanadium	Experimental average oxidation state of vanadium (AV)
R-VO_2	+4	+3.98
Aged R-VO_2	+4	+4.27

Figure 2.39 shows the XRD patterns of the obtained sodium vanadium fluorophosphates when R-VO_2 and Aged R-VO_2 are employed as precursors. The use of Aged R-VO_2 leads to a pure $Na_3V_2O_2(PO_4)_2F$ product (V4_4 sample). However, when R-VO_2 is employed V4_5 sample is obtained which contains a little amount of unreacted VO_2 as impurity.

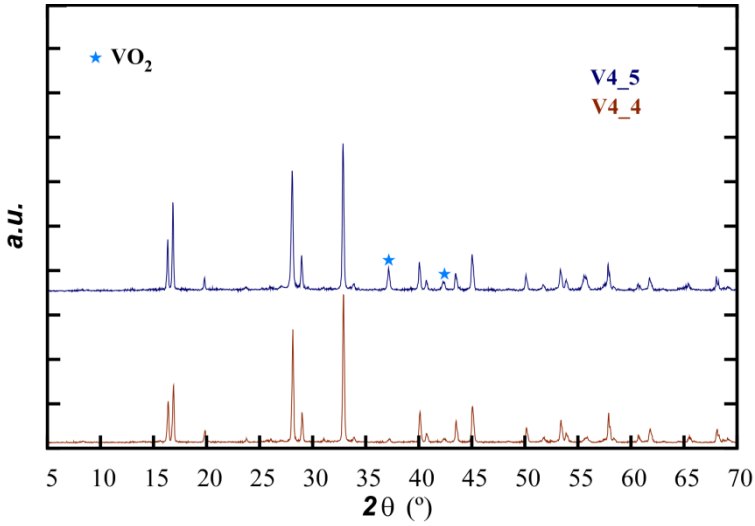

Figure 2.39 *XRD pattern of obtained compounds using Aged R-VO_2 and R-VO_2 as precursors.*

As it can be observed, only when using aged reagents $Na_3V_2O_2(PO_4)_2F$ phase is purely obtained (V4 and V4_4 samples, respectively). In these two cases a mixture of vanadium IV-V is present in the Aged R-V_2O_3 and Aged R-VO_2 reagents. This way, it seems that the reaction taking place when no V(III) is present in the reactants could

correspond to the one described in reaction Eq. 2.6. Only vanadium (IV) would react even if some proportion of vanadium (V) is present. Regarding the obtained product, vanadyl (VO^{2+}) is the more stable vanadium form in aqueous medium.

$$2VO_2 + 2NaH_2PO_4 \cdot H_2O + NaF + O_2 \rightarrow Na_3V_2O_2(PO_4)_2F + 4H_2O + O_2 \quad \text{(Eq. 2.6)}$$

SEM micrographs of the different V_2O_3 reagents are presented in Figure 2.40.

It can be seen that particle size is about 50 µm for the three oxides. However, particles from Middle-Aged R-V_2O_3 and Aged R-V_2O_3 appear to be more rounded than those of R-V_2O_3 in the lowest magnification micrographs. Higher magnification images of these materials (Figure 2.40d and f), on the contrary, show that the smooth surface of R-V_2O_3 particles adopts nanoflake and nanowire texture for Middle-Aged R-V_2O_3 and Aged R-V_2O_3 reagents, respectively. Thus, a clear evolution of the particles surface can be observed with V_2O_3 material aging.

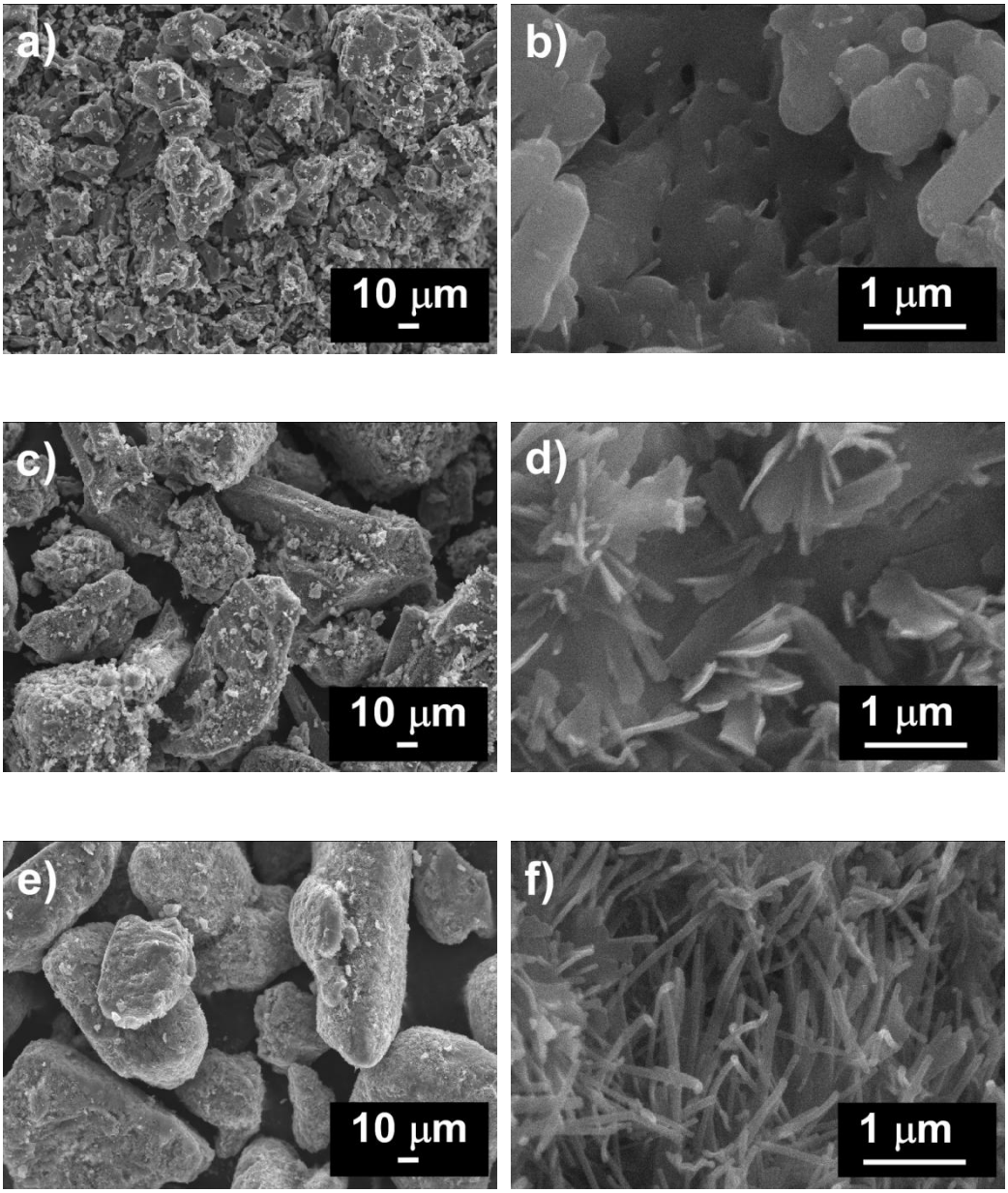

Figure 2.40 *SEM micrographies of R-V_2O_3* ***a)*** *x500 and* ***b)*** *x25000, Middle-Aged R-V_2O_3* ***c)*** *x500 and* ***d)*** *x25000 and Aged R-V_2O_3* ***e)*** *x500 and* ***f)*** *x25000.*

Figure 2.41 depicts SEM images corresponding to VO_2 reactants, where a similar phenomenon is observed with aging.

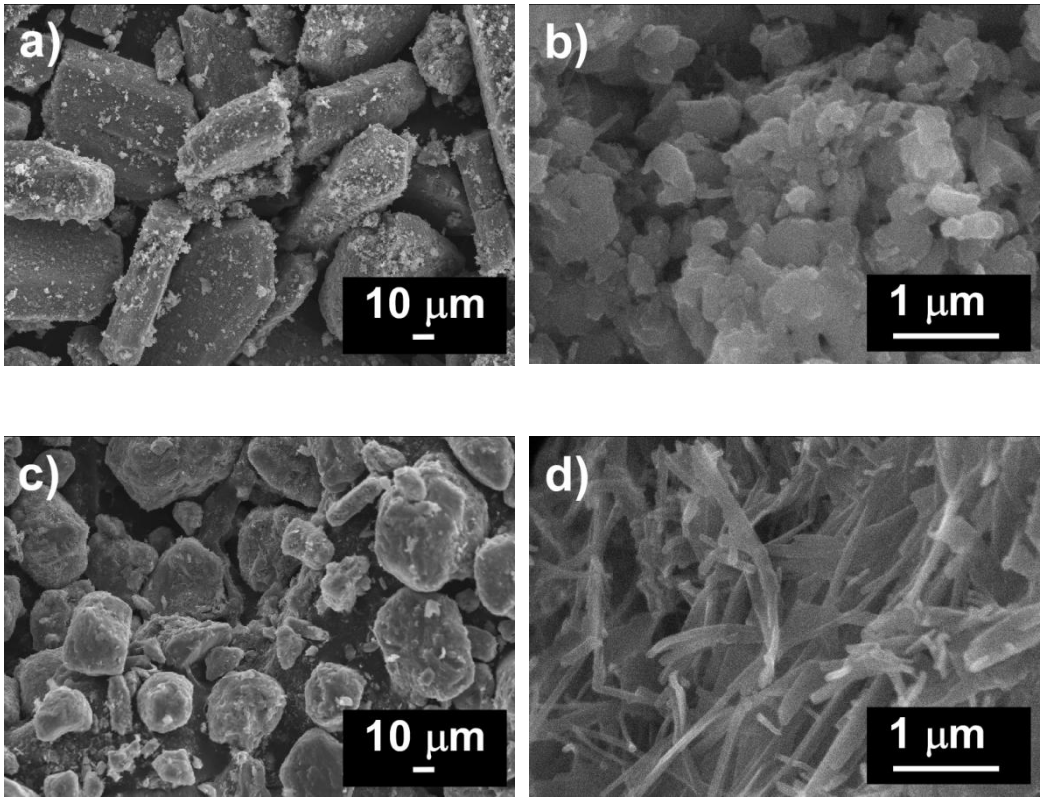

Figure 2.41 *SEM micrographies of R-VO_2* ***a)*** *x500 and* ***b)*** *x25000 and Aged R-VO_2* ***c)*** *x500 and* ***d)*** *x25000.*

Lower magnification micrographs (Figure 2.6a and c) present apparently smoother and more rounded particles for the aged compound, whereas higher magnification images (Figure 2.41b and d) show that nanowires have grown in the surface of the particles of Aged R-VO_2.

Figure 2.42 depicts FTIR spectrum of the analysed vanadium oxides together with V_2O_5 reagent (R-V_2O_5).

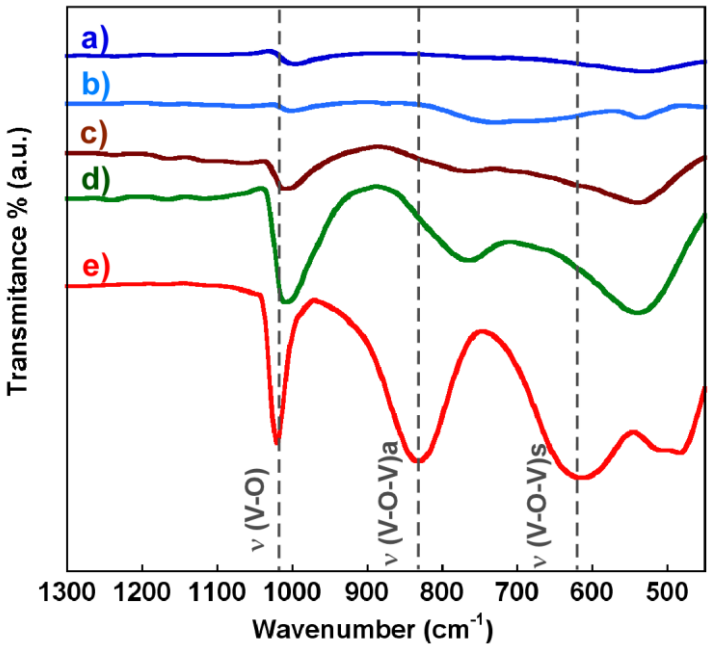

Figure 2.42 *FTIR spectra* ***a)*** *Middle-Aged R-V_2O_3* ***b)*** *R-VO_2* ***c)*** *Aged R-VO_2* ***d)*** *Aged R-V_2O_3 and* ***e)*** *R-V_2O_5.*

The three main bands appearing in the spectra have been assigned to V-O and V-O-V stretching modes in the different materials and are gathered in Table 2.11. Vibration band at 1022 cm^{-1} arises from the very short, terminal V=O bond (1.58 Å) in V_2O_5, V-O-V asymmetric stretch shows a characteristic band at 831 cm^{-1} while V-O-V symmetric stretch mixed with the deforming vibrations of the vanadium oxygen polyhedra present a band at 613-482 cm^{-1} [153].

V_2O_3, VO_2 and V_2O_5 spectra have been ordered by the oxidation state obtained by chemical titration, from the most oxidised one (R-V_2O_5, Figure 2.42e) to Middle-Aged R-V_2O_3 (Figure 2.42a). Spectrum of R-V_2O_3 is not shown due to problems related to its obtaining. From Figure 2.42 it can be seen a clear trend in the registered bands: the three of them become weaker and shift to lower wavenumbers when vanadium

153 Guerra, E.M.; Mulato, M. *J. Sol-Gel Sci. Technol.*, **2009**, 52, 315-320.

oxidation state decreases. This shift is caused by a decrease in the V-O bond strength, since the radius of vanadium increases with decreasing oxidation state resulting in longer V-O bonds and the consequent softening of the vibration [154,155].

Table 2.11 *Wavenumber evolution of different vanadium (III), vanadium (IV) and vanadium (V) oxides.*

	Oxidation State	ν(V-O)	ν(V-O-V)a	ν(V-O-V)s
R-V_2O_3	+3.01			
Middle-Aged R-V_2O_3	+3.49	995	756	530
R-VO_2	+3.98	1001	729	536
Aged R-VO_2	+4.27	1009	752	536
Aged R-V_2O_3	+4.41	1009	764	540
R-V_2O_5	+5	1022	831	613
V_2O_5 from bibliography [154]	+5	1020	828	594

Characterisation of vanadium (III) and vanadium (IV) oxide reagents by X-ray diffraction, scanning electron microscopy and infrared spectroscopy indicate that these materials have suffered from some kind of degradation with air and humidity exposure. The different reagents present a progressive change of colour from black to green as oxidation is more pronounced, which is also associated to a modification of the surface of the particles to form nanoflakes or nanowires as it has been presented in SEM micrographies. The mixed valence of the partially and completely aged vanadium oxides has been confirmed by chemical titration and FTIR measurements. Aditionally, the extra diffraction maxima observed in Middle-Aged R-V_2O_3, Aged R-V_2O_3 and Aged R-VO_2 materials could correspond to unidentified secondary phases or to a loss of symmetry of the structure due to the evolution of vanadium (III) and vanadium (IV) oxides to mixed valence oxides.

Thus, it has been established that these different vanadium oxide reagents undergo oxidation processes during long and medium term storage linked to an increase of material surface. These modifications can make the materials more reactive in the hydrothermal medium used for the synthesis of $Na_3V_2O_2(PO_4)_2F$ phase, what is in good

154 Botto,I.L.; Vassallo, M.B.; Baran, E.J.; Minelli, G. *Mater. Chem. Phys.*, **1997**, 50, 267–270.
155 Scheurell, K.; Kemnitz, E. *J. Mater. Chem.*, **2005**, 15, 4845–4853.

agreement with the fact that totally pure $Na_3V_2O_2(PO_4)_2F$ phase is only obtained with Aged R-V_2O_3 and Aged R-VO_2, while a part of V_2O_3 or VO_2 remains unreacted when new reactants are used.

This way, different strategies were tried to prepare pure $Na_3V_2O_2(PO_4)_2F$ by using not aged V_2O_3 and VO_2 reactants by hydrothermal synthesis. Table 2.12 gathers the description of every attempt when using different V_2O_3 reagents.

Table 2.12 Different attempts to obtain $Na_3V_2O_2(PO_4)_2F$ phase when using V_2O_3 reagents.

Sample	Reagent used	V_2O_3:$NaH_2PO_4 \cdot H_2O$:NaF ratio	Reaction time	Other conditions
V4	Aged R-V_2O_3	1:2:1	65 h	
V4_3A	R-V_2O_3	1:2:1	**1 week**	
V4_3B	R-V_2O_3	1:2:1	65 h	**Less amount of R-V_2O_3**
V4_3C	R-V_2O_3	1:2:**3**	65 h	
V4_3D	Ball Milled R-V_2O_3	1:2:1	65 h	**5h Ball Milling**
V4_3D2	Ball Milled R-V_2O_3	1:2:1	65 h	**10h Ball Milling**

The first hypothesis considered was that the new species grown on the surface of the vanadium oxides were more easily soluble in water, so either the newer reactants, being less soluble, needed longer times (V4_3A) or lower concentrations to react in the hydrothermal conditions (V4_3B); or being the secondary species dissolved in water, the real NaF:vanadium oxide ratio was higher than expected so higher proportions of NaF were used (V4_3C).

The second approach to get pure $Na_3V_2O_2(PO_4)_2F$ by using not aged V_2O_3 and VO_2 reactants was to subject new vanadium oxide reagents to a ball milling treatment in order to force their aging process (V4_3D, V4_3D2).

Figure 2.43 depicts the X-ray diffractograms of the compounds obtained for each case. As previously described, only when using Aged R-V_2O_3 $Na_3V_2O_2(PO_4)_2F$ phase is purely obtained (V4 sample). The increase of reaction time from 65 hours to one week (V4_3A sample) did not improve the purity of the phase when R-V_2O_3 was used as starting reactant. A decrease in the concentration of R-V_2O_3 while maintaining the ratio

between the reagents (V4_3B sample) in order to avoid solubility problems resulted in a lower amount of unreacted V_2O_3, although it was still present. The use of a higher amount of NaF (V4_3C sample) to ensure the complete reaction of the V_2O_3 as well as the employment of ball milled R-V_2O_3 during 5 or 10 hours (V4_3D and V4_3D2 samples respectively) led to higher amount of unreacted V_2O_3 in the final product.

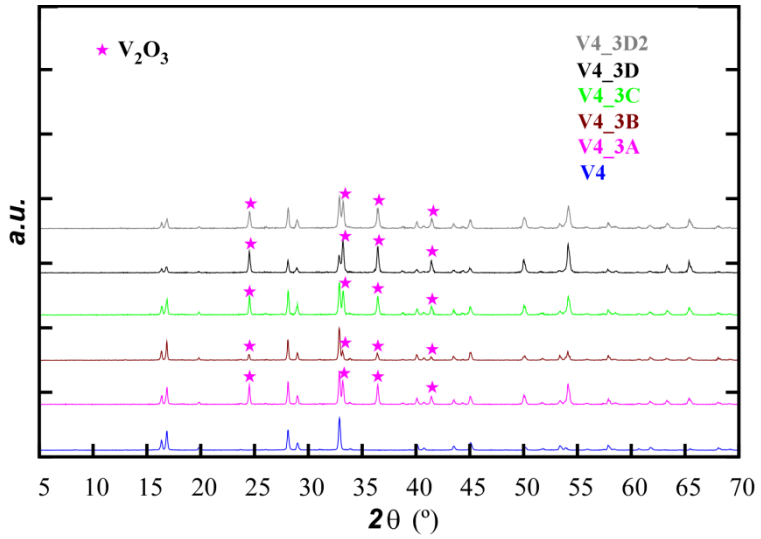

Figure 2.43 *XRD pattern of obtained compounds for the different attempts for the obtaining of pure $Na_3V_2O_2(PO_4)_2F$ when using V_2O_3 reagents.*

Table 2.13 gathers the different synthesis attempts of $Na_3V_2O_2(PO_4)_2F$ synthesis from VO_2 reagents. In this case, only ball milling of the starting VO_2 reactant was tried as alternative synthesis process.

Table 2.13 *Different attempts to obtain $Na_3V_2O_2(PO_4)_2F$ phase when using VO_2 reagents.*

Sample	Reagent used	VO_2:$NaH_2PO_4{\cdot}H_2O$:NaF ratio	Reaction time	Other conditions
V4_4	Aged R-VO_2	1:2:1	65 h	
V4_5	R-VO_2	1:2:1	65 h	
V4_5A	R-VO_2	1:2:1	65 h	**5h Ball Milling**

Figure 2.44 presents the X-ray diffractograms of the compounds obtained for each case.

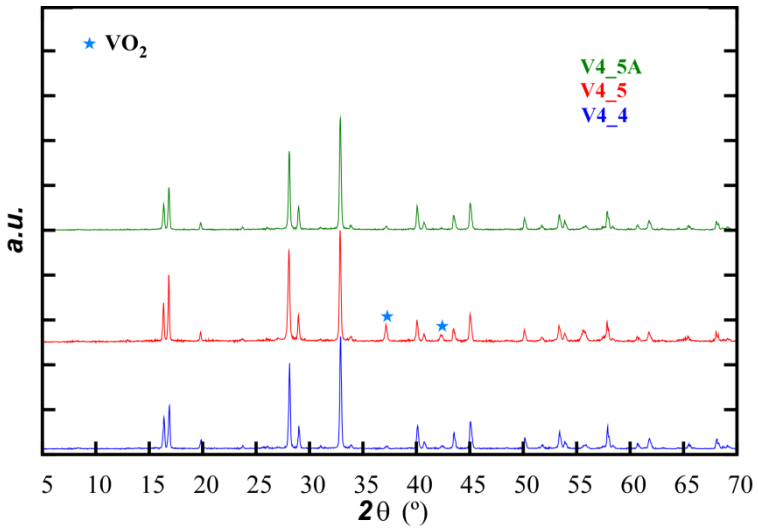

Figure 2.44 *XRD pattern of obtained compounds for the different attemps for the obtaining of pure $Na_3V_2O_2(PO_4)_2F$ when using VO_2 reagents.*

In contrast to the behaviour shown by vanadium (III) oxide reagents a similar XRD pattern is obtained when using both, Aged R-VO_2 and a ball milled R-VO_2 during 5 hours (samples V4_4 and V4_5A, respectively). This implies the possibility of getting the pure $Na_3V_2O_2(PO_4)_2F$ phase by the use of R-VO_2 previously modified by a 5 hour ball milling treatment. This milling treatment would induce the same kind of surface and chemical modification on the reactant, leading to pure $Na_3V_2O_2(PO_4)_2F$ material.

2.4 Study on $NaVPO_4F$ phase

In order to elucidate the existence of $NaVPO_4F$ phase (named as NVPF from now on) different attempts were carried out. First of all, the direct synthesis of this phase was tried. Afterwards, the electrochemical delithiation and further sodiation of $LiVPO_4F$ phase (named as LVPF) was studied. Finally, the chemical delithiation and sodiation of starting LVPF material was analysed.

2.4.1 Experimental

This part was carried out in the *Institut de Chimie de la Matière Condensée de Bordeaux* (ICMCB) in Bordeaux, France.

The synthesis process to obtain the $LiVPO_4F$ phase (LVPF sample) by ceramic method took place in two steps. First, VPO_4/C composite precursor was synthesised. For this purpose, V_2O_5 (Sigma-Aldrich, 99.99% purity) and $NH_4H_2PO_4$ (Fluka, 99.5% purity) were mixed in an agate mortar in stoichiometric 1:2 ratio. Carbon black (TIMCAL Super S©) was added as reducing agent in 10% molar excess. This mixture was annealed twice under argon atmosphere at 300ºC during 8 hours, first and 800ºC during 10 hours, second. The heating rate was 2ºC·min^{-1} in both cases. Second, VPO_4/C was mixed with LiF (Sigma-Aldrich, 99% purity) in stoichiometric 1:1 molar proportion. The reaction mixture was pelletised and maintained at 750ºC for 1 hour under argon atmosphere. Afterwards, the sample was quenched in liquid nitrogen. For the attempt of direct synthesis of $NaVPO_4F$ phase the same procedure was followed but instead of LiF, NaF (Sigma-Aldrich, 99% purity) was used.

Concerning the electrochemical delithiation and sodiation of LVPF sample, positive electrodes were manufactured by mixing 80 *wt.*% of active material, 10 *wt.*% of a mixture of two types of conductive carbons (graphite and TIMCAL Super S© S-black carbon (50:50 *wt.*%)) and 10 *wt.*% of polyvinylidenefluoride binder (PVDF 5130, Solvay) dissolved in N-methylpyrrolidone. A few mL of N-methylpyrrolidone (NMP) (Aldrich) were added and the resulting slurry was stirred for 1 hour. Afterwards it was coated on an aluminium foil using doctor blade technique. The electrode film was dried at 80^{o}C in an oven under vacuum for 24 hours.

For the general electrochemical delithiation of an electrode containing the LVPF sample and its further sodiation, circular electrodes were cut from the foil, pressed for better contact of the coated material and aluminium current collector, dried under vacuum overnight (80^{o}C) and finally transferred in an argon-filled glove box (Jacomex). The mass loading of the electrodes was about 3-4 mg·cm^{-2}. Electrochemical measurements were performed using metallic sodium as counter electrode, glass microfiber (Viledon) as separator and 1 M $NaPF_6$ in PC (polycarbonate) as electrolyte. The electrochemical evaluation of the electrodes was made in CR2032 coin cells with a Biologic VMP3

Multichannel potentiostat-galvanostat by galvanostatic cycling performed at a rate of C/100. After the electrochemical performance the electrodes were recovered and washed in an argon-filled glove box with DMC (dimethyl carbonate) in order to remove the remaining electrolyte ($NaPF_6$ residues).

Chemical delithiation of LVPF sample and further sodiation of the resulting material were chemically carried out using an excess of both, NO_2BF_4 in acetonitrile and $NaAlH_4$ in tetrahydrofuran (THF) as oxidizing and reducing agents, respectively. The oxidation of the $LiVPO_4F$ material (LVPF sample) led to VPO_4F compound (named as VPF) while its further chemical reduction promoted NVPF sample.

2.4.2 Direct synthesis of $NaVPO_4F$

Figure 2.45 depicts the X-ray diffractogram obtained for the attempt of direct synthesis of NVPF sample, which was indexed considering at least four phases and using the Full Pattern Matching mode of FULLPROF Suite software [134].

The XRD pattern shows that the main reflections correspond to the V^{3+}-only $Na_3V_2(PO_4)_2F_3$ phase described in the *$P4_2/mnm$* space group with the following cell parameters: a = b = 9.0362(3) Å; c = 10.7468(5) which are in good agreement with the ones reported by Shakoor *et al.* [156] and Ponrouch *et al.* [157].

156 Shakoor, R. A.; Seo, D.-H.. Kim, H.; Park, Y.U.; Kim, J.; Kim, S.-W.; Gwon, H.; Lee, S.; Kang, K. *J. Mater. Chem*., **2012**, 22,20535-20541.

157 Ponrouch, A.; Dedryvère, R.; Monti, D.; Demet, A.E.; Ateba Mba, J.M.; Croguennec, L.; Masquelier, C.; Johansson, P.; Palacín, M.R. *Energy Environ. Sci.*, **2013**, 6, 2361-2369.

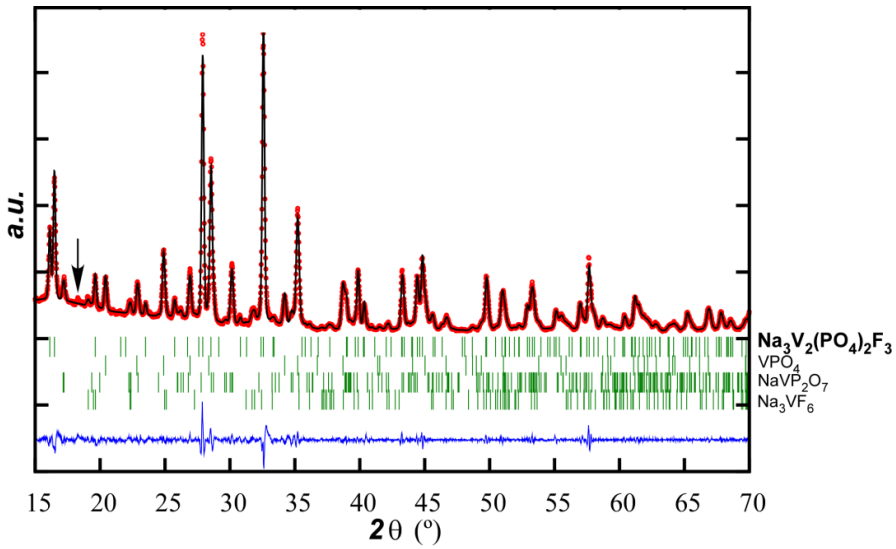

Figure 2.45 *Full Pattern matching refinement of the XRD diagram obtained for the direct synthesis of NVPF. Experimental (red circles), calculated (black line) XRD patterns and difference between them (blue lower line).*

A significant amount of unreacted VPO_4 can be appreciated in the X-ray diffractogram which indicates that the direct synthesis of NVPF phase by the mixture of VPO_4 and NaF in stoichiometric ratio (1:1) is not possible and instead, $Na_3V_2(PO_4)_2F_3$ phase is obtained. Little amounts of $NaVP_2O_7$ and Na_3VF_6 and an unidentified remaining reflection (marked with an arrow in Figure 2.45) appear also as impurities. All the identified phases are V^{3+}-rich phases.

2.4.3 Electrochemical delithiation/sodiation of $LiVPO_4F$

The ceramic synthesis of LVPF resulted in a material containing 5.86 *wt.*% of carbon. LVPF sample was examined by XRD, showing well-defined diffraction peaks, which indicate the crystallinity of the sample (see Figure 2.46). The diffraction pattern was indexed in the trigonal *P-1* space group with the lattice parameters that are given in

Table 2.14. These parameters match with the ones reported in literature for $LiVPO_4F$ material [148].

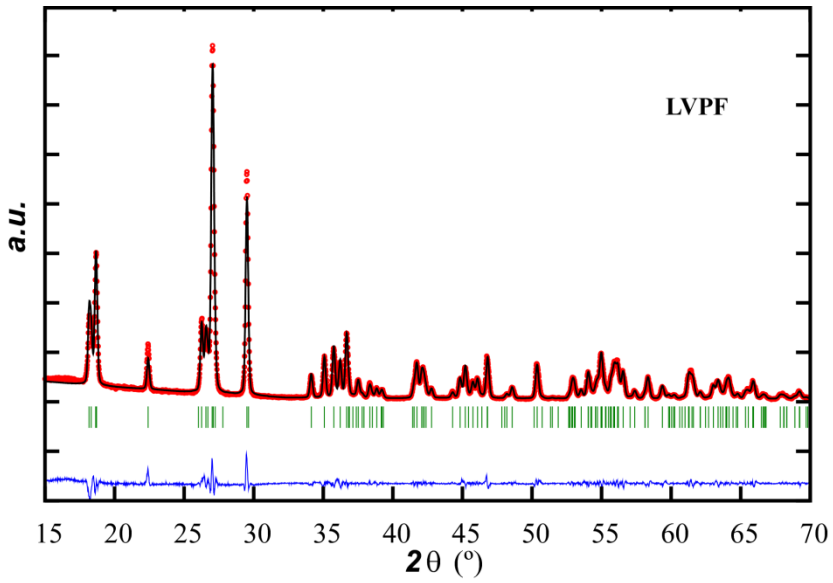

Figure 2.46 *Full Pattern matching refinement of the XRD diagram recorded for the LVPF sample. Experimental (red circles) and calculated (black line) XRD patterns and difference between them (blue lower line).*

Table 2.14 *Calculated cell parameters for the LVPF sample and the corresponding agreements factors*

Cell parameters (Å or º)	a = 5.1675 (2) Å; b = 5.3065(2) Å; c = 7.2593(2) Å	
	α = 107.602(2)º; β = 107.962(2)º; γ = 98.408(2)º	
Space Group	*P-1*	
R factors (%)	R_p = 11.1	R_B = 0.0967
	R_{wp} = 12.4	R_F = 0.0483
	R_{exp} = 4.40	χ^2 = 7.99

LVPF was employed as starting electrode material to perform different charge and discharge electrochemical curves. Figure 2.47 shows six representative charge/discharge cycles obtained at a rate of C/100 *vs.* sodium. Electrodes were extracted from four different cells and analysed at different states during the electrochemical charge and discharge process. Points 1 and 2 correspond to the electrodes stopped at the end of the first charge and of the first discharge, respectively, while points 3 and 4 represent the end of third and sixth discharges, respectively (see Figure 2.47).

Figure 2.48 depicts the XRD patterns corresponding to the electrodes extracted at points 1 to 4 in comparison with that of the LVPF starting material. Only 16-38º range is shown in order to avoid the reflections of the aluminium foil. The higher intensity of peak at 26.5º for LVPF electrode is due to the presence of graphite in the product (see the reflection marked with an arrow in Figure 2.48).

The shape of the charge curve of the first cycle in Figure 2.47 indicates a possible solid solution mechanism during this process, as the potential increases continuously upon deintercalation. A very different electrochemical behaviour has been observed for this material *vs.* a metallic lithium anode at a rate of C/50 by Ateba Mba *et al*. [148]. $LiVPO_4F$ shows two different *plateaux* at 4.24 and 4.28 V *vs.* lithium indicating the existence of an intermediate phase between them, *i.e.,* $Li_{\sim 2/3}VPO_4F$. Besides, the polarization of the first cycle is greater when testing the LVPF sample *vs.* sodium, ~0.5 V (see Figure 2.47) while in the case of Ateba Mba *et al.* this difference is only 0.1 V *vs.* lithium.

On the other hand, the XRD pattern of LVPF_point 1 in Figure 2.48 does not match with the diffractogram of VPO_4F [148], so it can be deduced that the obtained composition at the end of first charge in a LVPF cell *vs.* sodium does not match with the expected VPO_4F phase suggesting that not all the lithium ions were removed from the LVPF structure. In parallel to the deintercalation process, an interchange between the lithium ions from the $Li_{1-x}VPO_4F$ and the sodium ions from the electrolyte could have happened during the charge so that a mixture of lithium and sodium ions could remain in the structure at the end of this process. This could lead to a $(Li,Na)_xVPO_4F$ composition for LVPF_point 1 sample where the x value would be very close to zero.

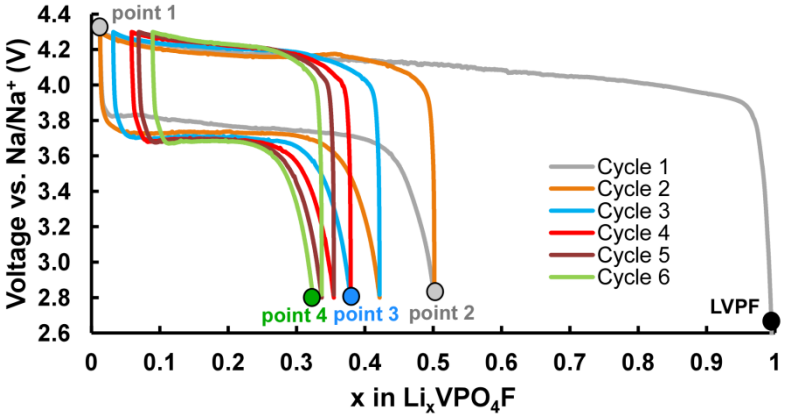

Figure 2.47 *Charge and discharge curves obtained at C/100 for Na//LVPF cells.*

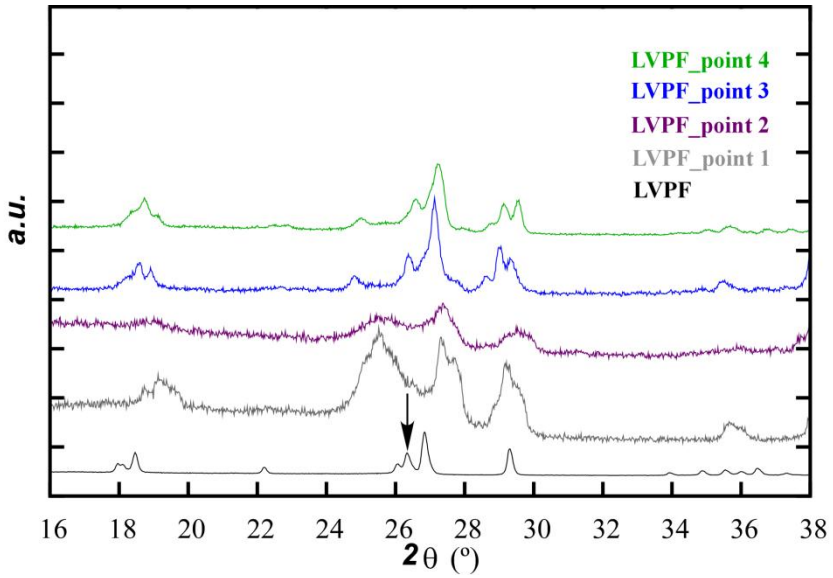

Figure 2.48 *XRD patterns of LVPF, LVPF_point 1, LVPF_point 2, LVPF_point 3 and LVPF_point 4 electrodes.*

The difference in size between the sodium and lithium ions (1.02 Å *vs.* 0.76 Å) would provoke different local environments in the structure leading to some disorders and distortions that could explain the global broadening of the XRD pattern of LVPF_point 1 (see Figure 2.48). During the following discharge the insertion of sodium would generate an even more disordered phase as it can be appreciated from the larger broadening of the XRD pattern of LVPF_point 2 sample (see Figure 2.48). On the contrary, after 3 and 6 cycles (see LVPF_point 3 and LVPF_point 4 in Figure 2.48, respectively) the material seems to be able to accommodate sodium in a more ordered structure, possibly due the fact that after a few cycles only sodium ions are participating in the intercalation and deintercalation process leading thus to the formation of Na_xVPO_4F phases where no different local compositions and structural environments are found. Moreover, it can be pointed out the difference between the first and the following discharge curves, these latter being *plateaux* (same voltage whatever the composition in alkali) and suggesting thus the occurrence of a two-phase reaction. It is also interesting to highlight the decrease in the sodium content as the number of cycles increases indicating that the accommodation of the sodium ions in this structure seems not to be as favourable as that for lithium ions.

2.4.4 Chemical delithiation/sodiation of $LiVPO_4F$

Chemically oxidised LVPF led to the formation of VPF sample. Figure 2.49 and Table 2.15 show the diffraction pattern and the crystallographic parameters of VPF sample, respectively. These parameters are in good agreement with the ones reported in the literature for VPO_4F phase [148]. Afterwards, the chemical sodiation of VPF sample was carried out.

Figure 2.50 shows the X-ray diffraction pattern of the obtained material in the range of 15-70º. The crystallographic parameters from $NaVOPO_4$ phase were employed as starting model [158]. As it can be seen, the obtained product presents wide diffraction peaks, which indicates its low crystallinity that could be associated to disorders. The reflections of the aluminium generated as by-product when $NaAlH_4$ was employed as reducing agent appear also in the diffractogram.

158 Song, J.; Xu, M.; Wang, L.; Goodenough, J.B. *Chem. Commun.*, **2013**, 49, 5280-5282.

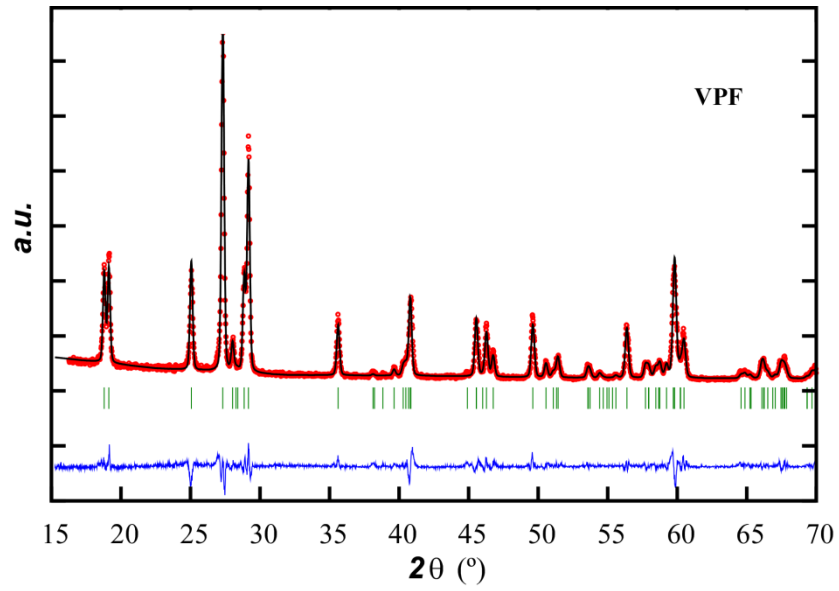

Figure 2.49 *Full Pattern matching of XRD diagram of VPF sample. Experimental (red circles), fitted (black line) and difference between them (blue lower line).*

Table 2.15 *Crystallographic and fitting parameters of VPF sample.*

Cell parameters (Å or º)	a = 7.1509(4) Å; b = 7.1012(4) Å; c = 7.3430(3) Å β = 121.182(4)º	
Space Group	*C 2/c*	
R factors (%)	R_p = 17.9 R_{wp} = 18.8 R_{exp} = 10.20	R_B = 0.141 R_F = 0.161 χ^2 = 3.76

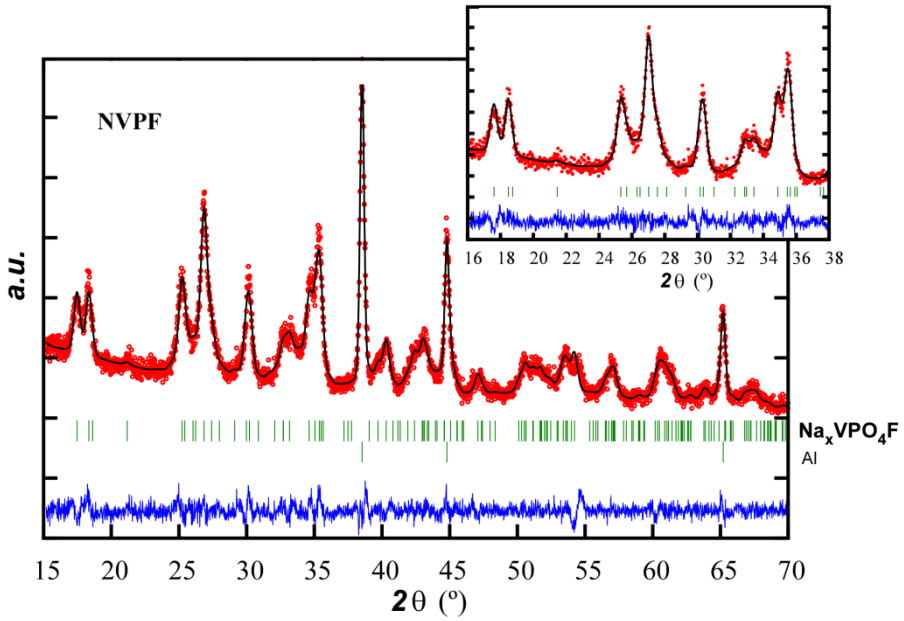

Figure 2.50 *Full Pattern matching of XRD diagram of NVPF. Experimental (red circles), fitted (black line) and difference between them (blue lower line). The inset shows the 16-38º range.*

Table 2.16 *Crystallographic and fitting parameters of NVPF sample.*

Cell parameters (Å or º)	a = 6.587(1) Å; b = 8.380(2) Å; c = 7.097(2) Å	
	β = 116.15(1)º	
Space Group	*P 2$_1$/c*	
R factors (%)	R_p = 24.0	R_B = 0.427
	R_{wp} = 22.7	R_F = 0.436
	R_{exp} = 18.71	χ^2 = 1.47

Until now, different compounds have been erroneously associated to a $NaVPO_4F$-named phase in the literature [159-162]. However, the obtained XRD pattern (Figure 2.50) and the crystallographic parameters (Table 2.16) from the present work demonstrate the existence of a Na_xVPO_4F phase which is different from the ones found in the literature. Besides, the XRD pattern of the NVPF sample is similar to the one reported for $NaVOPO_4$ phase [158] which suggests the existence of a structural relationship between these two compounds. However, deeper studies are needed in order to confirm this hypothesis. The cell volume obtained for NVPF sample is 351.95 $Å^3$ which is unexpectedly smaller than the one for $NaVOPO_4$ phase (355.05 $Å^3$) so the sodium content in the Na_xVPO_4F phase must be quantified. It can be noted that if the phase obtained after chemical delithiation from LVPF and subsequent sodium intercalation in VPF is actually $NaVPO_4F$ in composition, the volume change by itself cannot explain the small mobility of sodium ions in this framework. Indeed, the cell volume change between VPF and NVPF would be 10.32% which is very similar to that observed between VPF and LVPF, 9.13%. On the other hand, the improvement of the NVPF material in order to obtain a better crystallinity as well as the performance of preliminary electrochemical tests for the Na_xVPO_4F phase (theoretical capacity of 143 $mAh \cdot g^{-1}$) need to be carried out.

On the contrary, the attempt to obtain the $NaVPO_4F$ phase by the electrochemical insertion of sodium into the chemically obtained VPF sample was not successful. The choice of the potential window, 2.8 – 4.3 V *vs.* Na, was made considering its analogy to the Li//LVPF lithium system but an opening of the voltage window to lower voltages would be interesting in order to reproduce the conditions used in the chemical sodiation when the strong reducing agent $NaAlH_4$ is employed. Another possibility for the unsuccessful sodiation of chemically obtained VPF sample would be the appearance of some modifications in the surface of the material which could be detrimental for a subsequent electrochemical performance.

159 Barker, J.; Saidi, M.Y.; Swoyer, J.L. *Electrochem Solid-State Lett.*, **2003**, 6, A1-A4.

160 Zhuo, H.; Wang, X.; Tang, A.; Liu, Z.; Gamboa, S.; Sebastian, P.J., *J. Power Sources*, **2006**, 160, 698-703.

161 Liu, Z.; Wang, X.; Wang, Y.; Tang, A.; Yang, S.; He, L., *T. Nonferr. Metal Soc.*, **2008**, 18, 346-350.

162 Lu, Y.; Zhang, S.; Li, Y.; Xue, L.; Xu, G.; Zhang, X. *J. Power Sources*, **2013**, 247, 770-777.

These results show that even if it is not possible to directly synthesise the $NaVPO_4F$ phase the chemical delithiation of $LiVPO_4F$ and further chemical sodiation of VPO_4F product leads to a never reported Na_xVPO_4F phase. A similar behaviour has been observed to obtain the electrochemically active $NaFePO_4$ olivine phase [163].

163 Casas-Cabanas, M.; Roddatis, V.; Saurel, D.; Kubiak, P.; Carretero-González, J.; Palomares, V.; Serras, P.; Rojo, T. *J. Mater. Chem.*, **2012**, 22, 17421-17423.

2.5 Chapter Summary

In this chapter the hydrothermal synthesis and characterisation of a family of sodium vanadium fluorophosphates are presented: $Na_3V_2O_{2x}(PO_4)_2F_{3-2x}$. The synthesis took place in two steps where a ceramic precursor (VPO_4/C) was first obtained. The x value of the formula, and consequently fluorine and oxygen content, varied with the carbon content in the product. When less than 1 *wt.*% of carbon is present in the sample, resulting compound is very close to V^{4+} $Na_3V_2O_2(PO_4)_2F$ end-member (x = 1). However, V^{3+} - $Na_3V_2(PO_4)_2F_3$ extreme phase (x = 0) has not been possible to obtain regardless the high amount of carbon used (~50 *wt.*%). Intermediate amounts of carbon in the final product lead to V^{3+}/V^{4+} mixed valence compounds where $0 < x < 1$. A deep characterisation of the MV_KC sample containing a moderate amount of electrochemical grade carbon (~6 *wt.*%) revealed an oxidation state of +3.8 for the vanadium, that is, x = 0.8 in the $Na_3V_2O_{2x}(PO_4)_2F_{3-2x}$ formula.

On the other hand, a novel single step hydrothermal synthesis is employed for the obtaining of a carbon free V^{4+} $Na_3V_2O_2(PO_4)_2F$ phase (V4 sample). The absence of *in-situ* carbon makes necessary the carbon coating of the sample for a good electrochemical performance. Additionally, some issues regarding the state of conservation of the vanadium oxides used as precursor for the preparation of pure $Na_3V_2O_2(PO_4)_2F$ phase are described.

Concerning the synthesis of $NaVPO_4F$ phase it is not possible to obtain it by direct synthesis of VPO_4 and NaF in stoichiometric ratio, not even by the electrochemical delithiation and further electrochemical sodiation of $LiVPO_4F$ starting material (LVPF electrode), at least in the potential window considered. On the contrary, the chemical delithiation and further sodiation of the $LiVPO_4F$ starting material (LVPF sample) lead to the formation of Na_xVPO_4F phase (NVPF sample) which shows a similar XRD pattern to that obtained for $NaVOPO_4$ phase.

Chapter 3. Electrochemical Characterisation of $Na_3V_2O_{2x}(PO_4)_2F_{3-2x}$ family

3.1 Introduction

This chapter describes the electrochemical tests performed on the $Na_3V_2O_{2x}(PO_4)_2F_{3-2x}$ compound family ($0 < x \leq 1$). First, the results obtained from the family of compounds prepared with different carbon amounts and types are presented (MV_AC or SC composites). Then, a deeper characterisation of $Na_3V_2O_{2x}(PO_4)_2F_{3-2x}$ when $x = 0.8$ phase is shown (MV_KC material). To finish with, electrochemical characterisation of the uncoated and carbon-coated V^{4+} extreme of the family ($x = 1$) is presented (V4, V4_FTT and V4_LTT samples).

3.2 Experimental

All the studied materials were tested in Swagelok cells *vs.* a sodium metal anode. For the series of sodium-vanadium fluorophosphate samples prepared by varying the type and amount of carbon (MV_AC (Active Carbon) and MV_SC (S-black Carbon)) electrolyte consisted on a porous glass fiber sheet soaked in a solution of 1M $NaClO_4$ in EC:PC (ethylene carbonate:propylene carbonate, 1:1 volume) placed between the two electrodes. The cathodes were prepared as pellets containing 75 *wt.*% active material, 20 *wt.*% conductive carbon (Ketjen black) and 5 *wt.*% binder (PVDF). Laminate cathodes were also prepared with the best performing sample (MV_SC2 – 6 *wt.*%) by

using a doctor blade K Control Coater 101. Slurry mixture was made of 80 *wt.*% active material, 10 *wt.*% conductive carbon (Timcal C-nergy Super C65) and 10 *wt.*% polyvinylidenefluoride binder (PVDF in N-methylpyrrolidone, 5 *wt.*%). The electrodes were dried at 80^{o}C in a vacuum oven for 24 hours before their use. Electrochemical cycling was performed at two rates, C/10 and 1C, between 2.5 and 4.5 V *vs.* Na/Na^{+}, although this upper limit was modified to 4.3 V after the first measurements due to the limited electrolyte stability window.

On the other hand, the positive electrodes for MV_KC and V4, V4_LTT and V4_FTT samples were manufactured as laminates by mixing 80 *wt.*% active material, 10 *wt.*% conductive carbon (Timcal C-nergy Super C65) and 10 *wt.*% binder (PVDF in N-methyl pyrrolidone, 5 *wt.*%). Afterwards, the electrodes were coated on an aluminium foil using a doctor blade K Control Coater 101. The electrode film was dried at 80^{o} C in a vacuum oven for 24 hours.

For the general electrochemical characterisation of both, $V^{3.8+}$ MV_KC and V^{4+} V4, V4_LTT and V4_FTT compounds, circular electrodes were cut from the foil, pressed for better contact of the coated material and aluminium current collector, dried under vacuum overnight (120^{o}C) and finally transferred to an argon-filled glove box. The mass loading of the electrodes was about 3 and 4 $mg \cdot cm^{-2}$ for MV_KC and V4 (including LTT and FTT samples) phases, respectively. Electrochemical measurements were performed using metallic sodium as counter electrode, glass microfiber (Whatman, GF/A) as separator and 1 M $NaPF_6$ in EC:DMC (ethylene carbonate:dymethil carbonate, 1:1 volume) as electrolyte. In the case of MV_KC phase 2 *wt.*% of FEC additive (mono-fluoroethylene carbonate) was added to the electrolyte. The electrochemical evaluation of the samples was made by galvanostatic cycling performed at different rates, ranging from C/20 to 5C, between 2.8 and 4.3 V *vs.* Na/Na^{+}. Cyclic voltammetry was carried out for Na//MV_KC half cells at scan rates ranging from 0.1 $mV \cdot s^{-1}$ to 1 $mV \cdot s^{-1}$.

3.3 Electrochemical Characterisation of $Na_3V_2O_{2x}(PO_4)_2F_{3-2x}$ $(0 < x < 1)$

Electrochemical tests were performed *vs.* Na/Na^{+} at C/10 and 1C rates. Figure 3.51 shows the discharge curves for the second cycle of compounds MV_AC1, MV_AC2,

MV_SC2 and MV_SC4 tested in pellet electrodes. Charge curves are not shown because they are affected by parasitic electrolyte decomposition due to the high cut-off voltage (4.5 V) [164].

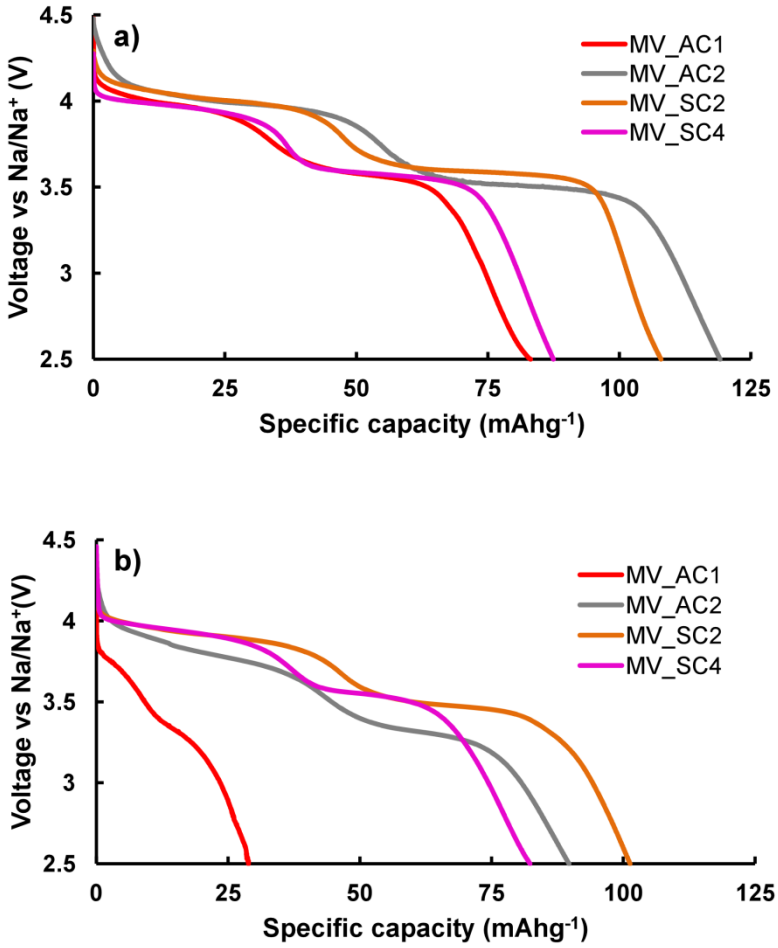

Figure 3.51 *Discharge curves of MV_AC1, MV_AC2, MV_SC2 and MV_SC4 samples with pellet electrodes at* ***a)*** *C/10 and* ***b)*** *1C.*

164 Ponrouch, A.; Marchante, E.; Courty, M.; Tarascon, J-M.; Palacín, M.R. *Energy Environ. Sci.*, **2012**, 5, 8572-8583.

As it can be observed, all materials present similar electrochemical curves, containing two *plateaux* of about the same length, located at 3.6 and 4.1 V *vs.* Na/Na^+. The relative length of these *plateaux* is conserved even when discharge specific capacity is lower at higher rate (1C). The curves present the same features as those described in literature [165,166]. The high voltage of both discharge *plateaux* makes these compounds really promising materials for high energy positive electrodes for sodium-ion batteries. Table 3.17 gathers the maximum discharge values for both rates.

Table 3.17 Discharge capacity value for the MV_AC and MV_SC samples at C/10 and 1C.

Sample	Discharge C/10 ($mAhg^{-1}$)	Discharge 1C ($mAhg^{-1}$)
MV_AC1 - <1*wt.*% active C	83	29
MV_AC2 - 1.7 *wt.*% active C	120	88
MV_SC2 - 6.1 *wt.*% S-black C	110	100
MV_SC4 - 57 *wt.*% S-black C	85	80

Sample MV_AC1 shows a good discharge value at C/10 but not so good at moderate rate (1C). This can be attributed to: (i) the lack of a good carbon coating on the sample before electrode preparation, and (ii) its lower conductivity, due to the minimum amount of V^{3+} present in this sample. On the other hand, MV_AC2 provides the best specific capacity at C/10 (about 92% of the theoretical specific capacity), but this value decays at 1C due to both the low amount of carbon and the lower conductivity of active carbon compared to the electrochemical grade carbon.

Phase MV_SC2 presents good specific capacity values at both C/10 and 1C rates, which can be due to its moderate electrochemical grade carbon content. On the other hand, MV_SC4 shows worse results at both rates, probably due to the excess of carbon in the sample. The carbon excess in the electrode can block the access of the electrolyte to the active material, isolating fluorophosphate grains, as it has been demonstrated for $LiFePO_4$/C composites [167].

165 Barker, J.; Saidi, M.Y.; Swoyer, J.L. *Electrochem Solid-State Lett.*, **2003**, 6, A1-A4.
166 Sauvage, F.; Quarez, E.; Tarascon, J.; Baudrin, E. *Solid State Sci.*, **2006**, 8, 1215–1221.
167 Palomares, V.; Goñi, A.; Gil de Muro, I.; De Meatza, I.; Bengoechea, M.; Cantero, I.; Rojo, T. *J. Electrochem. Soc.*, **2009**, 156, A817-A821.

After the analysis of the electrochemical behaviour of the materials, and taking into account that compound MV_SC2 provided the best results, with a 6.1 *wt.*% electrochemical grade carbon, a greater mass of this material was synthesised in order to study its electrochemical performance when forming laminate electrodes. Figure 3.52 shows the charge-discharge curves of the produced laminates.

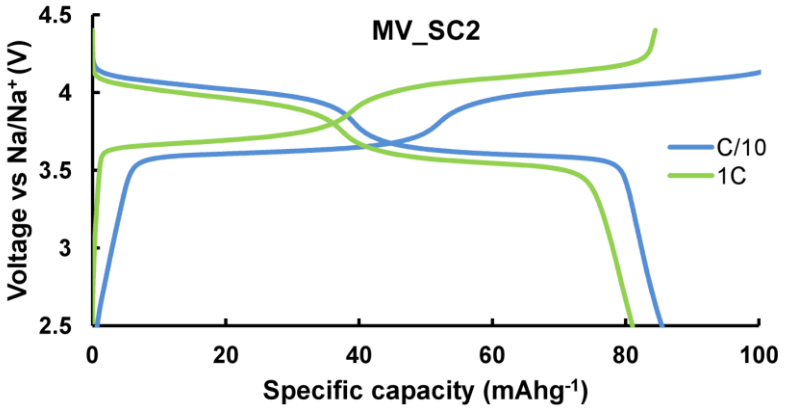

Figure 3.52 *Charge and discharge cycles of the sample MV_SC2 with laminate electrode at C/10 and 1C.*

These curves exhibit the same features as the ones previously described for pellet electrodes. This material reacts in two *plateaux* with the same size at high voltages *vs.* Na/Na^+. Moreover, negligible polarization is observed between charge and discharge at slow rate (C/10), being lower than 0.1 V for the curves at 1C. The specific capacity values obtained at C/10 (84 $mAhg^{-1}$) and 1C (80 $mAhg^{-1}$) are slightly lower than those obtained with pellet electrodes. Laminate electrodes of this phase have been tested for 5 cycles at C/10 and for 25 cycles at 1C in order to evaluate the cyclability of this compound. Figure 3.53 presents the evolution of the specific capacity of the laminate of sample MV_SC2 with cycling. A low capacity fading and no increase of polarization are observed when increasing the cycling rate from C/10 to 1C. Moreover, the phase MV_SC2 exhibits a very high cycling stability with almost no capacity fade after 30 cycles.

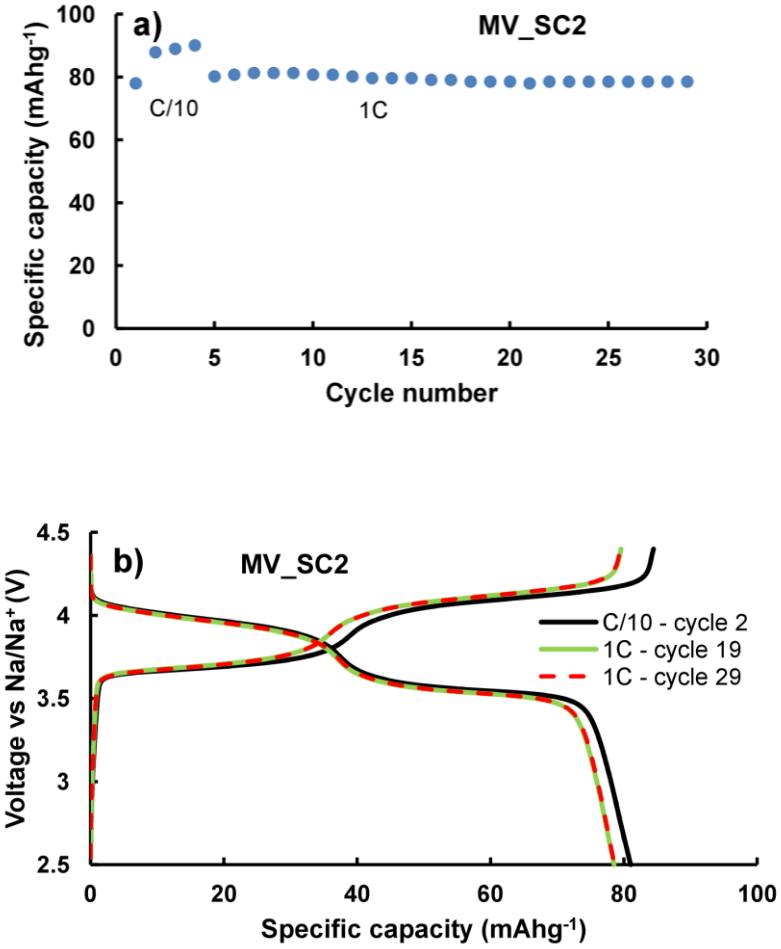

Figure 3.53 ***a)*** *Cyclability and* ***b)*** *Different charge-discharge curves of the laminate electrode MV_SC2 during cycling.*

All the investigated materials present high reaction voltages distributed in two *plateaux* of the same length at 3.6 and 4.1 V *vs.* Na/Na^+. These operation voltages are among the highest found in the literature for sodium-based systems (see Table 3.18).

Table 3.18 Main electrochemical characteristics of possible cathodic materials for sodium-ion batteries.

Formula	Ref.	Operating voltage *vs.* Na/Na^+ (V)	Theoretical specific capacity ($mAhg^{-1}$)	Max. energy density ($Wh \cdot kg^{-1}$)
$Na_3V_2(PO_4)_3$	[168-170]	1.5 and 3.5	118	413
Na_2FePO_4F	[171,172]	3 V	135	405
$NaFePO_4$	[173-175]	2.7 and 3.2	154	493
$Na_2FeP_2O_7$	[176]	~3V	97	292
$Na_3V_2(PO_4)_2F_3$	[177,178]	3.6 and 4.1	128	525
$Na_3V_2O_2(PO_4)_2F$	[166,179]	3.6 and 4.0	130	520
$Na_3V_2O_{2x}(PO_4)_2F_{3-2x}$	[this work, 180]	3.6 and 4.1	~130	~533

168 Plashnitsa, L. S.; Kobayashi, E.; Noguchi, Y.; Okada, S.; Yamaki, J-I. *J. Electrochem. Soc.*, **2010**, 157, A536-A543.

169 Saravanan, K.; Mason, C.W.; Rudola, A.; Wong, K.H.; Balaya, P. *Adv. Energy Mater.*, **2013**, 3, 444-450.

170 Jiang, Z.; Han, W.; Lu, X.; Yang, H.; Hu, Y.-S.; Zhou, J.; Zhou, Z.; Li, J.;Chen, W.; Chen, D.; Chen, L. *Adv. Energy Mater.*, **2012**, 3, 156-160.

171 Recham, N.; Chotard, J-N.; Dupont, L.; Djellab, K.; Armand, M.; Tarascon, J-M. *J. Electrochem. Soc.*, **2009**, 156, A993-A999.

172 Ellis, B.L.; Makahnouk, W.R.M.; Rowan-Weetaluktuk, W.N.; Ryan, D.H.; Nazar, L.F. *Chem. Mater.*, **2010**, 22, 1059-1070.

173 Moreau, P.; Guyomard, D.; Gaubicher, J.; Boucher, F. *Chem. Mater.*, **2010**, 22, 4126-4128.

174 Zaghib, K.; Trottier, J.; Hovington, P.; Brochu, F.; Guerfi, A.; Mauger, A.; Julien, C.M. *J. Power Sources*, **2011**, 196, 9612-9617.

175 Casas-Cabanas, M.; Roddatis, V.; Saurel, D.; Kubiak, P.; Carretero-González, J.; Palomares, V.; Serras, P.; Rojo, T. *J. Mater. Chem.*, **2012**, 22, 17421-17423.

176 Kin, H.; Shakoor, R.A.; Park, C.; Lim, S.Y.; Kim, J.-S.; Jo, Y.N.; Cho, W.; Miyasaka, K.; Kahraman, R.; Jung, Y.; Choi, J.W. *Adv. Func. Mater.*, **2013**, 23, 1147-1155.

177 Shakoor, R. A.; Seo, D.-H.. Kim, H.; Park, Y.U.; Kim, J.; Kim, S.-W.; Gwon, H.; Lee, S.; Kang, K. *J. Mater. Chem.*, **2012**, 22, 20535-20541.

178 Ponrouch, A.; Dedryvère, R.; Monti, D.; Demet, A.E.; Ateba Mba, J.M.; Croguennec, L.; Masquelier, C.; Johansson, P.; Palacín, M.R. *Energy Environ. Sci.*, **2013**, 6, 2361-2369.

179 Xu, M.; Wang, L.; Zhao, X.; Song, J.; Xie, H.; Lu, Y.; Goodenough, J.B. *Phys. Chem. Chem. Phys.*, **2013**, 15, 13032-13037.

180 Park, Y.-U.; Seo, D. H.; Kwon, H.-S.; Kim, B.; Kim, J.; Kim, H.; Kim, I.; Yoo, H.-I.; Kang, K. *J. Am. Chem. Soc.*, **2013**, 135, 13870-13878.

Taking into account the results obtained from the electrochemical characterisation of this family of compounds, a possible redox process is proposed for charge and discharge in the following reaction:

Charge: $Na_3V_2O_2(PO_4)_2F \rightarrow NaV_2O_2(PO_4)_2F + 2Na^+ + 2e^-$

Discharge: $NaV_2O_2(PO_4)_2F + 2Na^+ + 2e^- \rightarrow Na_3V_2O_2(PO_4)_2F$

According to this proposed mechanism, the electrochemical reaction taking place would correspond to V^{4+}/V^{5+} redox pair. This hypothesis is proposed after the observation of the same electrochemical curves for sample MV_AC1 (which consists mainly of V^{4+}) and the rest of the series (mixed valence V^{3+}/V^{4+} compounds). This way, charge process would consist on V^{4+} oxidation to V^{5+} with the extraction of 2 Na^+ ions from the structure, reverting in discharge (theoretical specific capacity of about 130 $mAhg^{-1}$). Thus, the low amount of V^{3+} in the materials would not take part in the electrochemical reaction, but would play a role enhancing intrinsic active material´s conductivity. Therefore, the two voltage *plateaux* would not correspond to two oxidation states for vanadium, but would be related to the extraction/insertion of two types of crystallographic sodiums from/into the structure.

3.4 Electrochemical Characterisation of $Na_3V_2O_{2x}(PO_4)_2F_{3-2x}$ (x = 0.8)

The electrochemical behaviour of MV_KC composite was investigated by both cyclic voltammetry and galvanostatic cycling. The comparison between the voltammograms is shown in Figure 3.54. The graphic presents two pairs of peaks at about 3.75 V and 4.1 V (anodic) and 3.45 V and 4.0 V (cathodic) corresponding to the faradaic extraction/insertion of sodium from/into $Na_3V_2O_{2x}(PO_4)_2F_{3-2x}$ (x = 0.8). The values of the redox potentials agree with those reported in the literature [166,177] and in the present work. The broadness of the redox peaks at low scan rate (0.1 $mV \cdot s^{-1}$) indicates the complexity of the electrochemical mechanism. Chihara *et al.* [181] and Shakoor *et al.* [177] have investigated by *ex situ* XRD analysis of cycled electrodes the electrochemical mechanism of the reversible Na extraction from the $Na_3V_2(PO_4)_2F_3$

181 Chihara, K.; Kitajou, A.; Gocheva, I.D; Okada, S.; Yamaki, J.-i. *J. Power Sources*, **2013**, 227,80-85.

material. Both groups reported that the electrochemical reaction occurs through a single-phase reaction with negligible (~2%) volume variation. Similar single-phase mechanism is expected for the MV_KC material which could explain the broad shape of the redox peaks observed in the cyclic voltammograms. Electrochemical reaction mechanisms are studied in Chapter 4.

Anodic (extraction) and cathodic (insertion) peaks shift to higher and lower voltages, respectively when increasing the scan rate from 0.1 to 1 $mV \cdot s^{-1}$. This is due to the increased polarization at high sweep rates because of kinetic limitations associated with the sodium diffusion through the active material. However, these potential shifts are moderate, which suggests that MV_KC presents fast kinetics and rapid storage mechanism.

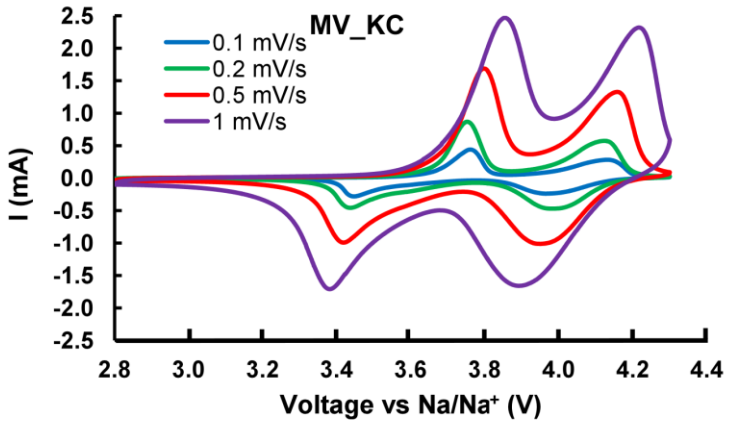

Figure 3.54 *Cyclic voltammetry of MV_KC at scan rates from 0.1 $mV \cdot s^{-1}$ to 1 $mV \cdot s^{-1}$.*

A typical charge-discharge curve (C/20) of the composite is shown in Figure 3.55a. The electrochemical charge presents two pseudo-*plateaux* of similar length at 3.6 and 4.1 V *vs.* Na/Na^+. The specific capacity measured at C/20 is about 100 $mAhg^{-1}$ which corresponds to ~80% of the theoretical capacity, equally distributed among the lower (3.6 V) and the higher potential (4.1 V). A qualitative evaluation of the mechanism can be done by derivation of the galvanostatic curves. Observation of the dQ/dV curve

(Figure 3.55b), indicates that there is more than one electrochemical process running at the two operating voltages. Thus, the mechanism of Na extraction/insertion from/into MV_KC is not simple and involves complex processes.

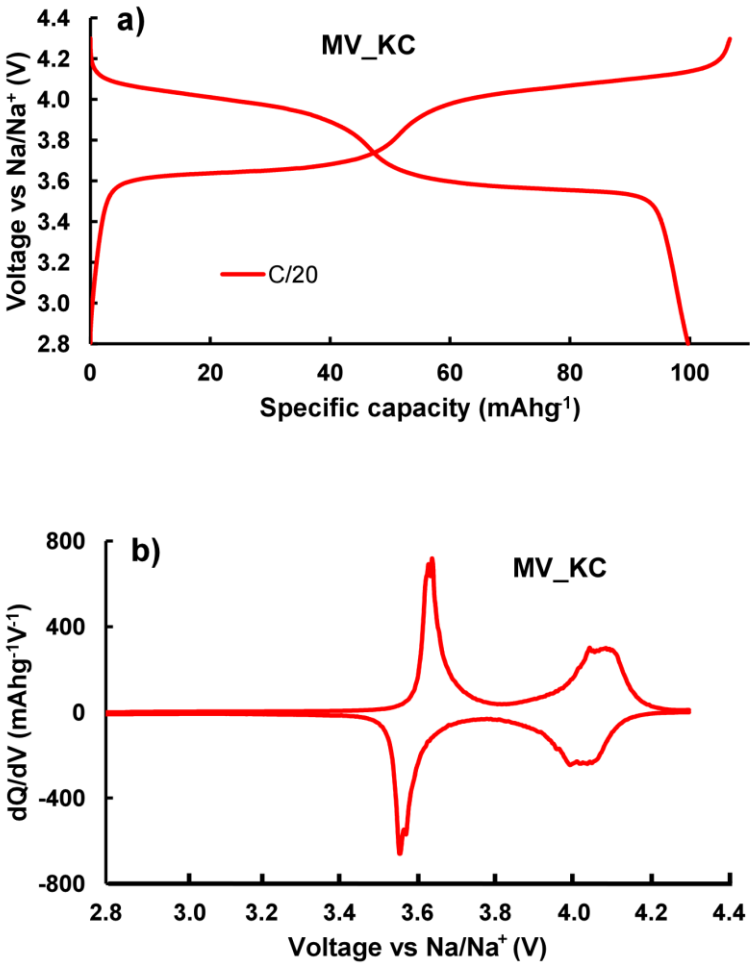

Figure 3.55 ***a)*** *Typical galvanostatic Na^+ extraction/insertion curves from/into MV_KC and* ***b)*** *corresponding dQ/dV curve.*

Rate capabilities of MV_KC at charging rates ranging from C/20 to 5C between 2.8 and 4.3 V are shown in Figure 3.56a.

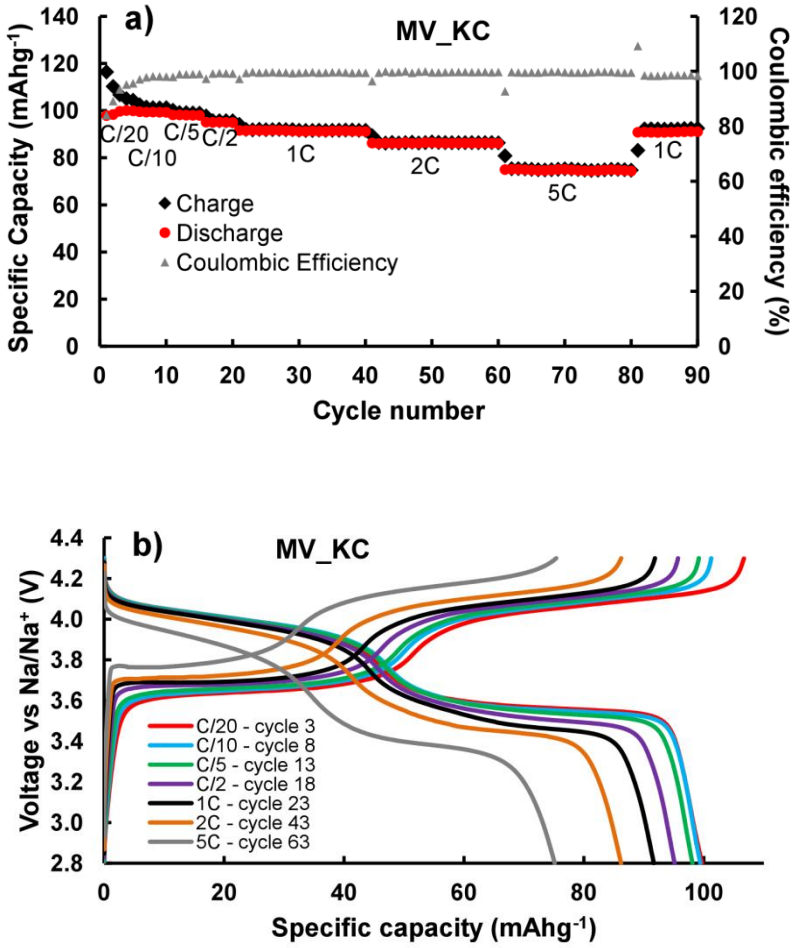

Figure 3.56 ***a)*** *Specific charge/discharge capacity of MV_KC at different C rates and* ***b)*** *typical galvanostatic Na^+ extraction/insertion curves from/into $Na_3V_2O_{2x}(PO_4)_2F_{3-2x}$ (x = 0.8) at different charging rates from C/20 to 5C.*

The material shows excellent specific capacity values for charging rates up to 5C. Indeed, the measured specific capacity at a rate of C/20 is 100 $mAhg^{-1}$. This value decreases to 99 $mAhg^{-1}$ at C/10, 98 $mAhg^{-1}$ at C/5, 95 $mAhg^{-1}$ at C/2, 91 $mAhg^{-1}$ at 1C, 86 $mAhg^{-1}$ at 2C, and finally, 75 $mAhg^{-1}$ at 5C. Although low coulombic efficiency is

observed in the first cycles, *e.g.,* for the first cycle at C/20 the coulombic efficiency is only 83%; it progressively increases to 95% after 5 cycles becoming higher than 99% after 15 cycles. The voltage profile and the discharge/charge capacity evolution of MV_KC at increasing current from C/20 to 5C are presented in Figure 3.56b. A small increase of the polarization is observed with increasing current.

Cycling stability has been evaluated by repetitive charge-discharge at 1C rate for 200 cycles. Prior to long term cycling, 3 cycles at lower rate have been carried out in order to stabilise the sodium metal anode. The evolution of the capacity upon cycling is given in Figure 3.57. As it can be seen, MV_KC composite exhibits an excellent cycling stability. The 1C rate capacity is 95 $mAhg^{-1}$ at the beginning of the cycling and 90 $mAhg^{-1}$ with a coulombic efficiency > 99% after 200 cycles which corresponds to 95% capacity retention.

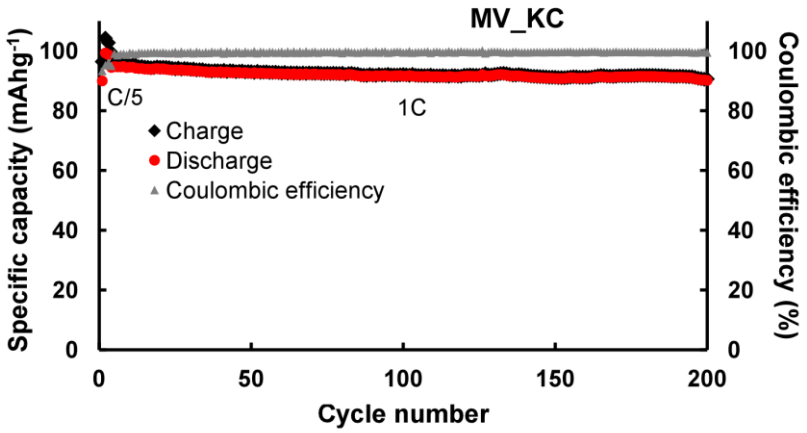

Figure 3.57 *Cycling stability of MV_KC over 200 cycles with a charge/discharge rate of 1C. The first 3 cycles were recorded with C/5.*

As it has been seen, MV_KC material exhibits high capacities, rate capabilities, excellent reversibility and stability upon cycling. These features make MV_KC a very promising cathode for sodium-ion batteries.

3.5 Electrochemical Characterisation of $Na_3V_2O_2(PO_4)_2F$

The electrochemical characterisation of V4 and V4_FTT materials has been carried out by repetitive galvanostatic cycling at different rates. Figure 3.58 and Figure 3.59 show the charge/discharge and discharge curves extracted from one cycle at each rate for the two samples, respectively. Both materials show two *plateaux* of approximately the same length at 3.6 and 4.0 V which corresponds to the Na extraction/insertion from/into $Na_3V_2O_2(PO_4)_2F$ phase. Up till now, only two works have been reported in the literature related to the electrochemical performance of this phase [166,179].

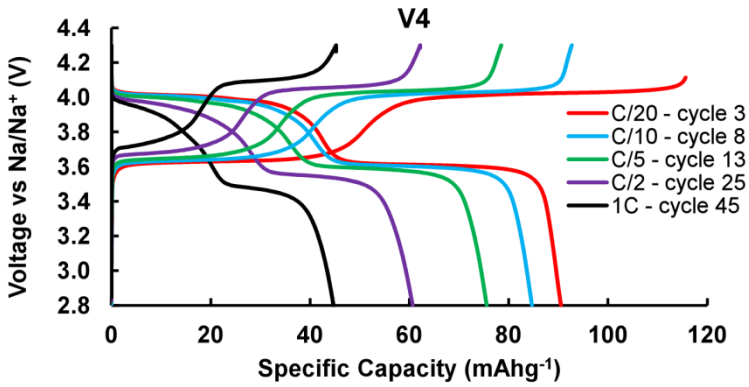

Figure 3.58 *Charge and Discharge curves of V4 sample.*

A lower capacity together with an increase of the polarization is observed when increasing the current density. It is worth noting that the loss of capacity affects both *plateaux* equally. The polarization is less pronounced for V4_FTT, which suggests the beneficial effect of carbon coating on the electrochemical performance.

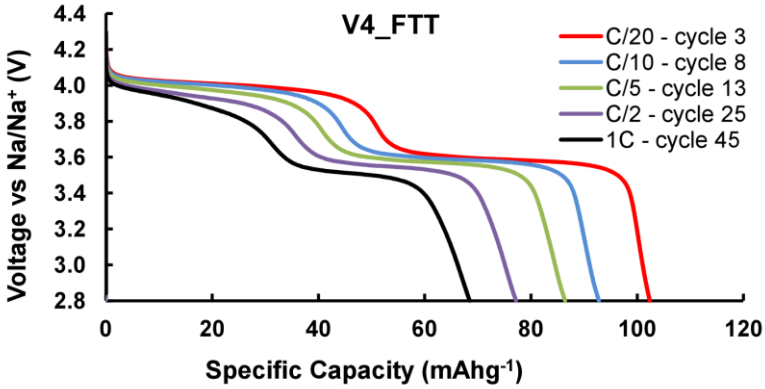

Figure 3.59 *Discharge curves of V4_FTT sample.*

In the case of V4_LTT, as it has been previously mentioned in the structural characterisation (see Chapter 2), the sample undergoes a partial decomposition into $Na_3V_2(PO_4)_3$. This latter phase is also electroactive, and its performance as cathode *vs.* a metallic sodium anode [182] and, as both positive and negative electrodes in a symmetric cell has been recently reported [183].

Figure 3.60 shows the discharge curve obtained from V4_LTT at C/5 in a sodium half-cell. Three *plateaux* at 4.0, 3.6 and 3.3 V *vs.* Na/Na^+ can be observed. The first two, at 4.0 and 3.6 V, correspond to the $Na_3V_2O_2(PO_4)_2F$ compound while the third one, at 3.3 V, is characteristic of the $Na_3V_2(PO_4)_3$ secondary phase. The total specific capacity obtained from V4_LTT is about 80 $mAhg^{-1}$ at C/5 which is comparable to the one obtained from V4_FTT at the same rate. However, although $Na_3V_2(PO_4)_3$ contributes to

182 Jian, Z.; Zhao, L.; Pan, H.; Hu, Y.-S.; Li, H.; Chen, W.; Chen, L., *Electrochem. Commun.*, **2012**, 14, 86-89.

183 Noguchi,Y.; Kobayashi, E.; Plashnitsa, L.S.; Okada, S.; Yamaki, J.-I. *Electrochim. Acta.* **2012**, 101, 59-65.

the total capacity, its lower working voltage makes it a less attractive candidate for its use as positive electrode material for sodium-ion batteries [184].

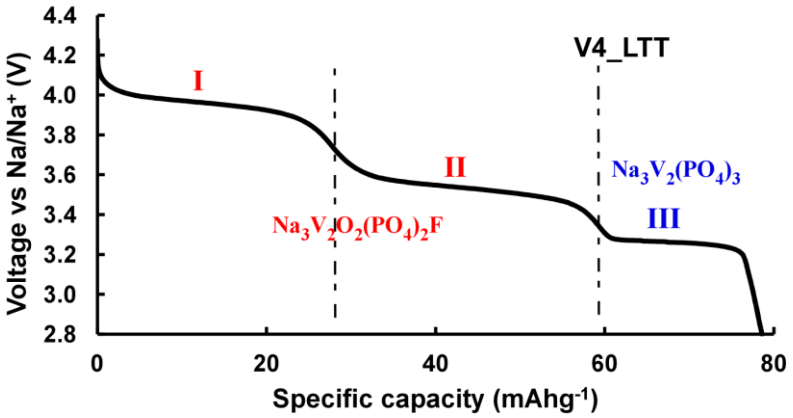

Figure 3.60 *A discharge curve of V4_LTT sample.*

Electrochemical performance of V4 and V4_FTT materials has been more thoroughly studied. The charge/discharge specific capacity values of these two samples at rates ranging from C/20 to 2C are shown in Figure 3.61a and Figure 3.61b, respectively. At low rates, the coulombic efficiency is about 70% and increases to more than 98% after a few cycles. The initial low values could be due to the decomposition and other side reactions of the electrolyte as reported in recent publications [185,186].

Higher specific capacity values are obtained for V4_FTT than for V4 in the same cycling conditions. At C/20, the uncoated V4 material exhibits a reversible capacity of 91 $mAhg^{-1}$ whereas V4_FTT discharges 102 $mAhg^{-1}$ (70 and 78% of the 130 $mAhg^{-1}$ theoretical value respectively).

184 Palomares, V.; Serras, P.; Villaluenga, I.; Hueso, K. B.; Carretero-Gonzalez, J.; Rojo, T. *Energy Environ. Sci*. **2012**, 5, 5884-5901.

185 Jian, Z.; Han, W.; Lu, X.; Yang, H.; Hu, Y-S.; Zhou, J.; Zhou, Z.; Li, J.; Chen, W.; Chen, D.; Chen, L. *Adv. Energy Mater.* **2013**, 3, 156-160.

186 Pan, H.; Lu, X.; Yu, X.; Hu, Y-S.; Li, H.; Yang, X-Q.; Chen. L. *Adv. Energy Mater.* **2013**, 3, 1186-1194.

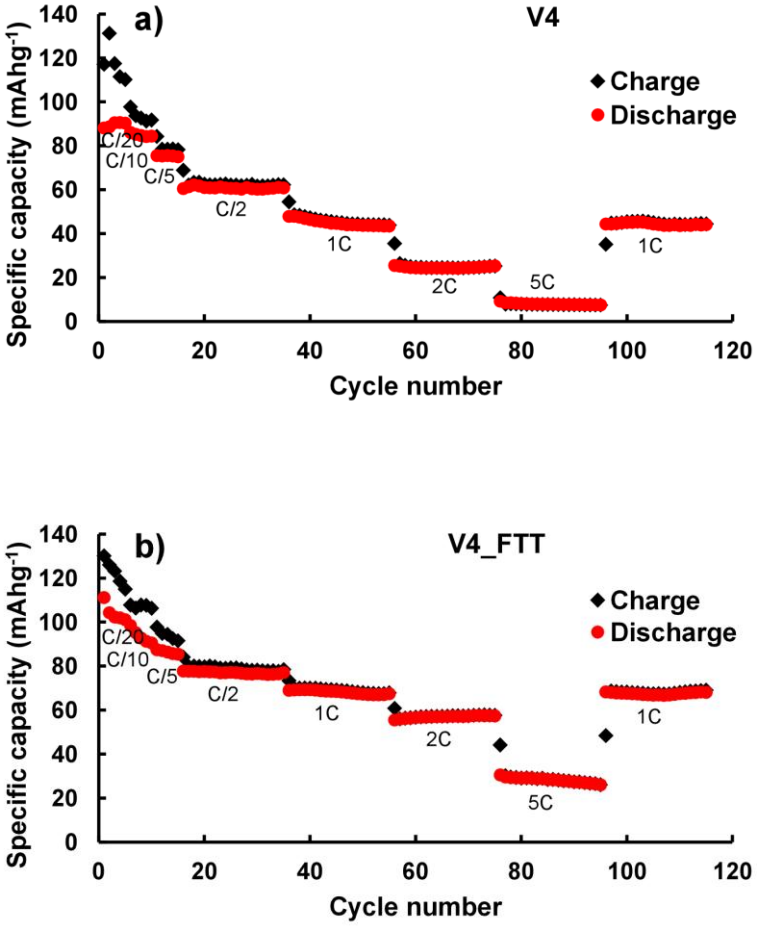

Figure 3.61 *Rate capability of **a)** V4 and **b)** V4_FTT sample.*

The specific capacity for uncoated V4 sample rapidly decreases with increasing charging rates and becomes almost negligible at 5C, whereas V4_FTT presents higher performance (Figure 3.62). The difference between them is constant for the lower rates but it increases more steeply from 1C, where specific capacity rises from 45 $mAhg^{-1}$ to 68 $mAhg^{-1}$ with carbon coating. The growing difference between V4_FTT and V4 at high rates can be related to an enhancement of the electronic conductivity and the Na^+ diffusion ability of electrode materials when carbon coating is applied. The capacity fade

at slow rates could be related to the type of binder used as recently reported by Sun *et al.* [187].

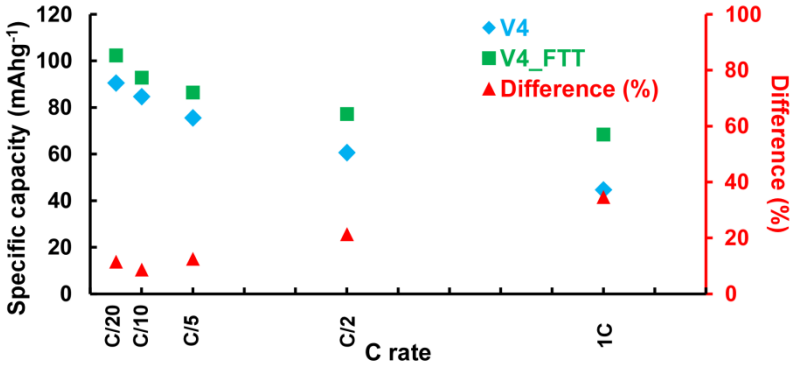

Figure 3.62 *Comparison of discharge specific capacity values between V4 and V4_FTT samples.*

Thus, it can be said that the V4 sample, *i.e.,* $Na_3V_2O_2(PO_4)_2F$, presents good electrochemical features as cathode for sodium-ion batteries and that carbon coating is a good method to improve its electrochemical performance. However, control of the thermal treatment process is determinant in optimising this process in order to use this phase in a commercial sodium-ion battery.

187 Sun, Y.; Zhao, L.; Pan, H.; Lu, X.; Gu, L.; Hu, Y-S.; Li, H.; Armand, M.; Ikuhara, Y.; Chen, L.; Huang, X. *Nat. Commun.* **2013**, 4:1870.

3.6 Chapter Summary

The electrochemical behaviour of a series of sodium vanadium fluorophosphates has been studied in this chapter. Electrochemical tests have been performed both in pellet and laminate electrodes.

Intermediate amounts of carbon present in the $Na_3V_2O_{2x}(PO_4)_2F_{3-2x}$ final product (1 – 50 *wt.*% C) lead to V^{3+}/V^{4+} mixed valence phases ($0 < x < 1$) while a sample containing almost only V^{4+} is obtained in a composite with less than 1 *wt.*% of carbon. All samples show two reaction voltages at 3.6 and 4.1 V *vs.* Na/Na^+ and good specific capacity values especially when an electrochemical grade carbon is employed. Moreover, the material containing a moderate amount of this type of carbon (~6 *wt.*%) shows the best electrochemical results. The similarity between the results provided by both, V^{3+}/V^{4+} mixed valence compounds and a sample containing mostly V^{4+} could indicate that the reaction taking place would correspond to V^{4+}/V^{5+} redox pair and that V^{3+} would not participate in the electrochemical reaction but would enhance the material´s conductivity.

A deeper analysis of the MV_KC sample with a carbon content of ~6 *wt.*%, which presents an average oxidation state of +3.8 for the vanadium, shows excellent stability and reversibility especially at high charge/discharge rates and a cycle life of more than 200 cycles.

V4 sample ($Na_3V_2O_2(PO_4)_2F$ material) has also been electrochemically tested. The absence of *in-situ* carbon in the synthesised product makes it necessary to employ an *ex-situ* carbon coating in order to improve the conductivity of the material and hence its electrochemical performance. However, control of the thermal treatment process is determinant in order to avoid the degradation of the material and the appearance of secondary phases such as $Na_3V_2(PO_4)_3$. The carbon coated material prepared by impregnation and a flash thermal treatment, exhibits good rate capabilities and excellent cycling stability.

It must be noted that all the presented materials show two *plateaux* at *ca.* 3.6 and 4.1 V *vs*. metallic sodium of the same length, which is consistent with their belonging to the same family of compounds, $Na_3V_2O_{2x}(PO_4)_2F_{3-2x}$ ($0 < x \leq 1$).

Chapter 4. Study of the Electrochemical Mechanism of $Na_3V_2O_{2x}(PO_4)_2F_{3-2x}$ family

4.1 Introduction

Compounds of $Na_3V_2O_{2x}(PO_4)_2F_{3-2x}$ family are promising cathodes for sodium-ion batteries but further studies are required to elucidate their electrochemical and structural behaviour. As the sodium carries the charge of this material during battery function it is important to know how it behaves crystallographically in order to better understand its evolution. For this purpose *ex-situ* and *in-situ* characterisation is essential.

The electrochemical mechanism of both, $V^{3.8+}$ mixed valence $Na_3V_2O_{2x}(PO_4)_2F_{3-2x}$ (x = 0.8) compound (labelled as MV_KC, and named as MV from now on for greater clarity) and V^{4+} $Na_3V_2O_2(PO_4)_2F$ (named as V4) are studied in this chapter. Na_{3-y} notation is used in the corresponding formula of both materials when cycled electrodes are shown. Thus, the amount of interchanged sodium during charge/discharge (y) as well as the total sodium content present in the cycled electrodes (3-y) is represented.

Ex situ X-ray diffraction and XANES experiments have been carried out on *post mortem* electrodes stopped in different points of charge and discharge. However, *post mortem* data, which are collected at equilibrium conditions do not represent the true state of the

electrodes as electrochemical reaction proceeds, so *in-situ* studies appear as a complement to *ex-situ* ones.

Time-resolved *in-situ* neutron diffraction (ND) is the more lithium-sensitive technique for the characterisation of lithium-ion batteries, since the lithium scattering cross section in X-ray powder diffraction (XRD) data is very small. Using time-resolved *in-situ* ND, researchers have determined current-dependent electrode lattice fluctuations [142] as well as the effect of overcharging a lithium-ion battery [143], and more recently the evolution of lithium site occupancy and location as function of charge/discharge [144]. Sodium, with a larger atomic number, can potentially be tracked in real-time during a time-resolved *in-situ* synchrotron XRD experiment. The ability to track sodium as a function of charge and discharge provides unparalleled insight into the function of a sodium-ion battery.

Overall, the following features have been determined for both, MV and V4 materials on *post mortem* electrodes stopped at different points of electrochemical reaction and while electrochemically cycling in real time. The lattice parameter and volume evolution as well as the vanadium oxidation state change have been monitored. Furthermore, by *in-situ* synchrotron X-ray diffraction the sodium progression at the two crystallographic sites in the crystal structure has been elucidated using appropriate constraints, and the rates of lattice and volume expansion/contraction and its relationship to sodium evolution and behaviour have been determined. The maximum sodium extraction at the most charged voltage (4.3 V) using a potentiostatic step in the electrochemical cycle and its influence is also shown.

Up till now, only *ex-situ* works have been reported in the field of sodium vanadium fluorophosphates. A detailed *ex-situ* study has been recently presented by Park *et al.* [145,146] to determine the sodium extraction/insertion mechanism of these materials.

142 Sharma, N.; Peterson, V.K. *Electrochimica Acta*, **2013**, 101, 79-85.

143 Sharma, N.; Peterson, V.K. *J. Power Sources*, **2013**, 244, 695-701.

144 Sharma, N.; Yu, D.; Zhu, Y.; Wu, Y.; Peterson, V. K. *Chem. Mater.*, **2013**, 25, 754-760.

145 Park, Y.-U.; Seo, D. H.; Kwon, H.-S.; Kim, B.; Kim, J.; Kim, H.; Kim, I.; Yoo, H.-I.; Kang, K. *J. Am. Chem. Soc.*, **2013**, 135, 13870-13878.

146 Park, Y. U.; Seo, D. H.; Kim, B.; Kim, J.; Lee, S.; Kim, B.; Kang, K. *Adv. Funct. Mater.*, **2014**, DOI: 10.1002/adfm.201400561.

Examination of the *ex-situ* XRD patterns of $V^{3.8+}$ $Na_{1.5}VPO_{4.8}F_{0.7}$ compound revealed the coexistence of a two-phase region in the first half of the charge indicating the presence of a stable intermediate phase between the two *plateaux* at 3.6 and 4.1 V *vs.* Na/Na^+. They also reported that the V^{3+} present in the $V^{3.8+}$ $Na_{1.5}VPO_{4.8}F_{0.7}$ phase creates a local environment similar to the one presented by $Na_3V_2(PO_4)_2F_3$ phase [147] leading to a high voltage V^{3+}/V^{4+} redox reaction. They assumed that 1.2 electrons are supplied per formula unit ($Na_{1.5}VPO_{4.8}F_{0.7}$) from the $V^{3.8+}$ / V^{5+} redox couple leading to a theoretical specific capacity of 155.6 $mAhg^{-1}$. X-Ray Absorption Near Edge Spectroscopy (XANES) studies revealed that an oxidation process happens while charging and that the reverse process occurs when discharging but no evolution of the value of the vanadium oxidation state was determined.

Concerning $Na_3V_2O_2(PO_4)_2F$ compound, it is complicated to exactly determine its crystal structure by the synthesis conditions used, due to the multiple compositions and in some cases space group symmetries found in literature [148,149]. In addition, multiple locations of sodium sites and polymorphism can be present at room temperature [148]. In terms of sodium insertion/extraction, the "α" modification is shown to reversibly cycle 1.12 Na ions per formula unit ($Na_3V_2O_2(PO_4)_2F$) [150] while in this work, the β polymorph with a carbon-coated synthetic procedure, reversibly cycles 1.56 Na ions per formula unit (see Chapter 3). Additional works as the one presented by Xu *et al.* shows that the reversible capacity of $Na_3V_2O_2(PO_4)_2F$/graphene electrodes exceed 100 $mAhg^{-1}$ after 200 cycles at a C/20 current rate [151].

147 Shakoor, R. A.; Seo, D.-H.. Kim, H.; Park, Y.U.; Kim, J.; Kim, S.-W.; Gwon, H.; Lee, S.; Kang, K. *J. Mater. Chem*., **2012**, 22,20535-20541.

148 Tsirlin, A.; Nath, R.; Abakumov, A.; Furukawa, Y.; Johnston, D.; Hemmida, M.; Krug von Nidda, H.-A.; Loidl, A.; Geibel, C.; Rosner, H. *Phys. Rev. B,* **2011**, 84, 014429/1-014429/16.

149 Massa, W.; Yakubovich, O.; Dimitrova, O. *Solid State Sci.*, **2002**, 4, 495-501.

150 Sauvage, F.; Quarez, E.; Tarascon, J.; Baudrin, E. *Solid State Sci.*, **2006**, 8, 1215–1221.

151 Xu, M.; Wang, L.; Zhao, X.; Song, J.;Xie, H.; Lu, Y.; Goodenough, J.B. *Phys.Chem. Chem. Phys.*, **2013**, 15, 13032-13037.

4.2 Experimental

4.2.1 Post mortem electrodes preparation

Positive electrode laminates were manufactured as previously described in Chapter 3. These electrodes were cycled and stopped at different points of charge/discharge. Swagelok cells were disassembled and positive electrodes were washed in dimethylcarbonate (DMC) to remove remaining electrolyte.

4.2.2 Ex-situ X-ray diffraction (XRD) and Synchrotron X-Ray Absorption Near Edge Spectroscopy (XANES)

Ex-situ laboratory-based and high resolution synchrotron X-ray diffraction patterns have been collected for MV material. V4 sample was analysed only by high resolution synchrotron X-ray diffraction. A Cu Kα radiation (λ= 1.54056 Å) was employed for the obtaining of laboratory-based XRD patterns between 10 and 90º at room temperature. High-resolution synchrotron XRD data were collected on the Powder Diffraction beamline (10-BM-1) [152] at the Australian Synchrotron using a wavelength of λ = 0.83696(2) Å, determined using the NIST 660a LaB_6 standard reference material. Powder samples were packed and sealed in 0.5 mm glass capillaries and data were collected for 6 minutes at ambient temperature using Debye-Scherrer geometry. Rietveld refinements were carried out using the GSAS [153] software suite with the EXPGUI [154] software interface. Lattice parameters, atomic positions and atomic displacement parameters (ADPs) of all atoms were refined independently. For the sodium sites the ADPs and occupancies were refined individually, *i.e.,* occupancies refined while ADPs fixed and *vice versa* until both parameters converged.

The *ex-situ* evolution of vanadium oxidation state during charge/discharge process was also followed by X-Ray Absorption Near Edge Spectroscopy (XANES) using cycled

152 Wallwork, K.S.; Kennedy, B.J. and Wang, D. *AIP Conference Proceedings*, **2007**, 879, 879-882.
153 Larson, A.C. and Von Dreele, R.B. *General Structure Analysis System (GSAS)* Los Alamos National Laboratory Report LAUR, **1994**, 86-748.
154 Toby, B.H. *J. Appl. Crystallogr.*, **2001**, *34*, 210-213.

post mortem electrodes stopped at different steps of voltage during the electrochemical reaction. These experiments were conducted on the XAFS beamline of the Elettra Synchrotron (Trieste, Italy) for sample MV and on the B18-Core EXAFS beamline at the Diamond Synchrotron (Didcot, UK) for V4. For both cases, XANES data were collected at the vanadium K-edge (5465 eV) in transmission mode and at room temperature, with a step size of ΔE = 0.1 eV for the edge region. Energy calibration was established by measuring simultaneously a vanadium foil inserted between the second and third ionization chambers. All the spectra were normalised by a standard procedure [155] using Athena analysis software [156]. XANES spectra of specifically prepared V^{3+} $Na_3V_2(PO_4)_3$, V^{4+} ($Na_3V_2O_2(PO_4)_2F$) and V^{5+} ($VOPO_4{\cdot}2H_2O$) standards were also measured for reference. These standards were prepared such that the structures were as similar as possible to that of the studied samples. However, it was not possible to employ $VOPO_4{\cdot}2H_2O$ sample as V^{5+} standard when fitting MV spectra and instead the most charged *post mortem* electrode was used as reference.

4.2.3 In situ synchrotron X-ray diffraction (XRD)

To carry out the *in-situ* high resolution synchrotron X-ray diffraction tests the electrode laminates were pressed to 100 kN using a flat plate press (MTI corporation) and dried overnight at 100°C before transfer to the Ar-filled glovebox. Coin cell casings and stainless spacers with 3 and 5 mm diameter holes, respectively, were used for the construction of the coin cells for the *in-situ* measurements. They contained sodium metal (~1 mm thickness), glass fiber separators with 1M $NaPF_6$ in EC:DMC (ethyl carbonate:dimethyl carbonate 1:1 *wt.*%) electrolyte solution. Further details regarding coin cell construction and beamline setup can be found in [157,158]. *In-situ* synchrotron XRD data were collected on the Powder Diffraction beamline [152] at the Australian Synchrotron with a refined wavelength of λ = 0.68816(2) Å, determined using the NIST LaB_6 660b standard reference material.

155 Koningsberger, D. and Prins, R. "X-Ray Absorption: Principles, Applications, Techniques of EXAFS, SEXAFS, and XANES", Wiley-Interscience: New York, **1988**.

156 Ravel B. and Newville, M. *J. Synchrotron Rad.*, **2005**, *12*, 537-541.

157 Gummow, R. J.; Sharma, N.; Feng, R.; Han, G.; He, Y., *J. Electrochem. Soc.*, **2013**, 160, A1856-A1862.

158 Brant, W.; Schmid, S.; Gu, Q.; Du, G.; Sharma, N., *J. Power Sources*, **2013**, 244, 109-114.

Data were collected continuously in 4 minute acquisitions when working with both, MV and V4 samples. Rietveld refinements were carried out using the GSAS [153] software suite with the EXPGUI [154] software interface. Reflections arising from the aluminium current collector (cubic *Fm*-3*m*, *a* = 4.05994(8) Å) and sodium metallic anode (cubic *Im*-3*m*, *a* = 4.3218(8) Å) were excluded as their positions did not overlap with many cathode reflections.

MV sample was cycled once offline (charge/potentiostatic hold/discharge) and stored for 8 days before *in-situ* synchrotron XRD experiments. It was then charged at a current rate of 0.3 mA, held at 4.3 V for 2 hours (potentiostatic step) to extract all possible sodium at this voltage and discharged to 2.5 V at -0.3 mA (~C/3.5).

For V4 sample, one cycle of the cell was performed offline, charging to 4.3 V and discharging to 2.5 V at a current rate of ± 0.3 mA. *In-situ* synchrotron X-ray diffraction experiments were performed within a day after this process. Due to problems during experimental procedure, it was not possible to do a potentiostatic step in the offline cycle for V4 sample. Then, the cell was galvanostatically charged to 4.3 V, potentiostatically held at 4.3 V for 2 hours to ensure equilibration at the charged state before being discharged to 2.5 V while obtaining the X-ray diffraction patterns. The charge/discharge processes were carried out at ± 0.3 mA (~C/3).

Rietveld analyses of the *in-situ* data were undertaken by initially refining the lattice parameters followed by systematically refining atomic positional and isotropic displacement parameters (ADPs). Constraints were used to minimise the number of refineable variables, *e.g.,* constraining the atomic displacement parameters of all the oxygen sites to be equal. The positional parameters of the two sodium sites Na(1) and Na(2) were refined for the first *in-situ* dataset and fixed, then the occupancies of these sites were refined. The datasets were divided into regions and sequential refinements were performed in regions where a solid-solution type reaction was persistent.

4.3 Electrochemical Mechanisms

4.3.1 Ex-situ measurements

4.3.1.1 Ex-situ X-Ray Diffraction (XRD) and X-Ray Absorption Near Edge Spectroscopy (XANES) for $Na_3V_2O_{2x}(PO_4)_2F_{3-2x}$ (x = 0.8)

The structural evolution of cathode materials during sodium insertion/extraction is an indicator of the long term stability of the electrode, *e.g.,* volume expansion/contraction, and performance or potential characteristics of the battery, *e.g.,* solid-solution or two-phase mechanism of sodium extraction/insertion. Electrode-containing test cells were equilibrated at the potentials indicated in Figure 4.63 and extracted from these test cells for *post mortem* or *ex-situ* XRD and XANES analysis.

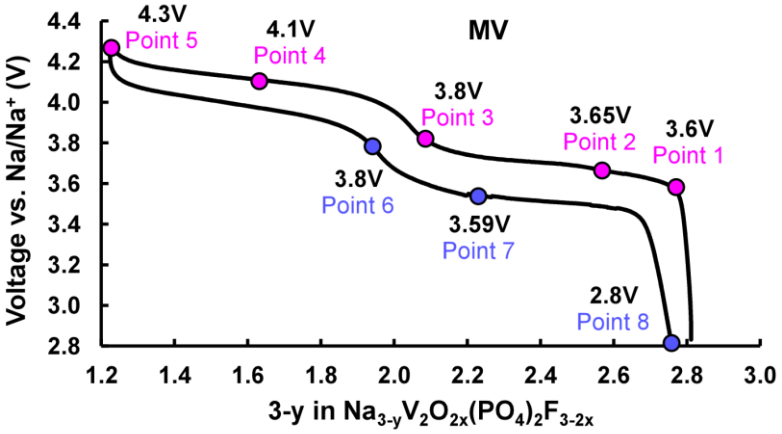

Figure 4.63 *Points during charge/discharge of MV sample where post mortem electrodes were extracted for their analysis by XRD and XANES.*

Figure 4.64 shows the diffractograms of *post mortem* electrodes stopped at the points signalled in Figure 4.63. All the diffraction diagrams present $Na_{3-y}V_2O_{2x}(PO_4)_2F_{3-2x}$ (x = 0.8) as major phase. Nonetheless, small quantities of AlF_3 have been observed

especially at higher state of charge. This can be due to aluminium current collector corrosion to form AlF_3 after cell disassembly. Analysis of *ex situ* XRD data in terms of lattice parameters is gathered in Table 4.19 and depicted in Figure 4.65.

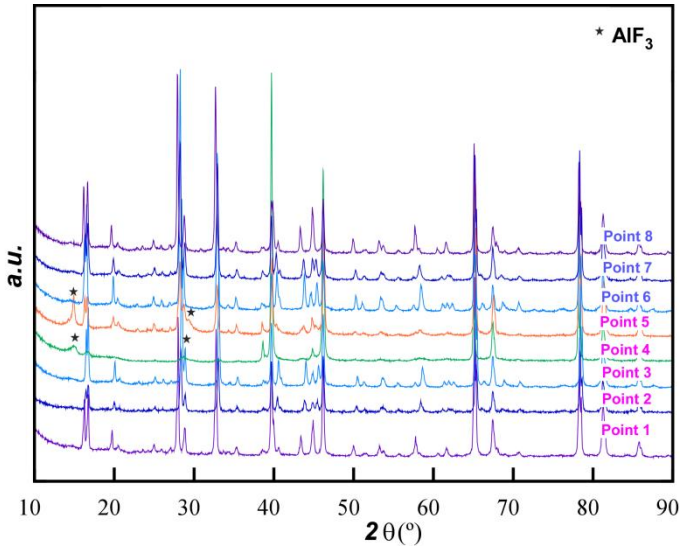

Figure 4.64 *Laboratory-based XRD patterns corresponding to post mortem electrodes from points shown in Figure 4.63.*

Table 4.19 *Evolution of lattice parameters of the MV cathode during charge (C)/discharge (D) extracted from patterns from Figure 4.64.*

Sample	Parameter a (Å)	Parameter c (Å)
Raw MV	9.030(3)	10.644(7)
C- 3.6 V – point 1	9.02(1)	10.63(2)
C- 3.65 V – point 2	8.95(2)	10.70(3)
C- 3.8 V – point 3	8.92(1)	10.71(2)
C- 4.1 V – point 4	8.914(6)	10.73(1)
C- 4.3 V – point 5	8.910(4)	10.74(1)
D- 3.8 V – point 6	8.923(8)	10.71(1)
D- 3.59 V – point 7	8.96(1)	10.68(2)
D- 2.8 V – point 8	9.023(8)	10.63(1)

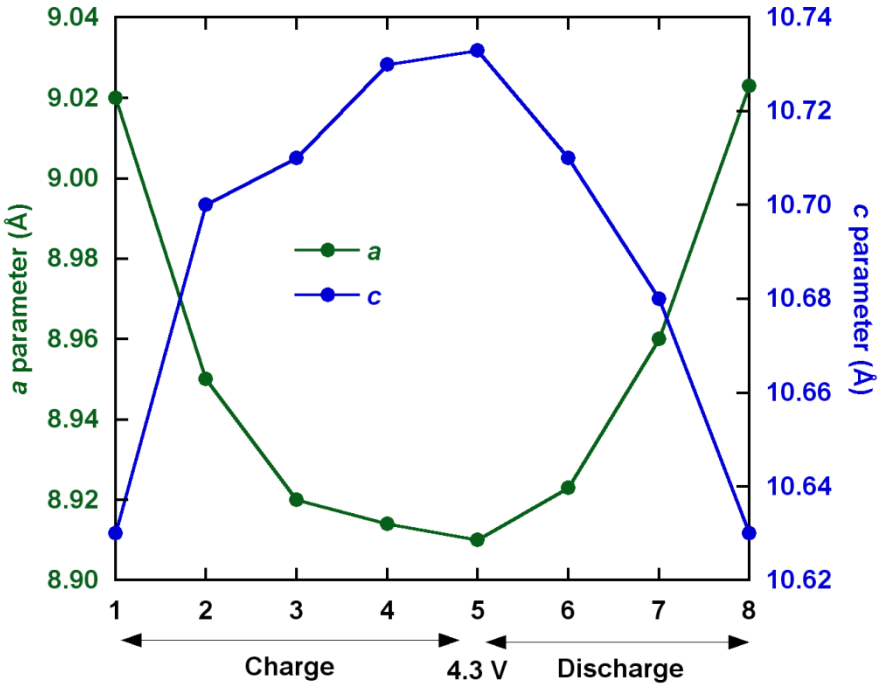

Figure 4.65 *Lattice parameter evolution of MV during charge and discharge from laboratory-based XRD data on post mortem electrodes where 1 to 8 on the x-axis refers to the points in the electrochemical charge/discharge curve shown in Figure 4.63.*

X-ray diffractograms show no evidence of two-phase behaviour, *e.g.,* reflection splitting, for any of the extracted electrodes in the equilibrated state. The reflections positions shift to different 2θ values indicating an expansion and contraction of the lattice, consistent with a solid-solution type structural evolution during charge/discharge. As shown in Table 4.19, *a* lattice parameter decreases while *c* lattice parameter increases during charge. This process reverses during discharge. The overall lattice volume follows the same trend as *a* parameter during charge/discharge. The changes in *a* and *c* lattice parameters suggest that the tunnels in this structure are enlarged in *z* direction and shrink in (110) direction with sodium extraction during charge (Figure 4.66).

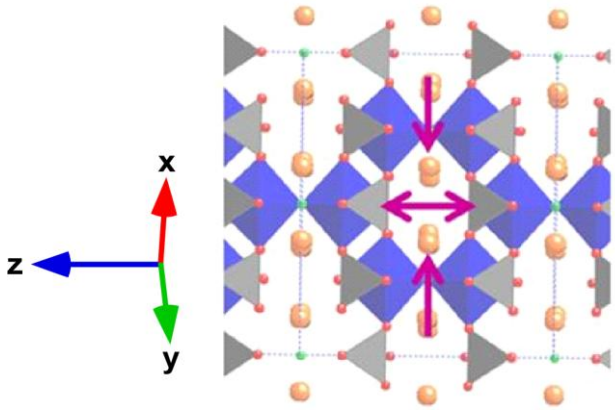

Figure 4.66 *Evolution of the a and c parameters of sample MV with charging (sodium extraction).*

To determine the crystal structure of the as-synthesised MV material more precisely, high resolution synchrotron XRD data were collected. Rietveld refinements were undertaken with a number of structural models, and the starting model of Le Meins *et al.* [159] gave the best initial fit to the data. The refinement was started with the lattice parameters followed by the atomic positional ones. Next, the atomic isotropic displacements parameters were independently refined, and finally the occupancy of the two sodium crystallographic sites. A small amount of the VPO_4 secondary phase was also present in this sample and was modelled in *Cmcm* space group with refined lattice parameters of *a* = 5.2404(5), *b* = 7.7782(7) and *c* = 6.2858(6) Å. The phase fractions of VPO_4: MV were 2.1(6)% : 97.9(1)%. The final fit to the data and the structure are shown in Figure 4.67 while refined structural details are presented in Table 4.20.

159 Le Meins, J.-M.; Crosnier-Lopez, M.-P.; Hemon-Ribaud, A. and Courbion, G. *J. Solid State Chem.*, **1999**, *148*, 260-277.

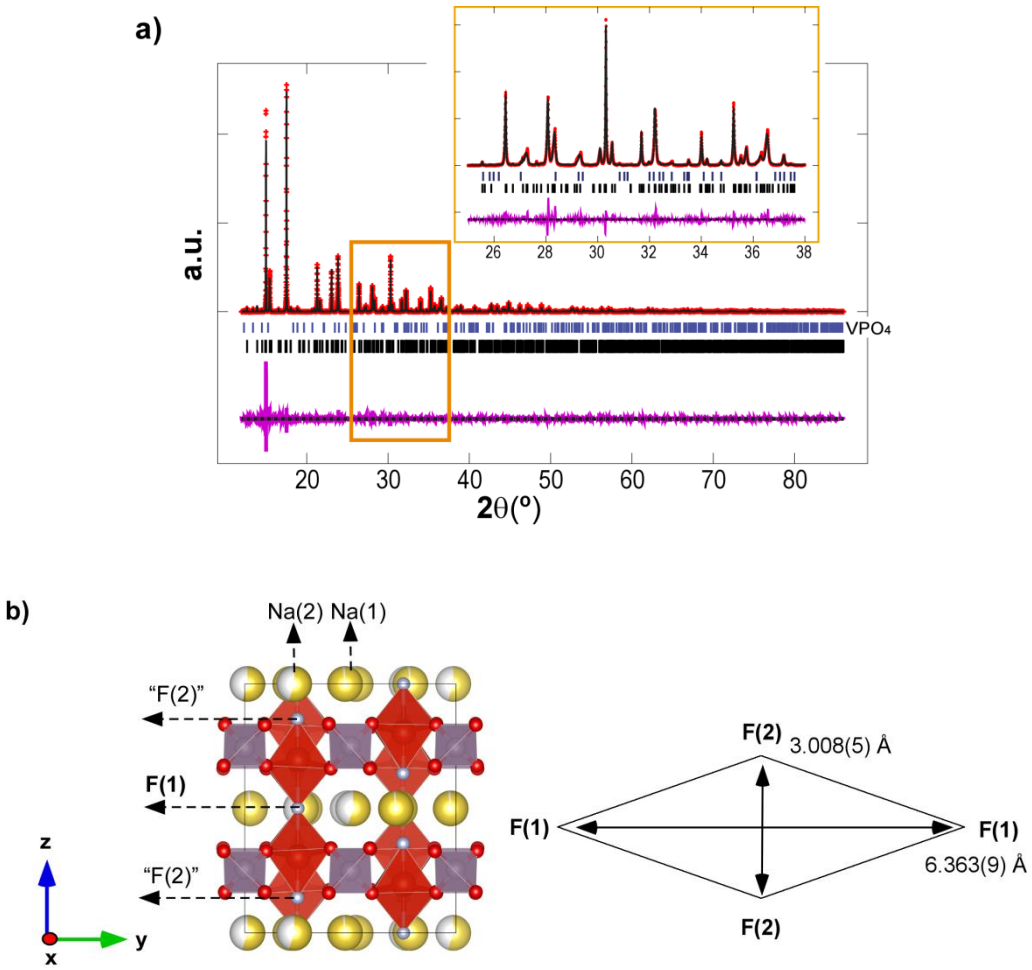

Figure 4.67 ***a)*** *Rietveld refined fit of the $Na_3V_2O_{2x}(PO_4)_2F_{3-2x}$ model to the synchrotron XRD data of the raw MV sample with the inset showing an enlarged $25 \leq 2\theta \leq 38^{\circ}$ region. Data are shown as crosses, the calculated Rietveld model as a line through the data, and the difference between the data and the model as the line below the data. The vertical reflection markers are for $Na_3V_2O_{2x}(PO_4)_2F_{3-2x}$ (lower markers) and VPO_4 (upper markers)* ***b)*** *The crystal structure of MV with PO_4 shown in purple and VO_4F_2 in red. Oxygen is red, fluorine is light blue and sodium is yellow with the shading indicating occupancy. The scheme on the right shows F(1)-F(1) and F(2)-F(2) distances obtained from the refinement.*

The obtained atomic positions together with the occupancies are in good agreement with the data given in the literature [159]. However, Na sites occupancy factor deviates slightly from the full occupation of Na(1) and half occupation of Na(2) site. These data suggest that little exchange between the two Na sites appears. The Na(1) site shows a large isotropic atomic displacement parameter suggesting that the sodium-ions are weakly centred at this atomic site.

The distribution of fluorine (F) and oxygen (O) on the anionic sites is difficult to determine due to the very similar scattering factors of these atoms when X-ray diffraction data are used. Thus, the bond valence sum (BVS) approach [160,161] was employed, showing that the BVS for the F(1) and F(2) sites were close to 1, the expected value for F. Additionally, the BVS for the O sites were found to be close to 2 in agreement with the BVS expected for O. However, the possibility of anion disorder on these sites exists. This fact would be manifested as a larger atomic displacement parameter directed to the vanadium site due to the variation in bond lengths between V-O and V-F. The F(1) site is the corner connecting site for the two connected vanadium octahedra and shows the largest bond length between vanadium and any anion in the sample (see Figure 4.67b). Thus, the F(1) site is an unlikely site for anion disorder. The F(2) site is 'open' to the sodium-ion channels and shows a large isotropic atomic displacement parameter indicating the possibility of F/O disorder on this site.

160 Brown, I.D.; Altermatt, D. *Acta Cryst.* **1985**, *B41*, 244-247.
161 Brese, N.E.; O'Keeffe, M. *Acta Cryst.,* ***1991****, B47*, 192-197.

Table 4.20 Refined crystallographic parameters for the MV sample.

***P4₂/mnm*, *a* = 9.03805(6) Å, *c* = 10.64035(13) Å; Na content: 3.04(3)**					
Atom	***x***	***y***	***z***	**Site Occupancy Factor**	**Isotropic Atomic Displacement Parameter (× 100)/Å²**
Na(1)	0.5249(8)	0.2185(9)	0	0.973(11)	4.50(32)
Na(2)	0.7659(13)	0.0127(11)	0	0.547(9)	1.43(29)
V(1)	0.24776(23)	0.24776(23)	0.19503(10)	1	0.55(2)
P(1)	0	0.5	0.25	1	0.69(28)
P(2)	0	0	0.2556(7)	1	0.72(28)
O(1)	0.0925(7)	0.3980(8)	0.1597(10)	1	0.76(27)
O(2)	0.0946(8)	0.0946(8)	0.1644(16)	1	0.60(40)
O(3)	0.4003(8)	0.4003(8)	0.1723(16)	1	1.30(40)
F(1)	0.2489(8)	0.2489(8)	0	1	1.38(10)
F(2)	0.2504(7)	0.2504(7)	0.35865(33)	1	3.57(10)

χ^2= 3.55, R_p = 4.70 %, wRp = 7.04 %

Table 4.21 Bond distances inside the vanadium coordination polyhedron of MV starting material.

Bond	Bond length (Å)
V-O(1)	1.989(8)
V-O(2)	1.989(8)
V-O(3)	1.98(1)
V-F(1)	2.075(1)
V-F(2)	1.741(4)

Additionally, Table 4.21 shows that the V-F(2) bond length is significantly smaller than the other V-O and V-F bond lengths which suggests that some of the oxygen on this site is double bonded to vanadium. In fact, the V-F(2) distance, 1.741(4) Å, is intermediate between a single V-F bond (~2.1 Å in the V^{3+} extreme phase, end-member) and a V=O double bond (1.64 Å in the V^{4+} extreme phase, end-member), confirming the partial substitution of F by O. Calculations on the amount of F and O extrapolated from this bond length, and assuming only V=O and V-F bonds (*i.e.*, no V-O bonds in V-F(2)), indicate a ratio of 23% F and 77% O. This corresponds to 23% V^{3+} and 77% V^{4+} and an average vanadium oxidation state of $V^{3.77+}$ which is consistent with the results obtained by other techniques described in Chapter 2 for the raw MV sample.

The evolution of the vanadium valence state of sample MV during the charge/discharge process has been followed by means of XANES spectroscopy at the vanadium K-edge. This technique is sensitive to both, the oxidation state and to the local structure of the absorber element, the vanadium atom in this case. In a qualitative way, a shift in the edge position towards higher energies with increasing vanadium valence is expected.

The XANES spectra of the *post mortem* electrodes of MV at different stages of the electrochemical Na extraction/insertion reaction are displayed in Figure 4.68. The shape of the spectra changes during the charge/discharge process, as can be seen in the position of the pre-edge and white line features, which indicates changes in the vanadium environment, as revealed by XRD measurements, and in the vanadium oxidation state. The edge position and shape of the completely reduced sample (2.8V) is practically identical to the as-synthesised sample (Raw MV) (see Figure 4.68b), which indicates a complete reversibility of the charge/discharge process, at least in terms of the active vanadium oxidation states.

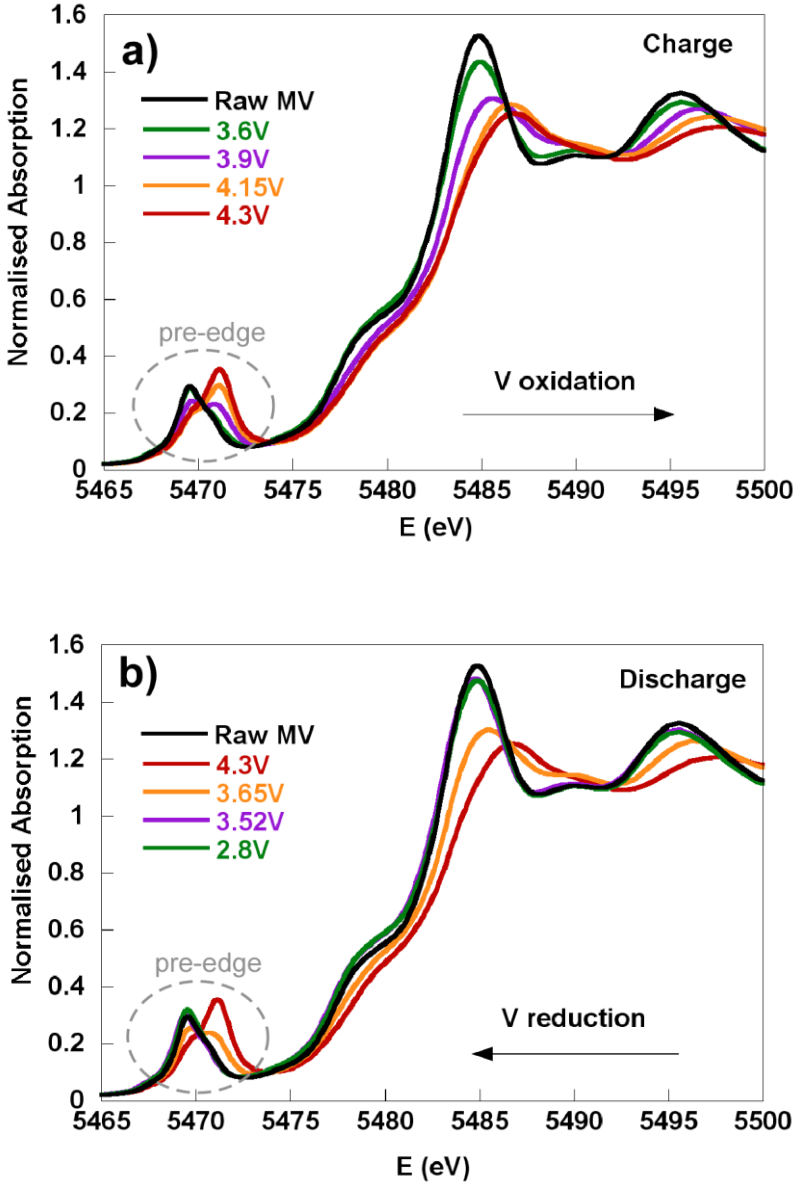

Figure 4.68 *Vanadium K-edge XANES spectra of the raw MV sample and the corresponding post mortem electrodes during* ***a)*** *charge and* ***b)*** *discharge.*

The pre-edge feature has been assigned to a forbidden transition 1s → 3d [162]. The intensity and position of this signal are related to the nature and symmetry of the vanadium ligands in the sample. Figure 4.69 presents the evolution of the pre-edge during the charge process, including $Na_3V_2(PO_4)_3$ –V^{3+} and $Na_3V_2O_2(PO_4)_2F$ – V^{4+} standards. Closer examination reveals the presence of a triplet structure, characteristic of octahedrally coordinated vanadium cations lacking an inversion centre [162].

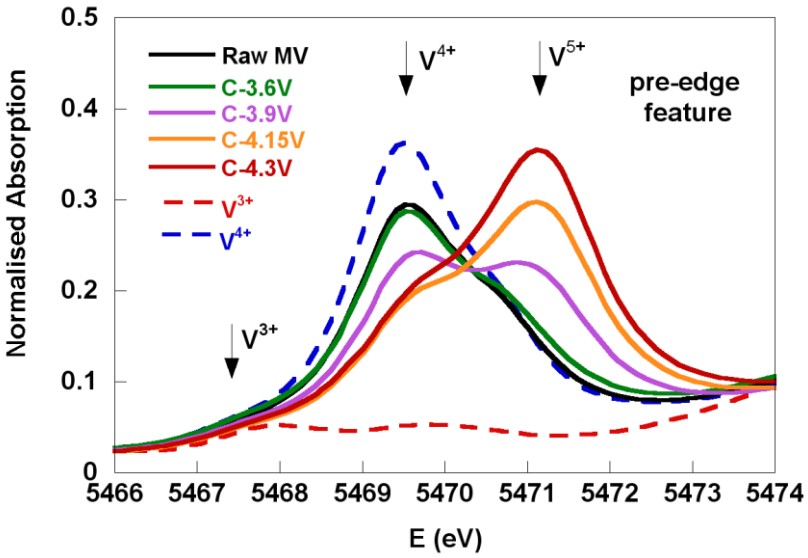

Figure 4.69 *Vanadium K-edge pre-edge feature of the raw MV sample, the corresponding post mortem electrodes during charge (continuous line) and the standards (dashed lines). Arrows indicate the position of the three characteristic peaks for V^{3+}, V^{4+} and V^{5+}."C" indicates charge.*

Taking into account the pre-edges of the V^{3+} and V^{4+}, and that of V^{5+} standards according to references [163,164], contributions to the pre-edge zone can be assigned to V^{3+} (5468 eV), V^{4+} (5469.5 eV) and V^{5+} (5471 eV) with increasing energy, as marked

162 Wong, J.; Lytle, F. W.; Messmer, R. P. and Maylotte, D. H. *Phys. Rev. B*, **1984**, *30*, 5596–5610.
163 Chalmin, E.; Farges, F.; Brown, G.E. Jr, *Contrib. Mineral. Petrol.*, **2009**, *157*, 111 – 126.
164 Farges, F. *Phys. Rev.*, **2005**, *B 71*, 155109.

with arrows in Figure 4.69. As observed, during the charge process, the first peak, lowest energy V^{3+}, is essentially constant. This appears to corroborate our hypothesis that proposes that V^{3+} does not participate in the oxidation process (see Chapter 3). Additionally, as charge proceeds, the second peak corresponding to V^{4+} decreases while the third peak corresponding to V^{5+} increases. This suggests that V^{4+} progressively oxidises and converts into V^{5+}.

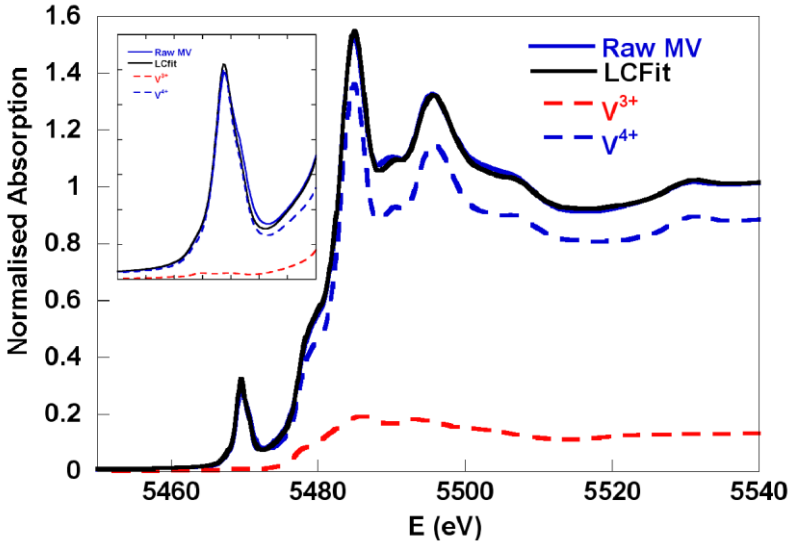

Figure 4.70 *XANES spectra of the raw MV sample and the corresponding fit to a linear combination of XANES profiles of V^{3+} and V^{4+} standards.*

The valence state of the starting sample can be obtained by fitting the XANES region to a linear combination of the V^{3+} and V^{4+} standards (Figure 4.70). This fitting indicates that there exists around 85% V^{4+} and 15% V^{3+} in the as synthesised MV sample which is in good agreement with the values obtained by other techniques (see Chapter 2). Another way for the estimation of the oxidation state of the raw MV sample can be made by fitting the pre-edge to a linear combination of the V^{3+} and V^{4+} standards (see inset from Figure 4.70) [163,164].This fitting indicates that there exists around 82% V^{4+} and 18% V^{3+} in the as-synthesised MV sample, which is consistent with the percentage estimated by the fitting of the overall XANES region (~85% V^{4+}) as well as by the rest of

the techniques employed in Chapter 2 (~80% V^{4+}). Lacking a V^{5+} standard, the average oxidation state of vanadium of the 4.3 V sample was estimated from the electrochemical curve, and found to be 75.4% of oxidised material corresponding to a $V^{4.5+}$ valence. To shed more light on the evolution of the vanadium valence during the oxidation/reduction of the samples, the XANES spectrum of each sample has been fitted using a linear combination of the totally reduced (Raw MV) and totally oxidised (C-4.3 V) samples [165]. An example of the fitting procedure and results is illustrated in Figure 4.71 (see Appendices for the rest of the fittings) showing a relatively straightforward approach with an acceptable fit. In this way, the relative amount of each component (*e.g.,* vanadium oxidation state distribution) in all intermediate states can be determined.

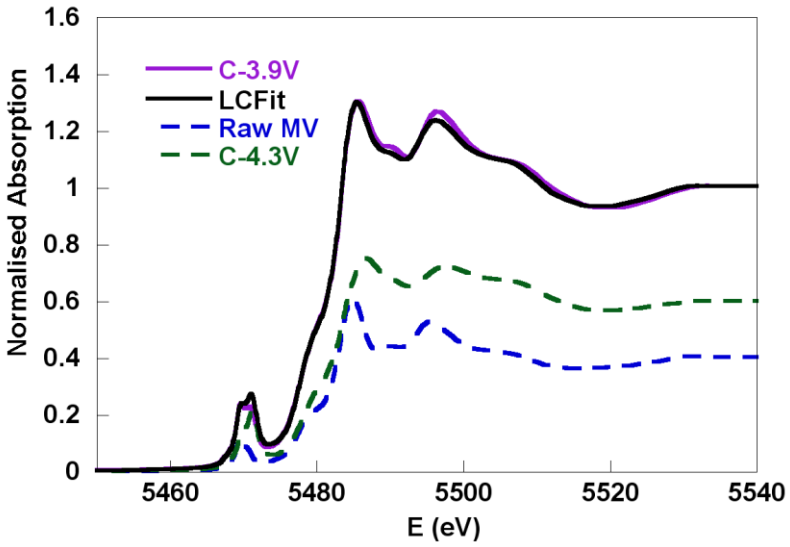

Figure 4.71 *XANES spectra of the C-3.9 V sample, and the corresponding fit to a linear combination of the raw MV sample and C-4.3 V XANES profiles (LCFit). "C" indicates charge.*

165 Pivko, M.; Arcon, I.; Bele, M.; Dominko, R. and Garberscek, M. *J. Power Sources,* **2012**, 216, 145-151.

Table 4.22 gathers the percentage of the two standards used for the fittings and the vanadium valence calculated from the fitting of the spectra. The XANES results show that during the cathode oxidation, the average vanadium valence progressively increases from $V^{3.8+}$ to $V^{4.5+}$, and that the process is completely reversible. Since the amount of V^{3+} is practically constant during the process, the following reaction can be proposed:

$$[\text{Raw MV}] = 20\%\ V^{3+} + 80\%\ V^{4+} \rightarrow [\text{C - "4.3 V"}] = 20\%\ V^{3+} + 10\%\ V^{4+} + 70\%\ V^{5+} \quad \text{(Eq. 4.1)}$$

Table 4.22 *Percentage of the two spectra used for fitting XANES data and the vanadium valence calculated from the fitting of the spectra. "C" indicates charge and "D" indicates discharge.*

Sample	Raw spectrum %	C-4.3 V spectrum %	Vanadium valence (XANES)
Raw MV	100(5)	0(5)	3.8(1)
C-3.6 V	85(5)	15(5)	3.9(1)
C-3.9 V	40(5)	60(5)	4.2(1)
C-4.15 V	7(5)	93(5)	4.4(1)
C-4.3 V	0(5)	100(5)	4.5(1)
D-3.65 V	43(5)	57(5)	4.2(1)
D-3.52 V	100(5)	0(5)	3.8(1)
D-2.8 V	100(5)	0(5)	3.8(1)

Therefore, these data indicate that, at the end of the reaction, nearly all the V^{4+} oxidises to V^{5+}, while the V^{3+} does not participate in the reaction.

4.3.1.2 Ex-situ Synchrotron X-Ray Diffraction (XRD) and X-Ray Absorption Near Edge Spectroscopy (XANES) for $Na_3V_2O_2(PO_4)_2F$

Due to the problems related to current collector corrosion when analyzing *post mortem* cathodes by laboratory X-ray diffraction, this study was not carried out for V4 sample.

High resolution synchrotron X-Ray diffraction was employed for the analysis of raw V4 sample. Figure 4.72 shows the Rietveld refinements of V4 sample and the crystal structure of the material. It adopts the *$P4_2/mnm$* symmetry and the following lattice parameters: *a* = 9.0319(5) Å and *c* = 10.6252(6) Å, corresponding to "β" $Na_3V_2O_2(PO_4)_2F$ phase as reported by Tsirlin *et al.* [148]. Table 4.24 presents the crystallographic parameters of the material with the bond valence sums (BVS) [161]. A refined sodium content of 3.07(3) is obtained with preferential occupation of the Na(1) site of 0.86(1) and with 0.67(1) Na on the Na(2) site. Even if the Na(1) site preference is maintained there are some differences in the sodium distribution compared to the fully occupied and half occupied Na(1) and Na(2) sodium sites shown in the literature [148].

The distributions of fluorine (F) and oxygen (O) are difficult to determine due to their similar X-ray scattering factors. Vanadium is octahedrally coordinated to 5 oxygens and 1 fluorine atom in $Na_3V_2O_2(PO_4)_2F$ phase. As can be seen in Table 4.23 the V-F(1) bond is of ~ 2.1 Å and the V-O bond distances around ~ 2 Å which are similar to the expected values of a V-F and a V-O single bond, respectively. The V-"F(2)" distance presents the expected value for a V=O (1.64 Å) which is typical of a vanadyl bond type in the V^{4+} end-member. This indicates that the F(1) site in Table 4.24 corresponds to a fluorine atom, while F(2) corresponds to oxygen. The BVS approach also shows good agreement with the oxidation states expected on the atoms in the structure [161]. This way, the oxidation state of vanadium is 3.94, close to 4, and the F(2) site (with V=O) presents a significantly larger BVS of 1.84 compared to the F(1) site of 1.16, supporting the assignment of O on the F(2) site.

Table 4.23 Bond distances inside the vanadium coordination polyhedron for starting V4 material.

Bond	Bond distance for starting V4 material (Å)
V-O(1)	1.987(7)
V-O(2)	2.02(1)
V-O(3)	2.03(1)
V-F(1)	2.123(1)
V-"F(2)"	1.605(4)

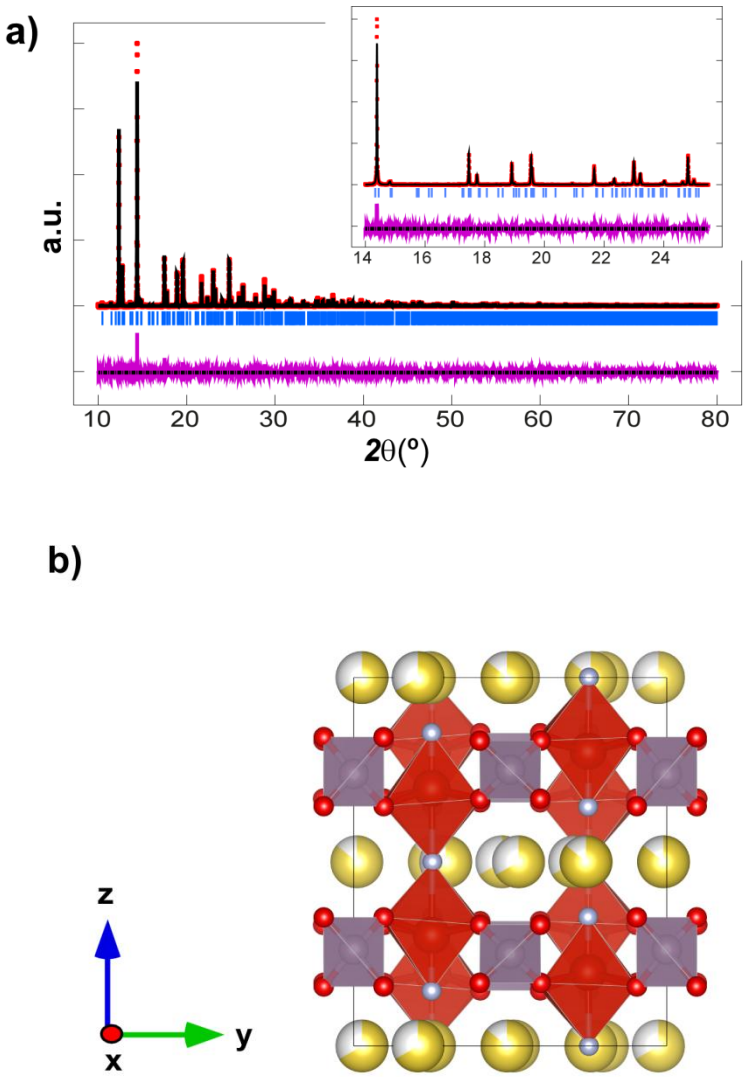

Figure 4.72 ***a)*** *Rietveld refined fit of $Na_3V_2O_2(PO_4)_2F$ model to the synchrotron XRD data with the inset showing an enlarged $14 \leq 2\theta \leq 25$ ^{o}region. Data are shown as crosses, the calculated Rietveld model as a line through the data, and the difference between the data and the model as the line below the data.* ***b)*** *The crystal structure of starting V4 material with PO_4 shown in purple and VO_4F_2 in red. Oxygen is red, fluorine is light blue and sodium is yellow with the shading indicating occupancy.*

Table 4.24 Refined crystallographic parameters for V4 sample.

***P4₂/mnm*, a = 9.0319(5) Å, c = 10.6252(6) Å; Na content: 3.07(3)**

Atom	*x*	*y*	*z*	Site Occupancy Factor	Isotropic Atomic Displacement Parameter (× 100)/Å²	BVS
Na(1)	0.5108(8)	0.2430(12)	0	0.862(10)	2.58*	1.12
Na(2)	0.7955(9)	0.0262(13)	0	0.672(12)	3.33*	1.06
V(1)	0.2508(4)	0.2508(4)	0.19976(10)	1	0.61(2)	3.94
P(1)	0	0.5	0.25	1	0.13(11)	5.78
P(2)	0	0	0.2616(6)	1	1.30(15)	4.36
O(1)	0.0953(9)	0.4030(9)	0.1721(5)	1	0.86(17)	2.20
O(2)	0.0959(8)	0.0959(8)	0.1610(11)	1	0.10(30)	2.03
O(3)	0.4039(8)	0.4039(8)	0.1493(11)	1	1.11(31)	2.11
F(1)	0.2489(12)	0.2489(12)	0	1	1.58(12)	1.16
"F(2)"	0.2510(14)	0.2510(14)	0.3508(4)	1	5.10(13)	1.84

*Refined in the first dataset and subsequently fixed

χ^2= 1.55, R_p = 3.24 %, wRp = 4.69 %

The charge/discharge processes of V4 material ($Na_3V_2O_2(PO_4)_2F$) were investigated by XANES spectroscopy at the vanadium K-edge, providing information about the local structure and oxidation state of vanadium. Qualitatively there is an expected shift of the edge position to higher energies with increased vanadium valence. The XANES spectra of the *post mortem* samples of V4 at different stages of the electrochemical Na extraction/insertion reaction are displayed in Figure 4.73.

The *post mortem* electrodes were extracted at similar points as the ones presented in Figure 4.63 for MV sample. The XANES spectra (Figure 4.73) clearly change during the charge/discharge process, evidenced by the changes in the position of the pre-edge, the edge, and the white line features, which indicate changes in the vanadium valence state. Concerning the pre-edge zone (Figure 4.74), as charge proceeds, the peak corresponding to V^{4+} decreases while the peak corresponding to V^{5+} increases which suggests that V^{4+} progressively oxidises and converts into V^{5+}.The edge position and shape of the completely reduced sample (2.8V) is practically identical to the as-synthesised V4 sample (labelled "Raw V4" in Figure 4.73), which indicates a complete reversibility of the charge/discharge process, at least in terms of the active vanadium oxidation states.

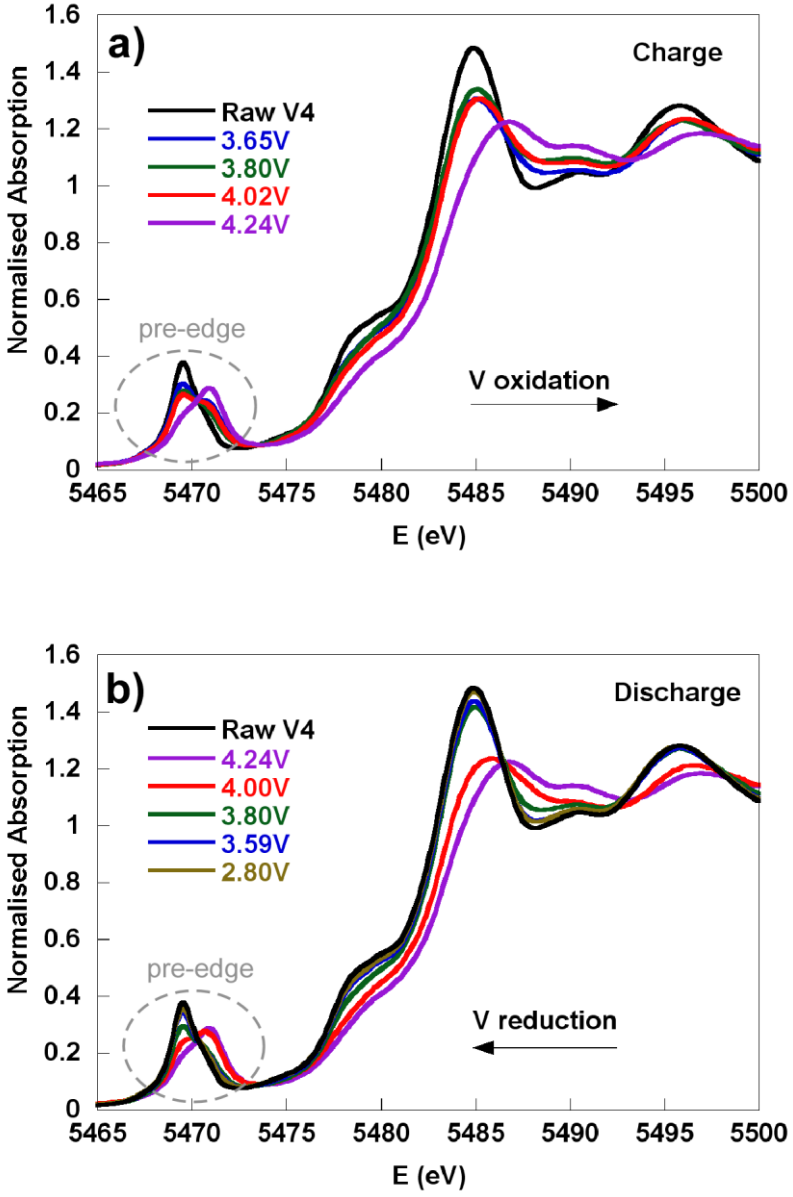

Figure 4.73 *Vanadium K-edge XANES spectra of the samples during the* ***a)*** *charge and* ***b)*** *discharge process.*

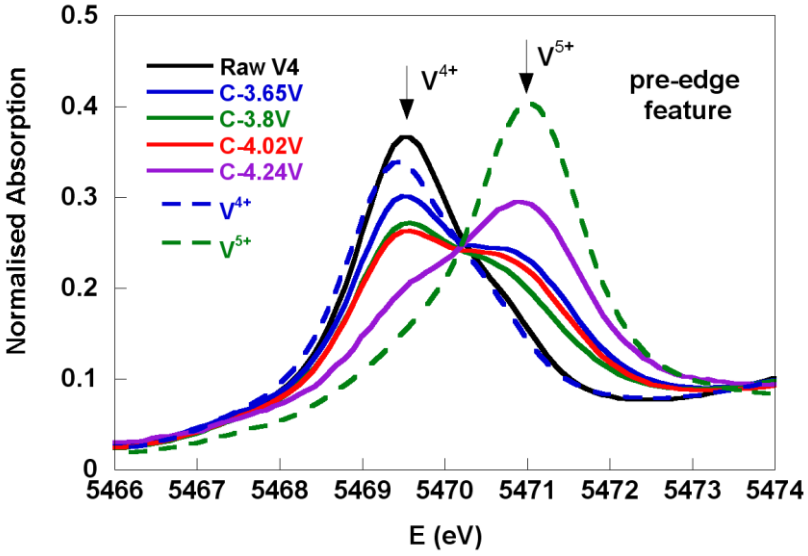

Figure 4.74 *Vanadium K-edge pre-edge feature of the raw V4 sample, the corresponding post mortem electrodes during charge (continuous line) and the standards (dashed lines). Arrows indicate the position of the peaks for V^{4+} and V^{5+}."C" indicates charge.*

To shed more light on the evolution of the vanadium valence during the oxidation/reduction process, the XANES spectrum of each sample was fitted using a linear combination of V^{4+} and V^{5+} standards. The V^{4+} standard sample is identical to the sample labelled "Raw V4" in Figure 4.73. For the sample with the highest V^{5+} content, "C-4.24V", the pre-edge and edge positions are well fitted, but there is some divergence in the post-edge region which is due to structural differences between $VOPO_4{\cdot}2H_2O$-V^{5+} standard and the "C-4.24V" sample (see Figure 4.75).

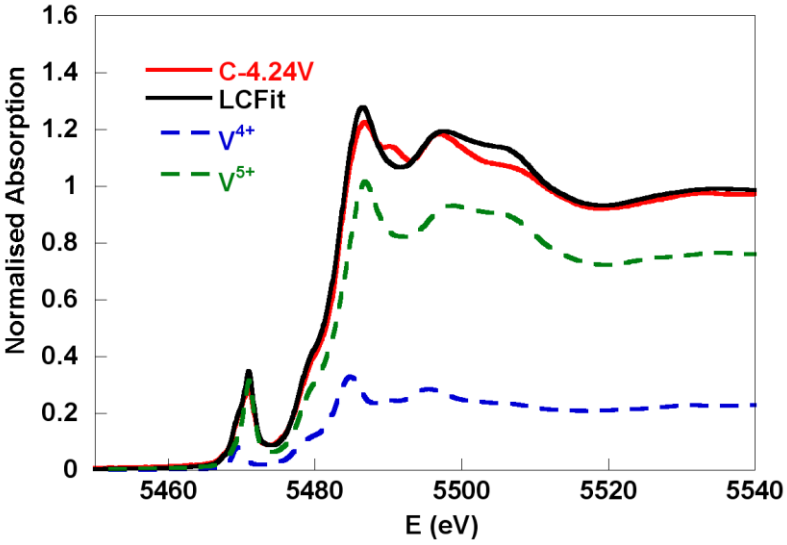

Figure 4.75 *XANES spectrum of the V4 sample equilibrated at 4.24 V during charge, and the corresponding fit considering a linear combination of V^{4+} and V^{5+} standards.*

An example of the fitting procedure is illustrated in Figure 4.76 (see Appendices for the rest of fittings), and using this procedure, the relative amount of each component or percentage of the V^{4+} and V^{5+} spectra (*e.g.,* vanadium oxidation state distribution) in the intermediate states are determined (Table 4.25).

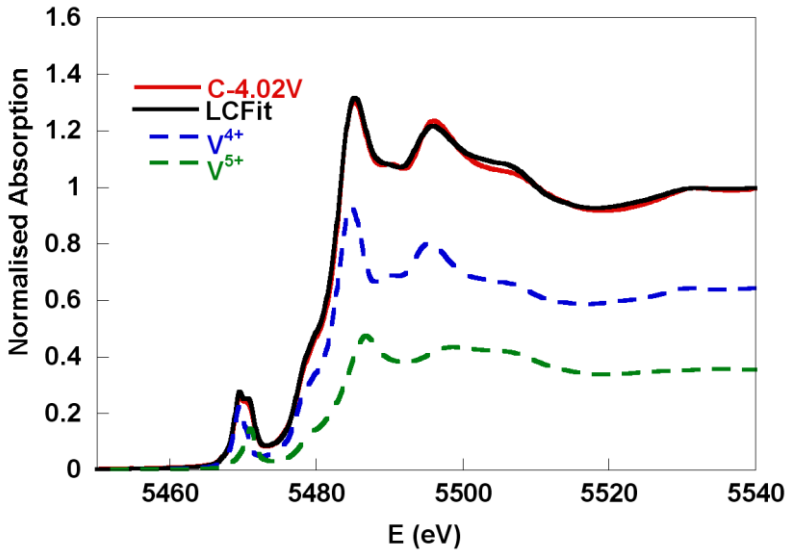

Figure 4.76 *XANES spectrum of the V4 sample equilibrated at 4.02 V during charge, and the corresponding fit considering a linear combination of V^{4+} and V^{5+} standards.*

Table 4.25 *Percentage of the V^{4+} and V^{5+} standard spectra used for fitting XANES data and the derived vanadium valence of each sample. "C" indicates charge and "D" indicates discharge.*

Sample	V^{4+} spectrum %	V^{5+} spectrum %	Vanadium valence (XANES)
Raw V4	100(5)	0(5)	4.0 (1)
C-3.65 V	70(5)	30(5)	4.3 (1)
C-3.80 V	75(5)	25(5)	4.3 (1)
C-4.02 V	64(5)	36(5)	4.4 (1)
C-4.24 V	23(5)	77(5)	4.8 (1)
D-4.00 V	43(5)	57(5)	4.6 (1)
D-3.80 V	84(5)	16(5)	4.2 (1)
D-3.59 V	94(5)	6(5)	4.1 (1)
D-2.80 V	99(5)	1(5)	4.0 (1)

The XANES results show that during the charge/discharge process, the average vanadium valence first increases from V^{4+} to $V^{4.8+}$, and then decreases back to V^{4+}.

4.3.2 *In-situ measurements*

4.3.2.1 *In-situ synchrotron X-Ray Diffraction (XRD) for $Na_3V_2O_{2x}(PO_4)_2F_{3-2x}$ (x = 0.8)*

First, the X-ray diffractogram of the MV cathode assembled in the electrochemical cell before starting the charge process was registered. Rietveld refinements of the initial cathode structure of sample MV were based on the model proposed by Le Meins *et al.* [159] and the results observed for the raw material in the 4.3.1.1 section of the present work using the diffraction pattern of the cell before cycling. The cathode material adopts the expected tetragonal $P4_2/mnm$ symmetry with lattice parameters a = 9.06730(16), c = 10.6530(5) Å and has a sodium content of 2.60(12) with a slight preferential occupation of the Na(2) site of 0.80(4) *vs.* 0.50(6) for the Na(1) site. Figure 4.77 shows the Rietveld refined fit of the initial structural model to the synchrotron XRD pattern of the cell after one cycle offline and 8 days storage at the beginning of the *in-situ* synchrotron XRD experiment. Table 4.26 presents the obtained crystallographic data for this structure.

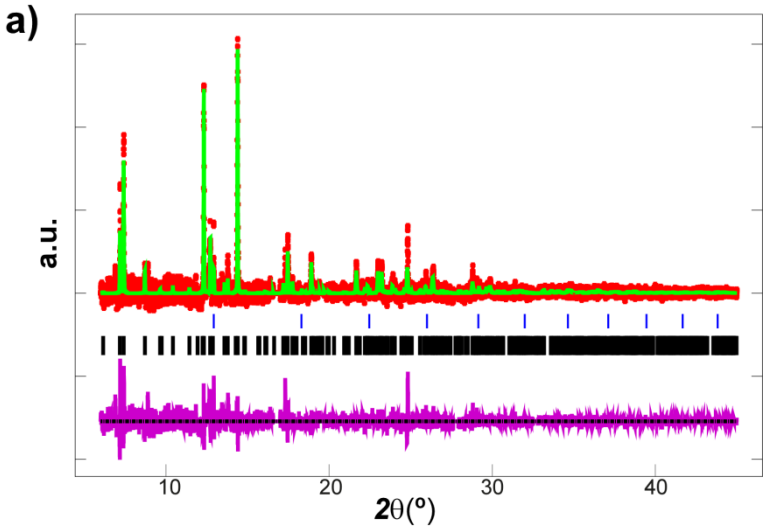

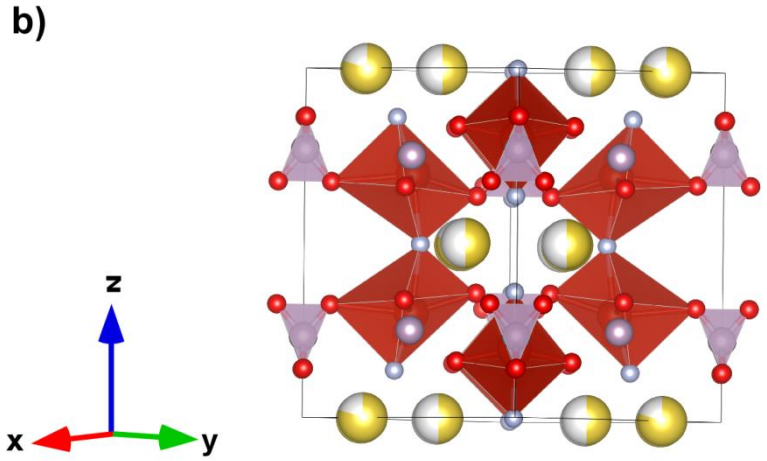

Figure 4.77 ***a)*** *Rietveld refinement of the $Na_3V_2O_{2x}(PO_4)_2F_{3-2x}$ model to the synchrotron XRD data of the MV cell before in-situ cycling. Data are shown as crosses, the calculated Rietveld model as a line through the data, and the difference between the data and the model as the line below the data. The vertical reflection markers are for $Na_3V_2O_{2x}(PO_4)_2F_{3-2x}$* ***b)*** *Crystal structure of MV with PO_4 shown in purple and VO_4F_2 in red. Oxygen is red, fluorine is light blue and sodium is yellow with the shading indicating occupancy.*

Table 4.26 *Refined crystallographic parameters for MV cathode at the beginning of the in-situ experiment.*

$P4_2/mnm$, a = 9.06730(16) Å, c = 10.6530(5) Å; Na content: 2.60(12)

Atom	*x*	*y*	*z*	Site Occupancy Factor	Isotropic Atomic Displacement Parameter (× 100)/Å²
Na(1)	0.5562	0.20262	0	0.50(5)	1.60(23)
Na(2)	0.72933	0.01458	0	0.80(4)	2.40(14)
V(1)	0.242(2)	0.242(2)	0.1979(7)	1	2.70(40)
P(1)	0	0.5	0.25	1	3.60(12)
P(2)	0	0	0.232(4)	1	3.80(12)
O(1)	0.124(3)	0.399(3)	0.162(2)	1	0.10(5)
O(2)	0.088(3)	0.088(3)	0.139(4)	1	0.10(5)
O(3)	0.436(3)	0.436(3)	0.176(4)	1	0.10(5)
F(1)	0.222(3)	0.222(3)	0	1	0.50(7)
F(2)	0.281(2)	0.281(2)	0.362(2)	1	0.50(7)

χ^2= 1.32, R_p = 2.70 %, wRp = 3.61 %

Structural analysis of the cell at the beginning of the *in-situ* experiment shows a sodium distribution different to the previously observed for the raw MV material (see Table 4.20 in section 4.3.1.1) which shows preferential Na(1) site occupation, while the MV cell shows sodium preferentially located on the Na(2) site. This rearrangement of sodium may be due to extended storage or the potentiostatic step applied in the first offline cycle. The total sodium content, 2.60(12), also illustrates a decrease with respect to the raw MV material, 3.04(3) (see Table 4.20 in section 4.3.1.1), probably due to cathode preparation process (material heating, pressing, *etc*.) or by some sodium interchange due to the contact with electrolyte in the half cell.

Time-resolved *in-situ* synchrotron XRD data provides a detailed reaction mechanism evolution of the MV electrode during a charge/potentiostatic hold/discharge. The overall reaction evolution is represented in Figure 4.78.

The reaction evolution undergoes a first solid solution stage followed by a two-phase region and a subsequent solid solution region until the end of the charge process. For the discharge, similar behaviour is observed.

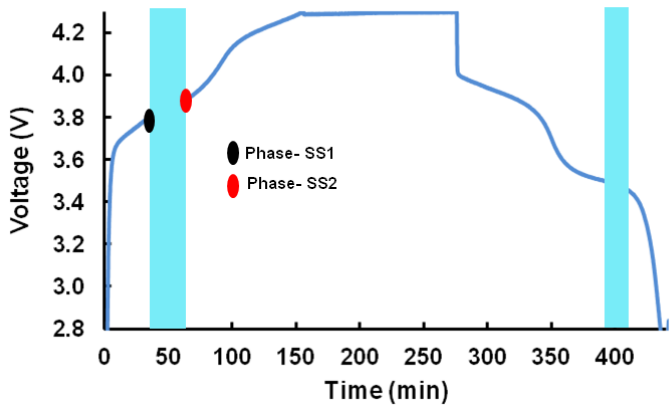

Figure 4.78 *The reaction mechanism evolution of the $Na_{3-y}V_2O_{2x}(PO_4)_2F_{3-2x}$ ($x = 0.8$) electrode during charge/potentiostatic hold/discharge with blue shading indicating two-phase processes.*

Figure 4.79 shows the evolution of (220), (113) and (222) reflections. As can be seen, two-phase regions appear where the two reflections coexist.

Charge of the MV cell begins with a solid solution mechanism until the appearance of a second set of reflections corresponding to a similar structure with slightly smaller *a* and larger *c* lattice parameters at a potential of ~3.7 V. This two-phase mechanism continues during the first *plateau*-like feature until 3.9 V where the second phase becomes dominant and undergoes further sodium removal *via* a second solid solution reaction until the end of charge, corresponding mainly to the second *plateau*-like feature. On discharge the inverse mechanism is observed with a little delay in the start of the two-phase region that appears at 3.5 V.

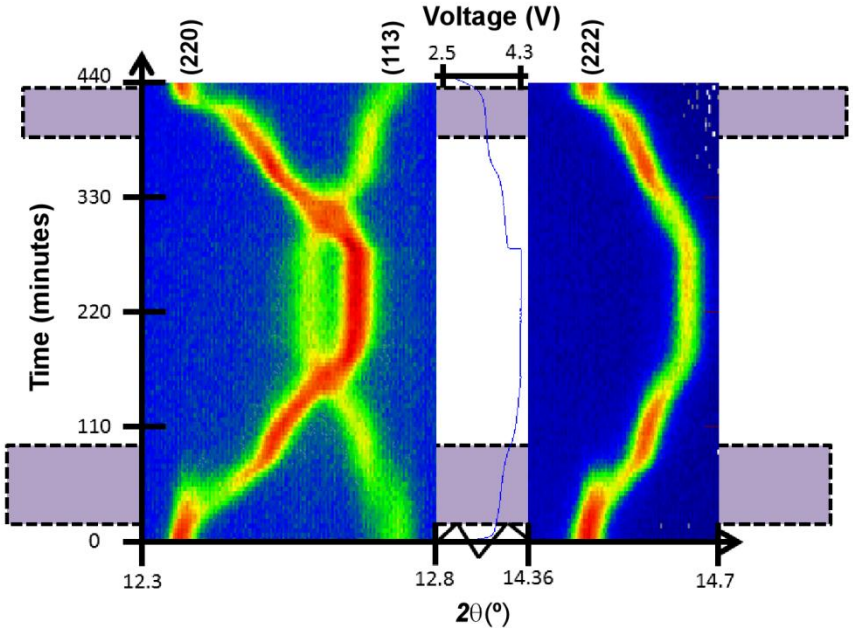

Figure 4.79 *Two-dimensional (2D) plots of the evolution of (220), (113) (left) and (222) (right) reflections by a colour scale vs. time and voltage during cycling of MV sample. Purple shaded areas mark two-phase regions where there are two sets of reflections.*

Individual diffraction patterns in Figure 4.80 show in more detail that in the two-phase

region, the (220) and (222) reflections undergo a transfer of intensity from one phase to another and this latter reflection experiences a change in the 2θ value and hence a change in the lattice parameters during the two-phase region.

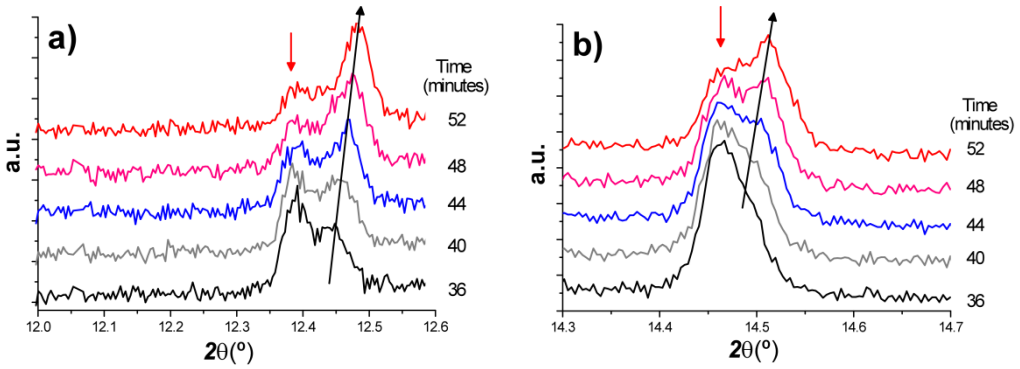

Figure 4.80 *Diffraction patterns from 36 to 52 minutes in the 2θ ranges of* ***a)*** *(220) and* ***b)*** *(222) reflection during cycling of MV sample.*

A closer look at the structures of the phase at the end of the initial solid solution region and the start of the second solid solution region (see Figure 4.78) can provide more information about the two-phase region in the charge mechanism.

Table 4.27 displays crystallographic parameters for these phases, the end of the first solid solution (named phase-SS1) and the start of the second solid solution region (named phase-SS2). Comparison of phase-SS1 and phase-SS2 structures reveals significant changes, but the overall symmetry is preserved. First, the lattice parameters change by 0.09896(46) and 0.0760(11) Å in *a* and *c* respectively, what leads to a *ca.* 1% change in lattice. Second, the sodium content decreases from 2.62 to 2.09, and the sodium site preference is switched between the first and second solid solution regimes. The first solid solution region shows dominant Na concentration on the Na(2) site and prevalent Na(1) occupation is found in the second solid solution region. This information indicates that the two-phase region is composed of a sodium-rich and a sodium-poor phase with approximate sodium ratios of 2.6 and 2.1, and that these compositions feature different distributions of sodium on the Na(1) and Na(2) sites. This phenomenon is observed in some Li-ion battery cathodes such as $LiCoO_2$ which shows regions of

two-phase behaviour with Li-rich and Li-poor variants, but both of which adopt the same crystal structure [166,167].

Table 4.27 *Crystallographic parameters for the cathode material at the end of the first solid solution region (phase-SS1) and the beginning of the second solid solution region (phase-SS2).*

Phase-SS1 - *P4₂/mnm*, *a* = 9.06024(20) Å, *c* = 10.6594(7) Å; Na content: 2.62(16))						
Phase-SS2 - *P4₂/mnm*, *a* = 8.96128(26) Å, *c* = 10.7354(4) Å; Na content: 2.09(9)						
Atom	***Phase***	***x***	***Y***	***z***	**Site Occupancy Factor**	**Isotropic Atomic Displacement Parameter (× 100)/Å²**
Na(1)	Phase-SS1	0.5562	0.20262	0	0.57(6)	2.10(23)
	Phase-SS2				0.683(33)	2.12
Na(2)	Phase-SS1	0.72933	0.01458	0	0.74(5)	1.30(14)
	Phase-SS2				0.364(31)	1.31
V(1)	Phase-SS1	0.2401(15)	0.2401(15)	0.1960(8)	1	2.70(40)
	Phase-SS2	0.2459(14)	0.2459(14)	0.1913(7)		3.30(40)
P(1)	Phase-SS1	0	0.5	0.25	1	4.70(13)
	Phase-SS2					3.30(13)
P(2)	Phase-SS1	0	0	0.235(5)	1	3.10(12)
	Phase-SS2			0.247(7)		7.10(19)
O(1)	Phase-SS1	0.1235(33)	0.3943(32)	0.1614(24)	1	0.60(50)
	Phase-SS2	0.121(4)	0.424(4)	0.162(4)		3.20(60)
O(2)	Phase-SS1	0.0847(30)	0.0847(30)	0.141(5)	1	0.60(50)
	Phase-SS2	0.101(5)	0.101(5)	0.178(6)		3.20(60)
O(3)	Phase-SS1	0.4345(32)	0.4345(32)	0.175(5)	1	0.60(50)
	Phase-SS2	0.417(4)	0.417(4)	0.140(5)		3.20(60)
F(1)	Phase-SS1	0.2202(34)	0.2202(34)	0	1	1.90(80)
	Phase-SS2	0.2755(33)	0.2755(33)			0.80(70)
"F(2)"	Phase-SS1	0.2807(27)	0.2807(27)	0.3636(25)	1	1.90(80)
	Phase-SS2	0.2877(21)	0.2877(21)	0.3579(22)		0.80(70)

Phase-SS1 - χ^2= 1.31, R_p = 2.72 %, wRp = 3.59 %
Phase-SS2' - χ^2= 1.31, R_p = 2.68 %, wRp = 3.55 %

The observation of the structures of phase-SS1 and phase-SS2 helps to understand why the transformation to the second solid solution occurs *via* a two-phase mechanism (Figure 4.81). As it can be seen, the phase-SS1 structure is highly distorted and presents relatively small channels in the (110) plane for the sodium ions, whilst phase-SS2 features channels that are more than 1 Å greater in F(1)-F(1) direction in (110) plane. Thus, to attain the structure that accommodates more facile Na-ion extraction

166 Sharma, N.; Peterson, V. K.; Elcombe, M. M.; Avdeev, M.; Studer, A. J.; Blagojevic, N.; Yusoff, R.; Kamarulzaman, N., *J. Power Sources,* **2010***, 195*, 8258-8266.

167 Takahashi, Y.; Kijima, N.; Tokiwa, K.; Watanabe, T.; Akimoto, J., *J. Phys.: Condens. Matter,* **2007***, 19*, 436202/1-436202/12.

requires the coexistence of these two phases, this way phase-SS2 develops at the expense of phase-SS1. The larger channels in phase-SS2 are likely to be more favourable for the facilitation of the solid solution reaction mechanism relative to phase-SS1.

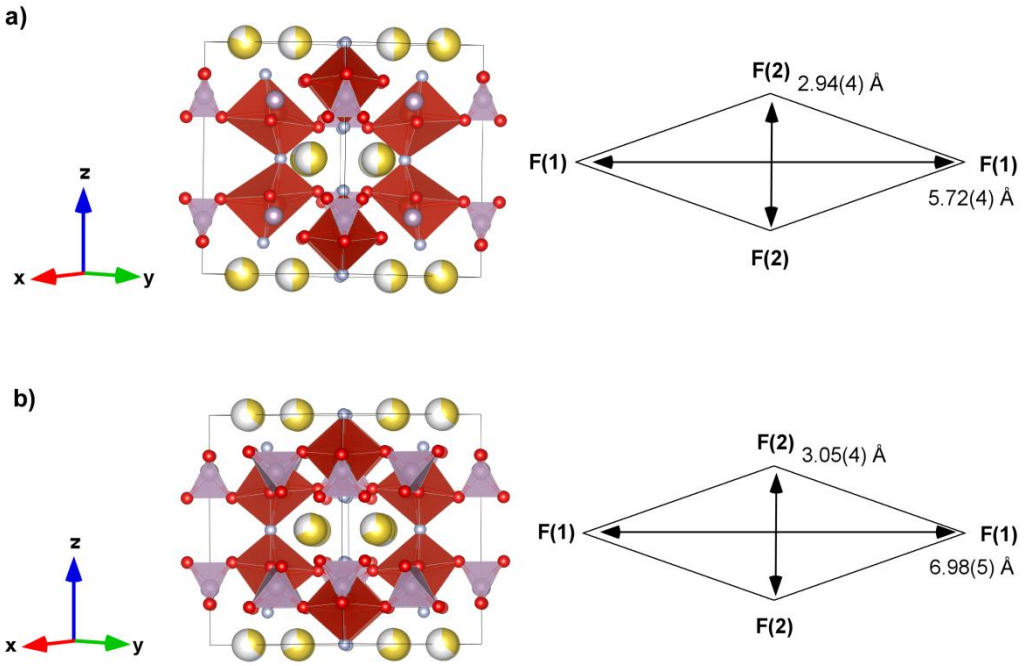

Figure 4.81 *Refined structures of **a)** phase-SS1 and **b)** phase-SS2. PO_4 are shown in purple and VO_4F_2 in red. Oxygen is red, fluorine is light blue and sodium is yellow with the shading indicating occupancy. Channel size in the (110) plane is indicated in the schemes on the right side.*

In order to analyse lattice evolution during the solid solution stages, different regions have been defined in the electrochemical reaction. Figure 4.82 shows these regions with the evolution of lattice parameters and unit-cell volume of the cathode as a function of time. Region 0 will not be commented due to the observation of minimal changes during this first solid solution region.

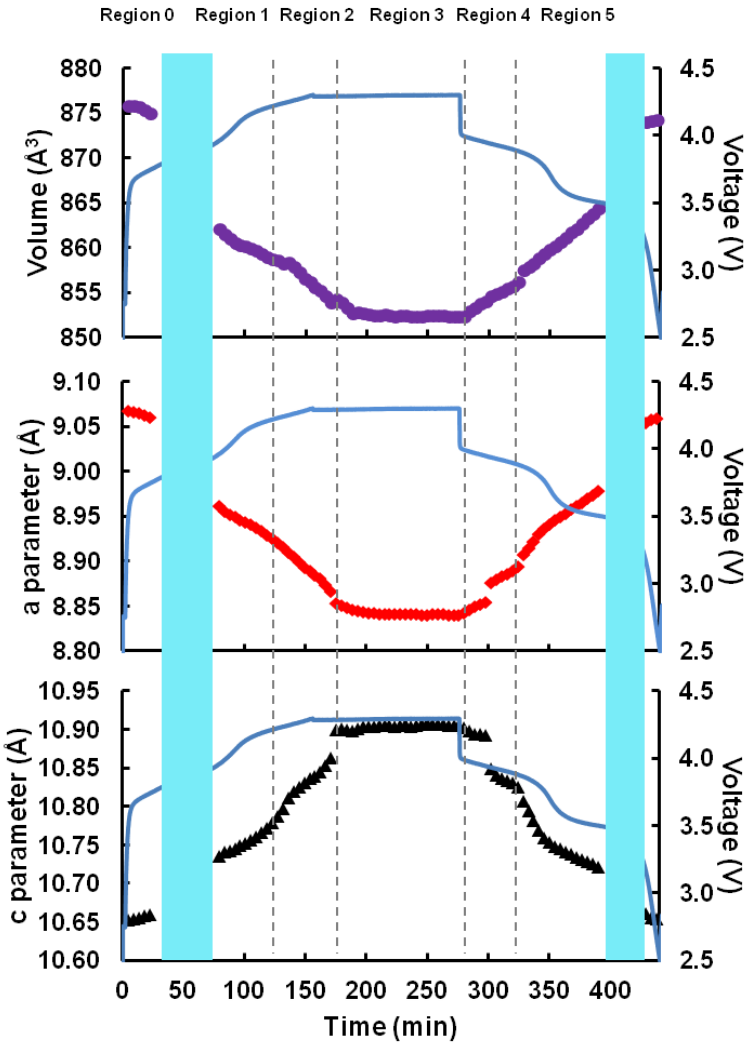

Figure 4.82 *Evolution of the lattice parameters and unit-cell volume of the MV cathode as a function of time, with the potential profile included. These parameters are derived from Rietveld refinements during solid solution type reactions. Regions are defined at the top and correspond to solid solution type reactions. Blue shaded areas represent the two-phase transitions as defined in Figure 4.78.*

The cathode structure clearly expands and contracts to accommodate the reversible extraction/insertion of sodium. During charge, contraction in *a* and expansion in *c* lattice parameters with overall volume decrease are registered. The inverse process is observed for discharge. However, these variations are not linear throughout the charge or discharge process, showing subtle changes in the rate of expansion and contraction, *e.g.*, the changes of the slope in *c* parameter at 135 and 346 minutes in Figure 4.82 (end of Region 1 and end of higher voltage *plateau* during discharge, respectively). Linear fits have been conducted in the different regions to gain an understanding of the kinetic evolution of the lattice (Table 4.28).

Table 4.28 *Rates of lattice parameter and volume change for the MV cell during the regions specified in the text and Figure 4.82. The rates are determined by slope of linear fits to the Rietveld-refined data in Figure 4.82.*

	Region 1 (charge)		**Region 2 (charge&pot.)**		**Region 3 (potentiostatic)**		**Region 4 (discharge)**		**Region 5 (discharge)**	
	Slope	R^2	Slope	R^2	Slope	R^2	Slope	R^2	Slope	R^2
Volume ($Å^3$/min)	-0.069(4)	0.97	-0.107(6)	0.97	-0.004(1)	0.57	0.090(4)	0.97	0.111(1)	0.99
c (Å/min)	0.00095(1)	0.97	0.0016(1)	0.99	0.00006(1)	0.63	-0.0020(1)	0.93	-0.0013(1)	0.90
a (Å/min)	-0.00076(2)	0.99	-0.00121(5)	0.99	-0.00008(1)	0.60	0.00126(7)	0.96	0.00111(4)	0.99

Comparison of the slopes (rate constants) in the different regions reveals that large changes are experienced between Region 1 and Region 2, which suggests that the final sodium extraction processes lead to a more dramatic change in the lattice and volume of the cathode. Additionally, the volume contraction and lattice parameter fluctuations registered in Region 2 continue until approximately 25 minutes into Region 3, the potentiostatic step. The lattice and volume stabilises with minimal fluctuation for the remainder of the potentiostatic region. This potentiostatic step was designed to ensure the structure had reached equilibrium at 4.3 V which is demonstrated by the decay in current; and also to ensure that the maximum possible amount of sodium was extracted at 4.3 V. Structural data extracted from the Rietveld analysis of the 'equilibrium structure' at 4.3 V during the potentiostatic step are displayed in Table 4.29 and the structure is plotted in Figure 4.83.

Table 4.29 *Cathode structure at the 4.3 V charged state during the potentiostatic step.*

***P4₂/mnm*, *a* = 8.84081(18) Å, *c* = 10.9043(6) Å; Na content: 0.77(4)**

Atom	*x*	*y*	*z*	Site Occupancy Factor	Isotropic Atomic Displacement Parameter (× 100)/Å²
Na(1)	0.5562	0.20262	0	0	2.12
Na(2)	0.72933	0.01458	0	0.377(21)	1.31
V(1)	0.2459(14)	0.2459(14)	0.1913(7)	1	3.90(40)
P(1)	0	0.5	0.25	1	5.50(13)
P(2)	0	0	0.275(4)	1	2.30(15)
O(1)	0.120(5)	0.416(4)	0.1681(27)	1	1.40(60)
O(2)	0.101(5)	0.101(5)	0.161(5)	1	1.40(60)
O(3)	0.402(4)	0.402(4)	0.127(4)	1	1.40(60)
F(1)	0.262(6)	0.262(6)	0	1	5.00(80)
F(2)	0.268(4)	0.268(4)	0.3462(19)	1	5.00(80)

χ^2= 1.35, R_p = 2.68 %, wRp = 3.67 %

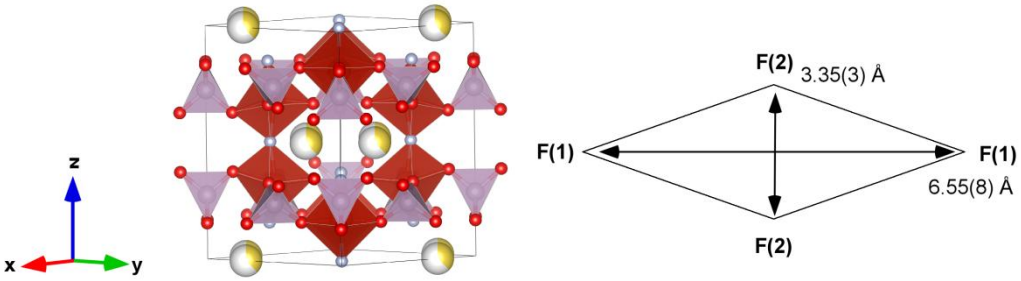

Figure 4.83 *Crystal structure of the MV cathode at the 4.3 V charged state during the potentiostatic step. PO_4 are shown in purple and VO_4F_2 in red. Oxygen is red, fluorine is light blue and sodium is yellow with the shading indicating occupancy. Channel size in the (110) plane is indicated in the scheme.*

It can be seen that sodium occupancy equates out to zero on the Na(1) site and averages to 0.38(2) on the Na(2) site, leading to a composition of $Na_{0.77(4)}V_2O_{2x}(PO_4)_2F_{3-2x}$ (x = 0.8). Indicative changes can be observed by comparing the bond distances of the starting MV material and the phase during potentiostatic step. Table 4.30 displays the bond distances inside the vanadium coordination polyhedron for these two phases. Shortening of all V-anion bond lengths is a clear indication of an increase of the vanadium oxidation state.

Table 4.30 *Bond distances inside the vanadium coordination polyhedron for the starting MV material and the phase in the potentiostatic step.*

Bond	Bond distance for starting MV material (Å)	Bond distance in the potentiostatic step (Å)
V-O(1)	1.989(8)	1.88(4)
V-O(2)	1.989(8)	1.81(6)
V-O(3)	1.98(1)	2.05(5)
V-F(1)	2.075(1)	2.00(1)
V-F(2)	1.741(4)	1.81(2)

On the other hand, evolution of sodium in the MV cell at the Na(1) and Na(2) sites is shown in Figure 4.84. Region 0 will not be commented due to the observation of minimal changes during this first solid solution region in charge.

The final state of the MV electrode effectively retains the same sodium occupation and distribution that at the beginning of the *in-situ* measurement, highlighting the reversibility at the atomic scale of this cathode material. Unlike *ex-situ* synchrotron XRD analysis on the raw MV powder (see Table 4.20 in section 4.3.1.1), the sodium distribution over the Na(1) and Na(2) sites is reversed at both the initial state and final discharged state, with Na(2) showing higher occupancy than Na(1). It should be noted that the electrode in this coin cell has been cycled once offline and this distribution maybe a result of this first cycle and subsequent storage. The same regions used for lattice parameters rate analysis are used to study sodium evolution during charge/potentiostatic hold/discharge. Region 1 shows the continuous extraction of sodium from Na(2) site and virtually no change in the sodium occupancy of the Na(1) site. This results, as shown in Figure 4.82, in a linear change in the lattice as expected by Vegard's law for solid solution type behaviour with ion insertion/extraction from one crystallographic site. At the onset of Region 2 (135 minutes), corresponding to a more dramatic increase in the rate of change in the lattice parameters, the sodium extraction mechanism changes and most of the removal of sodium occurs from the Na(1) site (Figure 4.84). However, an increase in the Na(2) site occupancy indicates that some of the sodium that comes out of the Na(1) site is either placed on the Na(2) site or is removed from the structure *via* this site. This process effectively continues until Na(1) is empty and Na(2) contains all the sodium (~175 minutes), corresponding to the beginning of Region 3.

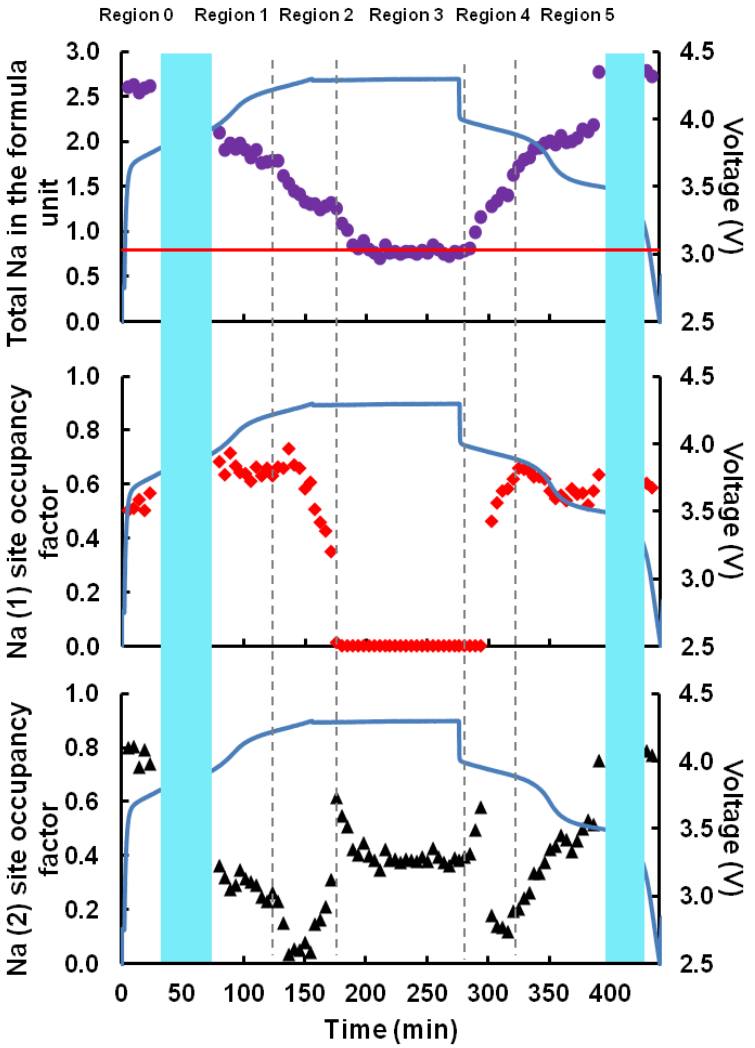

Figure 4.84 *Evolution of sodium occupancy between the sodium atomic sites Na(1) (red) and Na(2) (black) of MV cathode during function in a sodium-ion battery. The top panel contains the evolution of the total sodium content in the formula* $Na_{3-y}V_2O_{2x}(PO_4)_2F_{3-2x}$ *(x = 0.8) as a function of time and potential profile. Blue shaded areas represent the two-phase transitions, as defined in Figure 4.78.*

During the potentiostatic step, sodium is subsequently removed from the Na(2) site until an equilibrium sodium concentration is established with no further sodium extraction at 4.3 V (~225 minutes). In Region 4 sodium starts inserting on to the Na(2) site until it achieves a maximum occupation and then starts to reduce occupancy by concurrently moving or inserting onto the Na(1) site. The maximum occupation of 0.66(3) of Na(1) at the end of Region 4 is very similar to the Na(1) concentration in Region 1 during charge. Unlike charge where the Na(1) site maintains on average the 0.65(3) composition during Region 1, the Na(1) site occupancy drops slightly at the onset of Region 5 and seems to equilibrate on average at 0.56(3) (~335 minutes), lower than Region 1. During Region 5, sodium insertion occurs mostly on the Na(2) site which gradually increases in content while Na(1) is effectively constant. Thus, during discharge, the Na(1) site reaches a maximum value, so sodium insertion needs to occur on the Na(2) site and at a certain point in discharge both sites cannot handle any more sodium, so a two-phase process is initiated (~400 minutes).

The crystal structure of the cathode at the end of solid solution zone of Region 5 (~400 minutes) is detailed in Table 4.31 and illustrated in Figure 4.85. The channel dimension becomes too small along the *c* axis which drives the material to the subsequent two-phase transitions.

Table 4.31 Crystallographic parameters for the MV cathode material at the end of the lower voltage solid solution region (~400 minutes).

***P4₂/mnm*, *a* = 8.97847(27) Å, *c* = 10.7221(4) Å; Na content: 2.19(9)**

Atom	*x*	*Y*	*z*	Site Occupancy Factor	Isotropic Atomic Displacement Parameter (× 100)/Å²
Na(1)	0.5562	0.20262	0	0.58(4)	2.12
Na(2)	0.72933	0.01458	0	0.516(33)	1.31
V(1)	0.2473(16)	0.2473(16)	0.1969(7)	1	3.90
P(1)	0	0.5	0.25	1	1.74
P(2)	0	0	0.238(8)	1	9.76
O(1)	0.1241(30)	0.4276(30)	0.1653(31)	1	1.40
O(2)	0.104(4)	0.104(4)	0.168(5)	1	1.40
O(3)	0.4182(31)	0.4182(31)	0.153(5)	1	1.40
F(1)	0.261(6)	0.261(6)	0	1	5.45
F(2)	0.2827(23)	0.2827(23)	0.3645(22)	1	5.45

χ^2= 1.37, R_p = 2.77 %, wRp = 3.77 %

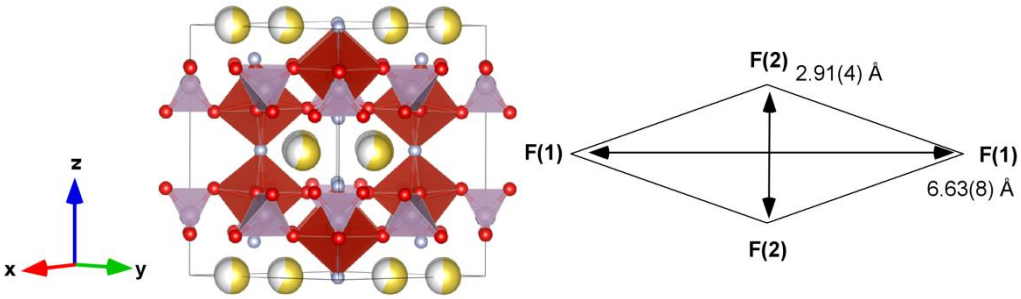

Figure 4.85 *Crystal structure of the MV cathode at the end of the lower voltage solid solution (~400 min). PO_4 are shown in purple and VO_4F_2 in red. Oxygen is red, fluorine is light blue and sodium is yellow with the shading indicating occupancy. Channel size in the (110) plane is indicated in the scheme on the right side.*

Figure 4.86 shows the site-specific occupancies and total sodium content for MV cell *vs.* specific capacity allowing direct comparison of the electrochemical capacity and the sodium atomic parameters. The cell exhibits a higher overall occupancy of the Na(1) site and lower occupancy of Na(2) sites throughout the electrochemical process except for the potentiostatic step. Besides, during this latter step the total sodium content in the cathode decreases below one, *i.e.,* 3-y < 1 (see Figure 4.86c) which would lead to a maximum extraction of sodium.

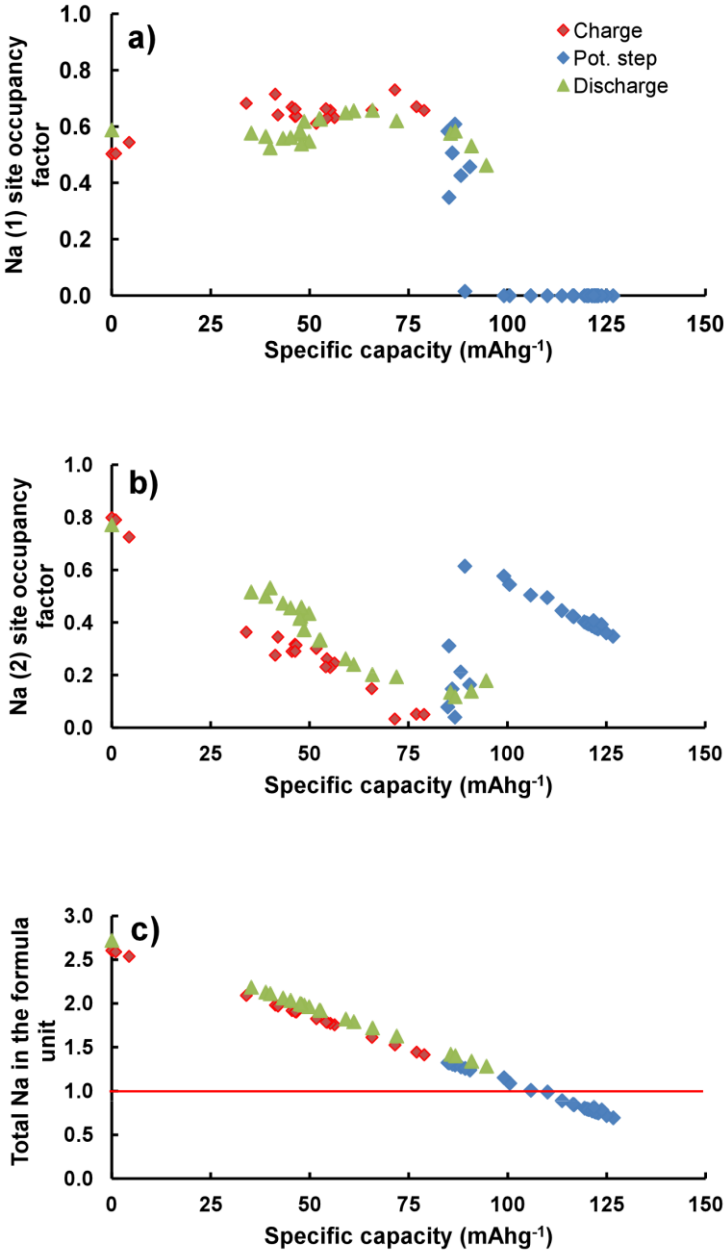

Figure 4.86 ***a, b)*** *Sodium occupancies and* ***c)*** *total content vs. specific capacity for the MV cell.*

The promise for this cathode material is the fact that the structure seems to be entirely reversible, even at the sodium distribution scale, and the majority of the charge/discharge process is a solid solution reaction. Besides, the total volume change between the two phases at the end of the first solid solution and the beginning of the second solid solution is ~ 1.5%.

4.3.2.2 In-situ synchrotron X-Ray Diffraction data (XRD) for $Na_3V_2O_2(PO_4)_2F$.

Time-resolved *in-situ* synchrotron XRD data provides a detailed reaction mechanism evolution of the V4 electrode during a charge/potentiostatic hold/discharge. The overall reaction evolution is represented in Figure 4.87.

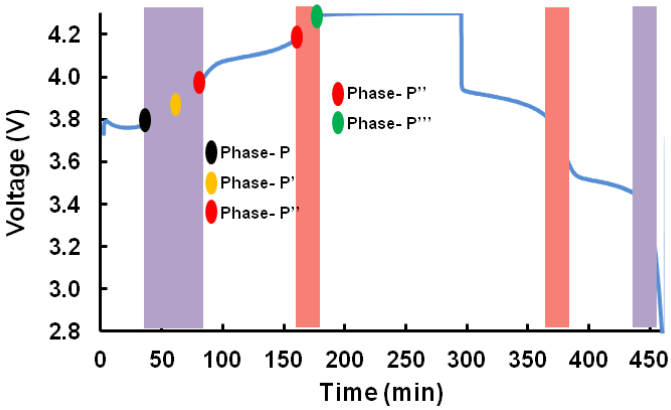

Figure 4.87 *The reaction mechanism evolution of the $Na_{3-y}V_2O_2(PO_4)_2F$ electrode during charge/potentiostatic hold/discharge with purple shading indicating two two-phase processes and red shading indicating two-phase behaviour.*

The reaction evolution undergoes a first solid solution stage until the appearance of a two two-phase region where there is a transition from a sodium-richer phase (named as P) to a sodium poorer phase (P' also referred to as the intermediate phase) and then, P' transforms in an even poorer sodium phase (P'') This two two-phase reaction continues until the beginning of the second voltage *plateau*-like feature were undergoes further

removal of sodium from P'' *via* a second solid solution stage for the majority of the higher potential *plateau*-like feature. Near the charged state, appears a new two-phase region where there is a transfer from a sodium-richer phase (P'') to a sodium-poorer phase (P'''). Overall in the charge process $Na_{3-y}V_2O_2(PO_4)_2F$ undergoes a two two-phase transition, followed by a solid solution region, before a final two-phase transition. Discharge proceeds *via* the same combination of solid solution-bipashic regions. However, it is significally asymmetric because the two-phase transition observed at the end of charge is not observed until halfway through discharge, *i.e.,* it is delayed. The low voltage two-phase behaviour is equally repeated.

Figure 4.88a presents the evolution of (220), (113) and (222) reflections during cycling. The 2D plot from Figure 4.88b (marked with a circle in Figure 4.88a) shows a region of three reflections coexisting (two two-phase region) during the first or lower potential *plateau*-like feature that merge during solid solution stages. A similar behaviour is observed for the two-phase region present at the end of charging process (Figure 4.88d (marked with a rectangle in Figure 4.88a)). Figure 4.88c evidences the existence of an intermediate phase P' while the presence of shoulders on all major reflections from Figure 4.88e confirms the presence of the two-phase region in the charge curve.

The use of high resolution *in-situ* data is essential to determine such a structural evolution in order to distinguish from a solid solution mechanism. It is interesting to note that $LiCoO_2$ cathodes in lithium-ion batteries feature a similar two-phase delithiation pathway from a lithium-rich ($Li_{0.93}CoO_2$) to a lithium-poor ($Li_{0.75}CoO_2$) compound [166,167]. Another notable similarity is the recent observation of an intermediate phase in the delithiation of $LiFePO_4$ to $FePO_4$ at high current rates (10C) [168]. In V4 cathode during charge, there are multiple two-phase reactions involved over the course of the lower potential *plateau*-like feature.

168 Orikasa, Y.; Maeda, T.; Koyama, Y.; Murayama, H.; Fukuda, K.; Tanida, H.; Arai, H.; Matsubara, E.; Uchimoto, Y.; Ogumi, Z., *J. Am. Chem. Soc.*, **2013**, 135, 5497-5500.

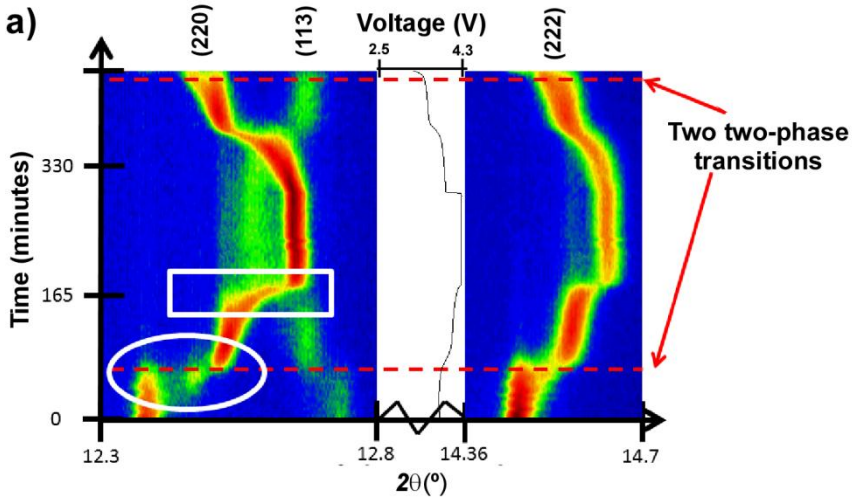
a)
(220)
(113)
Voltage (V)
2.5
4.3
(222)
Two two-phase transitions
Time (minutes)
330
165
0
12.3
12.8
14.36
14.7
2θ(º)

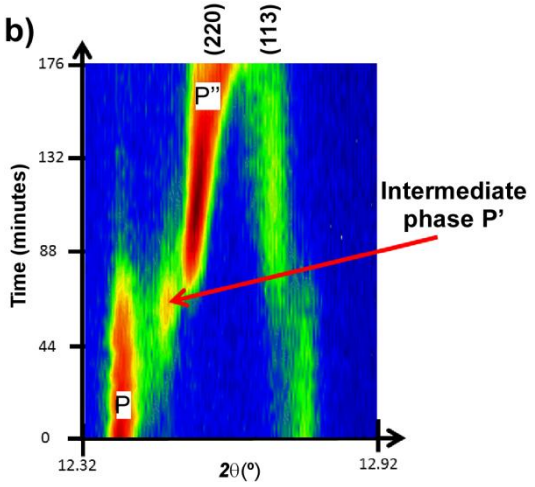
b)
(220)
(113)
176
132
88
44
0
Time (minutes)
P''
P
Intermediate phase P'
12.32
12.92
2θ(º)

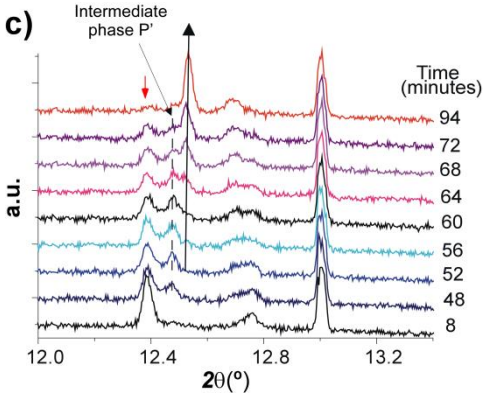
c)
Intermediate phase P'
Time (minutes)
94
72
68
64
60
56
52
48
8
a.u.
12.0
12.4
12.8
13.2
2θ(º)

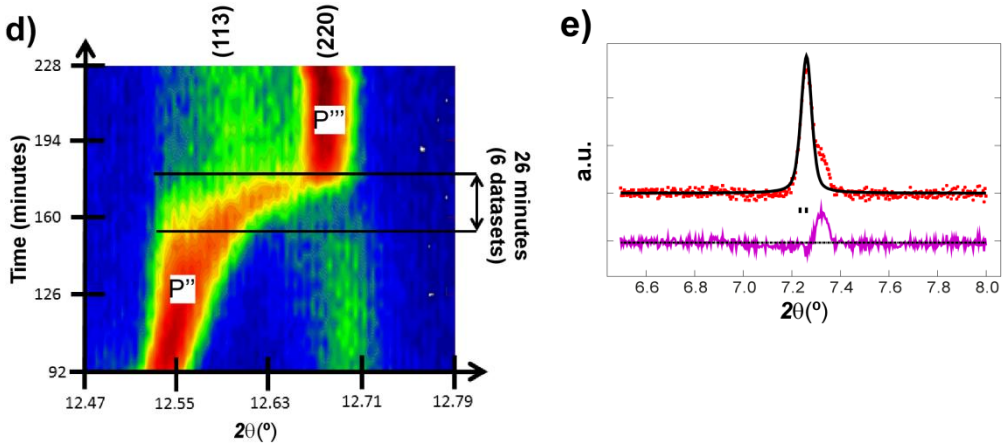

Figure 4.88 ***a)*** *Selected 2θ regions of in-situ synchrotron XRD data highlighting the evolution of the (220), (113) (left) and (222), (right) reflections by a colour scale and the potential profile.* ***b)*** *Selected (marked with a circle in a)) temporal region of in-situ data showing the two two-phase region and* ***c)*** *snapshots of the in-situ data of the (220) and (113) reflections with the phases P, P', P" shown.* ***d)*** *Selected (marked with a rectangle in a)) temporal region of in-situ data showing the two-phase region at higher charge of the (220) and (113) reflections with the phases P" and P"' shown.* ***e)*** *Rietveld refined fit of the $Na_{3-y}V_2O_2(PO_4)_2F$ model to the synchrotron XRD data in region $6.5 \leq 2\theta \leq 8.0$ º. Data are shown as crosses, the calculated Rietveld model as a line through the data, and the difference between the data and the model as the line below the data. The vertical reflection markers are for $Na_{3-y}V_2O_2(PO_4)_2F$.*

On the other hand, there is significant asymmetry in the reaction mechanism evolution between charge and discharge. The two-phase transition observed at the end of charge (P''-P''') does not appear until halfway through discharge (Figure 4.89). Thus, the higher potential *plateau*-like feature during discharge is a solid solution reaction mechanism, where it occurs the insertion of sodium into the sodium poor phase P''' leading to the delay of the two-phase transition on discharge. It seems that the phase formed at the end of charge (P''') is stable and can accommodate sodium trough a solid solution mechanism. After that, it needs to undergo a two-phase transition between the two

potential *plateaux* followed by a short solid solution region. Finally, a two two-phase reaction occurs leading back to the discharged state (see Figure 4.87).

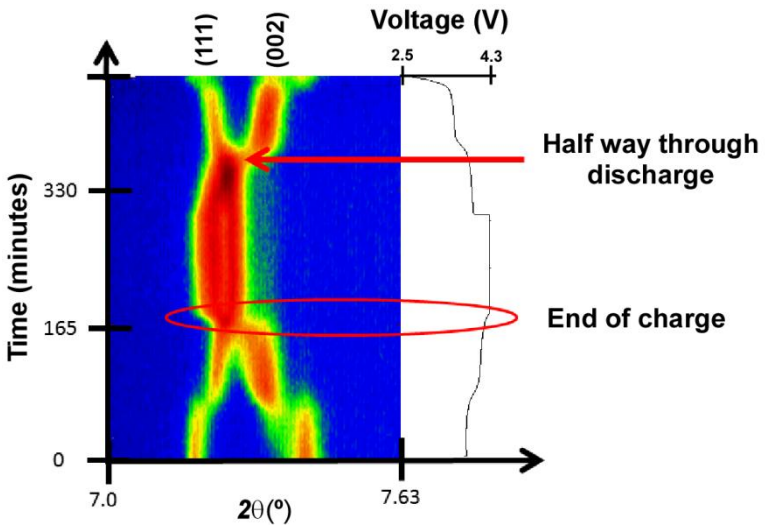

Figure 4.89 *Selected 2θ regions of in-situ synchrotron XRD data highlighting the evolution of the (111) and (002) reflections by a colour scale and the potential profile.*

Having qualitatively described the reaction mechanisms during charge/discharge, a more detailed description of the electrode behaviour concerning the lattice and sodium evolution is presented. Sequential Rietveld refinements in the solid solution regions allowed the tracking of both, the lattice and sodium evolution.

First, crystallographic details of phases P, P" and P"' are studied. P is referred to the starting electrode, P" to the electrode at the beginning of the solid solution on the higher potential *plateau*-like feature during charge (90 min. in Figure 4.87) and P"' to the 4.3 V charged electrode.

Table 4.32 shows crystallographic parameters of P, P" and charged P"' phases. The overall sodium content drops from 3.06(18) to 2.24(16) when moving from P to P", and there is a re-distribution of the location of the sodium from Na(1) site to Na(2).

Table 4.32 Crystallographic details of the phases belonging to P, P" and P"".

P - *P4₂/mnm*, a = 9.05506(17) Å, c = 10.6590(5) Å; Na content: 3.06(18)						
P" - *P4₂/mnm*, a = 8.95252(20) Å, c = 10.7623(6) Å; Na content: 2.24(16)						
P"" - *P4₂/mnm*, a = 8.84996(17) Å, c = 10.9144(6) Å; Na content: 1.24(13)						
Atom	***Phase***	***x***	***Y***	***z***	**Site Occupancy Factor**	**Isotropic Atomic Displacement Parameter (× 100)/Å²**
Na(1)	P	0.5091*	0.252*	0	0.93(6)	4.65*
	P"				0.44(5)	
	P""				0.42(4)	
Na(2)	P	0.794*	0.035*	0	0.60(7)	8.05*
	P"				0.68(6)	
	P""				0.20(5)	
V(1)	P	0.2531(16)	0.2531(16)	0.1996(7)	1	3.48*
	P"	0.2454(16)	0.2454(16)	0.1958(8)		
	P""	0.2411(15)	0.2411(15)	0.1807(8)		
P(1)		0	0.5	0.25	1	4.97*
P(2)	P	0	0	0.267(4)	1	3.86*
	P"			0.258(6)		
	P""			0.2900(30)		
O(1)	P	0.082(4)	0.3865(32)	0.1659(30)	1	1.29*
	P"	0.071(4)	0.3750(30)	0.1569(34)		
	P""	0.099(4)	0.412(4)	0.1555(30)		
O(2)	P	0.087(4)	0.087(4)	0.186(5)	1	1.29*
	P"	0.090(4)	0.090(4)	0.187(4)		
	P""	0.101(4)	0.101(4)	0.153(5)		
O(3)	P	0.394(4)	0.394(4)	0.1309(35)	1	1.29*
	P"	0.396(4)	0.396(4)	0.148(5)		
	P""	0.3750(29)	0.3750(29)	0.139(4)		
F(1)	P	0.2712(32)	0.2712(32)	0	1	1.41*
	P"	0.279(4)	0.279(4)			
	P""	0.270(4)	0.270(4)			
"F(2)"	P	0.245(4)	0.245(4)	0.3534(25)	1	7.54*
	P"	0.263(4)	0.263(4)	0.3477(27)		
	P""	0.2256(33)	0.2256(33)	0.3288(29)		

*Refined and fixed

P - χ^2= 1.25, R_p = 2.70 %, wRp = 3.61 %

P" - χ^2= 1.26, R_p = 2.60 %, wRp = 3.39 %

P"" - χ^2= 1.26, R_p = 2.55 %, wRp = 3.35 %

There is also a change in sodium site preference when comparing P" at 90 minutes, and P"" at 200 minutes (Figure 4.87). The Na(1) site shows higher occupancy than the Na(2) site for phase P"" and the overall sodium content drops to 1.24(13). Some authors as Tsirlin *et al.* [148] have reported the re-distribution of Na ions as a function of temperature in the "α" polymorph of $Na_3V_2O_2(PO_4)_2F$ phase. The sodium-ion interchange between the two crystallographic sites, as well as out of these sites, is an important factor in determining the overall performance of the cathode.

The change in sodium content per formula unit from the discharged state (P), 3.06(18), to charged 4.3 V state (P'''), 1.24(13), is 1.82(22). The charged composition of $Na_{1.24(13)}V_2O_2(PO_4)_2F$ corresponds to a vanadium valence of 4.88(7)+ which is extremely close to the maximum possible amount of sodium extraction from this electrode based on the $V^{4+/5+}$ redox couple.

The lattice evolution and rates of structural change are important to establish what happens to the structure of the cathode. In order to deeply analyse these parameters, the evolution is divided into regions. Figure 4.90 shows the lattice and unit-cell volume evolution of the V4 cathode as a function of charge and discharge. In terms of potential, Region 1 corresponds to the first charge *plateau*-like feature, Region 2 to most of the second charge *plateau*-like feature, Region 3 to the potentiostatic step, Region 4 to the first discharge *plateau*-like feature and Region 5 to the second discharge *plateau*-like feature.

Table 4.33 shows the rates of change of the lattice and unit-cell volume during each region. The V4 cathode structure expands and contracts to accommodate the reversible extraction/insertion of sodium. During charge, *a* lattice parameter decreases while *c* increases with overall volume decrease. The inverse process is observed for discharge. Differences in the rate of change of the lattice and volume are almost negligible when moving from Region 1 to Region 2. However, during discharge, there is a 1.3-4 fold increase between Region 4 and 5 in the rate of change of the lattice and volume. These two regions (4 and 5) correspond to the higher and lower potential features during discharge respectively. Although these may indicate interesting rates of structural changes in adjacent regions in either a charge or discharge processes, it is interesting to compare the rates of change of the lattice and volume at processes occurring predominantly at the higher potential *plateau*-like feature (during charge and discharge), *i.e.,* comparison between Region 2 and Region 4. Region 4 (discharge higher potential *plateau*-like feature) shows a 2 fold increase in the rates of lattice and volume change when compared to Region 2 (charge higher potential *plateau*-like feature). The comparison of the remaining processes shows a combination of increases and decreases in the rates of lattice and volume change, *e.g.,* during discharge *a* lattice parameter increases while *c* decreases. Thus, these kinds of changes are related to the processes occurring in the battery while the remaining rates of change adjust presumably to minimise structural stress with the sodium extraction/insertion processes.

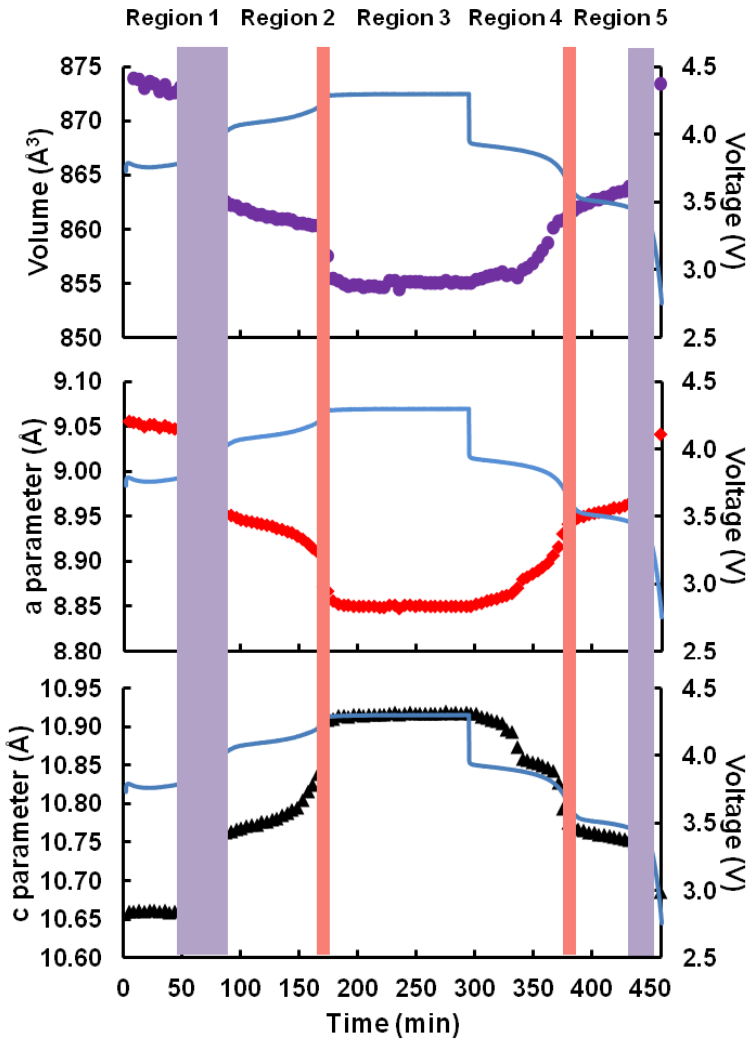

Figure 4.90 *Evolution of the lattice parameters and unit-cell volume of the V4 cathode as a function of time, with the potential profile included. These parameters are derived from Rietveld refinements during solid solution type reactions. Regions are defined at the top and correspond to solid solution type reactions. Purple shaded areas represent the two two-phase transitions and the red shaded areas represent the other two-phase transition, as defined in Figure 4.87.*

Table 4.33 *Rates of lattice parameter and volume change of the V4 cathode during the Regions specified in the text and Figure 4.90. The rates are determined by slope of linear fits to the Rietveld-refined data in Figure 4.90.*

	Region 1 (charge)		Region 2 (charge)		Region 3 (potentiostatic)		Region 4 (discharge)		Region 5 (discharge)	
	Slope	R^2	Slope	R^2	Slope	R^2	Slope	R^2	Slope	R^2
Volume ($Å^3$/min)	-0.027(5)	0.66	-0.027(1)	0.96	-0.002(1)	0.07	0.06(1)	0.71	0.047(2)	0.96
c (Å/min)	0.00003(2)	0.1	0.00061(5)	0.89	0.00044(6)	0.67	-0.0014(1)	0.93	-0.00035(1)	0.98
a (Å/min)	-0.00015(3)	0.71	-0.00043(2)	0.95	-0.000003(4)	0 02	0.00084(5)	0.96	0.00035(1)	0.98

The structure of the stabilised cathode in the potentiostatic step at 4.3 V (P’’’) is shown in Figure 4.91 and the structural details are presented as the P’’’ sample in Table 4.32. The bond distances for the vanadium coordination polyhedron are summarized in the following Table 4.34 and compared to the ones belonging to the V4 starting material (Table 4.23).

Table 4.34 *Bond distances inside the vanadium coordination polyhedron for starting V4 material and the P’’’ phase in the potentiostatic step.*

Bond	Bond distance for starting V4 material (Å)	Bond distance for P’’’ (charged at 4.3 V) in potentiostatic step (Å)
V-O(1)	1.987(7)	1.98(3)
V-O(2)	2.02(1)	1.78(5)
V-O(3)	2.03(1)	1.74(4)
V-F(1)	2.123(1)	2.01(1)
V-“F(2)”	1.605(4)	1.63(3)

The vanadium coordination sphere bond lengths shown in Table 4.34 indicates that the V=O vanadyl bond is maintained, named as V-F(2) bond, and the V-O bonds of V-O(1) are shorter than the corresponding to starting V4 compound, showing an indication of the increase in the vanadium oxidation state. The major change is observed in the V-O(2) and V-O(3) bond lengths which drop from 2.02(2) and 2.03(1) to 1.78(5) and 1.74(4) Å respectively, illustrating a higher charge on the central vanadium atom. Vanadium features a flexible coordination environment and a large distribution of bond

lengths and bonds are available in the literature [169]. For V^{5+} octahedral, a rule of thumb definition for the existence of V=O bonds are bond lengths below 1.74 Å [170], which for the charged cathode indicates that some of the V-O bonds are transferred to V=O, *e.g.,* V=O(2) and V=O(3). It is likely that this occurs in a random or disordered manner in the structure, *e.g.,* some V-O(2) bonds showing single while others show double bond character.

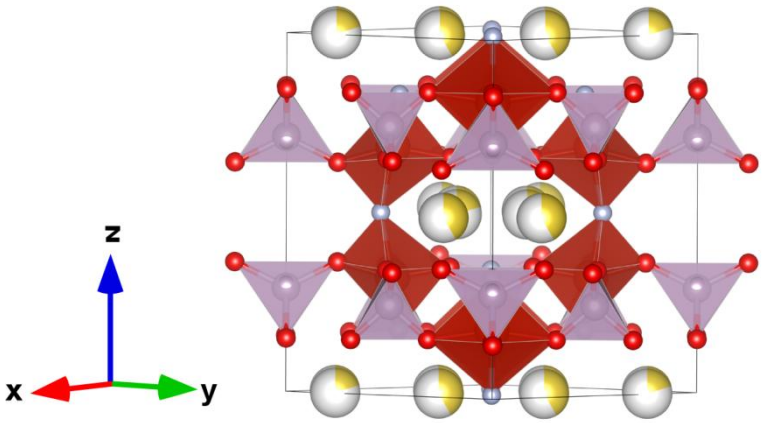

Figure 4.91 *The crystal structure of the cathode at the 4.3 V potentiostatically charged state (P''') – $Na_{1.24(13)}V_2O_2(PO_4)_2F$ with PO_4 shown in purple and VO_4F_2 in red. Oxygen is red, fluorine is light blue and sodium is yellow with the shading indicating occupancy.*

On the other hand, one of the most important aspects of cathode behaviour is how sodium is extracted and inserted. The time-resolved occupancy evolution of the sodium crystallographic sites as a function of charge/discharge sheds atomic-level insight on the cathode behaviour which is directly related to battery behaviour. Figure 4.92 shows the change in occupancy of the two sodium sites, Na(1) and Na(2), as a function of time during charge/potentiostatic hold/discharge. The observed fluctuations correspond to the refinement of the occupancies while sodium sites (atomic positions) remain fixed.

169 Schindler, M.; Hawthorne, F. C.; Baur, W. H. *Chem. Mater.,***2000**, 12, 1248-1259.

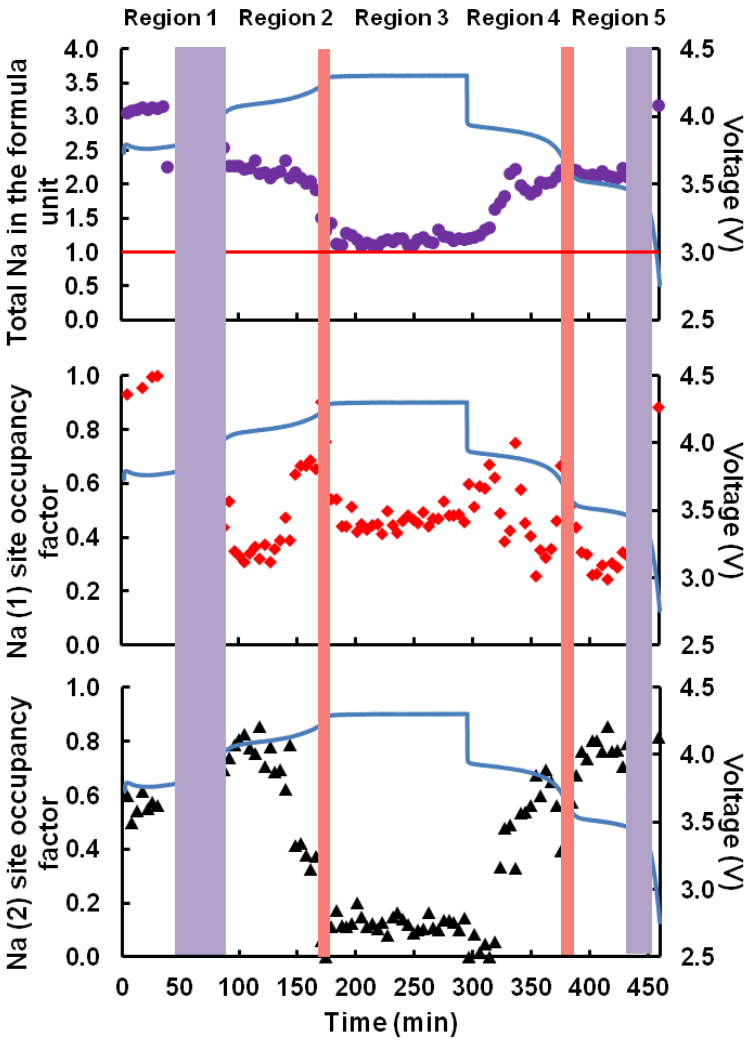

Figure 4.92 *Evolution of sodium occupancy between the sodium atomic sites Na(1) (red) and Na(2) (black) of V4 cathode during function in a sodium-ion battery. The top panel contains the evolution of the total sodium content in the formula* $Na_{3-y}V_2O_2(PO_4)_2F$ *as a function of time and potential profile. Purple shaded areas represent the two two-phase transitions and the red shaded areas represent the other two-phase transition, as defined in Figure 4.87.*

At the initial state of the cycle, the electrode inside the coin cell presents the same site occupancies and sodium content as the starting V4 material (see Table 4.24 in section 4.3.1.2), *i.e.*, full occupation of Na(1) site and half occupation of Na(2) resulting in a total sodium content of ~3. During Region 1 (Figure 4.92), even if the cell is cycling, there is no decrease in the sodium content and it remains almost constant. The same trend is observed from the small changes in the lattice parameters and volume from Region 1. Thus, this section would correspond to an unnoticeable solid solution of phase P.

During the two two-phase transition the total sodium content does not change. Then, during beginning of Region 2 (~90 minutes) the sodium content decreases due to the solid solution behaviour of phase P''. As shown in Table 4.32, there is a Na(2) site preference for P" compared to a Na(1) site preference for P in Region 1.

Between 90 and 150 minutes during Region 2, the Na(2) site occupancy increases reaching a maximum value before decreasing while the Na(1) site occupancy decreases and then stabilises until the end of Region 2 (Figure 4.92). The decrease of sodium content on Na(1) site and the increase in Na(2) site could indicate that sodium is extracted from Na(1) site trough Na(2) site. After that, a stable sodium content is obtained on the Na(1) site and further sodium extraction only occurs *via* the Na(2) site. At the end of Region 2 (~170 minutes) the sodium content on the Na(2) sites drops sharply and continues to drop to zero, possibly leading to the next two-phase transition. Sodium content increases on the Na(1) site resulting in a transfer of sodium from Na(2) to Na(1). The overall sodium content decreases with charging as expected, but the site occupancies show different behaviour.

At Region 3, in the potentiostatic step, the overall sodium content is 1.21(13) on average (Na (1) = 0.48(4) and Na (2) = 0.12(5)). The sodium content decreases from 1.51(7) to 1.25(14) within the 4.3 V potentiostatic step for over 20 minutes. The maximum amount of sodium is removed in this step and the electrode is close to equilibrium so that the capacity of the battery is directly affected.

During discharge, Between Region 4 and 5 there is a gradual decrease in the Na(1) site occupancy with a larger increase in the Na(2) site occupancy until the appearance of the two-phase region where a sharp change of the tendency of both sites occurs. Then,

the process is reversed and Na(1) and Na(2) behaves again as in the beginning of Region 4 (~320 minutes), that is, rapidly increasing in Na(2) site occupancy and a rapidly decreasing in Na(1) site. The quick switching of sodium content between the Na(1) and Na(2) sites corresponds to the pronounced changes in the lattice and volume parameters associated with the two-phase transition.

On the lower potential discharge *plateau*-like feature at Region 5, something similar to the beginning of Region 2 (~90-150 minutes) happens with the sodium distribution. Na(2) site occupancy increases reaching a maximum in Na(2) and minimum in Na(1) occupancy and then Na(2) decreases while Na(1) occupancy increases. The occupancy of Na(2) continues to drop below the occupancy of Na(1) which continues to increase resulting the site occupancies of Na(1) = 1, Na(2) = 0.44(6) at the discharged state, similar to the occupancies prior to cycling (Table 4.24 in section 4.3.1.2), corresponding again to the beginning of Region 1.

It seems that the use of a potentiostatic step under the conditions used in this work does not influence the charging process but it leads to some differences during discharge consistent with the rates of lattice and volume change. However, the completely discharged states appear to have similar sodium content, distribution and lattice parameters, suggesting that the charge process would restart from the same cathode situation.

Figure 4.93 shows the site-specific occupancies and total sodium content for V4 cell *vs.* specific capacity allowing direct comparison of the electrochemical capacity and the sodium atomic parameters. The V4 cell exhibits a lower overall occupancy of the Na(1) site and higher occupancy of Na(2) sites during both, charge and discharge. During the potentiostatic step, an overall Na(1) site preference is observed.

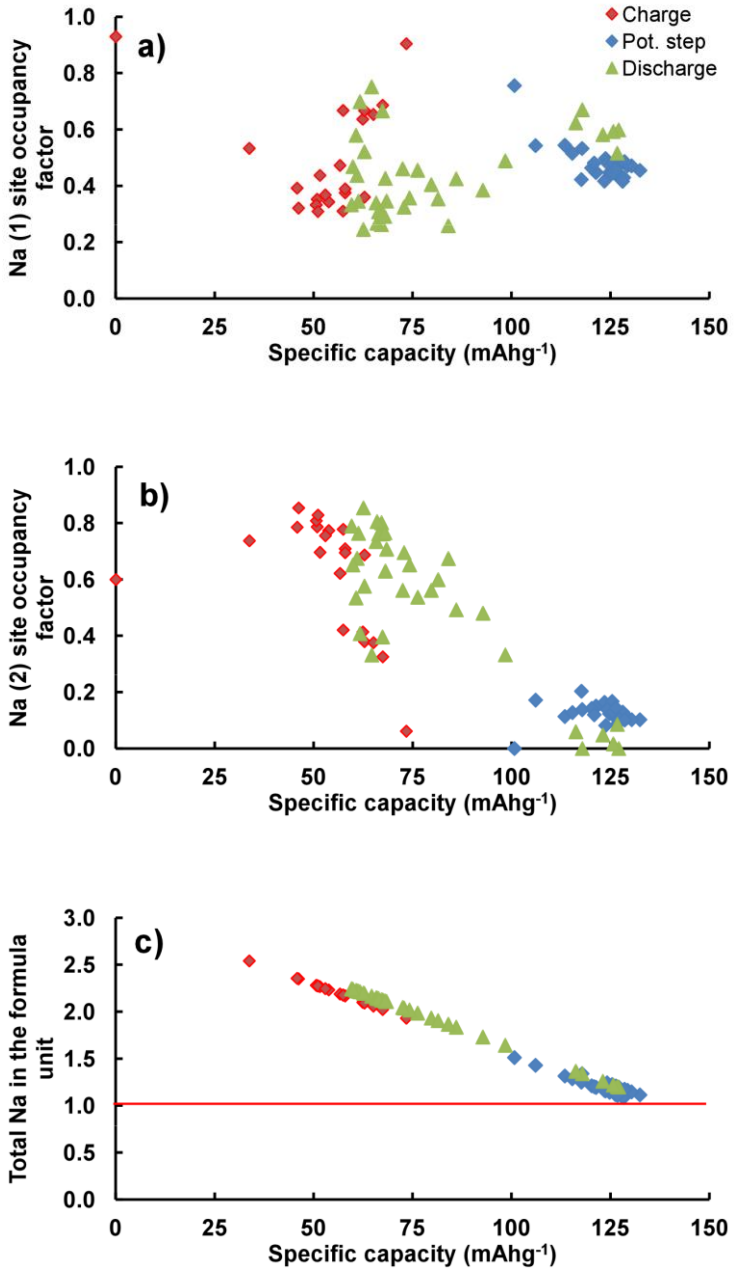

Figure 4.93 ***a, b)*** *Sodium occupancies and* ***c)*** *total content vs. specific capacity for the V4 cell.*

4.3.2.3 Comparison between $Na_3V_2O_{2x}(PO_4)_2F_{3-2x}$ (x = 0.8) and $Na_3V_2O_2(PO_4)_2F$ cathode evolution

Structural changes and electrochemical sodium extraction/insertion mechanism have been studied for two different starting materials: MV ($Na_3V_2O_{2x}(PO_4)_2F_{3-2x}$ (x =0.8)) and V4 ($Na_3V_2O_2(PO_4)_2F$). In both cases an offline cycle has been performed prior to a charge/potentiostatic hold/discharge cycling procedure. However the offline cycle of the MV sample consisted on a charge/potentiostatic hold/discharge and 8 days storage while in the case of sample V4 only a charge/discharge cycle and one day storage was applied. For this reason, due to the different conditions of the offline cycling, the possible comparison between the behaviour of these two materials would be for guidance only.

Both materials, MV and V4, show a very similar reaction mechanism. There is an initial solid solution, followed by a (two) two-phase region and a second solid solution transition. Besides, cycling of V4 cathode presents another biphasic zone after the second solid solution. During discharge, V4 presents the same processes but there is a delay in the appearance of the biphasic zone so the high voltage *plateau*-like feature shows a mainly solid solution transition.

Analysis of the lattice parameters and sodium evolution during electrochemical cycling demonstrates that the use of a potentiostatic step has an influence on subsequent discharge for both, MV and V4 based cathode materials. However, this step affects in a different way the two materials. For example, the potentiostatic step in the cell of MV compound may act to stabilise the charged structure so during initial discharge a slower rate of change in lattice parameters and volume is observed. In addition, the total volume change between the two phases at the end of the first solid solution (phase-SS1) and the beginning of the second one (phase-SS2) is ~1.5%. Something similar occurs for phases P, P'' and P''' analysed during the charge process for V4 cathode, where a ~1% of volume change is observed between them.

Concerning the sodium extraction, the minimum sodium content registered for the MV material is 0.77(4), while the amount of sodium for V4 phase is considerably higher; *i.e.,* 1.51(7) before the potentiostatic step and 1.25(14) after it. This indicates that, the $V^{3.8+}$ MV material provides a higher capacity due to the extraction/insertion of more sodium

compared to the V^{4+} phase. This could be related to the higher conductivity of $V^{3.8+}$ MV phase provided by both, the *in-situ* carbon content obtained when synthesising the material and the presence of V^{3+} in the sample. Another possibility would be that the V^{3+} present in the mixed valence $V^{3.8+}$ phase would be electrochemically active. Thus, its participation would lead to the $V^{3.8+}/V^{5+}$ redox reaction, so 2.4 sodium per formula unit ($Na_3V_2O_{2x}(PO_4)_2F_{3-2x}$ (x =0.8)) could be extracted as reported by Park *et al.* [145,146]. However, the real oxidation state of vanadium is hardly verified in literature and, as $Na_3V_2(PO_4)_2F_3$, $Na_3V_2O_2(PO_4)_2F$ and mixed valence $Na_3V_2O_{2x}(PO_4)_2F_{3-2x}$ ($0 < x < 1$) phases present very similar voltage *plateaux*, it is difficult to determine which of these phases is presented. In our case, the study of a V^{3+} rich phase would be necessary in order to confirm the hyphotesis proposed by Park *et al.* [145,146].

MV and V4 cells show different sodium site preferences all along the electrochemical reaction. An overall preference for Na(1) site during charge and discharge is observed for the MV cell while the opposite occurs for V4 cell. On the contrary, a Na(2) site preference can be detected for the potentiostatic step of MV cell while there is a low occupancy of Na(2) site during the potentiostatic hold of V4 cell. In any case, the sodium site occupancy and mobility in the tunnels of both compounds appear to be interchangeable and fluid.

Both the MV and the V4 cathodes seems to “reset” at the discharge state going back to the original composition after the cycling, something crucial for the longevity of the electrode which makes these materials persistent and flexible.

Despite the similarity of the $V^{3.8+}$ MV and V^{4+} V4 materials, these features show that the electrochemical behaviour of an electrode material is clearly dependant not only on the sodium extraction/insertion mechanism, the occupancy and distribution of sodium and the electrochemical cycling history but also on the synthesis process employed for the obtaining of the starting material, that determines material properties.

4.4 Chapter Summary

The evolution of $V^{3.8+}$ MV ($Na_3V_2O_{2x}(PO_4)_2F_{3-2x}$ (x = 0.8)) and V^{4+} V4 ($Na_3V_2O_2(PO_4)_2F$) materials during charge/discharge process was followed by both, *ex-situ* and *in-situ* techniques. Conventional and high resolution synchrotron X-ray diffraction was employed to follow the structural changes of the *post mortem* electrodes of MV sample while high resolution synchrotron X ray Absorption Near Edge Spectroscopy (XANES) provided the evolution of the vanadium oxidation state of the *post mortem* electrodes of both, MV and V4 samples. These data illustrated snapshots of the structural evolution of the compounds, showing the oxidation of the V^{4+} during charge and the inverse process occurring while discharging. The ~20% of V^{3+} present in the mixed valence $V^{3.8+}$ MV compound seemed to remain constant during the charge/discharge process.

Reaction mechanism evolution, lattice parameters and sodium evolution and the maximum possible sodium extraction under the applied electrochemical constraints, are some of the features that were determined for both MV and V4 materials by time-resolved *in-situ* synchrotron X-ray powder diffraction.

The reaction mechanism evolution of MV cathode undergoes a solid solution reaction with a two-phase region for the first lower-potential *plateau*-like feature while a predominantly solid solution behaviour is observed for the second higher-potential *plateau*-like feature. Lattice and volume evolution is clearly dependent on the Na extraction/insertion mechanism, the sodium occupancy and distribution amongst the two crystallographic sites, and the electrochemical cycling history. The comparison between the raw material and the material inside the cell shows that there is a Na site preference depending on the cycling history and that Na swaps from one site to the other during cycling. This suggests that sodium site occupancy and mobility in the tunnels is exchangeable and fluent, a favourable characteristic for a cathode in a sodium-ion battery.

On the other hand, the evolution of sodium at the two crystallographic sites during charge and discharge for V4 material revealed the atomic level perturbations that occur with electrochemically cycling. First, there is evidence of a region comprising at least three phases with subtly varying sodium compositions that transform *via* two two-phase reaction mechanisms. This process appears at the lower potential *plateau*-like feature

region during both charge and discharge. An extended solid solution region is found for majority of the cycling process, including most of the higher potential *plateau*-like feature. Additionally, a second two-phase region occurs near the highest charge state in the charging process and between the first and second *plateau*-like feature regions during discharge.

The electrochemical behaviour of the two electrode materials studied, MV and V4, show similar electrochemical reaction mechanism evolution where a simultaneous solid solution and two-phase region can be observed. However, the maximum sodium amount that can be extracted when a potentiostatic step is applied is higher for MV sample than for the V4 one which could be due to several reasons, such as better intrinsic conductivity, the presence of *in-situ* carbon in the mixed valent sample or to the more rigid structure of the only V^{4+} containing V4 sample. Nevertheless, both materials present high reversitibility and flexibility during charge/discharge process and the mobility of the sodium sites in the tunnels makes them good candidates as cathode materials for sodium-ion batteries.

Conclusions

- V^{3+} $Na_3V_2(PO_4)_2F_3$ and V^{4+} $Na_3V_2O_2(PO_4)_2F$ extreme phases belong to the $Na_3V_2O_{2x}(PO_4)_2F_{3-2x}$ family of compounds where the vanadium oxidation state varies between +3 and +4 for intermediate phases.

- The increasing amount of carbon employed in the hydrothermal synthesis of the sodium vanadium fluorophosphates leads to V^{3+} richer phases.

- The synthesis of $Na_3V_2O_{2x}(PO_4)_2F_{3-2x}$/C composites with a moderate electrochemical grade carbon proportion leads to mesoporous materials with good connectivity between the active material particles.

- Both, $Na_3V_2O_{2x}(PO_4)_2F_{3-2x}$/C (x = 0.8) and $Na_3V_2O_2(PO_4)_2F$ phases show to be stable, easy handling and scalable.

- A never reported Na_xVPO_4F phase has been successfully obtained by a chemical oxidation and further reduction of the $LiVPO_4F$ starting material. Further studies are needed to characterise this new material.

- $Na_3V_2O_{2x}(PO_4)_2F_{3-2x}$/C (x = 0.8) composite shows high operating voltage, good specific capacity values near to theoretical ones both at moderate and fast rates, and outstanding ciclability, which are excellent properties for a cathodic material for sodium-ion batteries.

- The carbon coating of hydrothermally prepared $Na_3V_2O_2(PO_4)_2F$ material by an optimized sucrose impregnation method leads to a composite with enhanced electrochemical performance.

- The redox activity of $Na_3V_2O_{2x}(PO_4)_2F_{3-2x}/C$ (x = 0.8) can be attributed to V^{4+}/V^{5+} pair, being the V^{3+} present in the sample electrochemically inactive.

- Both materials, $Na_3V_2O_{2x}(PO_4)_2F_{3-2x}/C$ (x = 0.8) composite and $Na_3V_2O_2(PO_4)_2F$, show a very similar reaction mechanism, with an initial solid solution, followed by a (two) two-phase region and a second solid solution transition. Besides, charge of $Na_3V_2O_2(PO_4)_2F$ cathode presents another biphasic zone after the second solid solution zone.

- Sodium evolution during electrochemical reaction of both $Na_3V_2O_{2x}(PO_4)_2F_{3-2x}/C$ (x = 0.8) and $Na_3V_2O_2(PO_4)_2F$ materials shows that sodium site occupancy and mobility in the structure tunnels is exchangeable and fluent, providing excellent properties for a cathode in a sodium-ion battery.

Bibliography

Abouimrane, A.; Weng, W.; Eltayeb, H.; Cui, Y.J.; Niklas, J.; Poluektov, O.; Amine, K. *Energy Environ. Sci.*, **2012**, 5, 9632-9638.

Armand, M.; Tarascon, J.M. *Nature*, **2008**, 451, 652–657.

Ateba Mba, J-M.; Masquelier, C.; Suard, E.; Croguennec, L. *Chem. Mater.*, **2012**, 24,1223 – 1234.

Barker, J.; Gover, R.K.B.; Burns, P.; Bryan, A.J. *Electrochem Solid-State Lett.*, **2006**, 9, A190-A192.

Barker, J.; Saidi, M.Y.; Swoyer, J.L. *Electrochem Solid-State Lett.*, **2003**, 6, A1-A4.

Barpanda, P.; Nishimura, S-I.; Yamada, A. *Adv. Energy Mater.*, **2012**, 2, 841-859.

Barpanda, P.; Ye, T.; Nishimura, S-I.; Chung, S-C.; Yamada, Y.; Okubo, M.; Zhou, H.; Yamada, A. *Electrochem. Commun.*, **2012**, 24, 116-119.

Bleaney, B.; Bowers, K.D. *Proc. R. Soc. London*, **1952**, Ser. A 214, 451-465.

Botto,I.L.; Vassallo, M.B.; Baran, E.J.; Minelli, G. *Mater. Chem. Phys.*, **1997**, 50, 267–270.

BP-Statistical Review of World Energy. June **2013**.

Brant, W.; Schmid, S.; Gu, Q.; Du, G.; Sharma, N. *J. Power Sources*, **2013**, 244, 109-114.

Brese, N.E.; O'Keeffe, *M. Acta Cryst.*, **1991**, B47, 192-197.

Brown, I.D.; Altermatt, D. *Acta Cryst.*, **1985**, B41, 244-247.

Brunauer, S.; Emmett, P.; Teller, E. *J. Am Chem. Soc.*, **1938**, 60, 309-319.

Carlin, R.L.; Va Duyneyeld, A.J. "Magnetic Properties of Transition Metal Compounds". Springer-Verlag New York Heidelberg Berlin, **1935**.

CARPS, California Codes: Public Utilities Code. Section 399.11-399.31. California Renewables Portfolio Standard Program, **2009**.

Casas-Cabanas, M.; Roddatis, V.; Saurel, D.; Kubiak, P.; Carretero-González, J.; Palomares, V.; Serras, P.; Rojo, T. *J. Mater. Chem.*, **2012**, 22, 17421-17423.

Catenacci, M.; Verdolini, E.; Bosetti, V.; Fiorese, G. *Energy Policy*, **2013**, 61, 403-413.

Chalmin, E.; Farges, F. and Brown, G.E. Jr, *Contrib. Mineral. Petrol.*, **2009**, 157, 111 – 126.

Chau, K.T.; Wong, Y.S.; Chan, C.C. *Ener. Conv. Manag.*, **1999**, 40, 1021-1039.

Chihara, K.; Kitajou, A.; Gocheva, I.D; Okada, S.; Yamaki, J.-I. *J. Power Sources*, **2013**, 227, 80-85.

Christensen, J.; Albertus, P.; Sanchez-Carrera, R.S.; Lohmann,T.; Kozinsky, B.; Liedtke, R.; Ahmed, J.; Kojic, A. *J. Electrochem. Soc.*, **2011**, 159, R1–R30.

Cluzel, C.; Douglas, C. **2012**. "Cost and performance of EV batteries, Element Energy". Final Report for the Committee on Climate Change.

CRC Handbook of Chemistry and Physics, ed. D.R. Lide, CRC Press, Boca Raton, 84th edn., **2003**.

Cuisinier, M.; Martin, J-F.; Dupré, N.; Yamada, A.; Kanno, R.; Guyomard, D. *Electrochem. Comm.*, **2010**, 12, 238-241.

D'Arienzo, M.; Ruffo, R.; Scotti, R.; Morazzoni, F.; Mari, C.M.; Polizzi, S. *Phys. Chem. Chem. Phys.,* **2012**, 14, 5945-5952.

Dell, R.M.; Rand, D.A.J. "Understanding batteries" RSC paperbacks. **2001**.

Delmas, C.; Fouassier, C.; Hagenmuller, P. *Physica B+C*, **1980**, 99, 81-85.

Dewulf, J.; Van der Vorst, G.; Denturck, K.; Van Langenhove, H.; Ghyoot, W.; Tytgat, J.; Vandeputte, K. *Resor. Conserv. Recy.*, **2010**, 54, 229-234.

Díaz-González, F.; Sumper, A.; Gomis-Bellmunt, O.; Villafáfila-Robles, R. *Renew. Sust. Energ. Rev.*, **2012**, 16, 2154-2171.

Ding, J.J.; Zhou, Y.N.; Sun, Q.; Fu, Z.W. *Electrochem. Commun.*, **2012**, 22, 85-88.

Divya, K.C.; Ostergaard, J. *Electric Power Syst. Res.*, **2009**, 79, 511-520.

Ellis, B.L.; Makahnouk, W.R.M.; Rowan-Weetaluktuk, W.N.; Ryan, D.H.; Nazar, L.F. *Chem. Mater.*, **2010**, 22, 1059-1070.

Ellis, B.L.; Ramesh, T.N.; Davis, L.J.M.; Goward, G.R.; Nazar, L.F. *Chem. Mater.* **2011**, 23, 5138–5148.

EPRI. Electricity Energy Storage Technology Options. **2010**.

Farges, F. Phys. Rev., **2005**, B 71, 155109.

Fielden, R.; Obrovac, M.N. "Structure and electrochemistry of $NaNiO_2$". Poster at: Honolulu PRiME 2012, 2012 Fall Meeting of The Electrochemical Society, **2012** Oct. 7 – 12, Honolulu, Hi.

Grey, C.P.; Dupre, N. *Chem. Rev.* **2004**, 104, 4493–4512.

Guerra, E.M.; Mulato, M. J. *Sol-Gel Sci. Technol.*, **2009**, 52, 315-320.

Guerrero, M.A.; Romero, E.; Barrero, F.; Milanes, M.I.; Gonzalez, E. CPE 2009: proceedings of compatibility and power electronics, Badajoz, Spain, May 20-22, **2009**.

Gummow, R. J.; Sharma, N.; Feng, R.; Han, G.; He, Y., *J. Electrochem. Soc.*, **2013**, 160, A1856-A1862.

Hadjipaschalis, I.; Poullikkas, A.; Efthimiou, V. *Renew Sustain Energy Rev.,* **2009**, 13, 1513-1522.

Han, M.H.; Gonzalo, E.; Casas-Cabanas, M.; Rojo, T. *J. Power Sources*, **2014**, 258, 266-271.

Hong, S.Y.; Kim, Y.; Park, Y.; Choi, A.; Choi, N.-S.; Lee, K.T. *Energy Environ. Sci.*, **2013**, 6, 2067-2081.

Hueso, K.B.; Armand, M.; Rojo, T. *Energy Environ. Sci.*, **2013**, 6, 734-749.

Ibrahim, H.; Ilinca, A.; Perron, J. *Renew Sustain Energy Rev.,* **2008**, 12, 1221-1250.

International Energy Agency (IEA) Statistics. "CO_2 emissions from fuel combustion. Highlights". **2013** Edition.

Jian, Z.; Han, W.; Lu, X.; Yang, H.; Hu, Y-S.; Zhou, J.; Zhou, Z.; Li, J.; Chen, W.; Chen, D.; Chen, L., *Adv. Energy Mater.,* **2013**, 3, 156-160.

Jian, Z.; Zhao, L.; Pan, H.; Hu, Y.-S.; Li, H.; Chen, W.; Chen, L., *Electrochem. Commun.*, **2012**, 14, 86-89.

Jiang, T.; Chen, G.; Li, A.; Wang, C.; Wei, Y. *J. Alloy Compd.*, **2009**, 478, 604-607.

Jiang, Z.; Han, W.; Lu, X.; Yang, H.; Hu, Y.-S.; Zhou, J.; Zhou, Z.; Li, J.; Chen, W.; Chen, D.; Chen, L. *Adv. Energy Mater.*, **2012**, 3, 156-160.

Julien, C.M.; Ait-Salah, A.; Mauger, A.; Gendron, F. *Ionics*, **2006**, 12, 21-32.

Kim, D.; Lee, E.; Slater, M.; Lu, W.; Rood, S.; Johnson, C.S. *Electrochem. Commun.*, **2012**, 18, 66-69.

Kin, H.; Shakoor, R.A.; Park, C.; Lim, S.Y.; Kim, J.-S.; Jo, Y.N.; Cho, W.; Miyasaka, K.; Kahraman, R.; Jung, Y.; Choi, J.W. *Adv. Func. Mater.*, **2013**, 23, 1147-1155.

Komaba, S.; Matsuura, Y.; Ishikawa, T.; Yabuuchi, N.; Murata, W.; Kuze, S. *Electrochem. Commun.*, **2012**, 21, 65-68.

Komaba, S.; Takei, C.; Nakayama, T.; Ogata, A.; Yabuuchi, N. *Electrochem. Commun.*, **2010**, 12, 355.

Koningsberger, D. and Prins, "R. X-Ray Absorption: Principles, Applications, Techniques of EXAFS, SEXAFS, and XANES"; Wiley-Interscience: New York, **1988**.

Koohi-Kamali, S.; Tyagi, V.V.; Rahim, N.A.; Panwar, N.L.; Mokhlis, H. Renew. *Sust. Energ. Rev.*, **2013**, 25, 135-165.

Langrock, A.; Xu, Y.; Liu, Y.; Ehrman, S.; Manivannan, A.; Wang, C. *J. Power Sources*, **2013**, 223, 62-67.

Larson, A.C. and Von Dreele, R.B. "General Structure Analysis System (GSAS)" Los Alamos National Laboratory Report LAUR, **1994**, 86-748.

Le Meins, J.-M.; Crosnier-Lopez, M.-P.; Hemon-Ribaud, A. and Courbion, G. *J. Solid State Chem.*, **1999**, 148, 260-277.

Liu, Z.; Wang, X.; Wang, Y.; Tang, A.; Yang, S.; He, L., *T. Nonferr. Metal Soc*., **2008**, 18, 346-350.

Liua, G.; Benyonb, P.; Benfella, K.E.; Bryanta, G.W.; Tatea, A.G.; Boydb, R.K.; Harrisc, D.J.; Walla, T.F. *Fuel*, **2000**, 79, 617-626.

Lu, X.C.; Xia, G.G.; Lemmon, J.P.; yang, Z.G. *J. Power Sources*, **2010**, 195, 2431-2442.

Lu, Y.; Zhang, S.; Li, Y.; Xue, L.; Xu, G.; Zhang, X. *J. Power Sources*, **2013**, 247, 770-777.

Martin, F.; Yamada, A.; Kobayashi, G.; Nishimura, S.I.; Kanno, R.; Guyomard, D. Dupré, N. *Electrochem. Solid-State Lett.*, **2008**, 11, A12-A16.

Masaud, T.M.; Lee, K.; Sen, P.K. NAPS 2010: proceedings of North American power symposium, Arlington, TX, USA, September 26-28, **2010**.

Masquelier, C.; Croguennec, L. *Chem. Rev.*, **2013**, 113, 6552-6591.

Massa, W.; Yakubovich, O.; Dimitrova, O. *Solid State Sci.*, **2002**, 4, 495-501.

Massiot, D.; Fayon, F.; Capron, M.; King, I.; Le Calvé, S.; Alonso, B.; Durand, J.O.; Bujoli, B.; Gan, Z.; Hoatson, G. *Magn. Reson. Chem.,* **2002**, 40, 70-76.

Mizushima, K.; Jones, P.C.; Wiseman, P.J.; Goodenough, J.B. *Mater. Res. Bull.*, **1980**, 15, 783-789.

Moreau, P.; Guyomard, D.; Gaubicher, J.; Boucher, F. *Chem. Mater.*, **2010**, 22, 4126-4128.

Nakamoto, K. “Infrared and Raman Spectra of Inorganic and Coordination Compounds” 5th ed. John Wiley &Sons, New York, **1997**.

New York Environmental Conservation Law, **2011**.

Noguchi,Y.; Kobayashi, E.; Plashnitsa, L.S.; Okada, S.; Yamaki, J.-I. *Electrochim. Acta.*, **2012**, 101, 59-65.

Oh, S.M.; Myung, S.T.; Hassoun, J.; Scrosati, B.; Sun, Y.K. *Electrochem. Commun.,* **2012**, 22, 149–152.

Orikasa, Y.; Maeda, T.; Koyama, Y.; Murayama, H.; Fukuda, K.; Tanida, H.; Arai, H.; Matsubara, E.; Uchimoto, Y.; Ogumi, Z., *J. Am. Chem. Soc.*, **2013**, 135, 5497-5500.

Palomares, V.; Casas-Cabanas, M.; Castillo-Martínez, E.; Han, M.H.; Rojo, T. *Energy Environ. Sci.*, **2013**, 6, 2312-2337.

Palomares, V.; Goñi, A.; Gil de Muro, I.; De Meatza, I.; Bengoechea, M.; Cantero, I.; Rojo, T. *J. Electrochem. Soc.*, **2009**, 156, A817-A821.

Palomares, V.; Serras, P.; Villaluenga, I.; Hueso, K. B.; Carretero-Gonzalez, J.; Rojo, T. *Energy Environ. Sci.,* **2012**, 5, 5884-5901.

Pan, H.; Hu, Y.-S.; Chen, L. *Energy Environ. Sci.*, **2013**, 6, 2338-2360.

Pan, H.; Lu, X.; Yu, X.; Hu, Y-S.; Li, H.; Yang, X-Q.; Chen. L. *Adv. Energy Mater.,* **2013**, 3, 1186-1194.

Park, Y. U.; Seo, D. H.; Kim, B.; Hon, K. P.; Kim, H.; Lee, S.; Shakoor, R. A.; Miyasaka, K.; Tarascon, J. M.; Kang, K. *Sci. Rep.*, **2012**, 2:704.

Park, Y. U.; Seo, D. H.; Kim, B.; Kim, J.; Lee, S.; Kim, B.; Kang, K. *Adv. Funct. Mater.*, **2014**, DOI: 10.1002/adfm.201400561.

Park, Y.; Shin, D.S.; Woo, S.H.; Choi, N.S.; Shin, K.H.; Oh, S.M.; Lee, K.T.; Hong, S.Y. *Adv. Mater.*, **2012**, 24, 3562-3567.

Park, Y.-U.; Seo, D. H.; Kwon, H.-S.; Kim, B.; Kim, J.; Kim, H.; Kim, I.; Yoo, H.-I.; Kang, K. *J. Am. Chem. Soc.*, **2013**, 135, 13870-13878.

Pavley, F.; Nunez, F. California Assembly Bil No. 32-GlobalWarming solutions Act of 2006, **2006**.

Pivko, M.; Arcon, I.; Bele, M.; Dominko, R. and Garberscek, M. *J. Power Sources*, **2012**, 216, 145-151.

Plashnitsa, L. S.; Kobayashi, E.; Noguchi, Y.; Okada, S.; Yamaki, J.-I. *J. Electrochem. Soc.*, **2010**, 157, A536–A543.

Ponrouch, A.; Dedryvère, R.; Monti, D.; Demet, A.E.; Ateba Mba, J.M.; Croguennec, L.; Masquelier, C.; Johansson, P.; Palacín, M.R. *Energy Environ. Sci.*, **2013**, 6, 2361-2369.

Ponrouch, A.; Marchante, E.; Courty, M.; Tarascon, J-M.; Palacín, M.R. *Energy Environ. Sci.*, **2012**, 5, 8572-8583.

Prakash, A.S.; Rozier, P.; Dupont, L.; Vezin, H.; Sauvage, F.; Tarascon, J.-M. *Chem. Mater.*, **2006**, 18, 407-412.

Qian, J.F.; Chen, Y.; Wu, L.; Cao, Y.L.; Ai, X.P.; Yang, H.X. *Chem. Commun.*, **2012**, 48, 7070-7072.

Ravel B.; Newville, M. *J. Synchrotron Rad.*, **2005**, 12, 537-541.

Recham, N.; Chotard, J-N.; Dupont, L.; Djellab, K.; Armand, M.; Tarascon, J-M. *J. Electrochem. Soc.*, **2009**, 156, A993-A999.

Rechargeable Battery Recycling Act, **2006**.

Roberts, B.P.; Sandberg, C. Proceedings of the IEEE **2011**, 99, 1139-1144.

Rodríguez-Carvajal, J.; Roisnel, T. www.llb.cea.fr/fullweb/winplotr/winplotr.htm.

Saravanan, K.; Mason, C.W.; Rudola, A.; Wong, K.H.; Balaya, P. *Adv. Energy Mater.*, **2013**, 3, 444-450.

Saravanan, K.; Mason, C.W.; Rudola, A.; Wong, K.H.; Balaya, P. *Adv. Energy Mater.*, **2013**, 3, 444-450.

Sauvage, F.; Quarez, E.; Tarascon, J.; Baudrin, E. *Solid State Sci.*, **2006**, 8, 1215–1221.

Scheurell, K.; Kemnitz, E. *J. Mater. Chem.*, **2005**, 15, 4845–4853.

Schindler, M.; Hawthorne, F. C.; Baur, W. H. *Chem. Mater.*, **2000**, 12, 1248-1259.

Senguttuvan, P.; Rousse, G.; Seznec, V.; Tarascon, J.M.; Palacín, M.R. *Chem. Mater.*, **2011**, 23, 4109-4111.

Shakoor, R. A.; Seo, D.-H.; Kim, H.; Park, Y.U.; Kim, J.; Kim, S.-W.; Gwon, H.; Lee, S.; Kang, K. *J. Mater. Chem.*, **2012**, 22, 20535-20541.

Sharma, N.; Peterson, V. K.; Elcombe, M. M.; Avdeev, M.; Studer, A. J.; Blagojevic, N.; Yusoff, R.; Kamarulzaman, N., *J. Power Sources*, **2010**, 195, 8258-8266.

Sharma, N.; Peterson, V.K. *Electrochimica Acta*, **2013**, 101, 79-85.

Sharma, N.; Peterson, V.K. *J. Power Sources*, **2013**, 244, 695-701.

Sharma, N.; Yu, D.; Zhu, Y.; Wu, Y.; Peterson, V. K. *Chem. Mater.*, **2013**, 25, 754-760.

Song, J.; Xu, M.; Wang, L.; Goodenough, J.B. *Chem. Commun.*, **2013**, 49, 5280-5282.

Sun, Y.; Zhao, L.; Pan, H.; Lu, X.; Gu, L.; Hu, Y-S.; Li, H.; Armand, M.; Ikuhara, Y.; Chen, L.; Huang, X. *Nat. Commun*. **2013**, 4:1870.

Takahashi, Y.; Kijima, N.; Tokiwa, K.; Watanabe, T.; Akimoto, J., *J. Phys.: Condens. Matter*, **2007**, 19, 436202/1-436202/12.

Tan, X.G.; Li, Q.M., Wang, H. *Int. J. Electric Power Energy Syst.*, **2013**, 44, 179-191.

Toby, B.H. J. *Appl. Crystallogr.*, **2001**, 34, 210-213.

Tollefson, J. *Nature*, **2008**, 456, 436–440.

Tsirlin, A.; Nath, R.; Abakumov, A.; Furukawa, Y.; Johnston, D.; Hemmida, M.; Krug von Nidda, H.-A.; Loidl, A.; Geibel, C.; Rosner, H. *Phys. Rev. B*, **2011**, 84, 014429/1-014429/16.

Uebou, Y.; Kiyabu, T.; Okada, S.; Yamaki, J.-I. *The Reports of Institute of Advanced Material Study*, Kyushu University, **2002**, vol. 16, pp. 1–5.

Vassilaras, P.; Ma, X.; Lin, X.; Ceder, G. *J. Electrochem Soc.*, **2013**, 160, A207-A211.

Vazquez, S.; Lukic, S.M.; Galvan, E.; Franquelo, L.G.; Carrasco, J.M. IEEE *T. Ind. Electron.*, **2010**, 57, 3881-3895.

Villeneuve, G.; Amorós, P.; Beltrán, D.; Drillon, M. "Dimers, regular and double chains in vanadyl phosphates" in "Organic and Inorganic Low Dimensional Crystalline Materials" (P. Delhaes et al. Eds.); NATO ASI Series **1987**,168, 417-420, Springer Science, New York.

Wade, N.S.; Taylor, P.C.; Lang, P.D., Jones, P.R. *Energ. Policy*, **2010**, 38, 7180-7188.

Wallwork, K.S.; Kennedy, B.J. and Wang, D. *AIP Conference Proceedings*, **2007**, 879, 879-882.

Wang, W.; Liu, X.H.; Mao, S.X.; Huang, J.Y. *Nano Lett.*, **2012**, 12, 5897-5902.

Wang, W.; Yu, C.; Lin, Z.; Hou, J.; Zhua, H.; Jiao, S. *Nanoscale*, **2013**, 5, 594-599.

Wang, X.; Gaustad, G.; Babbitt, C.W.; Richa, K. *Resor. Conserv. Recy.*, **2014**, 83, 53-62.

Wenzel, S.; Hara, T.; Janek, J.; Adelhelm, P. *Energy Environ. Sci.*, **2011**, 4, 3342-3345.

Whittingham, M.S.; *Prog. Solid State Chem.*, **1978**, 12, 41-99.

Wong, J.; Lytle, F. W.; Messmer, R. P. and Maylotte, D. H. *Phys. Rev. B*, **1984**, 30, 5596–5610.

Xiao, L.F.; Cao, Y.L.; Xiao, J.; Wang, W.; Kovarik, L.; Nie, Z.M.; Liu, J. *Chem. Commun.*, **2012**, 48, 3321-3323.

Xu, M.; Wang, L.; Zhao, X.; Song, J.; Xie, H.; Lu, Y.; Goodenough, J.B. *Phys. Chem. Chem. Phys.*, **2013**, 15, 13032-13037.

Yabuuchi, N.; Kajiyama, M.; Iwatate, J.; Nishikawa, H.; Hitomi, S.; Okuyama, R.; Usui, R.; Yamada, Y.; Komaba, S. *Nat. Mater.*, **2012**, 11, 512-517.

Yakubovich, O.V.; Karimova, O.V.; Mel'nikov, O.K. *Acta Cryst. C*, **1997**, 53, 395-397.

Yamada, A.; Chung, S.C.; Hinokuma, K. *J. Electrochem. Soc.*, **2001**, 148, A224-A229.

Yoshida, H.; Yabuuchi, N.; Komaba, S. “Na insertion mechanism in α-$NaFeO_2$ as positive electrode materials for Na-ion batteries”. Paper presented at: Honolulu PRiME 2012, 2012 Fall Meeting of The Electrochemical Society, **2012** Oct. 7 – 12, Honolulu, Hi.

Zaghib, K.; Dontigny, M.; Charest, P.; Labrecque, J.F.; Guerfi, A.; Kopec, M.; Mauger, A.; Gendron, F.;Julien, C.M. *J. Power Sources*, **2008**, 185, 698-710.

Zaghib, K.; Trottier, J.; Hovington, P.; Brochu, F.; Guerfi, A.; Mauger, A.; Julien, C.M. *J. Power Sources*, **2011**, 196, 9612-9617.

Zhuo, H.; Wang, X.; Tang, A.; Liu, Z.; Gamboa, S.; Sebastian, P.J. *J. Power Sources*, **2006**, 160, 698-703.

Appendices

Instrumental techniques

A.1. X-ray Powder Diffraction (XRD)

Laboratory-based X-Ray powder diffraction patterns were collected in a Bruker D8 Advance Vário diffractometer working with Cu K-α radiation (λ= 1.54056 Å) between 10 and 90º at room temperature when the analysis were carried out in the Research General Services (SGIker) of the University of the Basque Country (UPV/EHU). For laboratory-based X-ray diffraction (XRD) patterns collected in the *Institut de Chimie de la Matière Condensée de Bordeaux* (ICMCB) the following equipment and configuration were employed: a PANalitycal Bragg-Brentano θ-2θ geometry diffractometer equipped with a secondary monochromator over an angular range of 2θ = 5-80° (day acquisitions) 5-120° (overnight acquisitions) with a step of 0.02°. Each acquisition lasted for 2 hours (day acquisitions) or 16 hours (overnight acquisitions). The Cu-Kα radiation was generated at 45 KV and 40 mA (λ= 1.5418 Å). The samples were put on hygroscopic cell made of aluminum alloy, flattened with a piece of glass or prepared with the edge of a razor blade to avoid preferential orientations.

High-resolution synchrotron XRD data were collected on the Powder Diffraction beamline (10-BM-1) [1] at the Australian Synchrotron using a wavelength of λ = 0.83696(2) Å, determined using the NIST 660a LaB_6 standard reference material. Powder samples were packed and sealed in 0.5 mm glass capillaries and data were collected for 6 minutes at ambient temperature using Debye-Scherrer geometry.

In-situ synchrotron XRD data were collected on the Powder Diffraction beamline [1] at the Australian Synchrotron with a refined wavelength of λ = 0.68816(2) Å, determined using the NIST LaB_6 660b standard reference material.

The X-ray diffraction (XRD) is a versatile, rapid, sensitive, reproducible and non-destructive technique. For these reasons, it is considered one of the most important characterisation tools used in solid-state chemistry and materials science. XRD is one of the oldest and most frequently applied techniques in solid sate chemistry. It is used to identify crystalline phases inside solid materials by means of lattice parameters, crystals structure and to obtain an indication of the average grain size.

1 Wallwork, K.S.; Kennedy, B.J. and Wang, D. *AIP Conference Proceedings*, **2007**, 879, 879-882.

In 1895, W. Röntgen discovered a type of radiation that he could not fully understand, therefore he called it X-rays. This discovery enabled scientists to investigate crystalline structures at the atomic level as X-ray is an electromagnetic radiation of wavelength between 0.5 and 2.5 Å (1Å=1×10^{-10} m), which is about the same size as an atom and distance between atoms, and the X-ray photon has a high energy. This radiation occurs in the portion of the electromagnetic spectrum between gamma rays and the ultraviolet (Figure A.1).

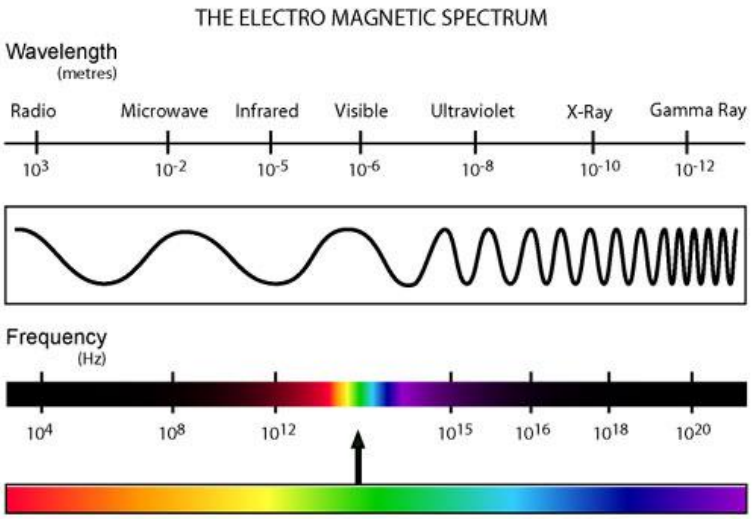

Figure A.1. *Electromagnetic spectrum.*

The X-ray diffraction technique is used to investigate the structure of matter at the atomic level. Each crystalline solid has its unique characteristic X-ray powder pattern which may be used as a "fingerprint" for its identification. Once the material has been identified, X-ray crystallography may be used to determine its structure, *i.e.* how the atoms pack together in the crystalline state and what the interatomic distance and angle are, etc.

Production of X-rays

The production of X-rays must be performed in vacuum and it is necessary to apply a difference of potential, of tens to hundreds kV, between cathode and a metallic target that works as an anode. Copper and molybdenum are the materials used for the target. When the cathode filament of tungsten is hot, it frees electrons by thermo ionic effect; they are accelerated through vacuum due to the difference of potential between cathode and anode. Before colliding with the metallic target, the electron has high kinetic energy; during this collision it will displace one electron in the internal layers of the atom close to the nuclei, ionising the atom. When an atom of the internal layer is ionised, an electron of the external layer will be dislocated to the internal layer, causing the emission of X-ray radiation characteristic of this atom.

In X-ray diffraction, two collecting data methods can be used, either reflection or transmission diffraction. The main differences between these methods are the beam collector position, in relation to the sample position and the thickness of the sample. In the reflection method, the incident beam will penetrate the top layers of the sample, being reflected towards the collector. The incident angle varies in order to sweep all possible angles to obtain constructive interference. For the transmission method, the beam passes through the sample. Samples of different thickness have to be used in the two different methods: in the reflection cases the sample has to be thick enough so the incident beam can only penetrate the top sample layer without reaching the sample support; in the transmission method, the sample has to be thin enough so that the incident beam can pass through the sample.

X-ray diffraction occurs due to the elastic scattering of X-ray photons by the electrons associated with each atom or ion in a periodic lattice that lies within the beam's path. The scattered monochromatic X-rays that are in phase give constructive interference. Figure A.2 illustrates how diffraction of X-rays by crystal planes can be used to derive lattice spacings by using the Bragg relation, also referred to as Bragg's law:

$$n\lambda = 2d \sin\theta \qquad \text{(Eq. A.1.1.)}$$

Where the variable *d* is the distance between atomic layers in a crystal, the variable lambda (λ) is the wavelength of the incident X-ray beam and *n* is an integer. The

wavelength, λ, of the X-ray is approximately the distance between atomic planes of a crystal.

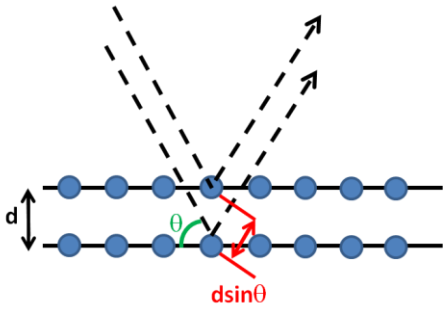

Figure A.2. *Illustration of the diffraction of X-rays by atoms in an ordered lattice. The X-rays interference constructively in directions given by Bragg's law.*

The polycrystalline or "powder" X-ray diffraction technique was developed by Debye and Scherrer, and independently by Hull in the period of 1914-1919. Their technique is classified as "fixed λ, varying θ" in which the oriented crystals in the specimen such that some of the (hkl) planes in some of them will be orientated, by chance, at the appropriate Bragg angles for reflection. All the planes at given d_{hkl}-spacing reflect at the same 2θ angle to the direct beam and all these reflected beams lie on a cone of semi-angle 2θ about the direct beam.

In 1918, Scherrer stabilised his famous relation giving mean crystallite size from the X-ray line profile width. In that sense "crystallite" is equivalent to "homogeneous domain giving rise to coherent diffraction", so that it is supposed that there is no complete break in the three-dimensional order inside of it, though there could be some limited distortion. Bertaut demonstrated in 1949 that the size distribution can be estimated by Fourier analysis of the diffraction line profile. The Bragg law expresses the ideal geometrical conditions of diffraction, it implies that the crystal dimensions can be considered as infinite compared to the distance between two diffraction centres, and otherwise a size effect broadens the Bragg peaks.

A.2. Elemental analysis

Elemental analysis were performed in the Research General Services (SGIker) of the University of the Basque Country (UPV/EHU) with an Eurovector 3000 equipment.

Elemental analysis is a process where a sample is analysed for its elemental and sometimes isotopic composition. Elemental analysis can be qualitative or quantitative. For organic chemists, elemental analysis or "EA" almost always refers to CHNX analysis, the determination of the mass fractions of carbon, hydrogen, nitrogen, and heteroatoms (halogens, sulfur) of a sample. This information is important to help to determine the structure of an unknown compound, as well as to help to ascertain the structure and purity of a synthesized compound.

The most common form of elemental analysis, CHN analysis, is accomplished by combustion. In this technique, a sample is burned at approximately 1020ºC in an excess of oxygen, and the combustion products, such as carbon dioxide (CO_2), water (H_2O), and nitric oxide (NO) are collected in traps or in chromatographic columns, where they are separated. The masses of these combustion products can be used to calculate the composition of the unknown sample.

The analysis of results is performed by determining the ratio of elements from within the sample, and working out a chemical formula that fits with those results. This process is useful as it helps to determine if a sample is a desired compound and can confirm the purity of a compound. The accepted deviation of elemental analysis results from the calculated is 0.4%.

A.3. Double Titration Method with $KMnPO_4$

The quantification of the average oxidation state of vanadium (AV) was done by a double titration method [2]. A scheme of the followed procedure is shown in Figure A.3. Vanadium-containing compounds were completely dissolved in a 2M H_2SO_4 solution at 80°C. The first titration with a 0.1N $KMnO_4$ solution was stopped when the overall colour of the solution abruptly changed to red (corresponding to the complete oxidation of the unknown initial oxidation state $V^{?+}$ to V^{5+}) and the total volume of the $KMnO_4$ solution consumed during the first titration (*Vol.*1) was measured. An excess amount of $FeSO_4(NH_4)_2SO_4{\cdot}6H_2O$ was added to the solution to reduce all V^{5+} ions to V^{4+} ions by the Fe^{2+}/Fe^{3+} redox couple. Then, an excess amount of $(NH_4)_2S_2O_8$ was added to fully oxidize residual Fe^{2+} to Fe^{3+} to ensure the accuracy of the second titration. The second titration with the 0.1N $KMnO_4$ solution was stopped when the overall colour of the solution abruptly changed to red (corresponding to the complete oxidation of V^{4+} to V^{5+}) and the total volume of the $KMnO_4$ solution consumed during the second titration (*Vol.*2) was measured. Finally, the average oxidation state of vanadium (AV) was calculated by the following equation:

$$AV = 5 - (Vol.1/Vol.2) \qquad \text{(Eq. A.3.1)}$$

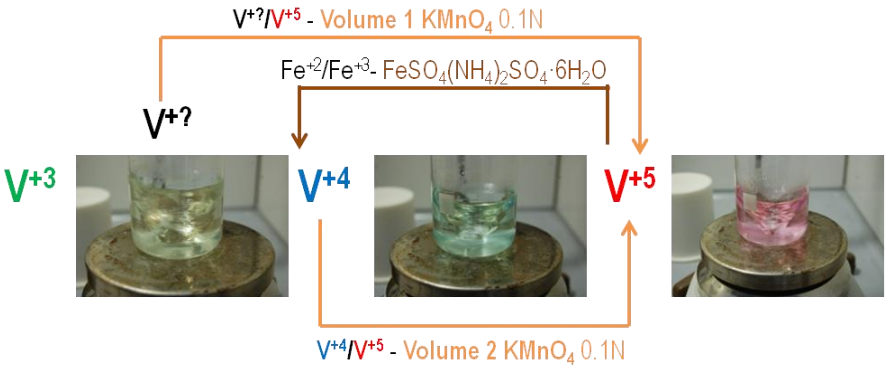

Figure A.3. *Titration procedure for the determination of the V oxidation state.*

2 Park, Y. U.; Seo, D. H.; Kim, B.; Hon, K. P.; Kim, H.; Lee, S.; Shakoor, R. A.; Miyasaka, K.; Tarascon, J. M.; Kang, K. *Sci. Rep.*, **2012**, 2:704.

A.4. Fourier Transform Infrared Spectroscopy (FTIR)

Fourier-transform infrared spectra (FTIR) were recorded from 4000 to 400 cm^{-1} on a FTIR-8400S Shimadzu spectrometer. The samples were dispersed in KBr and pressed into pellets.

Infrared Spectroscopy consists on the analysis of infrared light interacting with a molecule. This can be done in three ways by measuring absorption, emission and reflection. This technique is mainly used in organic and inorganic chemistry to determine functional groups in molecules. IR Spectroscopy measures the vibrations of molecules, and based on this it is possible to determine the functional groups. Generally, stronger bonds and light atoms will vibrate at a high stretching frequency (wavenumber). There have been many advances in the field of IR spectroscopy but the most notable was the application of Fourier Transformations to this technique thus creating an IR method that had higher resolution and a decrease in noise.

The components of an IR machine are the IR source, beam splitter, monochromator, a transducer, an analog to digital converter and a digital machine to quantify the readout. The IR light exits the source and becomes split into two beams, one to be directed to the sample and the other to a reference. The intensity of the beam is measured by the intensity emitted divided by the intensity observed, also known as the Transmittance. All frequencies are measured in wavenumber, cm^{-1}.

Infrared light imposed on a molecule will not create electronic transitions but it contains enough energy to interact with a molecule causing vibrational and rotational changes. For example, the molecule can absorb the energy contained in the incident light and the result is a faster rotation or a more pronounced vibration. The possible rotations are around the axis of symmetry for a given molecule or either of the two perpendicular axis. Vibrations can be in the form of a bend or a stretch for each bond (Figure A.4). In order for a vibrational mode in a molecule to be "IR active," it must be associated with changes in the dipole. A permanent dipole is not necessary, as the rule requires only a change in dipole moment.

For molecules with N atoms in them, linear molecules have 3N–5 degrees of vibrational modes, whereas nonlinear molecules have 3N–6 degrees of vibrational modes (also

called vibrational degrees of freedom). As an example H_2O, a non-linear molecule, will have (3×3)–6 = 3 degrees of vibrational freedom, or modes.

Simple diatomic molecules have only one bond and only one vibrational band. If the molecule is symmetrical, *e.g.* N_2, the band is not observed in the IR spectrum, but only in the Raman spectrum. Asymmetrical diatomic molecules, *e.g.* CO, however absorb in the IR spectrum. More complex molecules have many bonds, and their vibrational spectra are correspondingly more complex, *i.e.* big molecules have many peaks in their IR spectra.

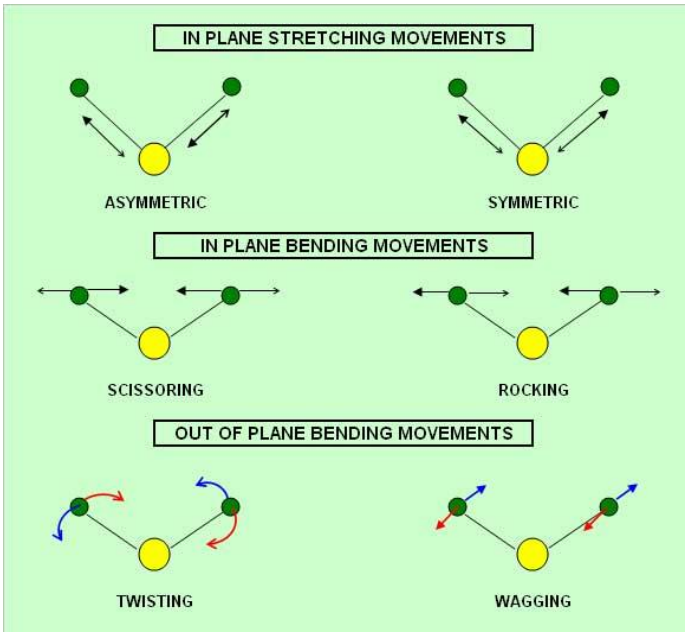

Figure A.4. *FTIR spectroscopy vibrational modes for molecules.*

A.5. Electron Paramagnetic Resonance (EPR)

A Bruker ELEXSYS 500 spectrometer equipped with a super-high-Q resonator ER-4123-SHQ, operating at X-band, was used to record the EPR polycrystalline spectra. The magnetic field was calibrated by a NMR probe and the frequency inside the cavity was determined with an integrated MW-frequency counter. The spin Hamiltonian parameters were estimated by comparison of the experimental spectra with those obtained by a computer simulation program working at the second order of the perturbation theory (WINEPR-Simfonia, version 1.5, Bruker Analytische Messtechnik GmbH).

When an alternating magnetic field of high frequency is applied to a substance, certain resonance effects are observed at particular values of the frequency and magnitude of the field. The effect involving the magnetic moment of the electron is called Electron Paramagnetic Resonance (EPR) or Electron Spin Resonance (ESR) when it is only due to electron spin. It can be observed in all substances except those which are diamagnetic as, for example, V^{5+}. Every electron has a magnetic moment and a spin quantum number (s = 1/2) with magnetic components m_s = +1/2 and m_s = -1/2. In the presence of an external magnetic field (H) the electron´s magnetic moment aligns itself either parallel (m_s = -1/2) or antiparallel (m_s = +1/2) to the field having a specific energy due to the Zeeman effect. Therefore, the separation between the lower and the upper state is given by Eq. A.5.1 for unpaired free electrons:

$$\Delta E = g_e \cdot \beta \cdot H \qquad \text{(Eq. A.5.1)}$$

where β is the Bohr magneton ($9.27 \cdot 10^{-21}$ Erg·G^{-1}) and g_e is the electron´s so-called "Landé factor" or the proportionality constant between the angular momentum of the electron and the magnetic momentum that it generates. Its value is 2.0023 for free electrons. This equation implies that the splitting of the energy levels is directly proportional to the magnetic field´s strength (Figure A.5).

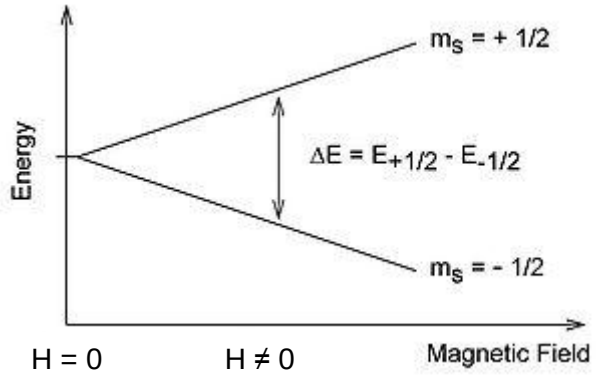

Figure A.5. *Splitting of energy levels for an unpaired electron when applying a magnetic field (Zeeman effect).*

An unpaired electron can move between the two energy levels by either absorbing or emitting a photon of energy $h\nu$ such that the resonance condition, $h\nu = \Delta E$, is obeyed. This leads to the fundamental equation of EPR spectroscopy:

$$h\nu = g \cdot \beta \cdot H \qquad \text{(Eq. A.5.2)}$$

Experimentally, this equation permits a large combination of frequency and magnetic field values, but the great majority of EPR measurements are made with microwaves in the 9000–10000 MHz (9–10 GHz) region, with fields corresponding to about 3500 G (0.35 T). Furthermore, EPR spectra can be generated by either varying the photon frequency incident on a sample while holding the magnetic field constant or doing the reverse. In practice, it is usually the frequency that is kept fixed. A collection of paramagnetic centres, such as free radicals, is exposed to microwaves at a fixed frequency. By increasing an external magnetic field, the gap between the m_s = +1/2 and m_s = -1/2 energy states is widened until it matches the energy of the microwaves, as represented by the double-arrow in the Figure A.5. At this point the unpaired electrons can move between their two spin states. Since there are typically more electrons in the lower state, due to the Maxwell–Boltzmann distribution, there is a net absorption of energy, and it is this absorption that is monitored and converted into a spectrum. The upper spectrum in Figure A.6 is the simulated absorption for a system of free electrons

in a varying magnetic field. The lower spectrum is the first derivative of the absorption spectrum. The latter is the most common way to record and publish EPR spectra (see Figure A.6).

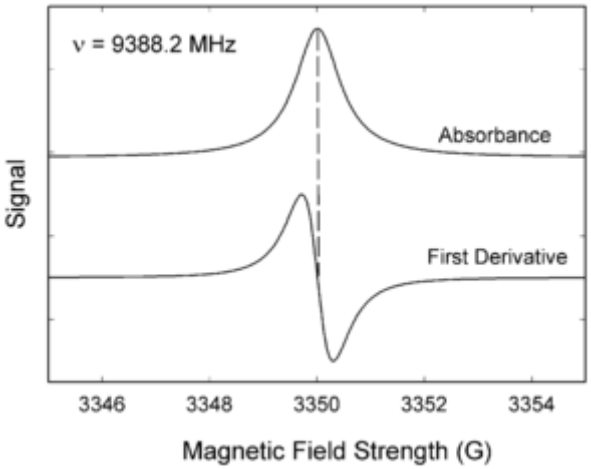

Figure A.6. *Absorption spectrum (upper) and first derivative of the absorption spectrum (lower) for EPR technique.*

For the microwave frequency of 9388.2 MHz, the predicted resonance position is a magnetic field of about $H = h\nu/g_e \beta = 0.3350$ tesla = 3350 gauss.

Knowledge of the *g*-factor can give information about a paramagnetic centre's electronic structure. Equation A.5.2 is used to determine *g* in an EPR experiment by measuring the field and the frequency at which resonance occurs. If *g* does not equal g_e the implication is that the ratio of the unpaired electron's spin magnetic moment to its angular momentum differs from the free electron value. Since an electron's spin magnetic moment is constant (approximately the Bohr magneton), then the electron must have gained or lost angular momentum through spin-orbit coupling. Because the mechanisms of spin-orbit coupling are well understood, the magnitude of the change gives information about the nature of the atomic or molecular orbital containing the unpaired electron.

The *g*-factor can have as many as three values, g_x, g_y and g_z, each corresponding to the value when the external magnetic field is parallel to one of three perpendicular directions (often lying along structural axes within the molecule). The equivalence or otherwise of these *g*-values is dependent upon the symmetry of the system under study and results in very different shapes of the EPR signal observed. This is shown in Figure A.7.

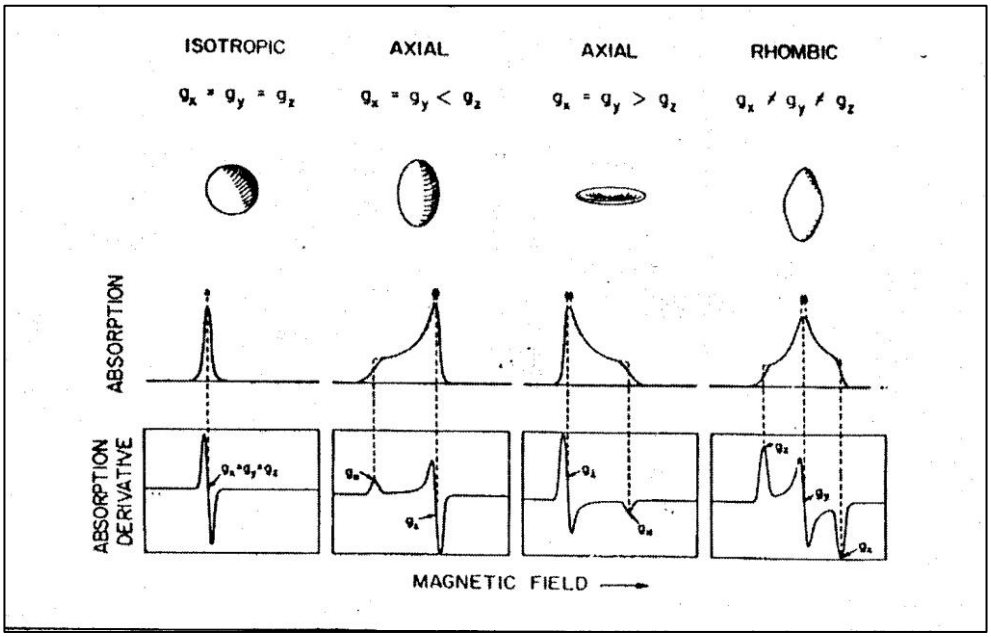

Figure A.7. *Different shapes of EPR signals [3].*

For systems with more than one unpaired electron (S > 1/2) the ground state can be split in the absence of an external magnetic field due to the local site symmetry – the zero-field splitting. For odd-electron systems this results in pairs of energy levels known as Kramer's doublets. The observed EPR spectrum can contain transitions within each of the ground-state Kramer's doublets.

3 http://www.uea.ac.uk/~fea06cbu/techni/epr/epr.htm.

There are two important conditions under which it may not be possible to observe an EPR signal, even when unpaired electrons are present:

1. If the system has an even number of unpaired electrons then zero-field splitting within the ground state may result in the EPR transitions being undetectable.

2. If the paramagnetic centres occur in pairs then coupling of the individual spins may result in the EPR signal being undetectable or even absent, although the individual centres may have an odd number of unpaired electrons.

In this sense, V^{3+} containing phases (no-Kramer systems) are hardly detected by this technique. However, V^{4+} presents an intense signal in the EPR spectra due to its Kramer doublets. When V^{3+}/V^{4+} mixed valence compounds are measured with this technique the corresponding V^{4+} signal becomes broader until it cannot be detected with the increasing V^{3+} amount in the sample. Nevertheless, the total disappearance of the signal does not imply necessarily a 100% content in V^{3+} in the material. The broadening of the V^{4+} signal only happens when the two vanadium types are coupled in the same phase. On the other hand, electrochemical grade carbons (S-black and Ketjen Black) present a narrow signal in the spectra, associated to free radicals in them.

A.6. Magnetic Susceptibility Measurements

Magnetic measurements of powered samples were carried out in the temperature range 2 – 300 K using a Quantum Design MPMS-7 Squid magnetometer and operating with a magnetic field of 0.1T. Samples were firstly cooled in the absence of any magnetic field (ZFC, Zero Field Cooling) and then, they were measured while applying magnetic field (FC, Field Cooling). These analysis were carried out in the Research General Services (SGIker) of the University of the Basque Country (UPV/EHU).

The magnetic susceptibility (χ) is a dimensionless proportionality constant that indicates the degree of magnetization of a material (*M*) in response to an applied magnetic field (*H*) as follows:

$$\chi = \frac{M}{H} \qquad \text{(Eq. A.6.1)}$$

Magnetic susceptibility (χ_m if it is referred to molar magnetic susceptibility) depends mainly on temperature and the number of unpaired electrons so that the following equation can be used to describe it:

$$\chi_m = \frac{N_A \cdot g^2 \cdot \beta^2 \cdot S \cdot (S+1)}{3 \cdot k_B \cdot T} = \frac{N_A \cdot \beta^2 \cdot \mu_{eff}}{3 \cdot k_B \cdot T} \qquad \text{(Eq. A.6.2)}$$

where, N_A is Avogadro´s number ($6.022 \cdot 10^{-23}$ mol^{-1}), *g* is the electron´s so-called "Landé factor" or the proportionality constant between the angular momentum of the electron and the magnetic momentum that it generates (2.0023 for free electrons), β is Bohr magneton ($9.274 \cdot 10^{-21}$ $Erg \cdot G^{-1}$), *S* is total spin number = n/2 (n: number of unpaired electrons), μ_{eff} is the effective magnetic moment and = $g \cdot \sqrt{S \cdot (S+1)}$ and k_B is the Boltzman constant ($1.38 \cdot 10^{-23}$ J/K).

Diamagnetism appears in all materials, and is the tendency of a material to oppose an applied magnetic field, and therefore, to be repelled by a magnetic field. However, in a material with paramagnetic properties (that is, with a tendency to enhance an external magnetic field), the paramagnetic behaviour dominates. Thus, despite its universal occurrence, diamagnetic behaviour is observed only in a purely diamagnetic material. In

a diamagnetic material, there are no unpaired electrons, so the intrinsic electron magnetic moments cannot produce any bulk effect.

In a paramagnetic material there are unpaired electrons, *i.e.* atomic or molecular orbitals with exactly one electron in them. While paired electrons are required by the Pauli exclusion principle to have their intrinsic ('spin') magnetic moments pointing in opposite directions, causing their magnetic fields to cancel out, an unpaired electron is free to align its magnetic moment in any direction. When an external magnetic field is applied, these magnetic moments will tend to align themselves in the same direction as the applied field, thus reinforcing it.

A ferromagnet, like a paramagnetic substance, has unpaired electrons. However, in addition to the electrons' intrinsic magnetic moment's tendency to be parallel to an applied field, there is also in these materials a tendency for these magnetic moments to orient parallel to each other to maintain a lowered-energy state. Thus, even when the applied field is removed, the electrons in the material maintain a parallel orientation.

Every ferromagnetic substance has its own individual temperature, called the Curie temperature (T_c), or Curie point, above which it loses its ferromagnetic properties. This is because the thermal tendency to disorder overwhelms the energy-lowering due to ferromagnetic order.

In an antiferromagnet, unlike a ferromagnet, there is a tendency for the intrinsic magnetic moments of neighbouring valence electrons to point in opposite directions. When all atoms are arranged in a substance so that each neighbour is 'anti-aligned', the substance is antiferromagnetic. Antiferromagnets have a zero net magnetic moment, meaning no field is produced by them.

Like ferromagnetism, ferrimagnets retain their magnetization in the absence of a field. However, like antiferromagnets, neighbouring pairs of electron spins like to point in opposite directions. These two properties are not contradictory, because in the optimal geometrical arrangement, there is more magnetic moment from the sublattice of electrons that point in one direction, than from the sublattice that points in the opposite direction.

The Néel temperature or magnetic ordering temperature, T_N, is the temperature above which an antiferromagnetic material becomes paramagnetic—that is, the thermal energy becomes large enough to destroy the macroscopic magnetic ordering within the material.

The five types of magnetism can be divided into two broad categories:

- Diamagnetism and ideal (Curie law) paramagnetism, characterised by non-cooperative behaviour of the individual magnetic moments.
- Nonideal (Curie-Weiss law) paramagnetism, ferromagnetism, antiferromagnetism and ferrimagnetism, which are all examples of cooperative phenomena.

Figure A.8 shows the different behaviour of magnetic susceptibility (χ) *vs.* temperature for three types of magnetism: Paramagnetism, ferromagnetism and antiferromagnetism.

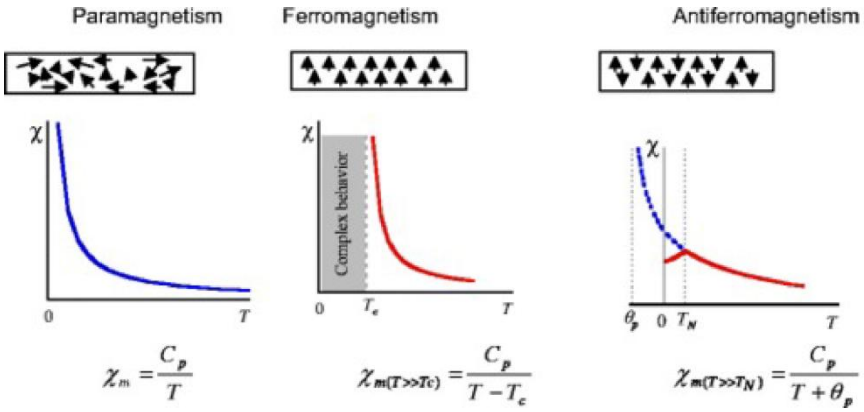

Figure A.8. *χ vs. Temperature for different types of magnetism [4].*

In a paramagnetic material the magnetization of the material is (approximately) directly proportional to an applied magnetic field. However, if the material is heated, this proportionality is reduced: for a fixed value of the field, the magnetization is

4 Julien, C.M.; Ait-Salah, A.; Mauger, A.; Gendron, F. *Ionics*, **2006**, 12, 21-32.

(approximately) inversely proportional to temperature. This fact is condensed by Curie's law:

$$\chi = \frac{C}{T} \qquad \text{(Eq. A.6.3)}$$

where, C is the Curie constant. However, Curie law is only a special case of a more general law, called the Curie-Weiss law.

$$\chi = \frac{C}{T - \theta} \qquad \text{(Eq. A.6.4)}$$

Here, ϴ is the Weiss constant with the dimensions of temperature and equal to zero for those substances which obey Curie´s law.

A.7. Nuclear Magnetic Resonance (NMR)

The ^{23}Na solid state Nuclear Magnetic Resonance (ssNMR) spectrum was recorded in a Bruker Avance III 500 spectrometer (11.7 Tesla magnet) using the standard 1.3 mm Bruker MAS probe. The spinning speed was set to 50 kHz at room temperature. A single pulse sequence was used, with 90º pulse duration of 1.3 μs and a recycle delay of 2 seconds. The ^{23}Na shift was referenced to 0.1 M NaCl (0 ppm). The ^{19}F spectra were recorded in a Bruker Avance III 200 MHz spectrometer (4.68 Tesla) with 50 kHz MAS frequency in order to avoid interference with the rotational sidebands. A single pulse sequence was used, with 90º pulse duration of 2 μs and a recycle delay of 5 seconds. The ^{19}F shift was referenced to solid LiF (-204 ppm). The recycle delay in this case was set to 3 s. These analysis were carried out in the CICEnergigune Research Centre in Miñano, Alava.

Nuclear Magnetic Resonance (NMR) is a nuclei specific spectroscopy which uses a large magnet to probe the intrinsic spin properties of atomic nuclei. Like all spectroscopies, NMR uses a component of electromagnetic radiation (radio frequency waves) to promote transitions between nuclear energy levels (Resonance).

Scientists primarily use liquid state NMR to understand the structure and dynamics of organic compounds. However, there are many compounds which either cannot be placed into solution or need to be studied in the solid state. Examples of such compounds are glasses, minerals, metals, and battery materials, with new solid state materials being developed daily. In NMR, magic-angle spinning (MAS) is a technique often used to perform experiments in solid-state NMR spectroscopy. By spinning the sample (usually at a frequency of 1 to 100 kHz) at the magic angle θ_m (*ca.* 54.74°, where $\cos^2\theta_m=1/3$) with respect to the direction of the magnetic field, the normally broad lines become narrower, increasing the resolution for better identification and analysis of the spectrum.

All nuclei, that is, neutrons and protons, composing any atomic nucleus, have the intrinsic quantum property of spin. The overall spin of the nucleus is determined by the spin quantum number, I. If the number of both the protons and neutrons in a given nucleus are even then I = 0, *i.e.* there is no overall spin. On the contrary, if $I \neq 0$ energy transitions are possible for the nucleus. A non-zero spin is thus always associated with

a non-zero magnetic moment (μ) via the relation $\mu = \gamma \cdot I$, where γ is the gyromagnetic ratio. It is this magnetic moment that allows the observation of NMR absorption spectra caused by transitions between nuclear spin levels. The magnetic moment (μ) is a vector and is partially aligned along the axis of the applied external magnetic field (B_0) in the *z* axis. Nuclei that posses spin align themselves according to their energy states due to the Zeeman effect. However, these vectors are not exactly parallel to *z* axis. Within B_0, there are more spins to precess with a component aligned with the +*z* direction. This population difference results in a net magnetization vector (M_0) in the +*z* direction. The greater the field B_0, the higher population difference and as the NMR signal depends on this difference in population a better signal will be obtained. A second magnetic field (B_1) is applied as a pulse at radiofrequencies (see Figure A.9) and its length and amplitude determine the movement of M_0 from *z* axis to *xy* plane (a 90º pulse tips M_0 fully into *xy* plane). Only the signal in the *xy* plane is "visible" and it is recorded as a FID signal. Then, by application of Fourier Transformation this signal is converted into a NMR spectrum.

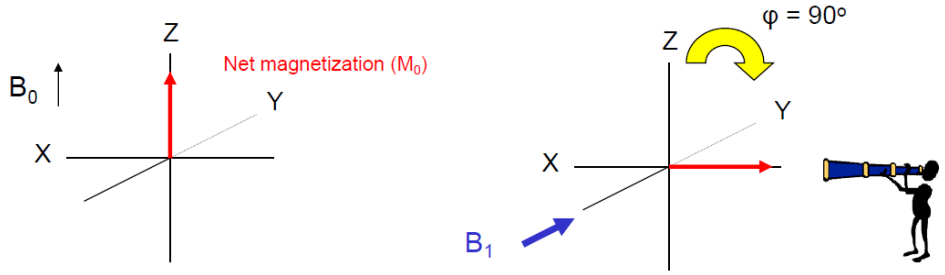

Figure A.9. *Tipping of M_0 from z axis to xy plane due to application of B1 pulse.*

The different element nuclei resonate at different frequencies in MHz so that 500 MHz NMR is referred to the resonance frequency of proton in that particular strength magnetic field. This is why probes need to be tuned in MHz when switching between certain nuclei. ^{1}H and ^{19}F are typically tuned on one channel, while ^{31}P, ^{13}C and ^{15}N on another (see Figure A.10)

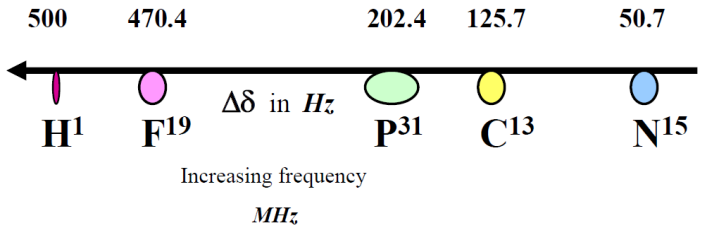

Figure A.10. *Frequency tunes of different nuclei.*

Vanadium has rich redox chemistry, and the V^{5+} is the only oxidation state that can be directly probed by ^{51}V NMR spectroscopy due to its diamagnetic nature. However, it is possible to study paramagnetic vanadium centres (as V^{3+} and V^{4+}) by recording NMR spectra of nuclei that are in close proximity to paramagnetic centres. For example, ^{31}P chemical shifts can be used in order to study paramagnetic vanadium centres in V-P-O containing compounds. For those only containing V^{5+} diamagnetic centres ^{31}P chemical shifts are usually in the range of 20-40 ppm, while for phosphorous atoms neighbouring paramagnetic V^{4+} centres, the ^{31}P NMR chemical shift is significantly larger, often in the region of 1600-2600 ppm. This effect is even more dramatic for V^{3+} species. This paramagnetic ^{31}P NMR line shift is directly proportional to the density of unpaired electrons at the position of the nucleus. Studying paramagnetic shifts is particularly useful in discovering medium and long-range structural information. The magnitude of the paramagnetic shift can provide valuable information about the number of paramagnetic vanadium species in the first and second coordination sphere of the atom, as well as on the oxidation state of such species.

A.8. Electron Microscopy

Morphological characterisation was made by both, Transmission Electron Microscopy (TEM) in a Philips CM200 microscope equipped with an EDAX Energy Dispersive X-ray Analysis (EDX) and Scanning Electron Microscopy (SEM) in a JEOL JSM-6400 and JEOL JSM-7000F microscopes equipped also with EDX Analysis. These analysis were carried out in the Research General Services (SGIker) of the University of the Basque Country (UPV/EHU).

Electron microscopy is a powerful tool for material characterisation at very high magnification. This technique is widely used to supply information on particle size, and shape of powders and also can observe fully or partially dense bodies to study porosity, and microstructure. A high-energy electron beam is used to acquire an image. Except for achieving images with higher magnification, the electron microscopy techniques can be used for qualitative and quantitative analysis of various specimen. A variety of processes can occur when a high energy incident electron interacts with the specimen. These processes generate signals that can be detected and provide more information about the specimen (Figure A.11).

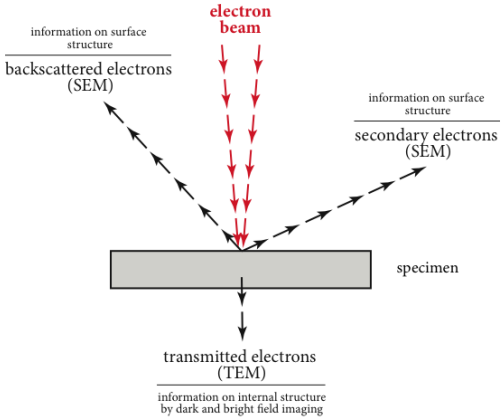

Figure A.11. *Representation of information produced by the interaction between specimen matter and the electron beam.*

Scanning Electron Microscopy (SEM)

The Scanning Electron Microscope (SEM) is one of the most powerful and versatile instruments used in research, development and manufacturing environments. The SEM has the ability to image a wide variety of sample types and sizes, often with minimal sample preparation, and is capable of generating multiple analysis signals, providing high-resolution information about the composition, phase, electrical, optical, and other properties of a sample.

A SEM picture shows the surface of materials; morphology and topography. In topography, some aspects can be observed, such as micro-texture, fracture and wearing of materials. The information obtained on powder morphology can be size and shape of the powders and confirmation of the existence of agglomerates and their nature (hard and soft). The main advantage of a SEM picture is the high quality 3-D image that can be obtained.

The SEM working principle is based on the emission of an electron beam by a tungsten filament when a difference in potential, which can vary from 5 and 30 keV, is applied. This voltage allows the acceleration of the electrons and induces the filament to heat up. The electrons interact with electrons in the sample, producing various signals that can be detected and that contain information about the sample's surface topography and composition (Figure A.12). The electron beam is generally scanned in a raster scan pattern, and the beam's position is combined with the detected signal to produce an image. SEM can achieve resolution better than 1 nanometer. Specimens can be observed in high vacuum, low vacuum and in some cases also in wet condition.

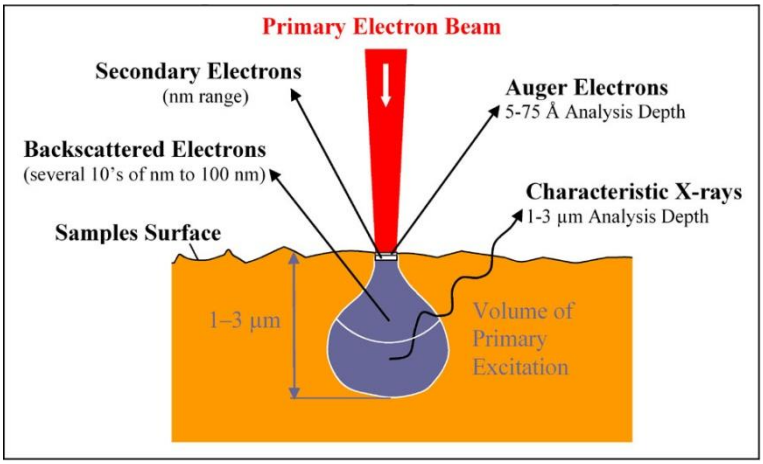

Figure A.12. *Illustration of some events that occur when a high-energy electron beam interacts with a specimen in a Scanning Electron Microscope.*

Transmission Electron Microscopy (TEM)

Transmission electron microscopy (TEM) is an extremely powerful tool for studying nanoscopic structural and morphological information of very fine particles. In TEM a thin solid specimen is bombarded, in high vacuum (~ 10^{-9} Torr), with a highly focussed and mono-energetic electron beam. Due to their high energy electrons propagate through the specimen and images can be obtained with the aid of sophisticated optics.

The image seen with a TEM is formed by an electron beam that passes through the specimen. The electron beam is produced in the microscope by either a thermionic or a field emission process. The generated electrons are accelerated through a voltage of about 100-400 keV. The accelerated electrons then travel through a stack of magnetic lenses. The condenser lens system, depending on the setting, provides a parallel or a convergent incident electron beam onto the sample where most of the electrons are transmitted. The transmitted electron beam then passes through the objective lens, which produces the image, and finally intermediate and projector lenses, which rotate the intermediate images and adjust their magnification onto a fluorescent viewing screen or onto a camera. The attenuation of the electrons beam depends on the

thickness of the sample, and therefore the transmitted electrons can be generally understood as forming two-dimensional projection of the sample mass.

Figure A.13 depicts the main features of a light microscope and the most used electron microscopes: Transmission (TEM) and Scanning (SEM) electron microscopes.

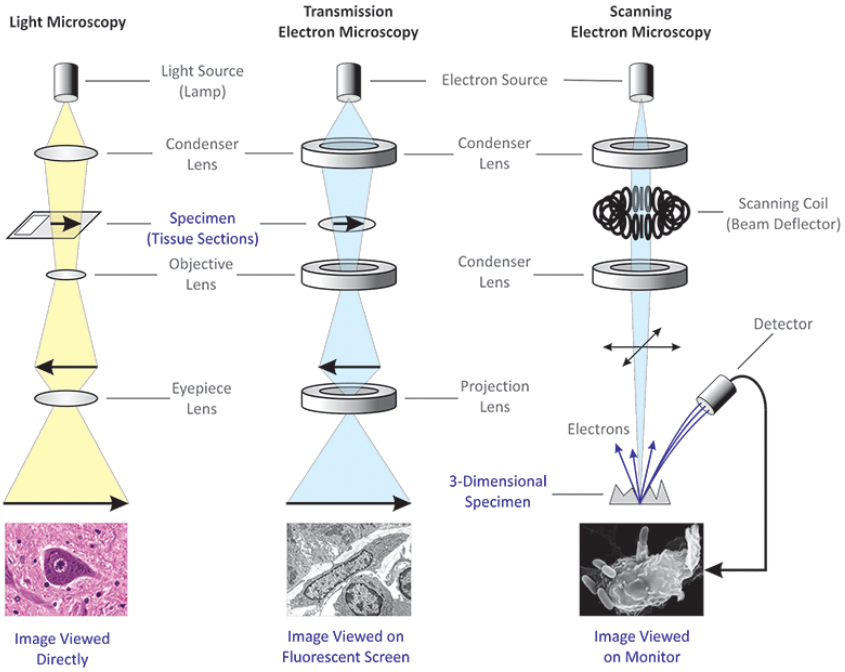

Figure A.13. *Main features of light microscope and TEM and SEM electron microscopes.*

A.9. BET

Specific surface area of the mesoporous samples was measured by nitrogen sorption and calculated based on the Brunauer–Emmet–Teller (BET) equation in the relative pressure (P/P^0) range of 0.05–0.35. These analysis were carried out in the CICEnergigune Research Centre in Miñano, Alava.

BET theory aims to explain the physical adsorption of gas molecules on a solid surface and serves as the basis for an important analysis technique for the measurement of the specific surface area of a material. In 1938, Stephen Brunauer, Paul Hugh Emmett, and Edward Teller published an article about the BET theory in a journal for the first time; "BET" consists of the first initials of their family names.

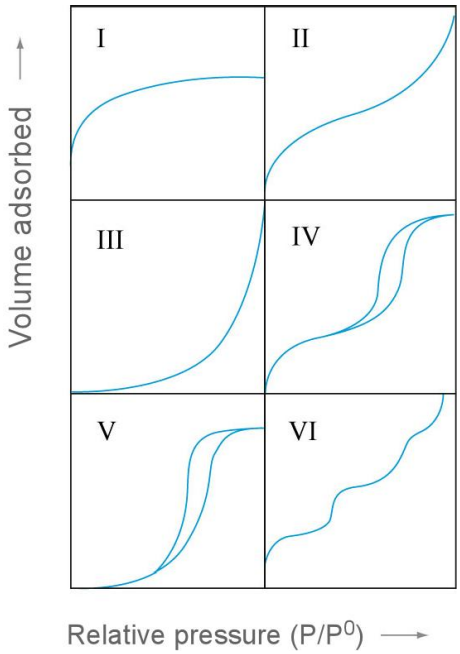

Figure A.14. *Types of adsorption isotherms.*

Adsorption experiments are conducted at a constant temperature and an empirical or theoretical representation of the amount adsorbed as a function of the equilibrium gas

pressure is called an adsorption isotherm. Depending mainly on the structure of solids, the adsorption of gases and vapours give rise to I-VI types of isotherms (Figure A.14). Type I is due to the adsorption on a microporous solid and is typical of chemisorption. Type II isotherms are usually observed in the physical adsorption of gases by non-porous solids. Type III isotherms given by non-porous or macroporous solids, are the characteristic of weak gas-solid interactions. Type IV isotherms describe mono and multilayer adsorption plus capillary condensation. These cases are associated with porous solids in which the adsorbate condenses in the small pores at $P < P^0$. A characteristic feature of the Type IV is its hysteresis loop which is associated with the secondary pore filling process of capillary condensation. Type V isotherms are given by mesoporous or microporous solids and are very much similar to Type III. Type VI isotherms are borderline cases between two or more of the above mentioned types.

The concept of the BET theory is an extension of the Langmuir theory, which is a theory for monolayer molecular adsorption, to multilayer adsorption. By the introduction of a number of simplifying assumptions, Brunauer, Emmet and Teller extended the Langmuir´s kinetic model to multilayer adsorption. The adsorption in the first layer was assumed to take place on an array of surface sites of uniform energy. Molecules in the first layer act as sites for multilayer adsorption, which in the simplest case approaches infinite thickness as $P \rightarrow P^0$. Summation of the amount adsorbed in all layers gives the isotherm equation (A.9.1).

$$V = \frac{V_m \cdot C \cdot P}{(P^0 - P)[1 + (C - 1)(P / P^0)]} \qquad \text{(Eq. A.9.1)}$$

where, P is adsorbate (gas) pressure, P^0 is saturated equilibrium vapour pressure of the adsorbate at the temperature at which the measurement is made, V is volume of gas adsorbed at a particular relative pressure, V_m is volume of gas in monomolecular layer and C constant which according to original theory, is related exponentially to the “first layer” heat of adsorption.

The volume V is measured as a function of P. When $P = P^0$ the equation has a singularity and $V \rightarrow \infty$. This accounts for the steep rise of the isotherm Type II (Figure A.14) as the pressure approaches P^0.

On rearrangement Eq. A.9.1 becomes Eq. A.9.2.

$$\frac{P}{V(P^0 - P)} = \frac{1}{V_m \cdot C} + \left(\frac{C-1}{V_m \cdot C}\right)\left(\frac{P}{P^0}\right) \qquad \text{(Eq. A.9.2.)}$$

$\frac{P}{V(P^0 - P)}$ is plotted against $\left(\frac{P}{P^0}\right)$ giving a straight line in the range of $0.05 \leq P/P^0 \leq 0.35$. The values of V_m and C can be calculated from the intercept and slope and the surface area can be obtained using Eq. A.9.3.

$$S = 0.269 \cdot A_m \cdot V_m \qquad \text{(Eq. A.9.3.)}$$

where A_m, the area occupied by one molecule, can be calculated by the Eq. A.9.4.

$$A_m = f\left(\frac{M}{\rho \cdot N_A}\right)^{2/3} \qquad \text{(Eq. A.9.4.)}$$

where, *M* is molecular weight of the adsorbate molecule, ρ is the density of the adsorbate, N_A is Avogadro´s number and *f* is packing factor. *f* = 1.091 for closest packing.

A.10. Thermal analysis

The thermogravimetric experiments were performed in a NETZSCH STA 449C termogravimetric analyser. The heating rate was 5ºC·min^{-1} under argon flow atmosphere between 25 and 500ºC.

Thermal analysis is a branch of materials science where the properties of materials are studied as they change with temperature. Several methods are commonly used. Simultaneous Thermal Analysis (STA) generally refers to the simultaneous application of Thermogravimetry (TGA) and Differential Scanning Calorimetry (DSC) to one and the same sample in a single instrument. The test conditions are perfectly identical for the TGA and DSC signals (same atmosphere, gas flow rate, vapour pressure of the sample, heating rate, thermal contact to the sample crucible and sensor, radiation effect, etc.).

Simultaneous Thermal Analysis (STA) is a method in which changes in physical and chemical properties of materials are measured as a function of increasing temperature or time. It can provide information about physical phenomena, such as second-order phase transitions, including vapourization, sublimation, absorption, adsorption and desorption. In addition, it can provide information about chemical phenomena including chemisorptions, desolvation, decomposition and solid-gas reactions.

Thermogravimetric analysis (TGA) is commonly used to determine selected characteristics of materials that exhibit either mass loss or gain due to decomposition, oxidation, or loss of volatiles.

Thermogravimetric analysis relies on a high degree of precision in three measurements: mass change, temperature, and temperature change. Therefore, the basic instrumental requirements for TGA are a precision balance with a pan loaded with the sample, and a programmable furnace. The furnace can be programmed either for a constant heating rate, or for heating to acquire a constant mass loss with time. The sample is placed in a small, electrically heated furnace equipped with a thermocouple to monitor accurate measurements of the temperature by comparing its voltage output with that of the voltage *vs.* temperature table stored in the computer's memory. A reference sample may be placed on another balance in a separate chamber.

The TGA instrument continuously weighs a sample as it is heated to temperatures of above 1000°C. Usually thermobalances are coupled to FTIR and mass spectrometers. As the temperature increases, various components of the sample are decomposed and the weight percentage of each resulting mass change can be measured. Results are plotted with temperature on the x-axis and mass loss on the y-axis. The data can be adjusted using curve smoothing and first derivatives are often also plotted to determine points of inflection for more in-depth interpretations.

A.11. Electrochemical Measurements

All the electrochemical characterisation of the materials presented in this work was performed on electrochemical cells. The essential components of an electrochemical cell are a positive and a negative electrode, an electrolyte, a separator and a housing (container). The positive and negative electrodes have to be as close to each other as possible, so as to minimize the internal resistance of the cell. Typically, this resistance is of the order of milliohms (mΩ) so that the voltage drop across the battery terminals shall not be too great when drawing heavy currents. The separator is a thin, usually porous, insulating material which role is to prevent the two electrodes from touching each other and, thereby, short-circuiting. The pores of the separator are filled with electrolyte and the ionic current is conveyed through these pores. The electrolyte is capable of conducting ions between the two electrodes but it must be an electronic insulator in order to avoid self-discharge and/or an internal short-circuit within the cell.

The chemical reactions which generate electricity take place at the two electrodes. Each electrode undergoes a half-cell reaction. An electrode is made up of the chemicals which undergo the reaction, known as the active material, and this is attached to a metal component, the current-collector. The driving force for the external current derived from a cell is the difference in the electrode potentials of the two half-cell reactions. During discharge, the reaction at the negative electrode is an oxidation (or anodic) reaction, with liberation of electrons, and that at the positive electrode is a reduction (or cathodic) reaction, with uptake of electrons. Since batteries are generally considered to operate in the discharge mode, the negative electrode is often known as the anode and the positive electrode as the cathode. The difference between the potentials at the positive and the negative electrodes gives the reversible voltage or open-circuit voltage of the cell, that is, the voltage across the terminals of the cell when there is no net current flow. The voltage of a battery measured on load (*i.e.* when drawing current) will be lower than that on open-circuit. This results from the internal impedance of the battery which is made up of polarization losses at the electrodes and ohmic (resistive) losses in the current-collectors, electrolyte and active materials.

Cyclic Voltammetry (CV)

Cyclic voltammetry or CV is a type of potentiodynamic electrochemical measurement. In a cyclic voltammetry experiment the working electrode potential is ramped linearly *vs.* time like linear sweep voltammetry. Cyclic voltammetry takes the experiment a step further than linear sweep voltammetry which ends when it reaches a set potential. When cyclic voltammetry reaches a set potential, the working electrode's potential ramp is inverted. This inversion can happen multiple times during a single experiment. The current at the working electrode is plotted *vs.* the applied voltage to give the cyclic voltammogram trace.

In cyclic voltammetry, the electrode potential ramps linearly *vs.* time as shown in Figure A.15. This ramping is known as the experiment's scan rate (V/s).

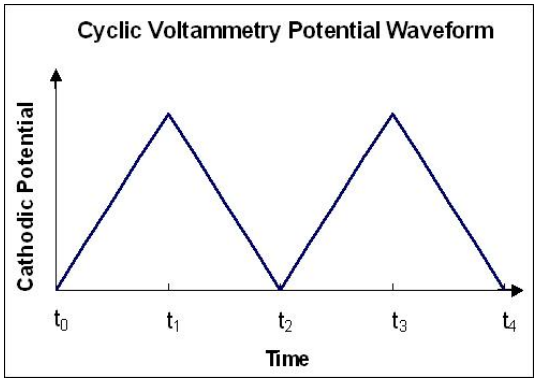

Figure A.15. *Cyclic Voltammetry waveform.*

The potential is applied between the reference electrode and the working electrode and the current is measured between the working electrode and the counter electrode. These data are then plotted as current (I) *vs.* potential (*E*). As the waveform shows, the forward scan produces a current peak for any analytes that can be reduced (or oxidized depending on the initial scan direction) through the range of the potential scanned. The current will increase as the potential reaches the reduction potential of the analyte, but then falls off as the concentration of the analyte is depleted close to the electrode

surface. If the redox couple is reversible then when the applied potential is reversed, it will reach the potential that will reoxidize the product formed in the first reduction reaction, and produce a current of reverse polarity from the forward scan. This oxidation peak will usually have a similar shape to the reduction peak. As a result, information about the redox potential and electrochemical reaction rates of the compounds are obtained.

Galvanostatic Cycling

In a galvanostatic cycling regime a constant current is employed both throughout the charging and the discharging process of a battery.

The charging of a secondary battery involves passing current electricity through the battery in order to reverse the discharge process. An electrochemical reduction reaction takes place at the negative electrode while electrochemical oxidation of the active material occurs at the positive electrode. The charging of a battery is therefore an electrolytic process. The conditions under which a secondary battery is charged are at least as important as the discharge conditions in determining its useful life.

When a cell/battery is discharged at a constant current, the storage capacity is the product, expressed in ampere-hours, of the current and the number of hours for which the cell/battery can be discharged to a defined cut-off voltage. The ampere-hour is a practical unit and is expressed in SI units as: 1 ampere-hour = 3600 coulombs. The value of the capacity depends not only upon the ambient temperature and upon the age/history of the cell, but also, to a greater or lesser extent, upon the rate of discharged employed. The higher the rate of discharge, the less the available capacity.

Considering the capacity and the stored energy available from a battery, it is essential to define both the discharge rate and the temperature to be employed. Battery manufacturers generally state a rated capacity (so called nominal or name-plate capacity) under specified discharge conditions, often the 5-h rate at 25ºC to a designed cut-off voltage. For convenience, the term C/t (where t is the discharge time in hours) is often used to define the rate at which the capacity is calculated. Thus, C/5 is the 5-h discharge rate and 2C is the 30-min rate. The amount of charge (capacity) withdrawn compared with the total amount which is available at the same discharge rate is the

depth-of-discharge (DOD). This ratio is usually expressed as a percentage. It follows that the state-of-charge (SOC) of a battery is the fraction of the full capacity that is still available for further discharge, *i.e.* SOC = [100 – (%DOD)]%.

Swagelok cell assembly

The electrochemical tests performed using Swagelok cell configuration were carried out in the CICEnergigune Research Centre in Miñano, Alava. The active material powder was mixed with Ketjen black carbon and PVdF powder in 75:20:5 *wt.*% proportion and ground with acetone using a mortar. Once acetone was evaporated pellets of the mixture were produced (10 mm diameter) using a press and applying up to 5 tons (Figure A.16a). Afterwards they were weighted and kept inside the glovebox.

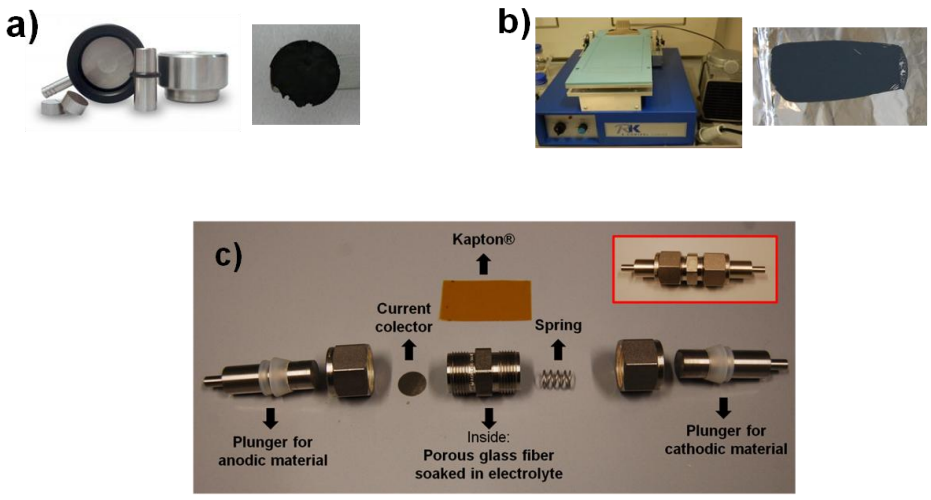

Figure A.16. ***a)*** *Pellet and* ***b)*** *laminate preparation for Swagelok cells.* ***c)*** *Swagelok cell assembly.*

For the preparation of laminate electrodes (Figure A.16b), active material and Cenergy (C-65) carbon were mixed with acetone in a mortar. Then, once the acetone was evaporated, the corresponding amount of a dissolution of NMP (N-methyl pyrrolidone) with 5 *wt.*% of PVdF was added in order to obtain the following proportion of active

material, C and PVdF: 80:10:10 *wt.*%. The resulting mixture was stirred for 1 hour and laminated on an aluminium foil using "doctor blade" technique. The laminate was dried at 80ºC in a vacuum oven for one day and then 10 mm. (7/16 inches) electrodes were cut. They were pressed up to 10 tons, weighted and dried under vacuum in a Buchi oven at 120ºC for one day. Afterwards they were kept inside the glovebox. Both, pellet and laminate electrodes were assembled in the Swagelok cell as shown in Figure A.16c where a glass fiber separator (11.5 mm or 1/2 inches) soaked in electrolyte is placed between the positive and the negative electrode, this latter consisting of metallic sodium.

Coin cell assembly

The electrochemical tests performed using Coin cell configuration were carried out in the *Institut de Chimie de la Matière Condensèe de Bordeaux* (ICMCB), in Bordeaux, France.

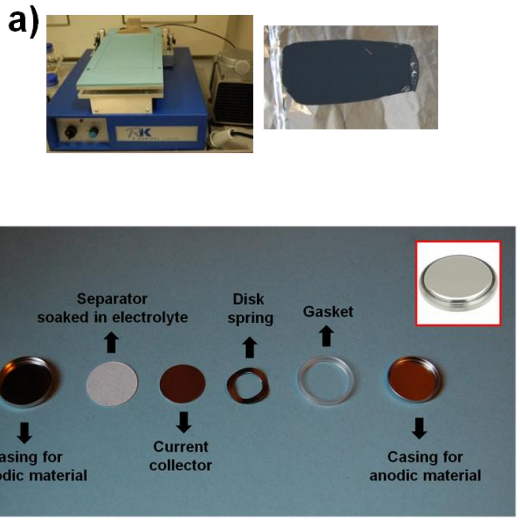

Figure A.17. ***a)*** *Laminate preparation for coin cells.* ***b)*** *2032 coin cell assembly.*

Laminate electrodes were prepared by mixing active material and a mixture of S-black and graphite carbon (50:50 *wt.*%) with acetone in a mortar. Then, once the acetone was

evaporated, the corresponding amount of a dissolution of NMP (N-methyl pyrrolidone) with 5 *wt.*% of PVdF was added in order to obtain the following proportion of active material, C and PVdF: 80:10:10 *wt.*%. The resulting mixture was stirred for 1 hour and laminated on an aluminium foil using "doctor blade" technique. The laminate was dried at 80ºC in an oven for one day and then 14 mm. electrodes were cut. They were pressed up to 10 tons, weighted and dried under vacuum in a Buchi oven at 80ºC for one day. Afterwards they were kept inside the glovebox.

Laminate electrodes were assembled in CR-2032 coin cell as shown in Figure A.17b where the positive electrode is connected through a glass fiber separator (18 mm) soaked in electrolyte to the negative electrode which consist of metallic sodium.

A.12. X-Ray Absorption Spectroscopy (XAS)

Vanadium K-edge X-ray (5465 eV) Absorption Near Edge Structure (XANES) and extended X-ray Absorption Fine Structure (EXAFS) were recorded in transmission at beamline XAFS of the Elettra Synchrotron Radiation Facility and B18 beamline of the Diamond Light Source synchrothron. During the measurements, the samples were kept at room temperature.

The powders and the different standards employed in Elettra and Diamond facilities were ground using a mortar, and afterwards combined with PVP or cellulose, respectively. In order to obtain an edge jump > 0.2 in the XAS spectra, around 10 mg of sample in 125 mg of PVP were mixed when working in Elettra and 10 mg of sample in 75 mg of cellulose were mixed while working in Diamond. Pellets of the mixture were produced using a press, and these were finally attached to the sample holder using small stripes of kapton.

XAS, or X-ray Absorption Spectroscopy, is a broadly used method to investigate atomic local structure as well as electronic states. Very generally, an X-ray strikes an atom and excites a core electron that can either be promoted to an unoccupied level, or ejected from the atom. Both of these processes will create a core hole.

XAS data are obtained by tuning the photon energy using a crystalline monochromator to a range where core electrons can be excited (0.1-100 keV photon energy). The "name" of the edge depends upon the core electron which is excited: the principal quantum numbers n = 1, 2, and 3 correspond to the K-, L-, and M-edges, respectively. For instance, excitation of a 1s electron occurs at the K-edge, while excitation of a 2s or 2p electron occurs at an L-edge (Figure A.18)

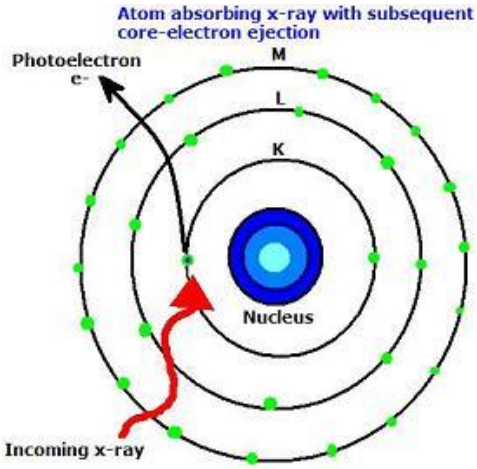

Figure A.18. *The wave vector of a photoelectron.*

There are two main regions found on a spectrum generated by XAS data (Figure A.19). The X-ray Absorption Near-Edge Structure XANES introduced in 1980 and later in 1983 called also NEXAFS (Near-edge X-ray Absorption Fine Structure) which are dominated by core transitions to quasi bound states (multiple scattering resonances) for photoelectrons with kinetic energy in the range from 10 to 150 eV above the chemical potential. In the high kinetic energy range of the photoelectron the scattering cross-section with neighbour atoms is weak and the absorption spectra are dominated by EXAFS (Extended X-ray Absorption Fine Structure) where the scattering of the ejected photoelectron off neighbouring atoms can be approximated by single scattering events.

The total absorption coefficient $\mu \cdot x$ is calculated as:

$$\mu \cdot x = \ln (I_0/I_1) \qquad \text{(Eq. A12.1)}$$

where μ is the absorption coefficient of the sample (in cm^{-1}), x is the thickness of the sample (in cm), I_0 is the incoming photon flux and I_1 is the transmitted photon flux from the sample (see Figure A.20). The edge jump is defined as the difference between the post and pre-edge absorption. For statistical reasons, the absorption coefficient should

have a post-edge absorption value between 1 and 2, mainly depending on the composition of the sample.

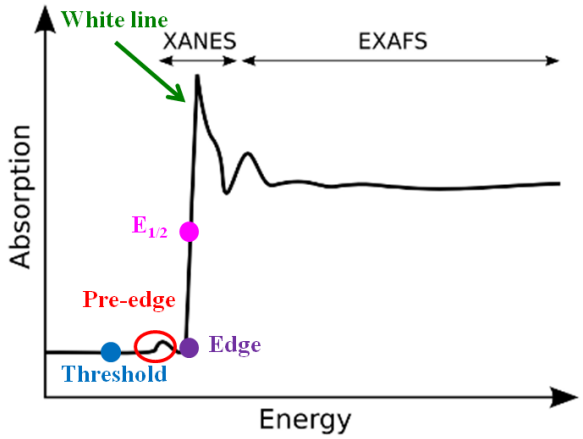

Figure A.19. *A typical absorption XAS spectrum.*

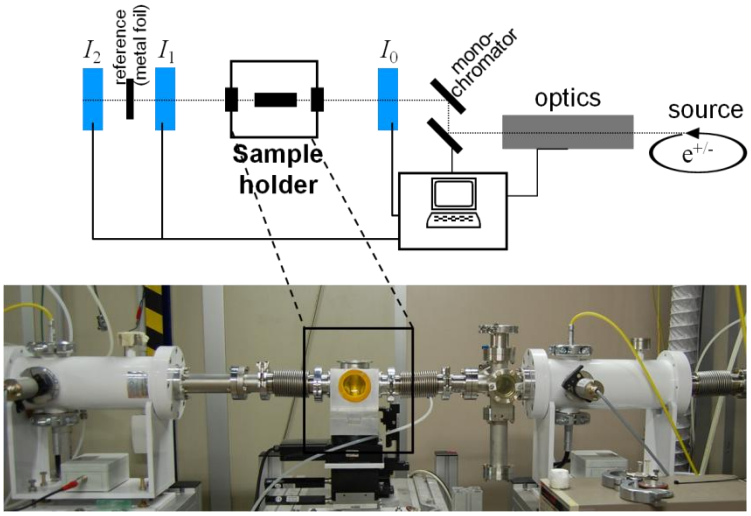

Figure A.20. *Experimental setup of a X-Ray Synchrotron line for XAS measurements.*

Supplementary Information

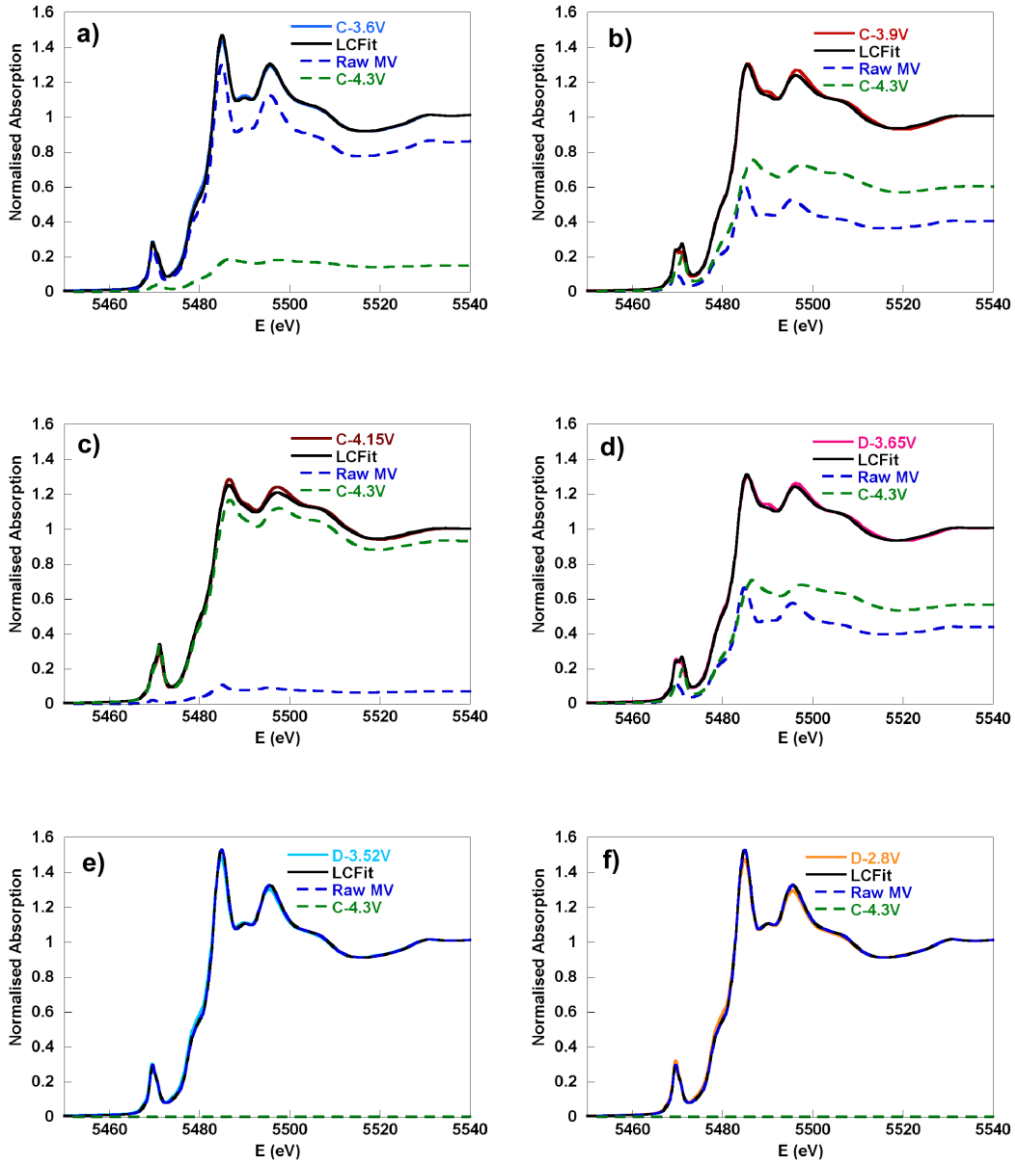

Figure A.21. *XANES spectra of different MV post mortem samples in charge (**a), b)** and **c)**) and discharge (**d)**, **e)** and **f)**), and the corresponding fit to a linear combination of the raw MV sample and C-4.3 V XANES profiles (LCFit). "C" indicates charge and "D" indicates discharge.*

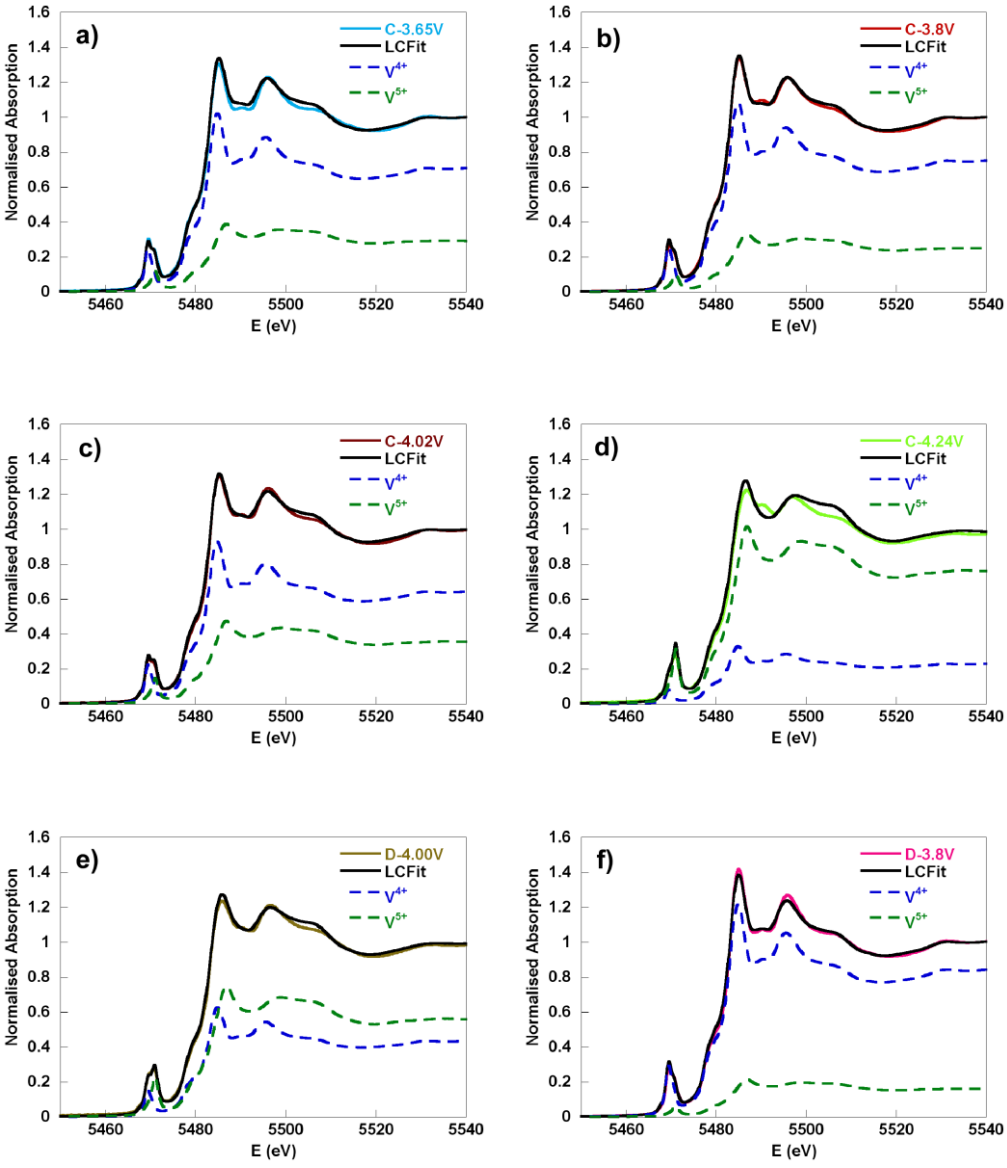
a)
C-3.65V
LCFit
V4+
V5+
b)
C-3.8V
LCFit
V4+
V5+
c)
C-4.02V
LCFit
V4+
V5+
d)
C-4.24V
LCFit
V4+
V5+
e)
D-4.00V
LCFit
V4+
V5+
f)
D-3.8V
LCFit
V4+
V5+
Normalised Absorption
E (eV)
0
0.2
0.4
0.6
0.8
1
1.2
1.4
1.6
5460
5480
5500
5520
5540

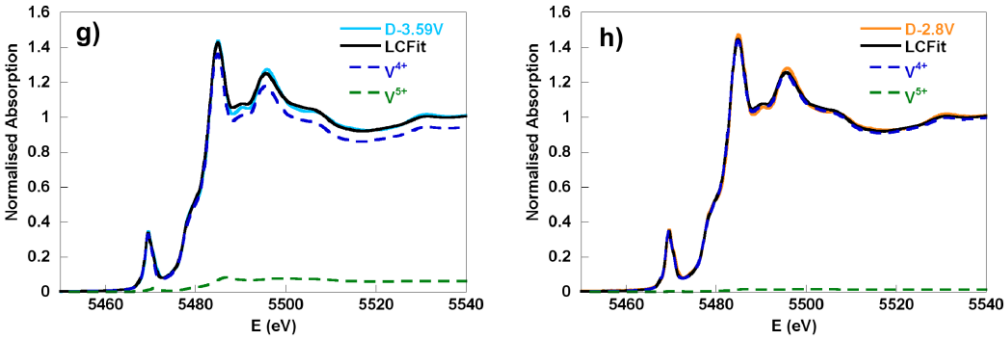

Figure A.22. *XANES spectra of different V4 post mortem samples in charge (**a), b)**, **c)** and **d)**) and discharge (**e)**, **f), g)** and **h)**), and the corresponding fit to a linear combination of the V^{4+} and V^{5+} standards XANES profiles (LCFit). "C" indicates charge and "D" indicates discharge.*

List of Publications

[1] "Na-ion batteries, recent advances and present challenges to become low cost energy storage systems".

Palomares, V.; **Serras, P.**; Villaluenga, I.; Hueso, K.B.; Carretero-González, J.; Rojo, T. *Energy Environ. Sci.* **2012**, 5,5884-5901.

[2] "Crystal chemistry of Na insertion/deinsertion in $FePO_4$-$NaFePO_4$".

Casas-Cabanas, M.; Roddatis, V.; Saurel, D.; Kubiak, P.; Carretero-González, J.; Palomares, V.; **Serras, P**.; Rojo, T. *J. Mater. Chem.* **2012**, 22, 17421-17423.

[3] "High voltage cathode material for Na-ion batteries of general formula $Na_3V_2O_{2x}(PO_4)_2F_{3-2x}$".

Serras, P.; Palomares, V.; Goñi, A.; Gil de Muro, I.; Kubiak, P.; Lezama, L.; Rojo, T. *J. Mater. Chem.* **2012**, 22, 22301-22308.

[4] "Electrochemical performance of mixed valence $Na_3V_2O_{2x}(PO_4)_2F_{3-2x}$ as cathode for sodium-ion batteries".

Serras, P.; Palomares, V.; Goñi, A.; Kubiak, P.; Rojo, T. *J. Power Sources.* **2013**, 241, 56-60.

[5] "Enhanced electrochemical performance of vanadyl (IV) $Na_3(VO)_2(PO_4)_2F$ by *ex-situ* carbon coating".

Serras, P.; Palomares, V.; Kubiak, P.; Lezama, L.; Rojo, T. *Electrochem. Commun.* **2013**, 34, 344-347.

[6] "Electrochemical Na extraction/insertion of $Na_3V_2O_{2x}(PO_4)_2F_{3-2x}$".

Serras, P.; Palomares, V.; Alonso, J.; Sharma, N.; López del Amo, J.M.; Kubiak, P.; Fdez-Gubieda, M.L.; Rojo, T. *Chem. Mater.* **2013**, 25, 4917-4925.

[7] "Structural evolution of high energy density V^{+3}/V^{+4} mixed valent $Na_3V_2O_{2x}(PO_4)_2F_{3-2x}$ (x = 0.8) sodium vanadium fluorophosphate using in-situ synchrotron X-ray powder diffraction".

Serras, P.; Palomares, V.; Rojo, T.; Brand, H.; Sharma, N. *J. Mater. Chem.A* **2014**, 2, 7766-7779.

[8] "Sodium distribution and reaction mechanisms of a $Na_3V_2O_2(PO_4)_2F$ electrode during use in a sodium-ion battery".

Sharma, N.; **Serras, P**.; Palomares, V.; Brand, H.; Alonso, J.; Kubiak, P.; Fdez-Gubieda, M.L.; Rojo, T. *Chem. Mater.* **2014**, 26, 3391-3402.

Batteries are one of the most determining energy storage devices. Among them, sodium-ion batteries are presented as the best alternative to lithium-ion batteries especially in the field of stationary energy storage due to the more abundance and lower cost of sodium. Thus, it is necessary to search and optimize new electrode and electrolyte materials in order to better understand the behaviour of these sodium based devices. One of the most promising cathodic materials for sodium-ion batteries are the sodium vanadium fluorophosphates. They show high voltage performance and long-term stability so they could lead to high energy density materials.

In this work the relationship between V^{3+} $Na_3V_2(PO_4)_2F_3$ and V^{4+} $Na_3V_2O_2(PO_4)_2F$ phases has been established as end members of $Na_3V_2O_{2x}(PO_4)_2F_{3-2x}$ family of compounds. Different compounds belonging to this family have been hydrothermally synthesised by variating the type and amount of *in-situ* carbon in the final product. Among them, $Na_3V_2O_{2x}(PO_4)_2F_{3-2x}$ (x = 0.8) and $Na_3V_2O_2(PO_4)_2F$ samples have been deeply studied. Several characterisation methods, such as X-ray diffraction, infrared spectroscopy, electronic microscopy, magnetic measurements and electron and neutron magnetic resonance (EPR and NMR, respectively) have been used to determine the most important features of each material. The influence of the different compositions and materials coatings on their electrochemical performance has also been evaluated. Finally, the electrochemical mechanism of $Na_3V_2O_{2x}(PO_4)_2F_{3-2x}$ (x = 0.8) and $Na_3V_2O_2(PO_4)_2F$ phases has been studied by both, *ex-situ* and *in-situ* analysis and the most remarkable differences and similarities between them have been discussed.

Paula Serras Malillos
July 2014